A Soft Chemistry Approach to Extended [Co_6Se_8] Materials

Anouck Champsaur

Submitted in partial fulfillment of the
requirements for the degree of
Doctor of Philosophy
in the Graduate School of Arts and Sciences

COLUMBIA UNIVERSITY

2018

ABSTRACT

A Soft Chemistry Approach to Extended [Co_6Se_8] Materials

Anouck Champsaur

This dissertation describes advances toward creating programmable building blocks and assembling them into new, tailored materials. I describe extended materials formed of bonded sets of cobalt selenide clusters. Rationally designed chemical transformations that form these sets give us precise control over the extent and dimensionality of the material.

The cobalt selenide clusters fundamental to this study are members of a larger class of clusters with the M_6E_8 core (M = metal, E = chalcogen). Chapter 1 introduces this family of clusters and reviews examples of previously made materials.

Chapter 2 unveils a family of site-differentiated clusters, $Co_6Se_8(CO)_x(PEt_3)_{6-x}$, their substitution reactions, and assembly into bridged dimers and trimers. Electrochemical methods were used to investigate electronic coupling between the cores, by comparing the electrochemical behavior of the dimer and trimer relative to their monomeric counterparts. We further performed magnetic susceptibility measurements of the monomers and assemblies.

Chapter 3 introduces electrocrystallization as a method to synthesize extended, crystalline, solid state compounds from superatomic building blocks. By electrocrystallizing redox-active [Co_6Se_8] clusters with labile ligands in the presence of an ionic template, we created a crystalline polymeric material that exhibits weaving at the nanoscale.

Chapter 4 presents a metal coordination approach to [Co_6Se_8] materials via reactive groups on the capping ligands. The redox-activity and multinuclearity of the superatom components creates a new level of complexity and synthetic sophistication to previously reported frameworks. In collaboration with Prof. Christopher Bejger (University of North Carolina at

Charlotte), I installed carboxylate groups on the surface of the cluster. With this building block in hand and a simple metal salt, $Zn(NO_3)_2$, we discovered two sets of distinct solvothermal reaction conditions that yielded two different solids. Both are homogenous, crystalline, porous solids whose dimensionality is tuned by subtle changes in reaction conditions. I further showed that the dimensionality could be further reduced by chemical exfoliation to yield free-floating sheets of zinc-coordinated clusters in which the porosity and redox-activity of the bulk solid is preserved.

Finally, Chapter 5 outlines a novel chemical transformation that dimerizes $[Co_6Se_8]$ units to form a material with an expanded core, $[Co_{12}Se_{16}]$, that exhibits electronic and optical properties distinct from the parent monomer. To accomplish this dimerization, I installed a reactive carbene on the $[Co_6Se_8]$ core to create a latent fusion site. We show by cyclic voltammetry, infrared spectroscopy, single crystal X-ray diffraction, and density functional theory calculations that the resulting fused $[Co_{12}Se_{16}]$ material exhibits strong electronic coupling and electron delocalization.

These chapters present novel synthetic approaches toward creating $[Co_6Se_8]$ materials with tuned dimensionality, size, and extensive charge delocalization.

TABLE OF CONTENTS

LIST OF FIGURES AND TABLES

ACKNOWLEDGEMENTS

It's been a privilege to spend the last five years in this scientific playground. I'd like to express my gratitude to the many people that supported me both scientifically and personally over the years.

First and above all I thank Colin Nuckolls and Mike Steigerwald. I am very fortunate to have wound up in this research group. Their synergistic ideas, writing styles, advising styles and approaches to science have been instrumental in my growth as a scientist. Colin has an infectious positive energy and a well of ideas that never runs dry. Many results presented here came from trying some of Colin's "wild" ideas. He is incredibly generous and kind to his students, and has a special ability to provide direction in a way that allowed me the space to make mistakes and be creative. I am grateful for the freedom and resources to explore interesting ideas, and his support and help transforming ideas into tangible projects. I will cherish his guidance and mentorship, and it'll be hard to find a better boss. Maybe I should stay. I am lucky to have had Mike Steigerwald as a second advisor. The work presented in this dissertation is largely born out of chemistry he developed, ideas he suggested, and his unique vision of science. He is a great listener and a deep thinker, and I spent countless hours in his office learning about science and discussing life. I am indebted to Mike for many important conversations and for encouraging me to think more critically about results.

Creative freedom can be quite intimidating, but I've been lucky to be surrounded by incredible students and postdocs who give me support and guidance. I am thankful to all present and former Nuckolls group members, and in particular those that welcomed me and helped me get on my feet in the beginning: Dan Paley, Tim Su, Nate Schuster, and Christopher Bejger.

I want to express my appreciation to all of my collaborators. Dan Paley performed the bulk of the crystallographic analysis in my graduate work. Christopher Bejger shared his framework project with me. Jaeeun Yu was incredibly helpful and I couldn't have finished the framework project without her. Alexandra Velian made important contributions to my first project and taught me some valuable inorganic synthesis tricks. Raúl Hernández Sánchez helped me bring together scattered results and thoughts when he joined the lab and I am grateful for his encouragement throughout. Taylor Hochuli has been a pleasure to work with in the cluster team. Bonnie Choi performed magnetic measurements. I am grateful to Patrick Batail, Cécile Mézière, and Magali Allain, my collaborators from Université d'Angers in France who worked with me on the cloth project. Patrick gave me a warm welcome to his lab when I visited, and his endless curiosity and unique vision have provided the inspiration for many ideas and projects. Lastly, I thank the Roy group for their help and support over the years, both with science and with wine (in particular: Bonnie, Evan, Andrew, Anastasia, and Doud).

I am indebted to Xavier Roy, who in addition to being a part of my thesis committee has been incredibly supportive from the beginning. He was always willing to talk to me about science and provide support, resources, and ideas. He kindly included me in his group meetings, and helped guide me when I first got started in the lab.

I would like to thank Latha Venkataraman for serving on my thesis defense committee. I wish I had sought her advice and mentorship sooner in my graduate career. I am also grateful to Xiaoyang Zhu for serving on my defense committee. I thank Tristan Lambert for serving on my second and fourth year defense committees.

I'm grateful for Ryan Hastie and her administrative and personal support, sense of humor, and keeping us in line. Thank you also to Liz Powell and KO Campbell for their administrative support in previous years.

I'm indebted to my undergraduate mentors: Bob Bergman gave me the confidence to pursue graduate school, and Ron Zuckermann created a wonderful lab environment. My youth soccer coach inspired a lasting discipline with athleticism and instilled in me that if you think you're good, that's as good as you'll ever be.

A family can take many forms and I am so grateful for my friends both inside and outside the department that have been there for me over the years, my climbing partners, and sisters from another mother.

Lastly, thank you to my family for the nurturing, love, and support. It is truly thanks to my parents Anne and Gérard, with their generosity, rigorous work ethic, and unconditional dedication to their children, that I am here. My dad taught me to be disciplined and find joy in work. My mom embodies kindness and compassion. My grandmother, Grany, has a rare curiosity and energy for the world even at the age of 98 that inspires me. I thank my brother for my musical education. My big sisters Marine and Amélie are constant sources of inspiration and are the epitome of successful, driven women, and Jeff is a wonderful brother-in-law.

For Maman, Papa, and Grany.

Chapter 1. Background and Introduction

1.1. Introduction

Atomically defined clusters of atoms typically exhibit physical properties beyond those of their constituent atoms.[1] The ability to manipulate both the composition of these nanoclusters and their inter-cluster binding and interactions enables us to expand our traditional periodic table to a third dimension. The idea that new phenomena (e.g. electronic, magnetic) will emerge in materials assembled from these nanoclusters motivates the Nuckolls group and others to develop novel superatomic building blocks. These would enable the preparation of molecules and solids that would otherwise be inaccessible by traditional synthetic methods, while maintaining the structural integrity and properties of the component building blocks. This dissertation focuses on the development of such nanoscale "atoms", termed "superatoms", whose composition and surface ligands can be selectively manipulated in order to create extended assemblies with emergent properties.

Superatoms have previously been defined as "cluster[s] consisting of more than one atom, but acting as a stable unit in some ways analogous to an atom".[1] The superatom concept was first established for aluminum clusters of discrete sizes synthesized from gas phase experiments.[2] Theoretical electronic structure analysis revealed that the chemically stable anionic cluster Al_{13}^-, for example, demonstrates high electronic affinities comparable to a chlorine atom, and thus as a discrete unit it mimics the behavior of individual halogen atoms.[3] A large number of molecular clusters fit within the aforementioned superatom definition, such as fullerenes (1 nm),[4] inorganic atomic clusters (1 - 2 nm),[5] and larger inorganic nanocrystals (up to 10 nm).[6] Herein, I will use the term "superatom" predominantly as a structural classification and limit my discussion to atomically precise metal chalcogenide clusters.

1.2. Metal Chalcogenide Clusters with Core Type $[M_6E_8]$ (M = Metal, E = Chalcogen)

The Nuckolls group focused its initial superatom synthetic efforts on $Co_6E_8(PR_3)_6$ clusters, which are members of a larger class of clusters with the $[M_6E_8]$ stoichiometry (M = metal, E = chalcogen). Although known since the 1980s,[7] these clusters have only recently re-emerged as identifiable building blocks for extended materials thanks to efforts in their synthetic tunability. Multiple desirable properties like redox activity, large magnetic moments, and luminescence arise in such superatoms.

Structurally, the inorganic $[M_6E_8]$ core is composed of an octahedron of metal atoms contained within a cube of face-capping chalcogen atoms (Figure 1.1). Passivating ligands L such as phosphines in the case of M = Co coordinate each metal atom to yield $M_6E_8L_6$.

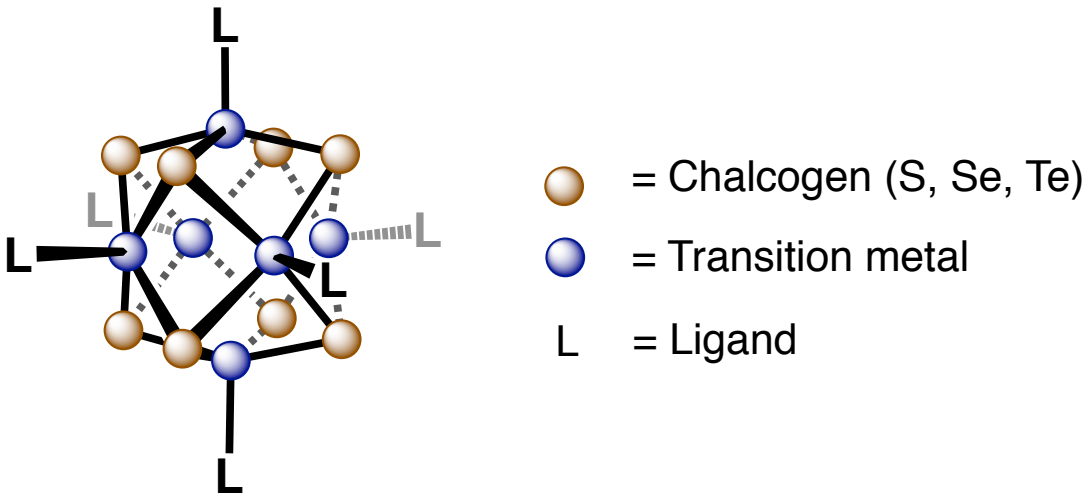

Figure 1.1. Structure of the metal chalcogenide superatom $M_6E_8L_6$ central to this dissertation (M = transition metal, E = chalcogen, L = ligand).

The $[M_6E_8]$ core is a constituent fragment of traditional inorganic materials with properties such as superconductivity and ferromagnetism (e.g., Chevrel[8] and Zintl[9] phases), historically synthesized via high temperature and pressure in the solid state. Multiple groups independently synthesized the first ligand-capped monomeric analogues of these solid state compounds via

three principal routes: (1) dimensional reduction from the bulk (excision),[7e, 10] (2) condensation of smaller clusters,[11] and (3) isolation of discrete clusters in the thermal reaction of phosphine chalcogenides with low valent transition metals.[7i, 7k] The latter "soft chemistry"[12] approach provides a significant advantage over the former with its mild conditions, fewer steps due to a solution-based synthesis from molecular components, and greater synthetic tunability. Isolating the fundamental building block of the Chevrel phases allowed for structural, electronic, and magnetic investigations of the individual clusters, which in turn led to further understanding of the bulk.

Concurrently, the discovery of isolable nanoparticles and their distinct, size-dependent photophysics and electronic structures was central to the development of our understanding of the nanosized regime and its intrinsic properties.[6b, 13]

1.3. $[M_6E_8]$ Clusters as Superatomic Precursors to Materials

The preparation of soluble $[M_6E_8]$ units also led to significant advances in the bottom-up synthesis of extended solids. Would a $[M_6E_8]$ monomer preserve its structural integrity when heated to form an extended solid? Steigerwald showed that upon heating, phosphine-capped $[M_6E_8]$ clusters converted to solid state transition metal chalcogenides in which the cluster core was severely distorted.[14] These very clusters, interestingly, were thus intermediates between their atomic precursors (phosphine chalcogenides and low valent transition metals) and extended semiconducting solids. The question remained: how could we synthetically manipulate a $[M_6E_8]$ monomer to rationally create new, interesting materials in which the core is structurally intact?

Multiple groups have explored this challenge (for M = W and Re), as using preformed $[M_6E_8]$ entities is a rational and facile method to impart their unique properties to new materials.

The dominating, common synthetic approach to such solids is through metal salt coordination to reactive groups on the capping ligands of the cluster (for examples, see DiSalvo,[15] Long,[16] Fedorov,[17] and Zheng[18]). Clusters with rhenium are particularly prominent in these examples, as their chemistry has been richly developed: site-differentiated $[Re_6Se_8]$ clusters have been synthesized and extensively studied,[19] as well as their assembly into oligomers,[20] supramolecular arrays,[21] and dendrimers.[22] These assemblies, while structurally interesting, do not exhibit significant inter-cluster interactions.

$[Co_6E_8]$ clusters present an open avenue for exploration. They are more electron-rich than other metal analogues and feature L-type rather than X-type metal-capping ligands. More notably, a significant advantage is that they are synthesized under mild conditions from molecular components, to the contrary of rhenium and molybdenum clusters, which are obtained principally from the dimensional reduction of parent solid state compounds. Therefore, the molecules and materials presented herein are truly assembled from the bottom up; that is, from atoms to superatoms to solids, in a controlled and directed fashion. The following section presents $[Co_6E_8]$-based materials that have emerged in recent years from the Roy and Nuckolls labs.

1.4. Materials from $[Co_6Se_8]$ Superatoms

A seminal 2013 paper from Roy, Steigerwald, and Nuckolls reports the formation of a charge transfer salt between electron-rich $Co_6Se_8(PEt_3)_6$ and electron-deficient C_{60}.[23] The structure of the resulting crystalline solid parallels that of an atomic analogue, the cadmium iodide (CdI_2) structure type, but on a nanometer scale instead of an Ångstrom scale. Furthermore, the material exhibits activated electronic transport and magnetic ordering. Thus, it seemed

possible to build solids from superatomic molecular clusters that (1) conserve the structural integrity of their building blocks, (2) are nanoscale analogues of atomic solids and (3) exhibit collective electronic and magnetic properties due to interactions between constituent building blocks. This work paved the way for a wide range of binary superatomic crystals (SACs) with novel materials properties both in the bulk and in exfoliated form.[24]

1.5. Synthetic Approaches Toward Reactive [Co_6Se_8] Monomers

The aim of my thesis work has been to create *covalent* assemblies of superatoms. My initial synthetic goal was thus to create suitable, reactive [Co_6Se_8] monomers. This can be achieved through two distinct approaches: (1) introducing novel, removable, reactive ligands on the cluster surface and (2) incorporating a secondary functionality on the capping ligand that can further react (e.g. olefins, -NH_2, -COOH, -RNC).

My initial challenge was to develop the chemistry necessary to manipulate the ligand environment around the [Co_6Se_8] core. To this end, I synthesized a family of regiochemically pure, atomically precise carbonylated clusters of the form $Co_6Se_8(CO)_x(PEt_3)_{6-x}$. The CO group is a synthetically useful handle that can be easily manipulated. Previous strategies toward $Co_6Se_8(PR_3)_6$ clusters employed stoichiometric combinations of $Co_2(CO)_8$, Se, and phosphine. In a new approach, we included a significant excess of Se, which effectively decreases the available reactive phosphine in the reaction mixture. The products are easily separated using fractional crystallization and column chromatography. The reaction chemistry that produces these new building blocks is detailed in Chapter 2. Professor Alexandra Velian (University of Washington; formerly a postdoc in the Nuckolls group) helped develop this reaction chemistry.

Using a different synthetic approach, we prepared a superatom with a reactive carboxylic

acid functionality, $Co_6Se_8(PEt_2PhCOOH)_6$. Because carboxylic acids readily coordinate metals, this cluster cannot be easily prepared from a carboxylate-containing phosphine. Therefore, I synthesized a reactive precursor, $Co_6Se_8(PEt_2PhBr)_6$ and converted each Br in this surprisingly robust superatom to a corresponding COOH through a 6-fold lithium/halogen exchange, addition of CO_2 gas, and acidification. This shows that the aryl halide is a good chemical handle for post-synthetic cluster modifications; many other standard organic transformations can be envisaged.

1.6. From $[Co_6Se_8]$ Monomers to Covalent Materials

The ensuing challenge was to probe the reactivity of these new species and directly connect $[Co_6Se_8]$ cores. The position of the CO group directs the formation of predetermined shapes and arrangements. I prepared the simplest combinations of superatoms, a linear dimer and trimer, by replacing the CO with a rigid ditopic linker, and investigated the electronic and magnetic properties of the ensembles. This work was reported in the manuscript titled "Building Diatomic and Triatomic Superatom Molecules "(*Nano Letters*, **2016**, *16*, 5273) and is discussed in Chapter 2.

A parallel collaboration with Professor Patrick Batail (Université d'Angers, France) sought to use an electrocrystallization technique to create solid state materials from our superatoms. Electrocrystallization is a tool that assembles molecular ions into ordered crystals; we wished to extend it to superatomic ions and access materials of unprecedented complexity. I was given the opportunity to travel to France and learn this technique firsthand in Professor Batail's laboratory. Multiple preliminary trials both at Angers and at Columbia led to an exciting discovery. I combined *trans*-$Co_6Se_8(CNC_6H_4NC)_2(PEt_3)_4$ (prepared from the *trans*-CO monomer and exhibiting a linear arrangement of coordinating isonitrile secondary groups) with a shape

complementary anionic template ($Mo_6O_{19}^{2-}$) in an electrocrystallization cell. The resulting structure is composed of two-dimensional interwoven superatom polymer strands that form a nanoscale box weave. This work was reported in the manuscript titled "Weaving Nanoscale Cloth through Electrostatic Templating" (*Journal of the American Chemical Society*, **2017***, 139*, 11718) and is outlined in Chapter 3.

In the pursuit of accessing 3D materials I assembled crystalline redox-active framework solids by combining a carboxylate-functionalized cluster ($Co_6Se_8(PEt_2PhCOOH)_6$) with Zn^{2+} salts in a solvothermal reaction. This work is described in Chapter 4, and was reported in the manuscript titled "Two-Dimensional Nanosheets from Redox-Active Superatoms " (*ACS Central Science*, **2017**, *3*, 1050). Professor Christopher Bejger (University of North Carolina at Charlotte; formerly a postdoc in the Nuckolls group) conceptualized this project, realized the first synthesis of the cluster using a different route, and developed some of the framework-forming conditions.

Finally, Chapter 5 outlines novel chemical transformations that allow us to covalently expand the $[Co_6Se_8]$ core to a $[Co_{12}Se_{16}]$ core through direct fusion. The resulting dimer exhibits electronic coupling and electron delocalization. I supplement electronic and optical experimental data with an understanding of the electronic structure using quantum chemical calculations. The key intermediate is obtained in one step from a carbonylated cluster and contains a carbene ligand that acts as a bifunctional protecting group for the Se and Co atoms involved in the subsequent fusion. This work resulted in a manuscript titled "Superatom Fusion and the Nature of Quantum Confinement" that is currently under review. In this chapter, I also discuss efforts to develop this chemistry to access extended materials.

Altogether, the results presented in this dissertation have led to a deeper understanding of the building blocks themselves, and have informed us how to further create new superatom-

based electronically coupled materials with tuned dimensionality, size, and extensive charge delocalization.

1.7. References

1. Claridge, S. A.; Castleman, A. W.; Khanna, S. N.; Murray, C. B.; Sen, A.; Weiss, P. S., *ACS Nano* **2009,** *3* (2), 244-255.

2. Bergeron, D. E.; Castleman, A. W.; Morisato, T.; Khanna, S. N., *Science* **2004,** *304* (5667), 84-87.

3. Khanna, S. N.; Jena, P., *Chem. Phys. Lett.* **1994,** *219* (5-6), 479-483.

4. (a) Kratschmer, W.; Lamb, L. D.; Fostiropoulos, K.; Huffman, D. R., *Nature* **1990,** *347* (6291), 354-358; (b) Kroto, H. W.; Heath, J. R.; Obrien, S. C.; Curl, R. F.; Smalley, R. E., *Nature* **1985,** *318* (6042), 162-163.

5. Khanna, S. N.; Jena, P., *Phys. Rev. B.* **1995,** *51* (19), 13705-13716.

6. (a) Murray, C. B.; Norris, D. J.; Bawendi, M. G., *J. Am. Chem. Soc.* **1993,** *115* (19), 8706-8715; (b) Steigerwald, M. L.; Alivisatos, A. P.; Gibson, J. M.; Harris, T. D.; Kortan, R.; Muller, A. J.; Thayer, A. M.; Duncan, T. M.; Douglass, D. C.; Brus, L. E., *J. Am. Chem. Soc.* **1988,** *110* (10), 3046-3050.

7. (a) Saito, T.; Imoto, H., *B. Chem. Soc. Jpn.* **1996,** *69* (9), 2403-2417; (b) Zhang, X.; Mccarley, R. E., *Inorg. Chem.* **1995,** *34* (10), 2678-2683; (c) Ehrlich, G. M.; Warren, C. J.; Vennos, D. A.; Ho, D. M.; Haushalter, R. C.; Disalvo, F. J., *Inorg. Chem.* **1995,** *34* (17), 4454-4459; (d) Cecconi, F.; Ghilardi, C. A.; Midollini, S.; Orlandini, A.; Zanello, P., *Polyhedron* **1986,** *5* (12), 2021-2031; (e) Mironov, Y. V.; Virovets, A. V.; Naumov, N. G.; Ikorskii, V. N.; Fedorov, V. E., *Chem. Eur. J.* **2000,** *6* (8), 1361-1365; (f) Long, J. R.; McCarty, L. S.; Holm, R. H., *J. Am. Chem. Soc.* **1996,** *118* (19), 4603-4616; (g) Christou, G.; Hagen, K. S.; Bashkin, J. K.; Holm, R. H., *Inorg. Chem.* **1985,** *24* (7), 1010-1018; (h) Fenske, D.; Ohmer, J.; Hachgenei, J.; Merzweiler, K., *Angew. Chem. Int. Ed.* **1988,** *27* (10), 1277-1296; (i) Hessen, B.; Siegrist, T.; Palstra, T.; Tanzler, S. M.; Steigerwald, M. L., *Inorg. Chem.* **1993,** *32* (23), 5165-5169; (j) Stuczynski, S. M.; Kwon, Y. U.; Steigerwald, M. L., *J. Organomet. Chem.* **1993,** *449* (1-2), 167-172; (k) Steigerwald, M. L.; Siegrist, T.; Stuczynski, S. M., *Inorg. Chem.* **1991,** *30* (10), 2256-2257.

8. Chevrel, R.; Hirrien, M.; Sergent, M., *Polyhedron* **1986,** *5* (1-2), 87-94.

9. Schafer, H.; Eisenman.B; Muller, W., *Angew. Chem. Int. Ed.* **1973,** *12* (9), 694-712.

10. Lee, S. C.; Holm, R. H., *Angew. Chem Int. Ed.* **1990,** *29* (8), 840-856.

11. Saito, T.; Yamamoto, N.; Nagase, T.; Tsuboi, T.; Kobayashi, K.; Yamagata, T.; Imoto, H.; Unoura, K., *Inorg. Chem.* **1990,** *29* (4), 764-770.

12. Schleich, D. M., *Solid State Ionics* **1994,** *70*, 407-411.

13. (a) Brus, L., *J. Phys. Chem.* **1986,** *90* (12), 2555-2560; (b) Chestnoy, N.; Harris, T. D.; Hull, R.; Brus, L. E., *J. Phys. Chem.* **1986,** *90* (15), 3393-3399.

14. Steigerwald, M. L., *Polyhedron* **1994,** *13* (8), 1245-1252.

15. Jin, S.; DiSalvo, F. J., *Chem. Mater.* **2002,** *14* (8), 3448-3457.

16. (a) Bennett, M. V.; Beauvais, L. G.; Shores, M. P.; Long, J. R., *J. Am. Chem. Soc.* **2001,** *123* (33), 8022-8032; (b) Shores, M. P.; Beauvais, L. G.; Long, J. R., *J. Am. Chem. Soc.* **1999,** *121* (4), 775-779.

17. (a) Naumov, N. G.; Soldatov, D. V.; Ripmeester, J. A.; Artemkina, S. B.; Fedorov, V. E., *Chem. Comm.* **2001,** (6), 571-+; (b) Tarasenko, M. S.; Naumov, N. G.; Naumov, D. Y.; Kuratieva, N. V.; Fedorov, V. E., *Russ. J. Coord. Chem.* **2006,** *32* (7), 494-503.

18. Selby, H. D.; Orto, P.; Carducci, M. D.; Zheng, Z. P., *Inorg. Chem.* **2002,** *41* (24), 6175-6177.

19. (a) Orto, P. J.; Nichol, G. S.; Wang, R. Y.; Zheng, Z. P., *Inorg. Chem.* **2007,** *46* (21), 8436-8438; (b) Willer, M. W.; Long, J. R.; McLauchlan, C. C.; Holm, R. H., *Inorg. Chem.* **1998,** *37* (2), 328-333; (c) Zheng, Z. P.; Long, J. R.; Holm, R. H., *J. Am. Chem. Soc.* **1997,** *119* (9), 2163-2171.

20. Selby, H. D.; Zheng, Z. P.; Gray, T. G.; Holm, R. H., *Inorg. Chim. Acta.* **2001,** *312* (1-2), 205-209.

21. (a) Selby, H. D.; Roland, B. K.; Zheng, Z. P., *Acc. Chem. Res.* **2003,** *36* (12), 933-944; (b) Selby, H. D.; Orto, P.; Zheng, Z. P., *Polyhedron* **2003,** *22* (22), 2999-3008.

22. (a) Roland, B. K.; Carter, C.; Zheng, Z. P., *J. Am. Chem. Soc.* **2002,** *124* (22), 6234-6235; (b) Wang, R. Y.; Zheng, Z. P., *J. Am. Chem. Soc.* **1999,** *121* (14), 3549-3550.

23. Roy, X.; Lee, C. H.; Crowther, A. C.; Schenck, C. L.; Besara, T.; Lalancette, R. A.; Siegrist, T.; Stephens, P. W.; Brus, L. E.; Kim, P.; Steigerwald, M. L.; Nuckolls, C., *Science* **2013,** *341* (6142), 157-160.

24. (a) Pinkard, A.; Champsaur, A. M.; Roy, X., *Acc. Chem. Res.* **2018,** *51* (4), 919-929; (b) Zhong, X. J.; Lee, K.; Choi, B.; Meggiolaro, D.; Liu, F.; Nuckolls, C.; Pasupathy, A.; De Angelis, F.; Batail, P.; Roy, X.; Zhu, X. Y., *Nano Lett.* **2018,** *18* (2), 1483-1488; (c) Voevodin, A.; Abella, L.; Castro, E.; Paley, D. W.; Campos, L. M.; Rodriguez-Fortea, A.; Poblet, J. M.; Echegoyen, L.; Roy, X., *Chem. Eur. J.* **2017,** *23* (54), 13305-13308; (d) O'Brien, E. S.; Trinh, M.

T.; Kann, R. L.; Chen, J.; Elbaz, G. A.; Masurkar, A.; Atallah, T. L.; Paley, M. V.; Patel, N.; Paley, D. W.; Kymissis, I.; Crowther, A. C.; Millis, A. J.; Reichman, D. R.; Zhu, X. Y.; Roy, X., *Nat. Chem.* **2017,** *9* (12), 1170-1174; (e) Ong, W. L.; O'Brien, E. S.; Dougherty, P. S. M.; Paley, D. W.; Higgs, C. F.; McGaughey, A. J. H.; Malen, J. A.; Roy, X., *Nat. Mater.* **2017,** *16* (1), 83-88; (f) Choi, B.; Yu, J.; Paley, D. W.; Trinh, M. T.; Paley, M. V.; Karch, J. M.; Crowther, A. C.; Lee, C. H.; Lalancette, R. A.; Zhu, X. Y.; Kim, P.; Steigerwald, M. L.; Nuckolls, C.; Roy, X., *Nano Lett.* **2016,** *16* (2), 1445-1449; (g) Lee, C. H.; Liu, L.; Bejger, C.; Turkiewicz, A.; Goko, T.; Arguello, C. J.; Frandsen, B. A.; Cheung, S. C.; Medina, T.; Munsie, T. J. S.; D'Ortenzio, R.; Luke, G. M.; Besara, T.; Lalancette, R. A.; Siegrist, T.; Stephens, P. W.; Crowther, A. C.; Brus, L. E.; Matsuo, Y.; Nakamura, E.; Uemura, Y. J.; Kim, P.; Nuckolls, C.; Steigerwald, M. L.; Roy, X., *J. Am. Chem. Soc.* **2014,** *136* (48), 16926-16931; (h) Turkiewicz, A.; Paley, D. W.; Besara, T.; Elbaz, G.; Pinkard, A.; Siegrist, T.; Roy, X., *J. Am. Chem. Soc.* **2014,** *136* (45), 15873-15876.

Chapter 2. Synthesis of Site-Differentiated $Co_6Se_8(CO)_x(PEt_3)_{(6-x)}$ Superatoms and Covalent Oligomers

2.1. Preface

This chapter is based on a published manuscript titled "Building Diatomic and Triatomic Superatom Molecules" by Anouck M. Champsaur, Alexandra Velian, Daniel W. Paley, Bonnie Choi, Xavier Roy, Michael L. Steigerwald, and Colin Nuckolls (*Nano Lett.*, **2016**, *16*, 5273). I synthesized and characterized all molecules with the help of Alexandra Velian. I performed all electrochemical measurements and analyses. Dan Paley performed single crystal refinement. Bonnie Choi carried out SQUID measurements.

2.2. Introduction

In this chapter, we create the superatomic[1-4] version of the simplest molecules, diatomic and linear triatomic molecules. The constituent superatoms are atomically defined clusters of metal chalcogenides that are capped with passivating two-electron ligands. The key to being able to discretely link these superatoms into superatom molecules (SMs) was to control the reaction chemistry of the capping ligands and to thereby program the intersuperatom bonding. These SMs have a rich electrochemical profile. Having control over the geometry, distance, and linker between the superatoms is crucial to further the understanding of how to promote electronic and magnetic coupling within SMs.

We developed a method to create $[Co_6Se_8]$ superatoms in which we program the metal–ligand bonds. We exclusively form the $[Co_6Se_8]$ core under simple reaction conditions with a facile separation of products that contain differential substitution of the core. The combination of $Co_2(CO)_8$ and PR_3 with excess Se gives the differentially and directionally substituted

superatoms, $Co_6Se_8(CO)_x(PR_3)_{(6-x)}$. The CO groups on the superatom can be exchanged quantitatively with phosphines and isonitriles. Substitution of the CO allows us to manipulate the type and length of chemical bridge between two redox-active superatomic centers in order to modulate intersuperatomic coupling.

Previous studies on colloidal semiconductors have gone to great lengths to link them together into discrete "nanocrystal molecules"[5-11] because the nanopositioning and linking of these electronic and magnetic nano-objects allows collective properties to emerge. The study here provides a means to synthesize ~1 nm superatoms and to couple them together into molecular form with atomic precision and having a well-defined surface definition/bonding.

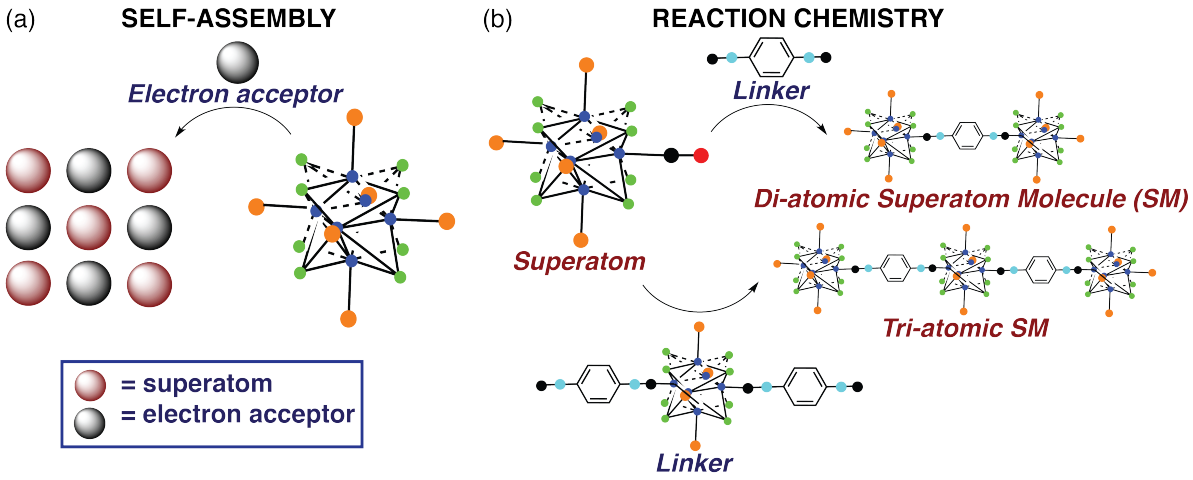

Figure 2.1. (a) Previously studied outer-sphere reactions of $Co_6Se_8(PR_3)_6$ superatoms. (b) We study here the inner-sphere reactions of $Co_6Se_8(CO)_x(PR_3)_{(6-x)}$.

Prior studies on superatoms have focused on the "outer-sphere" reaction chemistry of cobalt chalcogenide clusters and created solid-state materials via either the transfer of electrons from the cluster to acceptors such as fullerenes[12-14] or the molecular recognition of fullerenes by fluxional phenanthrene ligands (Figure 2.1a).[15] In these cases, the essential structure of neither the inorganic core of the superatoms nor the ligand shell changes. As such, superatoms in this context form extended solid-state materials with tunable properties. Those approaches have

relied on self-assembly and shape complementarity; here we describe reactions of the superatoms in which we manipulate the metal–ligand bonds by intentionally including labile surface-ligands. We prepare a series of superatoms, $Co_6Se_8(CO)_x(PR_3)_{(6-x)}$ (x = 1–5, R = Et, Ph) and show that they are stereochemically robust. These new superatoms undergo CO-displacement reactions with neutral two-electron donors (phosphines and isocyanides) and these reactions depend on the ligand arrangements of the initial superatoms. These "inner-sphere" reactions allow us to form diatomic and linear triatomic SMs (Figure 2.1b).

2.3. Synthesis of $Co_6E_8(CO)_x(PR_3)_{(6-x)}$ Superatoms (E = Se, Te; R = Et, Ph)

Superatoms having neutral cores capped with phosphine ligands are typically synthesized so that each ligand coordinates to a metal atom to form, for example, $M_6E_8(PR_3)_6$ structures (M = Cr, Co, Mo, Rh; E = S, Se, Te).[16-20] Substitution reactions of these phosphines are difficult because the M–P bonds tend to display low chemical reactivity at moderate temperatures and indiscriminate reactions at higher temperatures; the latter thermal reactions typically yield solid-state products.[21, 22] Moreover, the differentiation of one of the phosphines from another in a symmetrically substituted metal chalcogenide cluster is a vexing challenge.

Here we sought a bottom-up approach to SMs by developing simple solution-phase chemistry to synthesize electrically neutral and directionally substituted superatoms in one step. We were inspired by the rich reaction chemistry developed for $Re_6Se_8L_6$ clusters.[23-29] Our important finding is a simple and mild synthesis of heteroleptic $[Co_6Se_8]$ superatoms. The subsequent separation of different regioisomers is facile and efficient. We further demonstrate that the reaction chemistry of trans- and cis-dicarbonylated superatoms offers a clear path to linear, bent, cyclic, and oligomeric SMs.

Our synthesis of differentially substituted [Co_6Se_8] superatoms refines previous methods:[30-32] the combination of $Co_2(CO)_8$ and PR_3 with a significant excess of Se produces the family of substituted superatoms, Co_6Se_8 $(CO)_x(PR_3)_{(6-x)}$. We require some amount of phosphine to passivate the [Co_6Se_8] core, but the stoichiometric excess of Se effectively decreases the amount of phosphine available to displace the carbonyl groups and thus modulates x. While mixtures of the carbonylated superatoms are produced regardless of the initial reagent ratios, the PR_3/Se stoichiometry governs the average value of x. We separated particular superatoms using conventional silica gel chromatography, relying on the distinct and diagnostic ^{1}H NMR for each of the ligand substitution patterns around the [Co_6Se_8] core (Section 2.9 contains synthetic details).

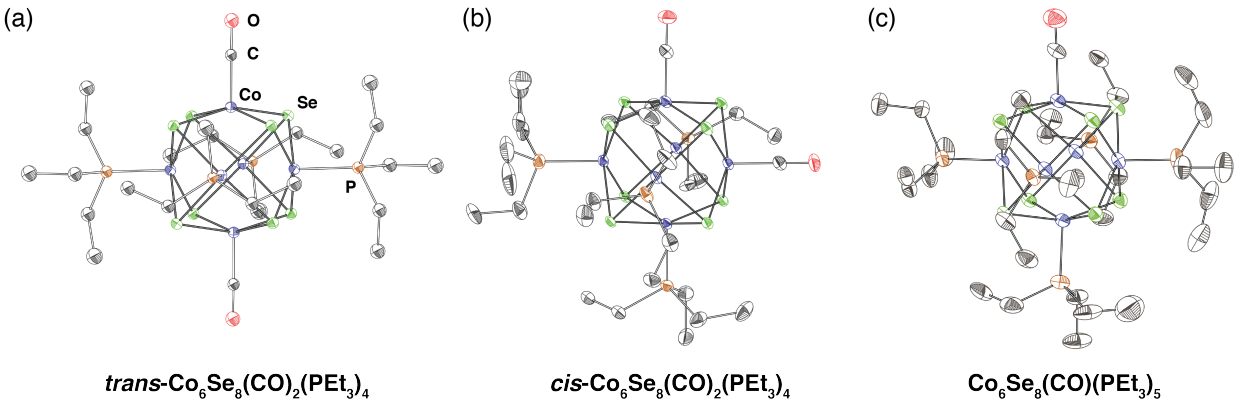

Figure 2.2. Molecular structure of differentially substituted superatoms: (a) *trans*-$Co_6Se_8(CO)_2(PEt_3)_4$, (b) *cis*-$Co_6Se_8(CO)_2(PEt_3)_4$, and (c) $Co_6Se_8(CO)(PEt_3)_5$. Atom labels are shown (a). Hydrogen atoms are omitted for clarity, and thermal ellipsoids are set at 50% probability level.

We focus on three basic [Co_6Se_8] superatom building blocks: two with two CO groups in either a *cis*- or *trans*- arrangement and the monocarbonylated superatom (Figure 2.2), because they constitute fundamental blocks with which to build diatomic and triatomic SMs as well as one- and two-dimensional materials. The [Co_6Se_8] superatom core is built from a slightly

distorted octahedron of six cobalt atoms each face of which is capped by a selenium atom. The superatomic cores of $Co_6Se_8(CO)_x(PR_3)_{(6-x)}$ are isostructural and they show no clear systematic trend in the Co–Co, Co–Se, or Co–P distances (Table 2.1).

By modifying the reaction and purification conditions, we also isolate and crystallographically characterize both *mer*- and *fac*-$Co_6Se_8(CO)_3(PEt_3)_3$, *cis*- and *trans*-$Co_6Se_8(CO)_4(PPh_3)_2$, *fac*-$Co_6Se_8(CO)_3(PPh_3)_3$, and $Co_6Se_8(CO)_5(PPh_3)$. Section 2.10 displays the molecular structures of all of these species obtained by SCXRD.

We also extended these reactions to tellurium: the same reaction conditions yield a distribution of $Co_6Te_8(CO)_x(PEt_3)_{(6-x)}$, as determined by ^{1}H NMR. Section 2.10 shows the crystal structures of the isolated *cis*- and *trans*- disubstituted cobalt telluride clusters. The tellurium-containing superatoms are more difficult to chromatograph due to their greater sensitivity to ambient conditions.

D [Å]	**Co-Co**	**Co-C**	**C-O**	**Co-Se**	**Co-P**
trans-CO	2.91-2.94	1.73(2)	1.14(2)	2.26-2.33	2.14
cis-CO	2.90-2.98	1.71(2)	1.15(2)	2.32-2.36	2.14
mono-CO	2.91-2.95	1.73(2)	1.12(3)	2.33-2.37	2.12-2.14
$(PEt_3)_6$	2.93-2.94	-	-	2.35-2.36	2.14

Table 2.1. Selected bond distances [Å] in molecular structures of *trans*-$Co_6Se_8(CO)_2(PEt_3)_4$, *cis*-$Co_6Se_8(CO)_2(PEt_3)_4$, $Co_6Se_8(CO)(PEt_3)_5$, and $Co_6Se_8(PEt_3)_6$.[1] The Co-C and C-O distances are listed with crystallographic esd's. The esd's on heavy atom-heavy atom distances were much less than 0.01 Å and have been omitted.

2.4. Substitution of $Co_6Se_8(CO)_x(PEt_3)_{(6-x)}$ Superatoms with Phosphines and Isonitriles

The CO ligands are chemically active and the substitution reaction is induced photochemically. This behavior is similar to that of metal carbonyl complexes undergoing dissociation and substitution of CO ligands upon photolysis.[33] Scheme 2.1 shows the substitution reactions in which two electron donors such as phosphines and isocyanides replace the CO of *trans*-$Co_6Se_8(CO)_2(PEt_3)_4$.

Room temperature irradiation of a THF solution of the superatom with a 200–400 nm broadband lamp allows a selective substitution of CO groups (note: UV light is not necessary and visible light works also). When we irradiate a solution of *trans*-$Co_6Se_8(CO)_2(PEt_3)_4$ containing two equivalents (per superatom) of the incoming electron donor ligand, we obtain the product in quantitative yields. When we treat the same superatom with less than 2 stoichiometric equivalents of the ligand, we obtain a mixture of the monosubstituted and disubstituted products (Scheme 2.1).

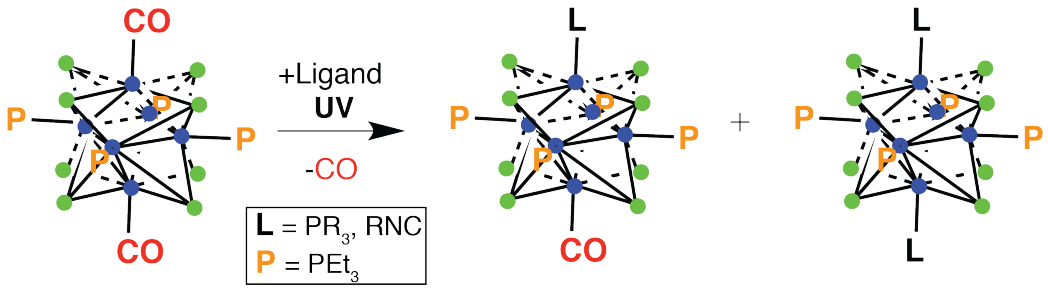

Scheme 2.1. Mono- and di-substitution of *trans*-$Co_6Se_8(CO)_2(PEt_3)_4$. The formation of products can be controlled by the stoichiometry of the ligand.

Figure 2.3 displays the structures of the differentially substituted superatoms *trans*-$Co_6Se_8(iPrNC)_2(PEt_3)_4$ and *trans*-$Co_6Se_8(Et_2PPhSMe)_2(PEt_3)_4$, obtained from treating *trans*-Co_6Se_8 $(CO)_2(PEt_3)_4$ with two equivalents of ligand.

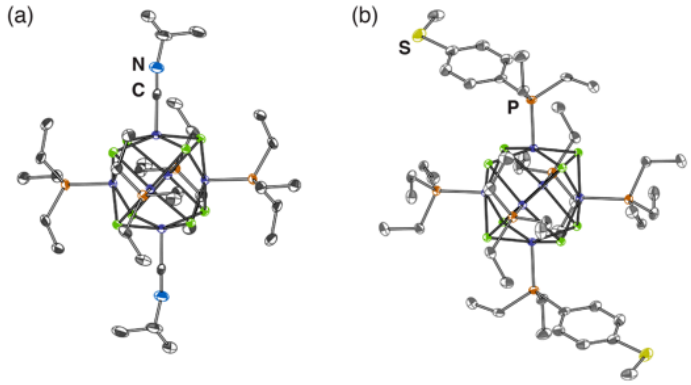

Figure 2.3. Molecular structure of (a) *trans*-$Co_6Se_8(^iPrNC)_2(PEt_3)_4$ and (b) *trans*-Co_6Se_8 $(PEt_2PPhSMe)_2(PEt_3)_4$.Thermal ellipsoids are set at 50% probability level.

There are two important findings in these reactions. (1) The stereochemistry of either the cis- or trans- arrangement of the CO groups is maintained in these reactions. The implication is that the phosphine ligands are not fluxional during this process. (2) The reactions only substitute the CO groups, not the phosphines. These two findings demonstrate that selective chemistry is possible to build up SMs and one-, two-, and higher-dimensional materials with either of the CO-substituted superatoms.

2.5. Preparing Linked [Co_6Se_8] Oligomers from $Co_6Se_8(CO)_x(PEt_3)_{(6-x)}$

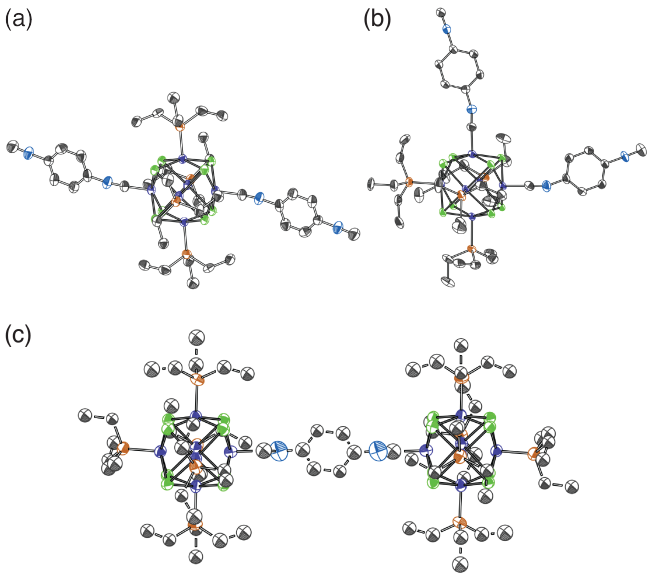

Figure 2.4. Molecular structure of (a) *trans*-$Co_6Se_8(CNC_6H_4NC)_2(PEt_3)_4$, (b) *cis*-$Co_6Se_8(CNC_6H_4NC)_2(PEt_3)_4$, and (c) the doubly oxidized di-atomic SM, $[Co_{12}Se_{16}(CNC_6H_4NC)(PEt_3)_{10}][PF_6]_2$. Hydrogen atoms and the PF_6^- anion have been omitted for clarity. Thermal ellipsoids are set at 50% probability level.

We create the simplest SMs, diatomic and acyclic triatomic SMs, by replacing the CO group with chemical bridges. Appropriate ditopic ligands link two redox-active superatomic centers, and varying these ligands modulates intersuperatomic coupling. The linking chemistry of the cis- and trans- dicarbonylated superatoms is similar; in making the SMs, we focus only on the chemical reactions of *trans*-$Co_6Se_8(CO)_2(PEt_3)_4$ isomer. In the SM aufbau, the *trans*-

$Co_6Se_8(CO)_2(PEt_3)_4$ is a link and $Co_6Se_8(CO)(PEt_3)_5$ is a cap. We chose 1,4-phenylene diisocyanide (CNC_6H_4NC), a rigid linear linker.

From the building blocks *trans*-$Co_6Se_8(CNC_6H_4NC)_2(PEt_3)_4$, 1,4-phenylene diisocyanide, and $Co_6Se_8(CO)(PEt_3)_5$, we synthesized a diatomic SM $Co_{12}Se_{16}(PEt_3)_{10}(CNC_6H_4NC)$ and linear triatomic SM $Co_{18}Se_{24}(PEt_3)_{14}(CNC_6H_4NC)_2$ (Figure 2.1b). We prepare the superatom in Figure 2.4a in quantitative yields from the photolysis of *trans*-$Co_6Se_8(CO)_2(PEt_3)_4$ in the presence of excess 1,4-phenylene diisocyanide.[34] We can form *cis*-$Co_6Se_8(CNC_6H_4NC)_2(PEt_3)_4$ similarly from its *cis*-CO precursor (Figure 2.4b). ^{1}H NMR confirms formation of the diatomic SM and the linear triatomic SM. All ^{1}H NMR spectra are displayed in Section 2.9.1.

Figure 2.4c displays the crystal structure of the diatomic SM in its doubly oxidized form $[Co_{12}Se_{16}(PEt_3)_{10}(CNC_6H_4NC)][PF_6]_2$. We isolate this by treating two equivalents of the oxidized superatom $[Co_6Se_8(CO)(PEt_3)_5][PF_6]$ with one equivalent of linker (see Section 2.9 for synthetic details). The diatomic SM is symmetrical about the linker with crystallographically equivalent $[Co_6Se_8]$ superatomic cores.

2.6. Electrochemical and Magnetic Properties of Oligomers

We used electrochemical methods[35] to investigate electronic coupling between the cores of the diatomic and linear triatomic SMs. In order to understand how the electronic properties of isocyanide-bridged superatom oligomers compare to those of a single $[Co_6Se_8]$

Superatom	0/+1	+1/+2	+2/+3
trans-$Co_6Se_8(CO)_2(PEt_3)_4$	-0.34 V	0.30 V	-
cis-$Co_6Se_8(CO)_2(PEt_3)_4$	-0.35 V	0.32 V	-
$Co_6Se_8(PEt_3)_6$	-1.03 V	-0.48 V	0.11 V

Table 2.2. Half-wave potentials for *trans*-$Co_6Se_8(CO)_2(PEt_3)_4$, *cis*-$Co_6Se_8(CO)_2(PEt_3)_4$, and $Co_6Se_8(PEt_3)_6$[2] in THF with 0.1 M $TBAPF_6$, versus Fc/Fc^+.

core, we prepared two monomers as points of reference: mono- and di-substituted superatoms with 2,6-dimethylphenyl isocyanide. The cyclic voltammograms of these monomers are displayed in Figure 2.5a. The isocyanide-substituted superatoms behave similarly to their CO-substituted analogues; the strong pi-acceptor ligands bonded to the $[Co_6Se_8]$ core make it less electron rich than the parent $Co_6Se_8(PEt_3)_6$. Table 2.2 contains half-wave potentials of bis-CO clusters and parent cluster. The E_p values (i.e., the peak value of the potential) of each superatom differ and are dependent upon the ligand environment.

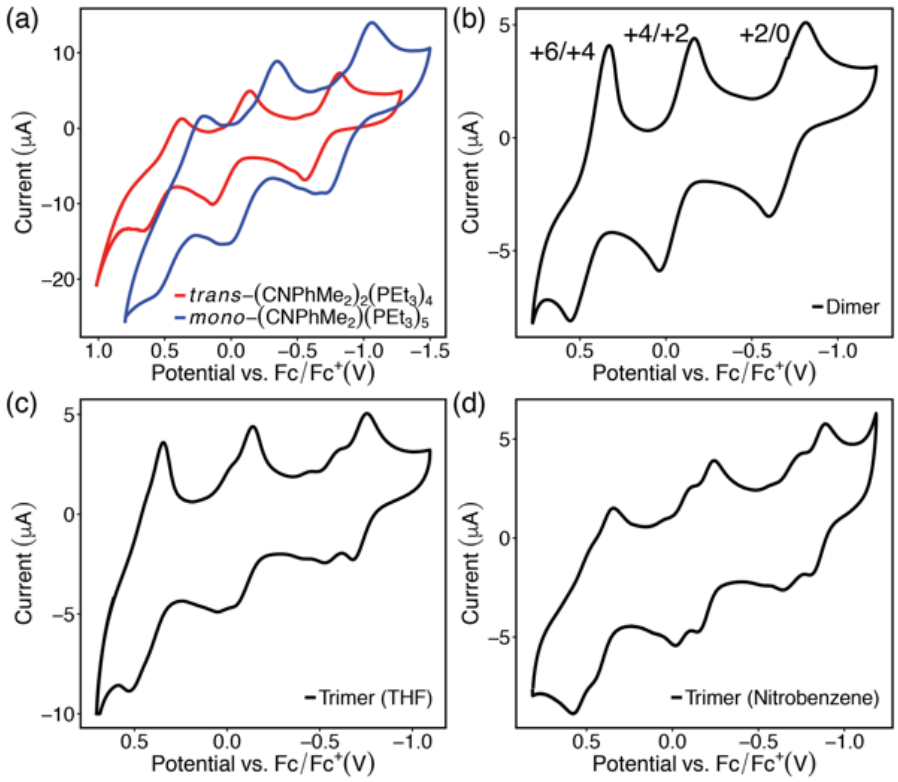

Figure 2.5. Cyclic voltammogram (CV) of (a) monomeric superatoms, *mono*-$CNPhMe_2$ (blue) and *trans*-$CNPhMe_2$ (red), (b) di-atomic SM and (c) tri-atomic SM in 0.1 M $TBAPF_6$ in THF with a 150 mV/s scan rate. (d) CV of trimer in 0.1 M $TBAPF_6$ in nitrobenzene with a 150 mV/s scan rate.

The electrochemistry of the diatomic SM and the linear triatomic SM is rich in information. While the neutral diatomic SM exhibits three reversible oxidation peaks (Figure 2.5b), the neutral triatomic SM exhibits discernible electrochemical splitting (Figure 2.5c). This

splitting is even more pronounced when the voltammogram is taken in nitrobenzene (Figure 2.5d), a solvent with a much higher dielectric constant, known to better stabilize charged species (ε_{THF} = 7.58 vs $\varepsilon_{nitrobenzene}$ = 34.82).[36] We determined that each of the three reversible oxidation peaks in the CV of the neutral diatomic SM (Figure 2.5b) corresponds to a two-electron event as follows: under the same conditions we measured the open circuit potential of the diatomic SM dication as –0.671 V versus the ferrocene/ferrocenium redox couple. This potential corresponds to the species formed after the first oxidation of the neutral dimer.

We can therefore assign each redox couple of the diatomic SM to the following states: 0/+2, +2/+4, and +4/+6. From our analysis of the diatomic SM redox pairs, we assign the first oxidation event (at E1/2 ~ –0.8 V in Figure 2.5c) in the trimer as the 0 to +3 transition. We therefore attribute the pronounced splitting behavior of the linear triatomic SM to the existence of two types of superatoms, bridging and terminal, whose redox potentials differ. The smooth redox peaks of the dimer arise because each is a terminal unit oxidized at the same potential.

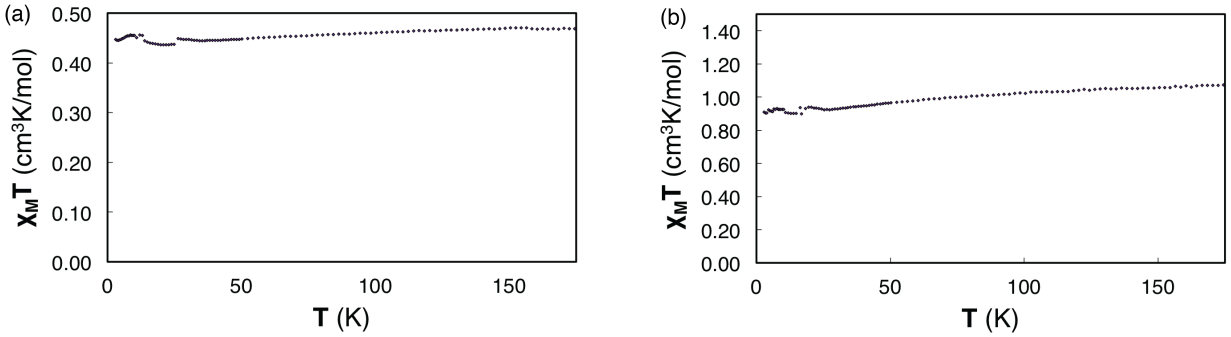

Figure 2.6. (a) Magnetic susceptibility data for $[Co_6Se_8(CO)(PEt_3)_5][PF_6]$. At T = 3 K, X_MT = 0.45 cm^{3}K/mol. (b) Magnetic susceptibility data for $[Co_{12}Se_{16}(PEt_3)_{10}(CNC_6H_4NC)][PF_6]_2$. At T = 3 K, X_MT = 0.91 cm^{3}K/mol. The di-atomic SM contains two non-interacting spins, each having X_MT of the monomeric species.

Magnetic susceptibility measurements of the oxidized superatom $[Co_6Se_8(CO)(PEt_3)_5][PF_6]$, as well as the doubly oxidized di-atomic SM $[Co_{12}Se_{16}(PEt_3)_{10}(CNC_6H_4NC)][PF_6]_2$ elucidate their open-shell characteristics (Figure 2.6).

Specifically, $[Co_6Se_8(CO)(PEt_3)_5][PF_6]$ shows a temperature-independent magnetic susceptibility (X_MT), with X_MT = 0.45 cm^3K/mol at T = 3 K, suggesting that the core contains one unpaired electron with a g-factor greater than 2 (spin-only value S = ½ of an unpaired electron is 0.375 cm^3K/mol for g = 2). The doubly oxidized di-atomic SM has X_MT = 0.91 cm^3K/mol at T = 3 K. This result suggests that the di-atomic SM contains two non-interacting spins, each having X_MT of the monomeric species.

2.7. Conclusions

In summary, we have found a simple method to synthesize and isolate $[Co_6Se_8]$ superatoms that are substituted with both phosphine and carbonyl ligands. The CO ligands can be replaced with two electron donors such as phosphines and isocyanides. From the *trans*-CO superatom and monocarbonylated superatom we can create di-atomic SMs and linear tri-atomic SMs that are linked together with diisocyanides. Forming these new SMs is an important step towards studying SMs in single molecule and materials applications. The method described here gives access to the vast number of magnetic and electroactive superatoms whose inter-superatom coupling can be easily varied by changing the linker. For example, we are exploring mixed Se/Te systems, which we can access by covalently linking $[Co_6Se_8]$ and $[Co_6Te_8]$ carbonylated superatoms. The hetero di-atomic superatoms offer a unique opportunity to study the magnetic coupling between two spins as the linker is modified. Moreover, the reaction of the *trans*-CO superatom and a di-topic linker would give rise to oligomeric SM chains.

2.8. General Synthesis Information

Unless otherwise noted, all reactions were performed in a nitrogen atmosphere using standard Schlenk techniques or in a nitrogen-filled glovebox. Triethylphosphine (99%) was purchased from Sigma-Aldrich. Selenium powder, tellurium powder, and dicobalt octacarbonyl (stabilized with 1-5% hexane) were obtained from STREM Chemicals. All other reagents were purchased from Sigma-Aldrich. Chemicals were used without further purification. Anhydrous and anaerobic solvents were obtained from a Glass Contour solvent system consisting of a Schlenk manifold with purification columns packed with activated alumina and supported copper catalyst. Chromatography was performed using a Teledyne Isco Combiflash Rf200 and Redisep Rf Silica columns. ^{1}H NMR spectra were recorded on a Bruker DRX300 (300 MHz), Bruker DRX400 (400 MHz) or a Bruker DMX500 (500 MHz) spectrometer. ^{31}P NMR spectra were recorded on a Bruker DMX500 (500 MHz) spectrometer and referenced to phosphoric acid (H_3PO_4). ^{77}Se spectra were recorded on a Bruker DMX500 (500 MHz) spectrometer. ^{1}H NMR chemical shifts were referenced to residual protons in the NMR solvent ($CHCl_3$: δ 7.26; C_6H_6 δ 7.16; CH_2Cl_2: δ 5.32).

Electronic absorption spectra were recorded using a 1.0 cm quartz cell on a Shimadzu UV-1800 spectrophotometer. Infrared (IR) spectra were recorded on a Perkin Elmer Spectrum400 FTIR spectrometer using a PIKE ATR attachment. Cyclic voltammetry (CV) was performed on a CHI600C electrochemical workstation using an Ag/AgCl electrode as the reference electrode at room temperature. The photochemical reactor lamp was purchased from Hanovia Specialty lighting LLC (Catalog number PC 451.050). The lamp is a medium-pressure mercury lamp emitting 200-400 nm broadband radiation. The lamp was placed inside a quartz jacket, with cooling water circulating throughout to maintain the reactions at ambient temperature. (Note: UV is not necessary for this reaction. Visible light also works well.)

Magnetic susceptibility measurements were performed using a Cryogenic R-700X SQUID magnetometer. The microcrystalline samples were loaded in a gel capsule inside a nitrogen-filled glovebox and mounted in a clear plastic straw. Crystallographic data for all compounds was collected on an Agilent SuperNova diffractometer using mirror-monochromated Cu Kα radiation.

2.9. Synthetic Procedures and Characterization of Compounds

Synthesis of $Co_6Se_8(CO)_x(PEt_3)_{(6-x)}$ isomers (x = 0-3; 3 Co_2CO_8: 12 Se: 6 PEt_3)

Inside the glovebox, Se (1.336 g, 16.90 mmol, 4 eq.) and Co_2CO_8 (1.446 g, 4.23 mmol, 1 eq.) were loaded in a 100 mL Schlenk flask. Toluene (20 mL) was added to the flask and the flask was then transferred to a Schlenk line under N_2. Neat PEt_3 (1.000 g, 8.46 mmol, 2 eq.) was syringed into the flask effecting effervescence. The reaction mixture was heated to 110 °C for 16 hours, during which time the color darkened to a deep brown. The reaction was monitored by IR and its completion was confirmed by the disappearance of bands associated with Co_2CO_8 and intermediate clusters (1700-1900 cm^{-1}) and the presence of an intense, broad band in the range 1970-1959 cm^{-1}. Upon cooling to room temperature, the mixture was filtered through a Celite plug, and the filtrate was evaporated *in vacuo*.

The crude ^1H NMR spectrum of the obtained solid reveals a mixture of products that include $Co_6Se_8(CO)(PEt_3)_5$, *cis*- and *trans*-$Co_6Se_8(CO)_2(PEt_3)_4$, and $SePEt_3$. A diagram of a TLC plate obtained by spotting the crude mixture on a silica TLC plate is shown below. Yields of the isolated clusters were calculated based on $Co_2(CO)_8$, the limiting reagent. *NOTE: the substitution reactions do not require 200-400 nm light. Visible light is sufficient.*

TLC of crude PEt_3 reaction mixture (10% ethyl acetate in hexanes)

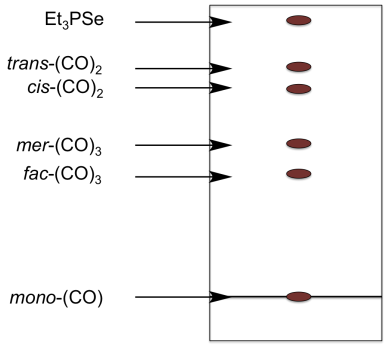

The compounds are separated as follows:

***trans*-$Co_6Se_8(CO)_2(PEt_3)_4$ (1).** The brown solid obtained by evaporating the solvent from the crude mixture (see above) was dissolved in toluene (15 mL) and gravity-filtered through a fine frit. The filtrate was saved and worked-up as described in the next section. The crystalline solid collected on the filter was washed with hexanes (10 mL), brought to constant mass (0.329 g, 0.22 mmol, 15.4% yield) and identified as spectroscopically clean *trans*-$Co_6Se_8(CO)_2(PEt_3)_4$. ^{1}H NMR (300 MHz, benzene-d_6) δ = 1.61 (dq, J = 9.5, 7.5 Hz, 24H), 0.87 (dt, J = 15.2, 7.5 Hz, 36H) ppm; ^{31}P NMR (202 MHz, CD_2Cl_2) δ = 63 (broad) ppm; ^{77}Se NMR (76.3 MHz, CD_2Cl_2) δ = –284 ppm.

***cis*-$Co_6Se_8(CO)_2(PEt_3)_4$ (2)**. The filtrate obtained after the removal of *trans*-$Co_6Se_8(CO)_2(PEt_3)_4$ (see above) was brought to constant mass *in vacuo* and the resulting solid was dissolved in a minimum amount of dichloromethane (~ 5 mL). The *cis*- product was purified by column chromatography (80 g Redisep Rf Silica) using a gradient from 0 to 10 % ethyl acetate/hexanes at a rate of 80 mL/min. The fractions containing the *cis*-$Co_6Se_8(CO)_2(PEt_3)_4$ cluster were collected and checked by TLC for purity. The pure fractions were combined, and brought to

constant mass (0.273 g, 0.180 mmol, 12.8% yield). ^{1}H NMR (400 MHz, benzene-d_6) δ = 1.78 (dq, J = 8.72, 7.65 Hz, 12 H), 1.56 (dq, J = 8.7, 7.65 Hz 12 H), 0.96 (dt, J = 15.5, 7.5 Hz 18 H), 0.81 (dt, J = 15.5, 7.5 Hz 18 H) ppm; ^{31}P NMR (161.9 MHz, benzene-d_6) δ = 72 (broad), 66 (broad) ppm; ^{77}Se NMR (76.3 MHz, CD_2Cl_2) δ = –284 ppm**.**

***mer*-$Co_6Se_8(CO)_3(PEt_3)_3$ (3).** The *mer*-$Co_6Se_8(CO)_3(PEt_3)_3$ cluster was also isolated from a few of these column fractions (see above), albeit in low yields and with less fidelity in the reactions. ^{1}H NMR (400 MHz, $CDCl_3$) δ = 1.81 (m, 6 H), 1.68 (m, 12 H), 1.02 (m, 9 H), 0.91 (m, 18 H) ppm; ^{13}C NMR (100.6 MHz, $CDCl_3$) δ: 27.5 (d, $^{1}J_{C\text{-}P}$ = 29 Hz), 27.2 (d, $^{1}J_{C\text{-}P}$ = 29 Hz) ppm; ^{31}P NMR (161.9 MHz, $CDCl_3$) δ = 69 (broad) ppm; ^{77}Se NMR (76.3 MHz, $CDCl_3$) δ = –226, –242 ppm.

Synthesis of $[Co_6Se_8(CO)(PEt_3)_5][PF_6]$ (4). During workup (see above), the $Co_6Se_8(CO)(PEt_3)_5$ cluster is oxidized on the silica column. To recover it, the loading cartridge used above to elute the reaction mixture was washed with a solution of $TBAPF_6$ (TBA = tetrabutylammonium; 0.075 g, 0.19 mmol) in acetonitrile (~ 100 mL). The dark brown solution, containing mostly $[Co_6Se_8(CO)(PEt_3)_5][PF_6]$ and $TBAPF_6$, was brought to constant mass and triturated with toluene (3 times). The resulting solid was dissolved in a minimum amount of dichloromethane (~ 5 mL) and loaded onto a packed silica plug (80 g). The silica plug was dried under a stream of air, and then the plug was washed with diethyl ether (~ 5 mL). Dichloromethane was used to elute the first dark brown band, containing pure $[Co_6Se_8(CO)(PEt_3)_5][PF_6]$. The solvent was evaporated from the collected fractions, yielding 0.159 g of brown material (0.091 mmol, 6.4% yield based on $Co_2(CO)_8$). ^{1}H NMR (300 MHz, $CDCl_3$) δ = 0.79 (s, 9H, broad), 0.07 (s, 36H, broad), -0.14

(d, J = 7.7 Hz, 6H, broad), -1.14 (d, J = 7.5 Hz, 24H) ppm; ^{31}P NMR (202 MHz, $CDCl_3$) δ = -143.97 (PF_6), -444.66 (broad), -495.35 (broad) ppm.

Synthesis of *fac*-$Co_6Se_8(CO)_3(PEt_3)_3$ (5) (3 Co_2CO_8: 28 Se: 6 PEt_3)

Inside the glovebox, Se (1.559 g, 19.80 mmol, 28 eq.) and $Co_2(CO)_8$ (0.724 g, 2.12 mmol, 3 eq.) were loaded in a 100 mL Schlenk flask. Toluene (24 mL) was added and the flask was transferred to a Schlenk line under N_2. Neat PEt_3 (0.500 g, 4.24 mmol, 6 eq.) was syringed into the flask effecting effervescence. The reaction mixture was heated to 105°C for 16 hours, during which time the color darkened to deep brown. The reaction was monitored by IR spectroscopy and its completion was confimed by the disappearance of bands associated with Co_2CO_8 and intermediate clusters (1700-1900 cm^{-1}) and the emergence of an intense, broad band centered between 1990 and 1959 cm^{-1}. Upon cooling to room temperature, the mixture was filtered through a Celite plug, and the filtrate was evaporated *in vacuo*. The resulting solid was dissolved in a minimum amount of dichloromethane (~ 5 mL). The product was purified by column chromatography (40 g Redisep Rf Silica) using a gradient from 0 to 10% ethyl acetate/hexanes at a rate of 80 mL/min. Some recovered fractions contained needle-like crystals of **(5) *fac*-$Co_6Se_8(CO)_3(PEt_3)_3$** (yield < 2%). These were recrystallized by diffusing hexane vapor into a toluene solution of the product.

Synthesis of $Co_6Se_8(CO)(PEt_3)_5$ (6) Method A. From the reaction of *cis*-$Co_6Se_8(CO)_2(PEt_3)_4$ with PEt_3 (the *trans*- isomer behaves similarly). Inside the glovebox, a Pyrex Schlenk flask was loaded with a solution of *cis*-$Co_6Se_8(CO)_2(PEt_3)_4$ (436 mg, 0.288 mmol, 1 eq.) in benzene (20 mL). A solution of triethylphosphine (58 mg, 0.490 mmol, 1.7 eq.) in benzene (5 mL) was added

dropwise. The reaction (under N_2) was then capped with a rubber septum and irradiated with a broadband lamp (200-400 nm) for 8 hours at room temperature during which time a mixture of $Co_6Se_8(CO)(PEt_3)_5$ and $Co_6Se_8(PEt_3)_6$ was formed. The solvent was concentrated to ~ 4 mL *in vacuo*. In the glove box, the reaction mixture was filtered through a 0.2 μm syringe filter to remove crystalline $Co_6Se_8(PEt_3)_6$, which remained in the filter. The filtrate was evaporated *in vacuo*, and the residue was analyzed by ^{1}H NMR spectroscopy, revealing it contained mostly the $Co_6Se_8(CO)(PEt_3)_5$ cluster along with traces of starting material. X-ray quality crystals of $Co_6Se_8(CO)(PEt_3)_5$ were grown from a mixture of diethyl ether and toluene at -20°C. Crystalline yield (based on *cis*-CO starting material): 44% (0.204 g, 0.127 mmol).

Method B. From the reduction of $[Co_6Se_8(CO)(PEt_3)_5][PF_6]$ with cobaltocene. $[Co_6Se_8(CO)(PEt_3)_5][PF_6]$ (4) (345 mg, 0.197 mmol, 1 eq.) was dissolved in tetrahydrofuran (THF, 10 mL) in a scintillation vial equipped with a magnetic stir bar. A solution of cobaltocene (37 mg, 0.197 mmol, 1 eq.) in THF (3 mL) was added dropwise, and the resulting mixture was stirred for an additional hour at which point the solvent was evaporated *in vacuo*. The solid was triturated with acetonitrile three times to remove the soluble $[CoCp_2][PF_6]$ (Cp = cyclopentadienyl). Yield (based on $[Co_6Se_8(CO)(PEt_3)_5][PF_6]$): 87% (0.276 g, 0.172 mmol).

^{1}H NMR (300 MHz, benzene-d_6) δ = 1.99 (dq, J = 9.4, 7.6 Hz, 6H), 1.78 (dq, J = 9.2, 7.5 Hz, 24 H), 1.12 (dt, J = 14.9, 7.5 Hz, 9H), 0.99 (dt, J = 15.0, 7.5 Hz, 36 H) ppm; ^{31}P NMR (202 MHz, benzene-d_6) δ = 68 (broad), 62 (broad) ppm.

Synthesis of *trans*-$Co_6Se_8(iPrNC)_2(PEt_3)_4$ (7). A Pyrex Schlenk flask was loaded with a solution of *trans*-$Co_6Se_8(CO)_2(PEt_3)_4$ (0.030 g, 0.020 mmol, 1 eq.) in THF (5 mL). A stock solution of isopropyl isocyanide (^{i}PrNC) was prepared by dissolving 0.1 mL (1.060 mmol) in THF (5 mL).

An aliquot of this stock solution (0.25 mL, 0.050 mmol of ^{i}PrNC, 2.5 eq.) was added dropwise to the stirring cluster solution, and the resulting mixture was irradiated using a broadband lamp (200-400 nm) for 5 hours at room temperature. The solvent was evaporated *in vacuo*. X-ray quality single crystals of *trans*-$Co_6Se_8(^{i}PrNC)_2(PEt_3)_4$ were grown by diffusing of hexanes vapor into a toluene solution of the cluster. Yield: 42% (0.013 g, 0.008 mmol). ^{1}H NMR (500 MHz, benzene-d_6) δ = 3.37 (hept, 2H), 1.88 (m, 24H), 1.07 (dt, *J* = 15.0, 7.5 Hz, 36H), 0.94 (d, J = 6.49, 12H) ppm; ^{31}P NMR (202 MHz, benzene-d_6) δ = 62 (broad) ppm.

Synthesis of *trans*-$Co_6Se_8(PEt_2C_6H_4SMe)_2(PEt_3)_4$ (8)

A Pyrex Schlenk flask was loaded with a solution of *trans*-$Co_6Se_8(CO)_2(PEt_3)_4$ (0.040 g, 0.026 mmol, 1 eq.) in THF (10 mL). Diethyl-4-thiomethylphenylphosphine (0.019 g, 0.089 mmol, 3.4 eq.), prepared as previously reported[1]) was dissolved THF (5 mL) and added dropwise to the stirring cluster solution. The reaction mixture was irradiated using a broadband lamp (200-400 nm) for 5 hours at room temperature. The solvent was evaporated *in vacuo*. X-ray quality single crystals were grown by slowly diffusing hexanes vapor into a toluene solution of the product. Yield: 79% (0.038 g, 0.007 mmol). ^{1}H NMR (500 MHz, benzene-d_6) δ = 7.61 (t, J = 8.2 Hz, 4H), 7.11 (d, J = 7.9 Hz, 4H), 2.55 – 2.31 (m, 8H), 1.97 (s, 6H), 1.86 (m, 24H), 1.08 (m, 48H) ppm; ^{31}P NMR (202 MHz, benzene-d_6) δ = 61 (broad), 57 (broad) ppm.

Synthesis of *trans*-$Co_6Se_8(CNC_6H_4NC)_2(PEt_3)_4$ (9)

A Pyrex Schlenk flask was loaded with a solution of *trans*-$Co_6Se_8(CO)_2(PEt_3)_4$ (0.224 g, 0.148 mmol, 1 eq.) in THF (20 mL). 1,4-Phenylene diisocyanide (0.096 g, 0.738 mmol, 5 eq.) was added (an excess of the linker is necessary to prevent oligomerization). The reaction mixture was

irradiated using a broadband lamp (200-400 nm) for 8 hours at room temperature. The solvent was evaporated *in vacuo*. The solid was triturated with acetonitrile three times to remove excess linker. This procedure was repeated twice. Yield: 67% (0.169 g. 0.098 mmol). X-ray quality crystals were grown from a mixture of THF and diethyl ether. ^{1}H NMR (500 MHz, benzene-d_6) δ = 6.61 (d, *J* = 8.6 Hz, 4H), 6.34 (d, *J* = 8.4 Hz, 4H), 1.82 (m, 24H), 1.02 (dt, *J* = 14.9, 7.4 Hz, 36H) ppm; ^{31}P NMR (161.9 MHz, benzene-d_6) δ = 62 (broad) ppm.

Synthesis of *cis*-$Co_6Se_8(CNC_6H_4NC)_2(PEt_3)_4$ (10)

A Pyrex Schlenk flask was loaded with a solution of *cis*-$Co_6Se_8(CO)_2(PEt_3)_4$ (0.042 g, 0.027 mmol, 1 eq.) in THF (10 mL). 1,4-Phenylene diisocyanide (0.018 g, 0.135 mmol, 5 eq.) was added (an excess of the linker is necessary to prevent oligomerization). The reaction mixture was irradiated using a broad band lamp (200-400 nm) for 8 hours at room temperature. The solvent was evaporated *in vacuo*. The solid was triturated with acetonitrile three times to remove excess linker. This procedure was repeated three times. Yield: 70% (0.032 g, 0.019 mmol). X-ray quality crystals were grown from a mixture of THF and diethyl ether. ^{1}H NMR (300 MHz, benzene-d_6) δ = 6.53 (d, *J* = 8.7 Hz, 4H), 6.31 (d, *J* = 8.6 Hz, 4H), 1.86 (m, 24H), 1.04 (m, 36H) ppm; ^{31}P NMR (161.9 MHz, benzene-d_6) δ = 66 (broad), 62 (broad) ppm.

Synthesis of $Co_6Se_8(CNC_6H_3Me_2)(PEt_3)_5$ (11)

A Pyrex Schlenk flask was loaded with a solution of $Co_6Se_8(CO)(PEt_3)_5$ (0.040 g, 0.025 mmol, 1 eq.) in THF (5 mL). 2,6-Dimethylphenyl isocyanide (0.003 g, 0.025 mmol, 1 eq.) in THF (1 mL) was added. The reaction mixture was irradiated using a broadband lamp (200-400 nm) for 5 hours at room temperature. The solvent was evaporated *in vacuo*. The solid was triturated with

acetonitrile three times to remove excess ligand. Yield: 84% (0.036 g, 0.021 mmol). ^{1}H NMR (500 MHz, benzene-d_6) δ = 6.69 (m, 3H), 2.49 (s, 6H), 2.04 – 1.96 (m, 6 H), 1.96 – 1.86 (m, 24H), 1.10 (m, 45H); ^{31}P NMR (161.9 MHz, C_6D_6) δ = 63 (broad), 60 (broad) ppm.

Synthesis of *trans*-$Co_6Se_8(CNC_6H_3Me_2)_2(PEt_3)_4$ (12)

A Pyrex Schlenk flask was loaded with a solution of *trans*-$Co_6Se_8(CO)_2(PEt_3)_4$ (0.070 g, 0.046 mmol, 1 eq.) in THF (5 mL). 2,6-Dimethylphenyl isocyanide (0.012 g, 0.092 mmol, 2 eq.) in THF (1 mL) was added. The reaction mixture was irradiated using a broadband lamp (200-400 nm) for 5 hours at room temperature. The solvent was evaporated *in vacuo*. The solid was triturated with acetonitrile three times to remove excess ligand. Yield: 75% (0.059 g, 0.034 mmol). ^{1}H NMR (500 MHz, benzene-d_6) δ = 6.70 (m, 6H), 2.50 (s, 12H), 1.86 (m, 24H), 1.05 (dt, J = 15.0, 7.5 Hz, 36H) ppm; ^{31}P NMR (161.9 MHz, C_6D_6) δ = 63 (broad) ppm.

Synthesis of dimer (neutral) $Co_{12}Se_{16}(PEt_3)_{10}(CNC_6H_4NC)$ (13)

A Pyrex Schlenk flask was loaded with a solution of $Co_6Se_8(CO)(PEt_3)_5$ (0.158 g, 0.098 mmol,1 eq.) in THF (10 mL). 1,4-Phenylene diisocyanide (6.4 mg, 0.049 mmol, 0.5 eq.) was added. The reaction mixture was irradiated using a broadband lamp (200-400 nm) for 3 hours at room temperature. The solvent was removed *in vacuo*. The remaining solid was triturated with diethyl ether three times. Yield: 85% (0.138 g, 0.042 mmol)^{1}H NMR (500 MHz, benzene-d_6) δ = 6.60 (s, 4H), 2.03 – 1.85 (m, 60H), 1.10 (m, 90H); ^{31}P NMR (161.9 MHz, C_6D_6) δ = 66 (broad), 62 (broad) ppm.

Synthesis of dimer (oxidized) $[Co_{12}Se_{16}(PEt_3)_{10}(CNC_6H_4NC)][PF_6]_2$ (14)

A Pyrex Schlenk flask was loaded with a solution of $[Co_6Se_8(CO)(PEt_3)_5][PF_6]$ (0.286 g, 0.163 mmol, 1 eq.) in THF (15 mL). 1,4-Phenylene diisocyanide (0.011 g, 0.082 mmol, 0.5 eq.) was added. The reaction mixture was irradiated using a broadband lamp (200-400 nm) for 4 hours at room temperature. The solvent was evaporated *in vacuo*. The remaining solid was triturated with toluene. This procedure was repeated until the solution turned colorless (usually 3 times). Yield: 72% (0.209 g, 0.059 mmol). X-ray quality crystals were grown from a mixture of THF and toluene. ^{1}H NMR (500 MHz, $CDCl_3$, 300K) δ = 7.99 (s, 4H), 0.82 (s, 18H), 0.14 (m, 84H), -0.99 (d, J = 7.7 Hz, 48H); ^{1}H NMR (500 MHz, CD_2Cl_2, 217K) δ = 8.39 (s, 4H), 0.59 (s, 18H), -0.59 (s, 72H), -0.97 (s, 12H), -2.68 (s, 48H); ^{31}P NMR (161.9 MHz, $CDCl_3$) δ = -144 (PF_6^-), -402 (broad), -452 (broad) ppm.

Synthesis of trimer (neutral): $Co_{18}Se_{24}(PEt_3)_{14}(CNC_6H_4NC)_2$ (15)

A Pyrex Schlenk flask was loaded with a solution of *trans*-$Co_6Se_8(CNPhNC)_2(PEt_3)_4$ (0.163 g, 0.095 mmol, 1 eq.) in THF (35 mL). $Co_6Se_8(CO)(PEt_3)_5$ (0.304 g, 0.189 mmol, 2 eq.) was added. The reaction mixture was irradiated using a broadband lamp (200-400 nm) for 6 hours at room temperature. The solvent was evaporated *in vacuo*. The remaining solid was triturated with diethyl ether four times. Yield: 76% (0.351 g, 0.072 mmol). ^{1}H NMR (500 MHz, benzene-d_6) δ = 6.61 (s, 8H), 2.07 – 1.76 (m, 84H), 1.06 (m, 126H); ^{31}P NMR (161.9 MHz, C_6D_6) δ = 63 (broad) ppm.

Synthesis of $Co_6Se_8(CO)_x(PPh_3)_{(6-x)}$ isomers (3 Co_2CO_8: 12 Se: 6 PPh_3)

Inside the glovebox, Se (1.336 g, 16.9 mmol, 12 eq.), $Co_2(CO)_8$ (1.446 g, 4.23 mmol, 3 equiv), and PPh_3 (2.219 g, 8.46 mmol, 6 eq.) were loaded in a 100 mL Schlenk flask. Toluene (20 mL)

was added and the flask was transferred to a Schlenk line under N_2. The reaction was stirred at 110°C for 16 hours, during which time the color darkened to deep brown. After cooling to room temperature, the mixture filtered through a Celite plug and the filtrate was evaporated *in vacuo*. The resulting solid was dissolved in a minimum amount of dichloromethane (~ 5 mL). The product was purified by column chromatography (80 g Redisep Rf Silica) using 20 % ethyl acetate/hexanes at a rate of 80 mL/min to afford the following clusters:

$Co_6Se_8(CO)_5(PPh_3)$, yield: 1.8% (0.036 g); *cis*-$Co_6Se_8(CO)_4(PPh_3)_2$, yield: 4.5% (0.103 g); *trans*-$Co_6Se_8(CO)_4(PPh_3)_2$, yield: 7.0% (0.161 g), *fac*-$Co_6Se_8(CO)_3(PPh_3)_3$, yield: 1.9% (0.049 g). These clusters were not further characterized, but their structures were solved by single-crystal X-ray diffraction.

Synthesis of $Co_6Te_8(CO)_x(PEt_3)_{(6-x)}$ isomers (3 Co_2CO_8: 12 Te: 6 PEt_3)

Inside the glovebox, Te (2.158 g, 16.9 mmol, 12 eq.) and Co_2CO_8 (1.446 g, 4.23 mmol, 3 eq.) were loaded in a 100 mL Schlenk flask. Toluene (20 mL) was added and the flask was transferred to a Schlenk line under N_2. Neat PEt_3 (1.000 g, 8.46 mmol, 8 eq.) was syringed into the flask effecting effervescence. The reaction mixture was heated to 110 °C for 16 hours, during which time the color darkened to deep brown. The mixture was filtered through a fine frit, concentrated *in vacuo* to 5 mL, and finally layered with hexanes. Single crystals of both the *cis*-CO and *trans*-CO isomers were present in the vial. These were collected and their structures were solved by single-crystal X-ray diffraction.

Synthesis of $[Co_6Se_8(PEt_3)_4]_l[CNC_6H_4NC]_m[CO]_n$ oligomers

A Pyrex Schlenk flask was loaded with a solution of *trans*-$Co_6Se_8(CO)_2(PEt_3)_4$ (0.062 g, 0.041 mmol, 1 eq.) and CNC_6H_4NC (0.005 g, 0.041 mmol, 1 eq.) in THF (5 mL) The reaction mixture was irradiated using a broadband lamp (200-400 nm) at room temperature. ^{1}H NMR spectra of

the reaction were measured at different time during the reaction. After 20 hours the reaction was stopped. We obtained a dark brown solution with a dark precipitate. The solid was centrifuged, washed with hexanes and dried (yield: 0.023 g). The IR spectrum of the red/brown solid is displayed in Figure 2.51. The solid was not further characterized.

NMR spectra

Figure 2.7. ^{1}H NMR ($CDCl_3$, 500 MHz) spectrum of diatomic SM **(13)** $Co_{12}Se_{16}(PEt_3)_{10}(CNC_6H_4NC)$.

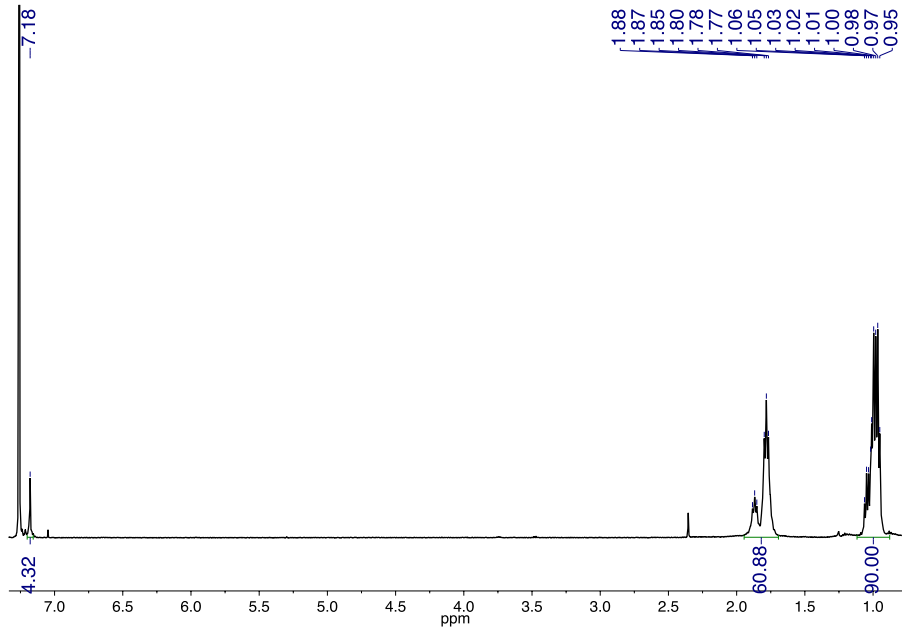

Figure 2.8. ^{1}H NMR (benzene-d_6, 500 MHz) spectrum of triatomic SM **(15)** $Co_{18}Se_{24}(PEt_3)_{14}(CNC_6H_4NC)_2$.

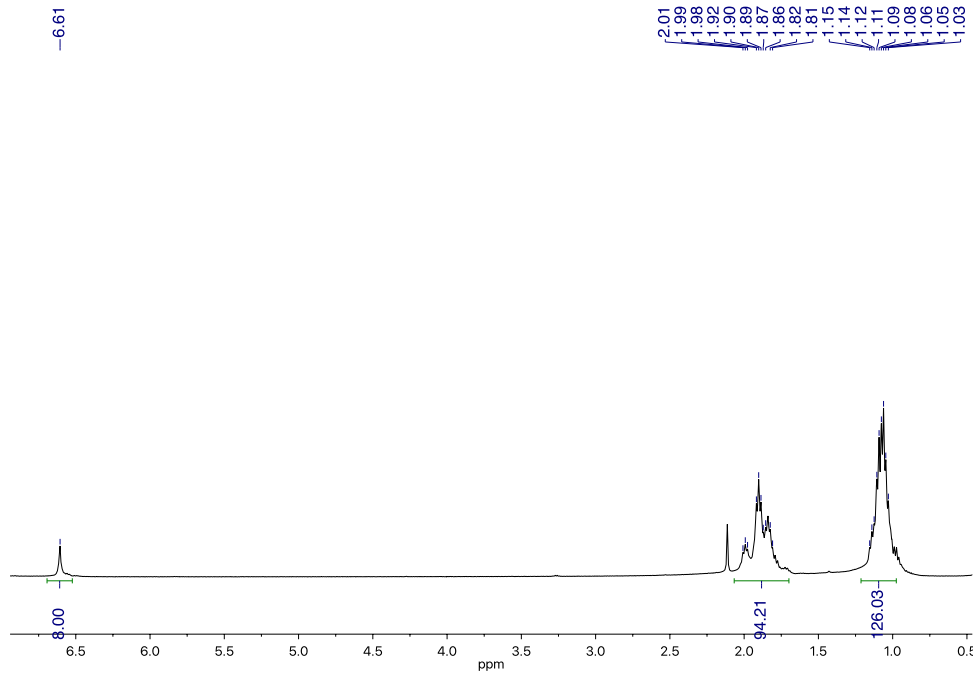

Figure 2.9. ^{1}H NMR (benzene-d_6, 500 MHz) spectrum of **(1)** *trans*-$Co_6Se_8(CO)_2(PEt_3)_4$.

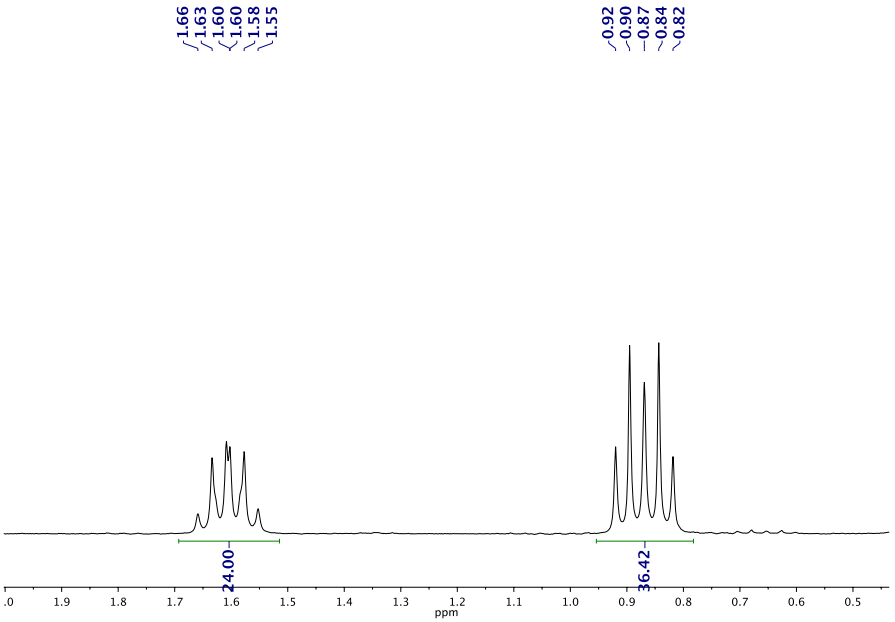

Figure 2.10. ^{31}P NMR (CD_2Cl_2, 500 MHz) spectrum of **(1)** *trans*-$Co_6Se_8(CO)_2(PEt_3)_4$. All ^{31}P NMR spectra look similar to this for the neutral species, with a broadened peak in the 60-70 ppm region.

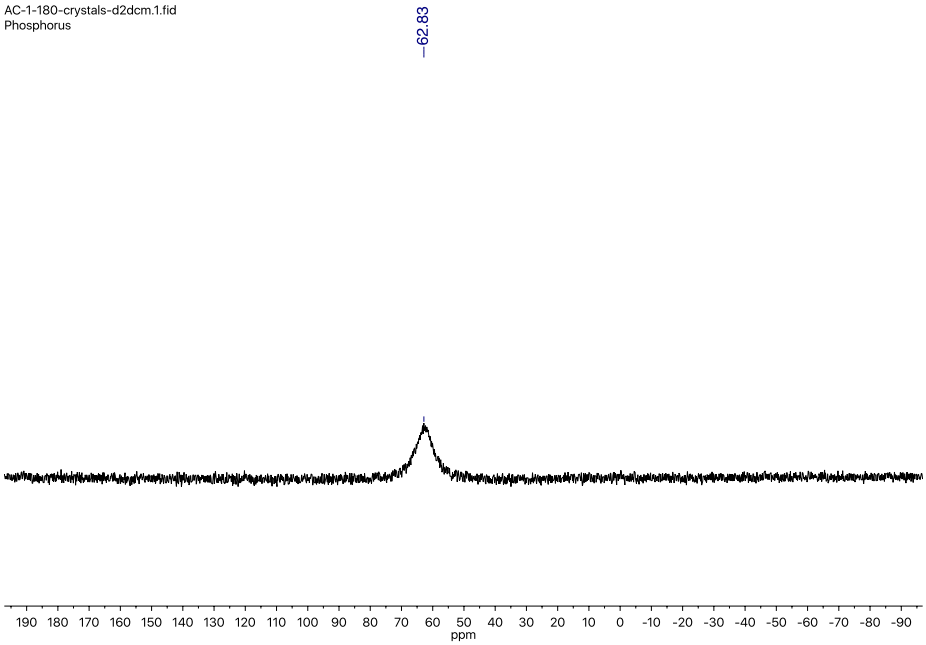

Figure 2.11. ^{1}H NMR (benzene-d_6, 500 MHz) spectrum of **(2)** *cis*-$Co_6Se_8(CO)_2(PEt_3)_4$.

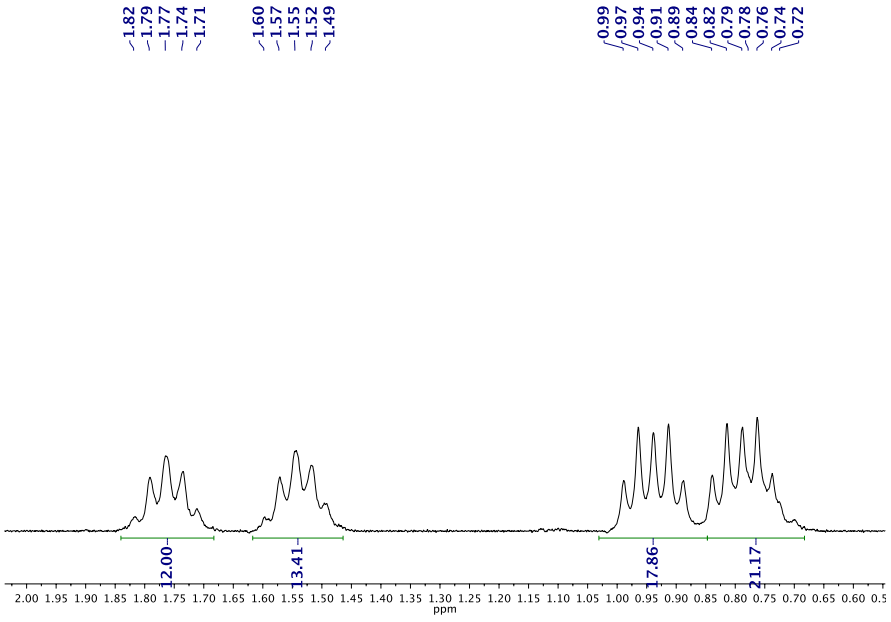

Figure 2.12. ^{1}H NMR ($CDCl_3$, 300 MHz) spectrum of **(4)** $[Co_6Se_8(CO)(PEt_3)_5][PF_6]$.

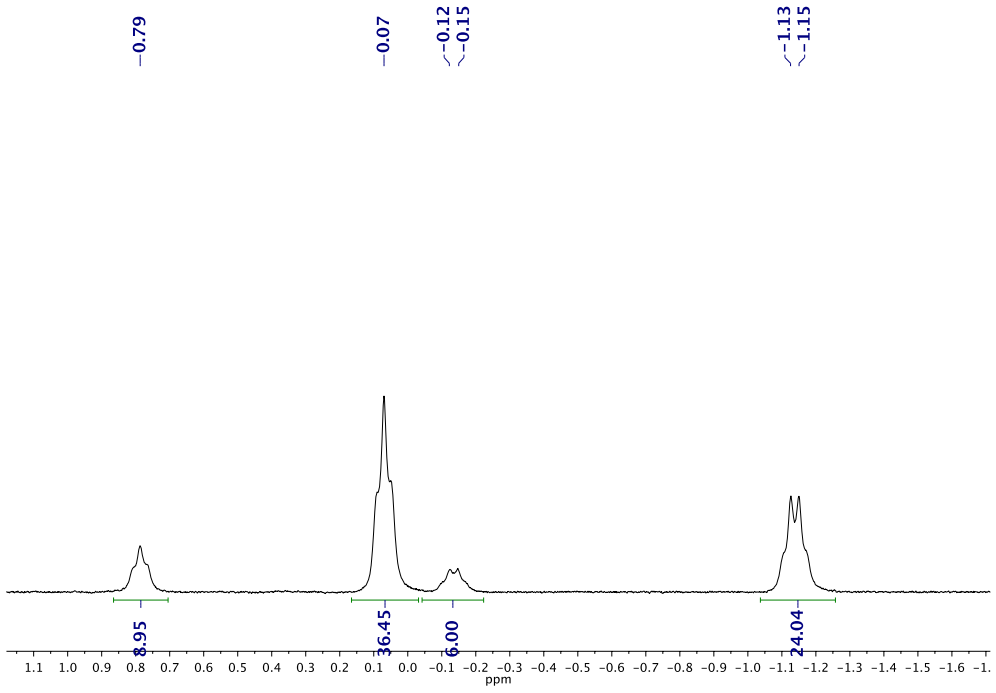

Figure 2.13. ^{1}H NMR (benzene-d_6, 500 MHz) spectrum of **(6)** $Co_6Se_8(CO)(PEt_3)_5$

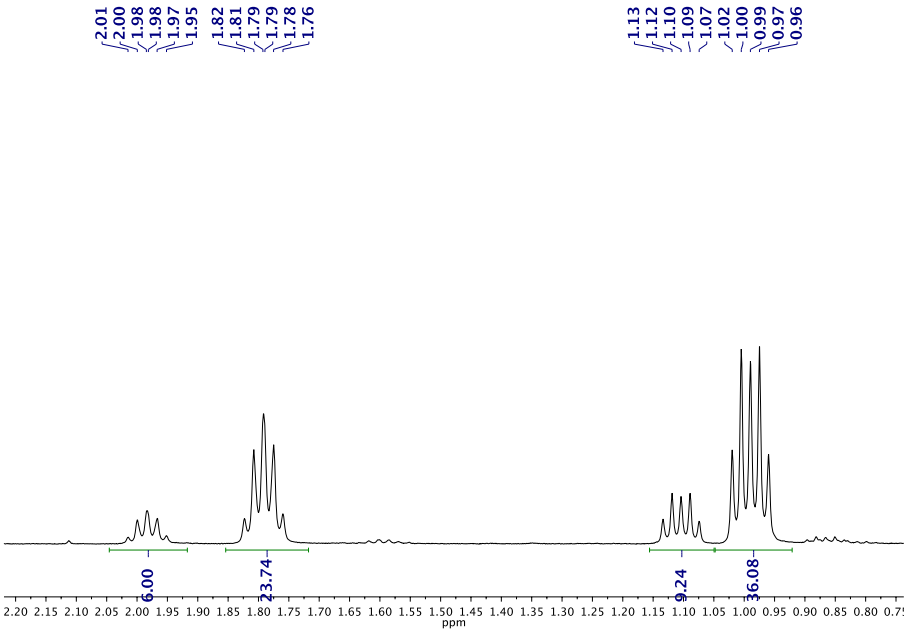

Figure 2.14. ^{1}H NMR (benzene-d_6, 500 MHz) spectrum of **(7)** *trans*-$Co_6Se_8(^{i}PrNC)_2(PEt_3)_4$.

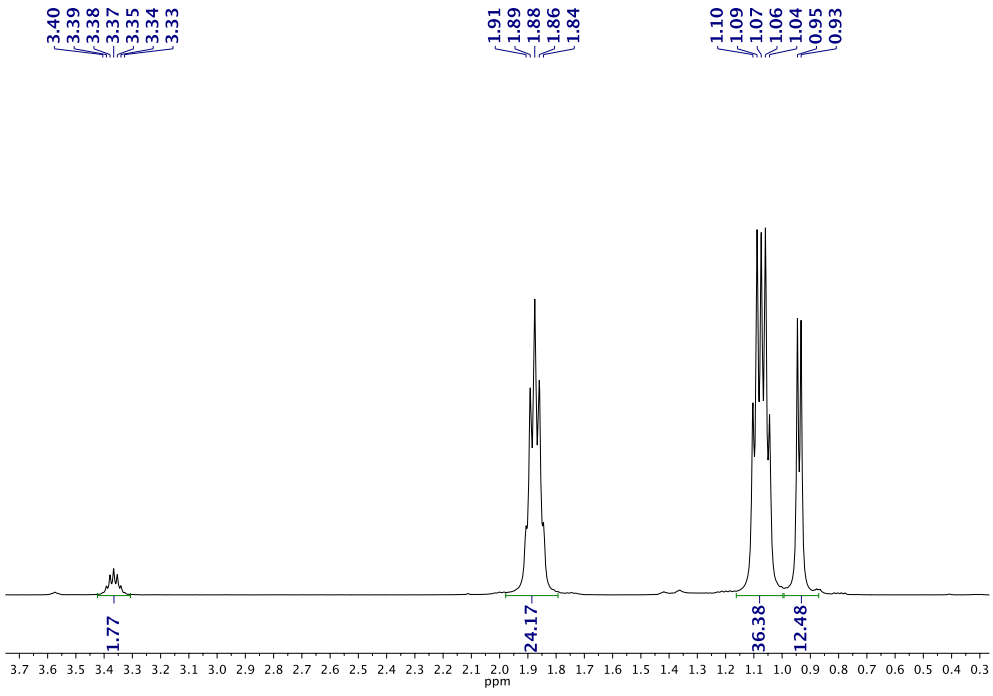

Figure 2.15a. ^{1}H NMR (benzene-d_6, 500 MHz) spectrum of **(8)** *trans*-$Co_6Se_8(PEt_2C_6H_4SMe)_2(PEt_3)_4$. One of the aromatic peaks is hidden by solvent peak.

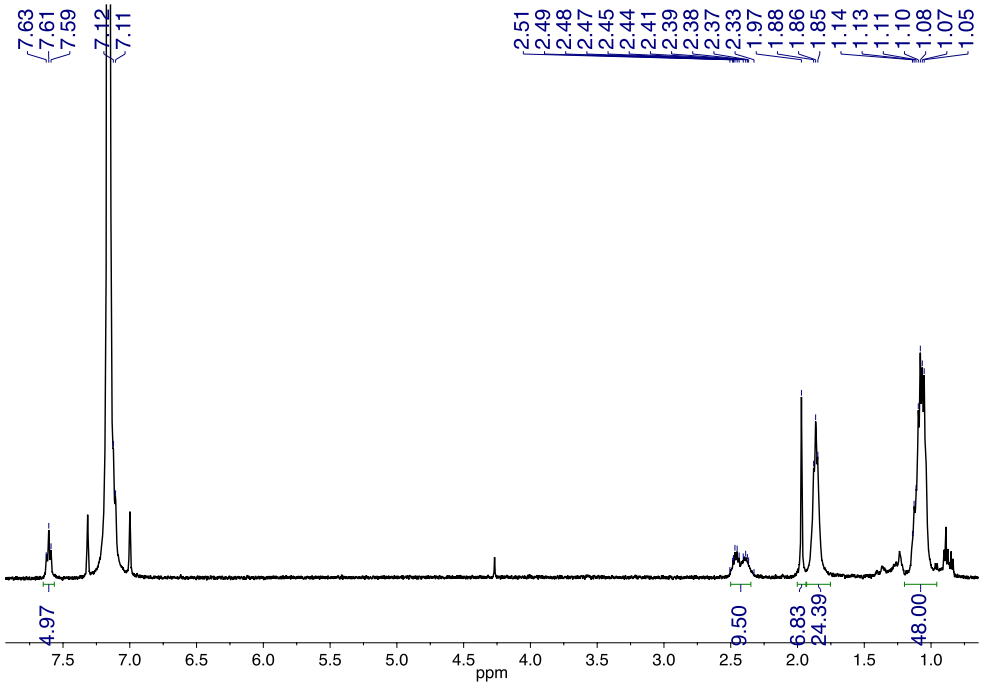

Figure 2.15b. ^{1}H NMR (CD_2Cl_2, 500 MHz) spectrum of **(8)** *trans* $Co_6Se_8(PEt_2C_6H_4SMe)_2(PEt_3)_4$.

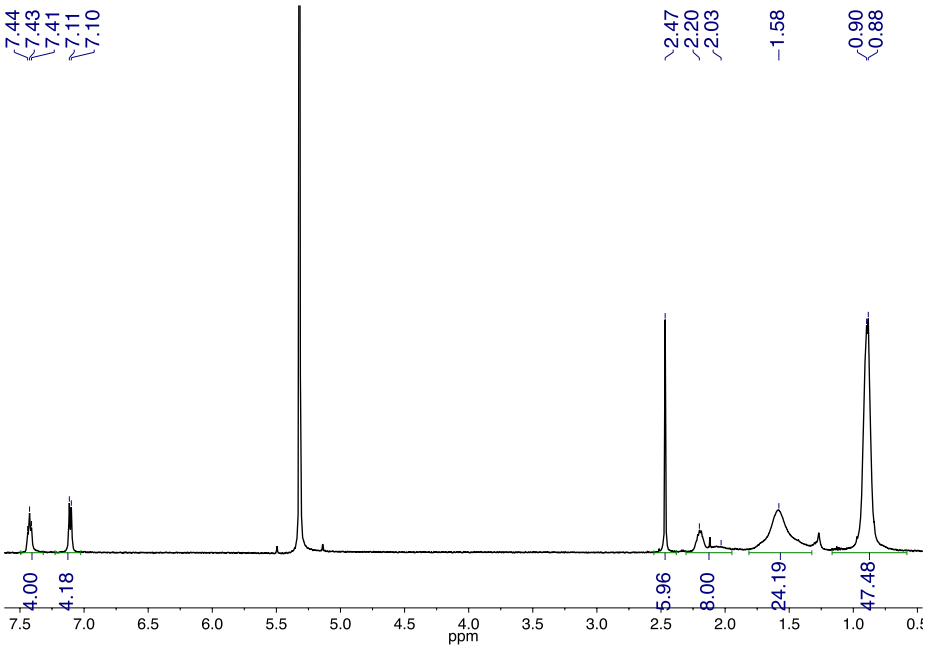

Figure 2.16. ^{1}H NMR (benzene-d_6, 500 MHz) spectrum of **(9)** *trans*-$Co_6Se_8(CNC_6H_4NC)_2(PEt_3)_4$.

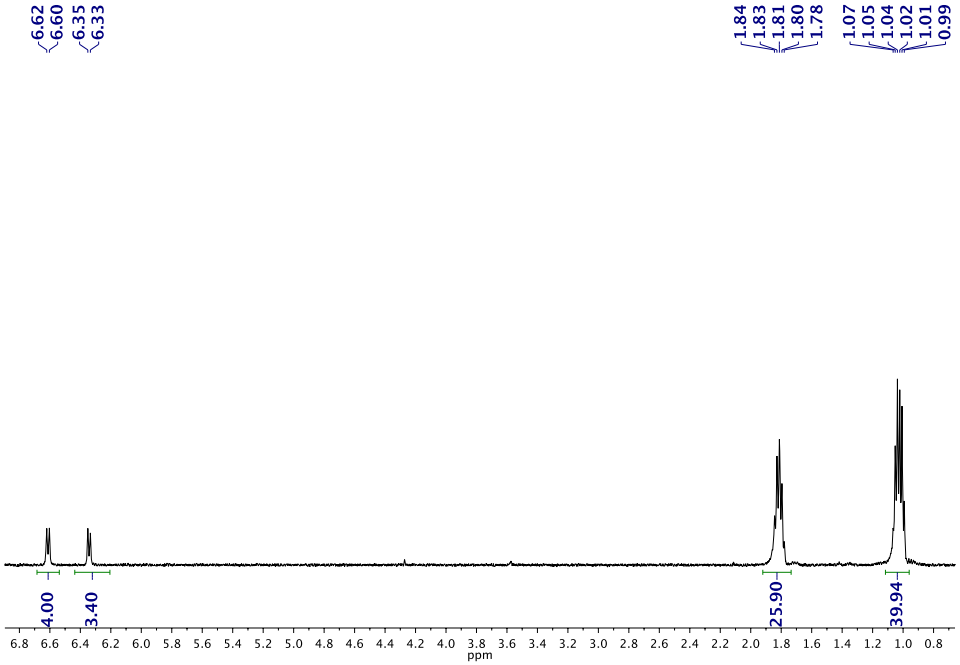

Figure 2.17. ^{1}H NMR (benzene-d_6, 500 MHz) spectrum of **(10)** *cis*-$Co_6Se_8(CNC_6H_4NC)_2(PEt_3)_4$.

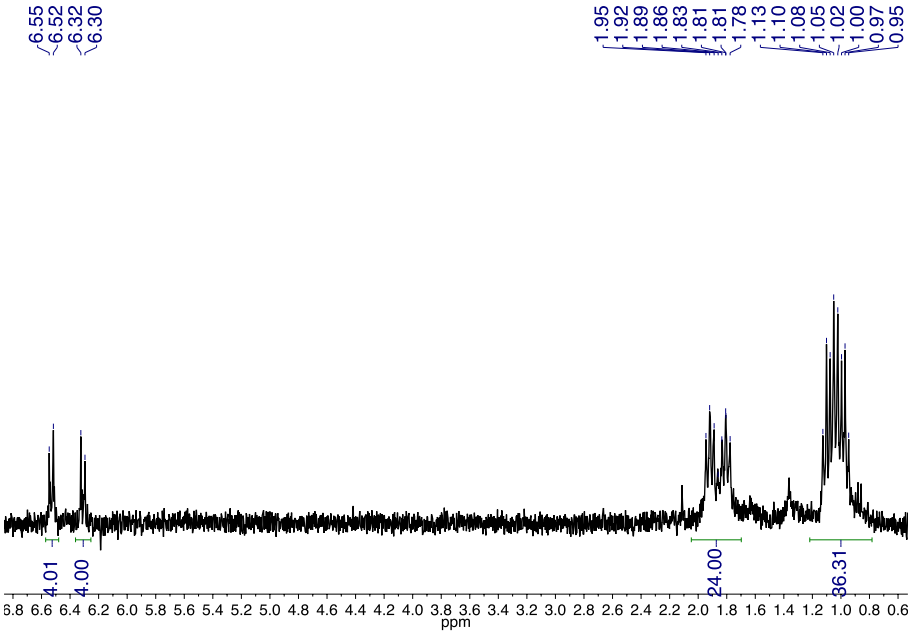

Figure 2.18. ^{1}H NMR (benzene-d_6, 500 MHz) spectrum of **(11)** $Co_6Se_8(CNC_6H_3Me_2)(PEt_3)_5$.

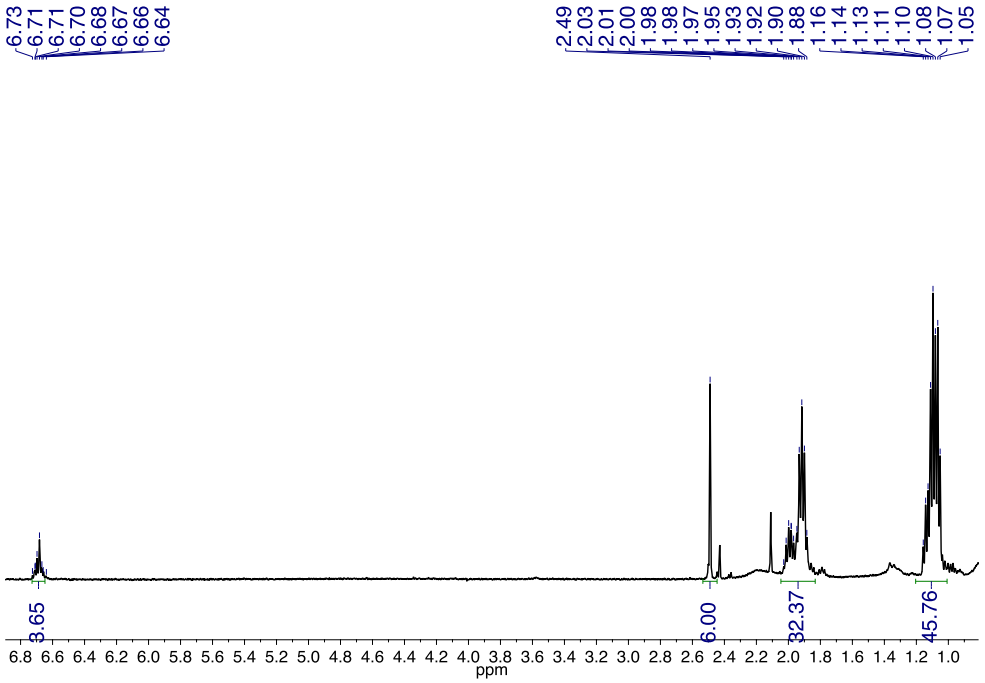

Figure 2.19. ^{1}H NMR (benzene-d_6, 500 MHz) spectrum of **(12)** *trans*-$Co_6Se_8(CNC_6H_3Me_2)_2(PEt_3)_4$.

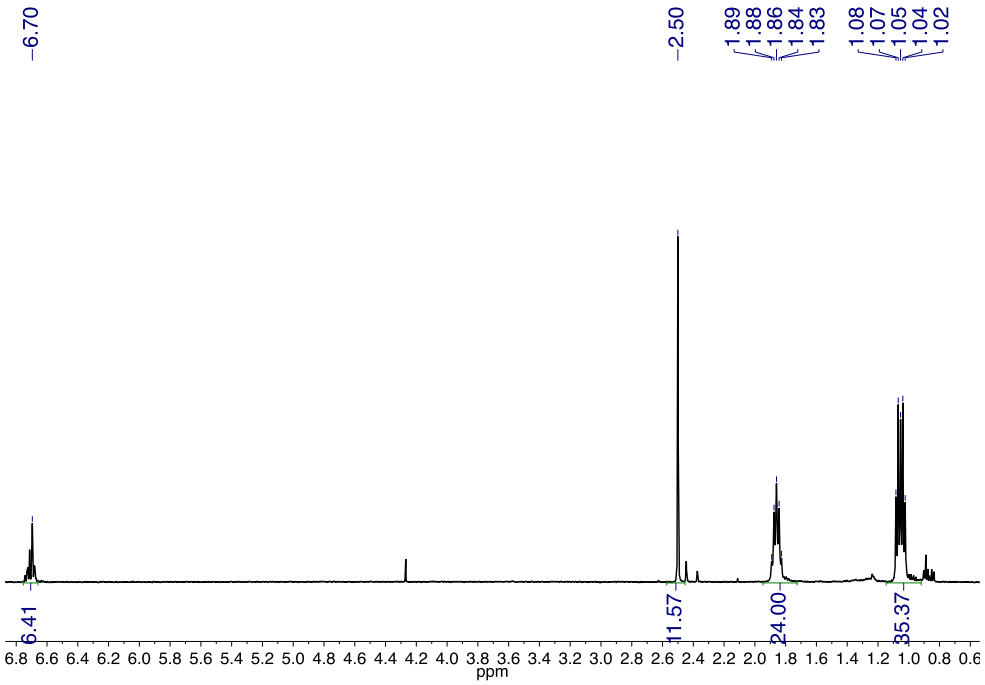

Figure 2.20a. ^{1}H NMR ($CDCl_3$, 500 MHz, 300K) spectrum of **(14)** $[Co_{12}Se_{16}(PEt_3)_{10}(CNC_6H_4NC)][PF_6]_2$. One peak is hidden (at -0.15 ppm) which becomes visible in CD_2Cl_2 at 217K (Figure 2.20b).

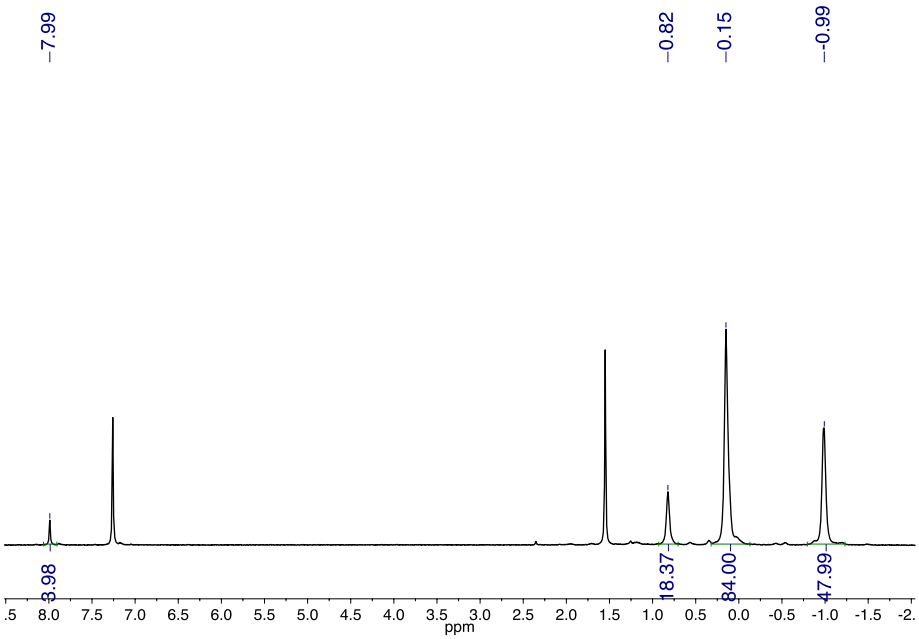

Figure 2.20b. ^{1}H NMR (CD_2Cl_2, 500 MHz, 217K) spectrum of **(14)** $[Co_{12}Se_{16}(PEt_3)_{10}(CNC_6H_4NC)][PF_6]_2$.

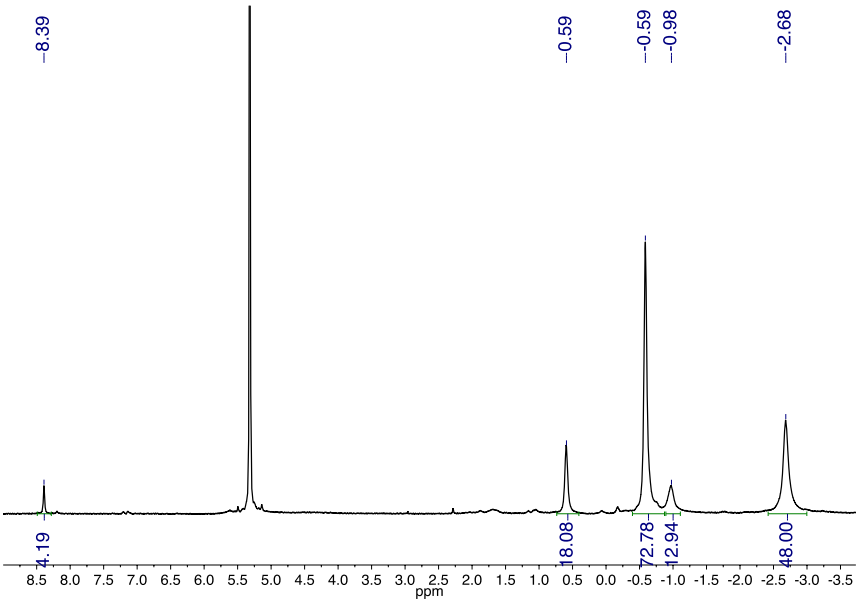

Infrared Spectra of Selected Compounds

Figure 2.21. Infrared spectrum of *mer*-$Co_6Se_8(CO)_3(PEt_3)_3$ **(3)** in the CO stretching region. Peaks are at 1979 and 1995 cm^{-1}, with a shoulder at 2009 cm^{-1}.

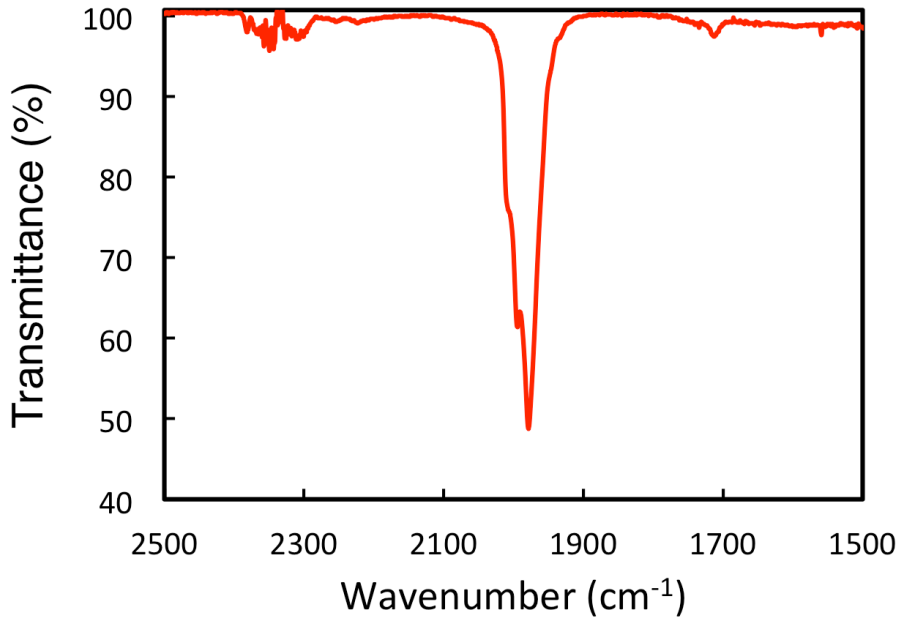

Figure 2.22. Infrared spectrum of $[Co_6Se_8(CO)(PEt_3)_5][PF_6]$ **(4)** in the CO stretching region. Peak is at 1983 cm^{-1}.

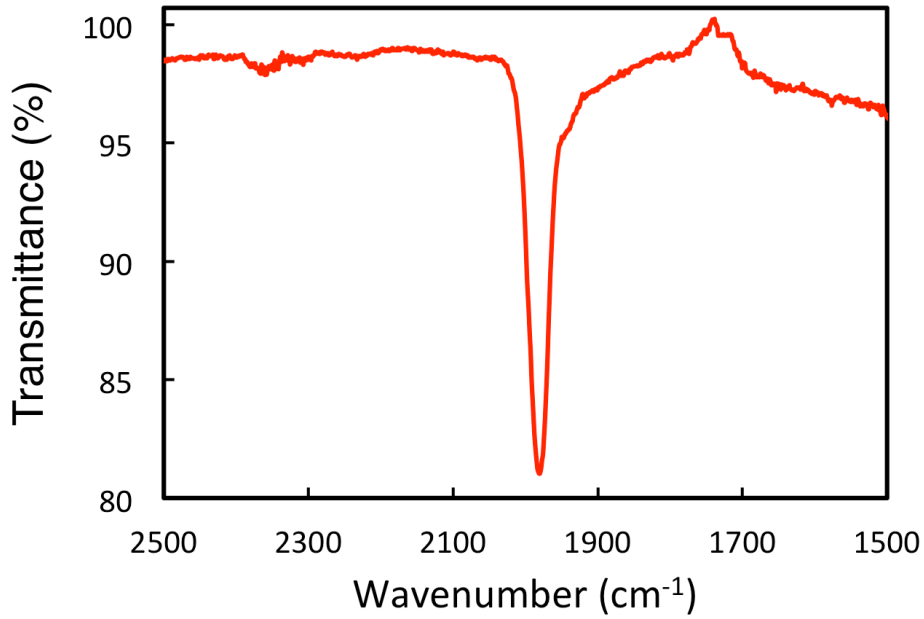

Figure 2.23. Infrared spectrum of *fac*-$Co_6Se_8(CO)_3(PEt_3)_3$ **(5)** in the CO stretching region. Peaks are at 1973 and 1994 cm^{-1}.

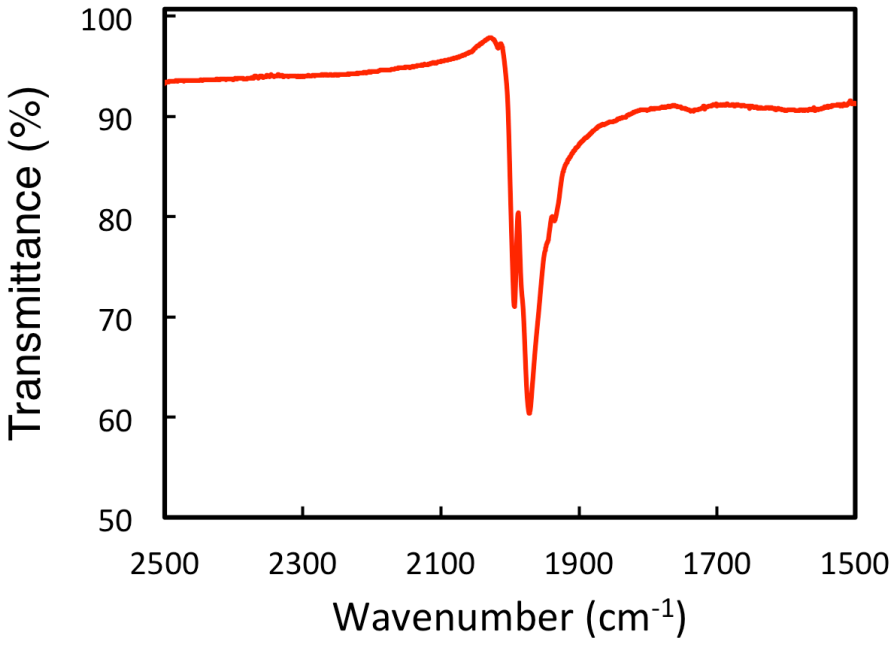

Figure 2.24. Infrared spectrum of $Co_6Se_8(CO)(PEt_3)_5$ **(6)** in the CO stretching region. Peak is at 1958 cm^{-1}.

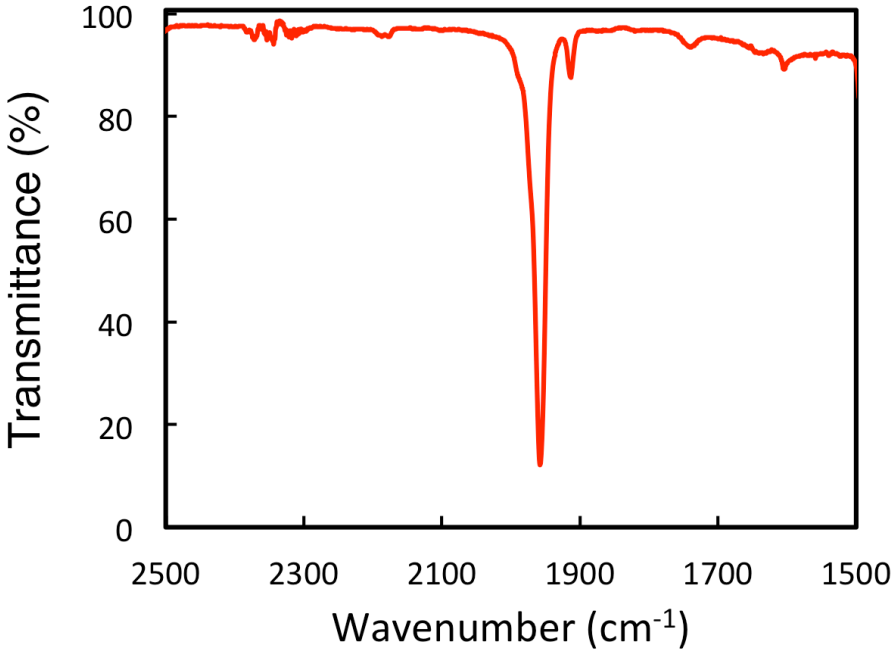

Figure 2.25. Infrared spectrum of *trans*-$Co_6Se_8(^iPrNC)_2(PEt_3)_4$ **(7)** in the CO/CN stretching region.

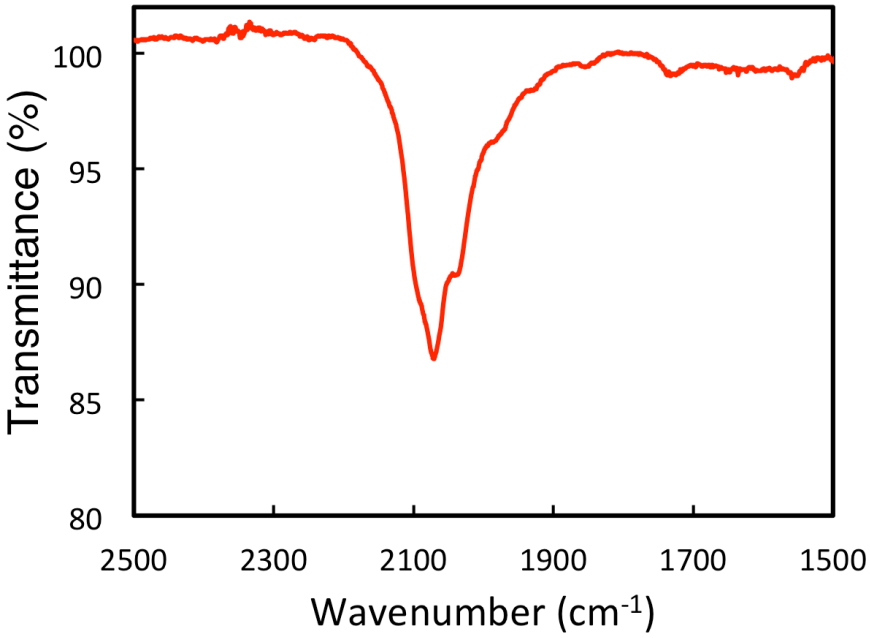

Figure 2.26. Infrared spectrum of *trans*-$Co_6Se_8(PEt_2C_6H_4SMe)_2(PEt_3)_4$ **(8).**

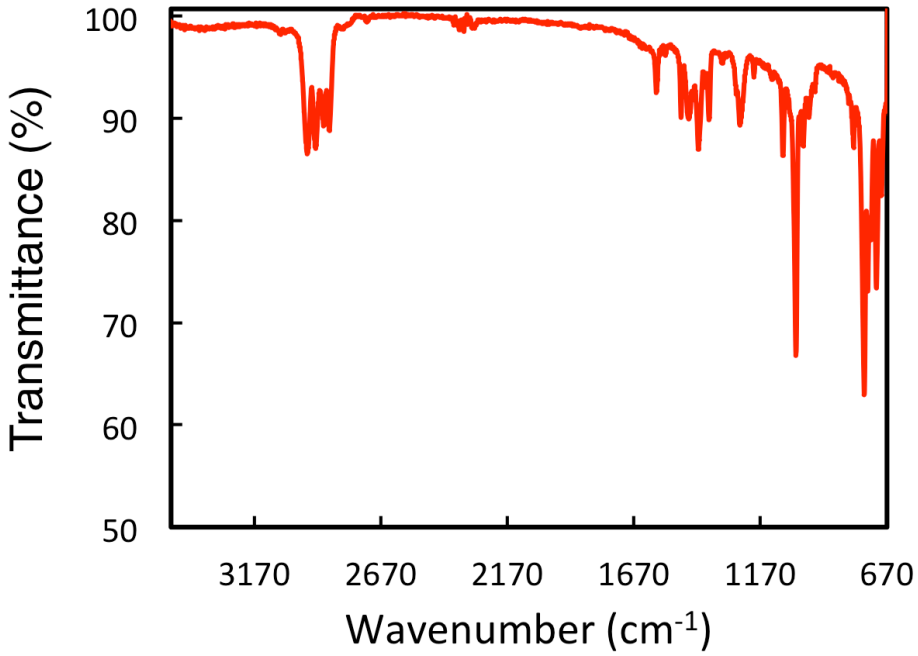

Figure 2.27. Infrared spectrum of *trans*-$Co_6Se_8(CNC_6H_4NC)_2(PEt_3)_4$ **(9)** in the CO/CN stretching region. The broad band in the range 1800-2100 cm^{-1} is due to Co-bound isocyanide. The sharp peak at 2119 cm^{-1} is the unbound isocyanide in the linker.

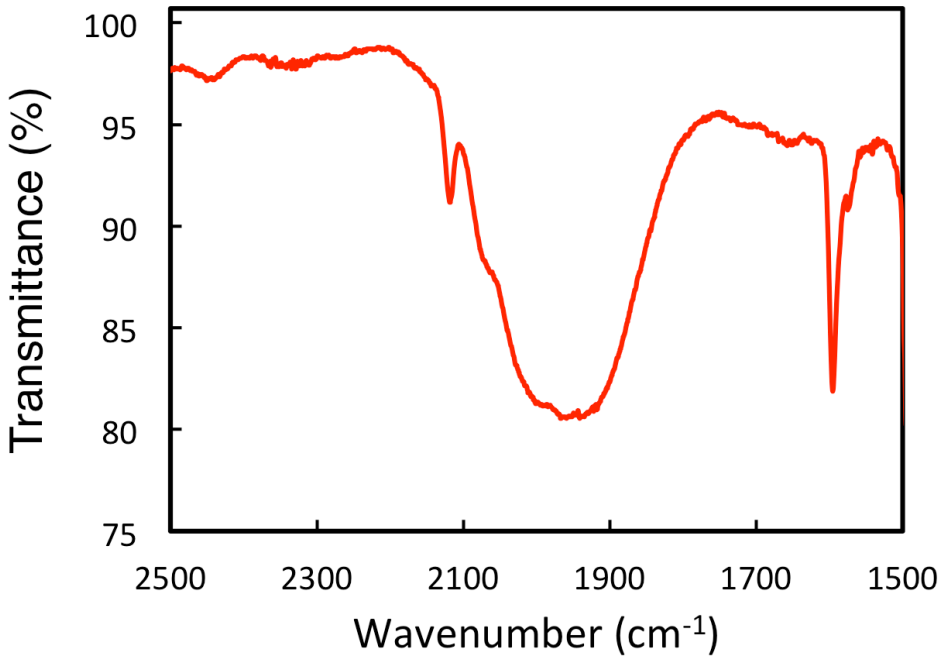

Figure 2.28. Infrared spectrum of *cis*-$Co_6Se_8(CNC_6H_4NC)_2(PEt_3)_4$ **(10)** in the CO/CN stretching region. The broad band in the range 1800-2100 cm^{-1} is due to Co-bound isocyanide. The sharp peak at 2119 cm^{-1} is the unbound isocyanide in the linker.

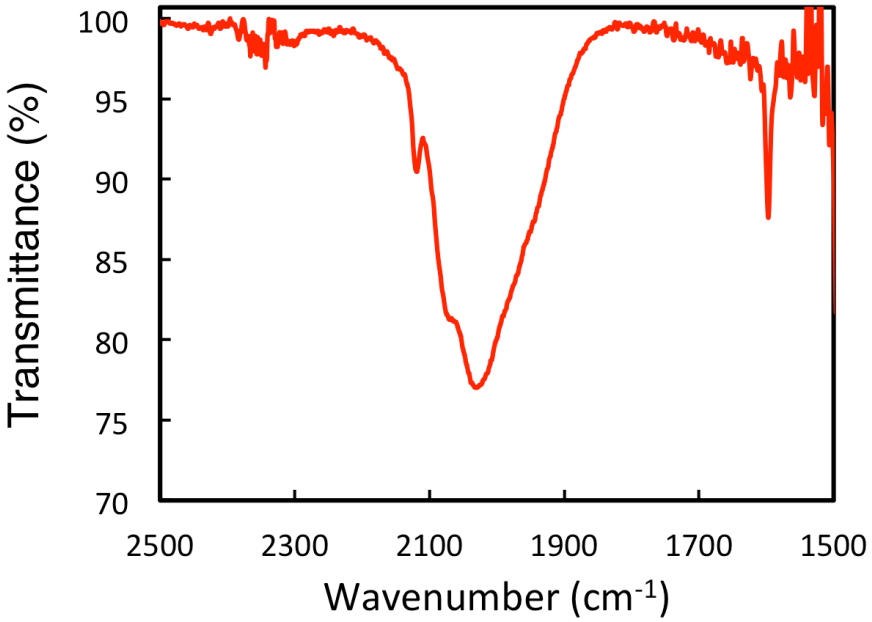

Figure 2.29. Infrared spectrum of $Co_6Se_8(CNC_6H_3Me_2)(PEt_3)_5$ **(11)** in the CO/CN stretching region.

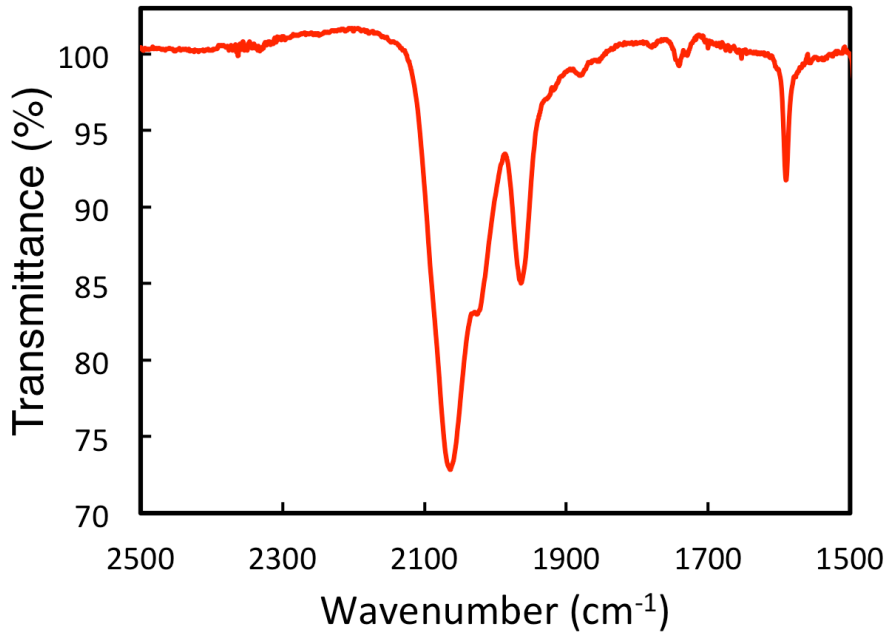

Figure 2.30. Infrared spectrum of *trans*-$Co_6Se_8(CNC_6H_3Me_2)_2(PEt_3)_4$ **(12)** in the CO/CN stretching region.

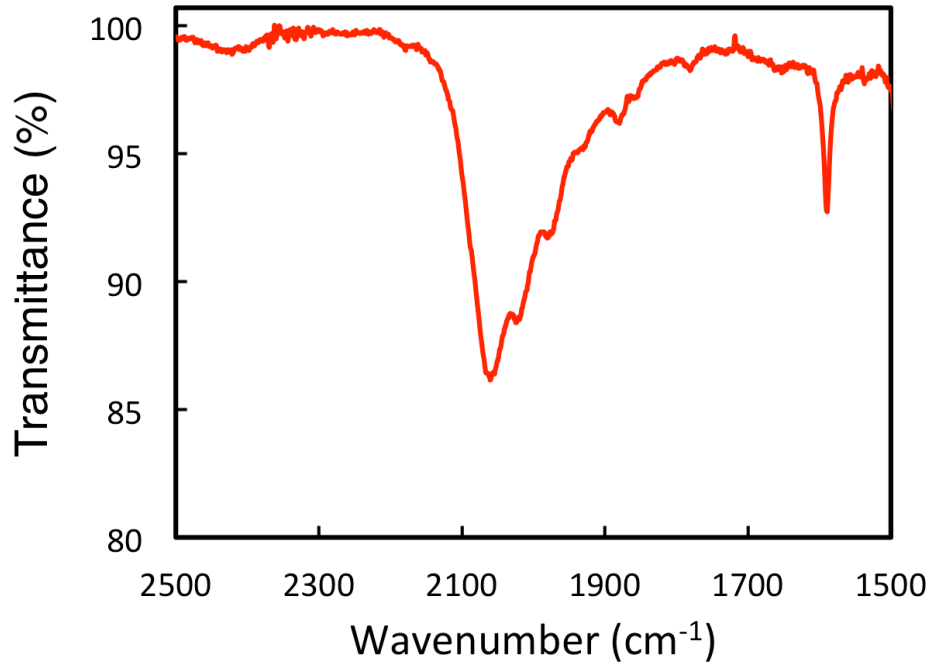

Figure 2.31. Infrared spectrum of $Co_{12}Se_{16}(PEt_3)_{10}(CNC_6H_4CN)$ **(13)** in the CO/CN stretching region.

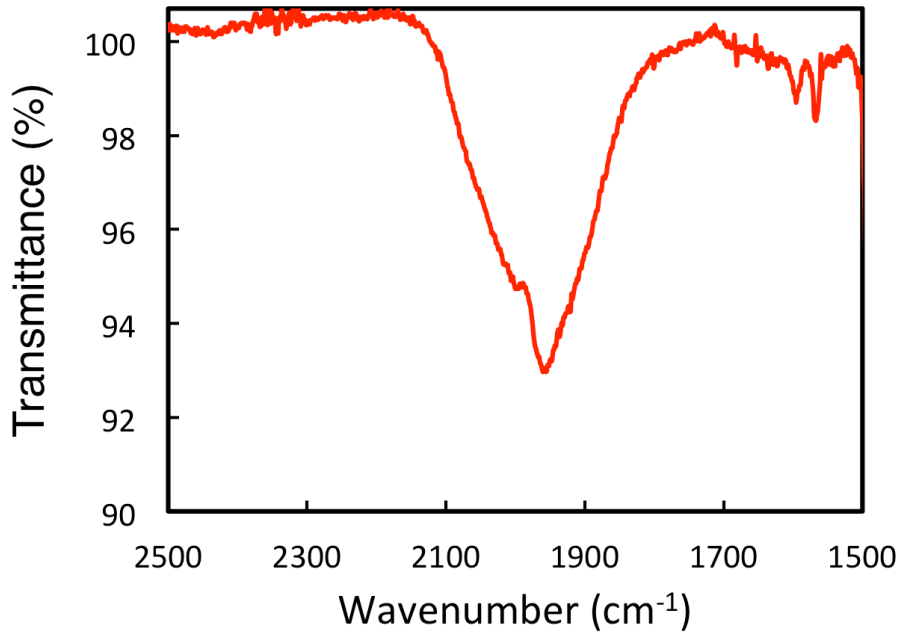

Figure 2.32. Infrared spectrum of $[Co_{12}Se_{16}(PEt_3)_{10}(CNC_6H_4CN)][PF_6]_2$ **(14)** in the CO/CN stretching region.

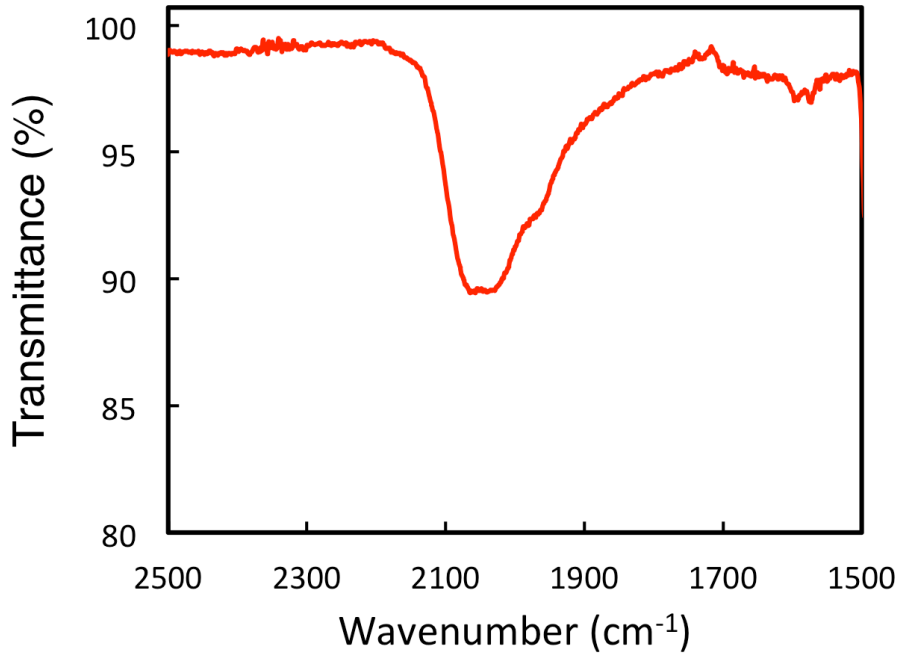

Figure 2.33. Infrared spectrum of $Co_{18}Se_{24}(PEt_3)_{14}(CNC_6H_4CN)_2$ **(15)** in the CO/CN stretching region.

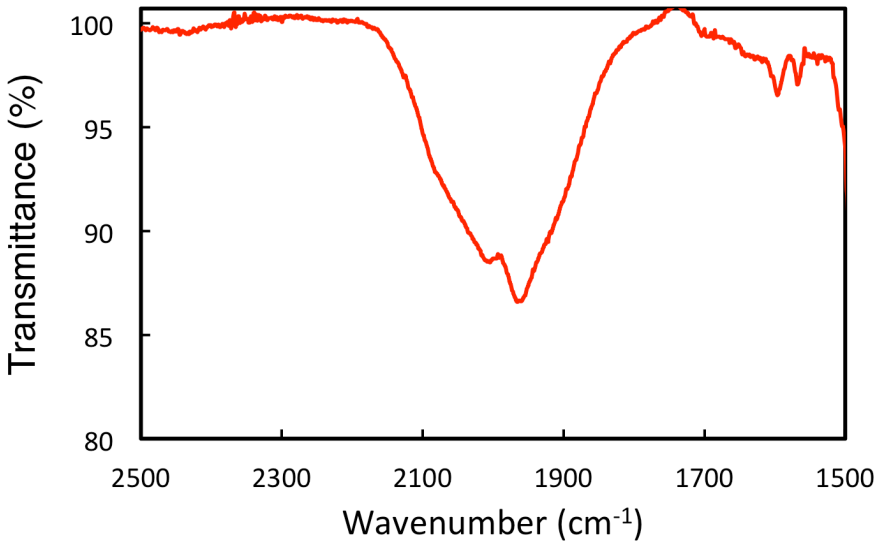

Figure 2.34. Infrared spectrum of the insoluble oligomer solids showing the CO/CN stretching region. The broad peak is characteristic for bound isocyanide ligands. This broadness is seen for the monomeric CNR clusters (as well as di-clusters and tri-clusters) prepared in this chapter.

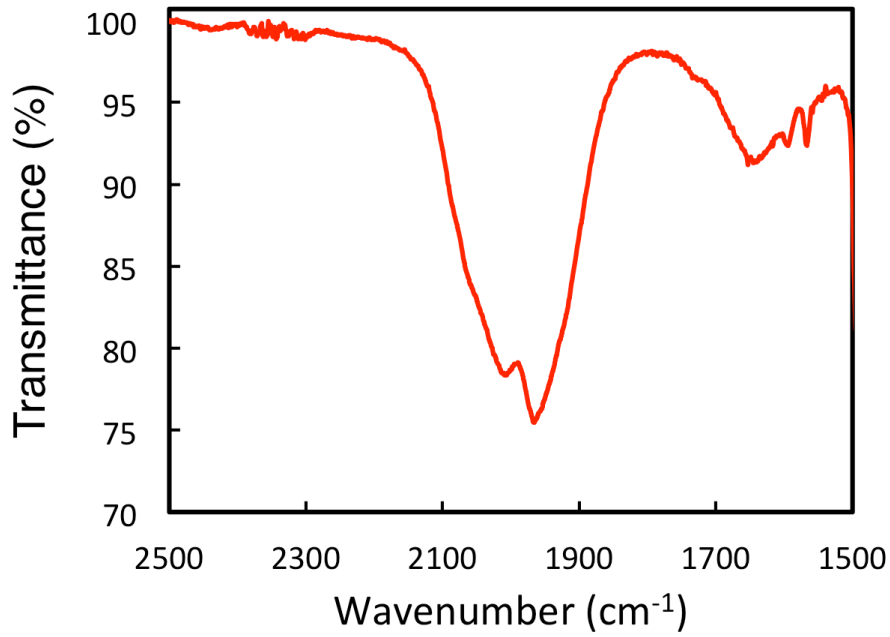

2.10. Single Crystal X-ray Diffraction

Single-crystal XRD experiments were performed on an Agilent SuperNova diffractometer using mirror-monochromated Cu Kα or Mo Kα radiation. In a typical experiment, crystals were mounted in oil on a MiTeGen microloop and cooled rapidly to 100 K on the diffractometer. Complete data were collected to 0.8 Å resolution. Data collection, integration, scaling (ABSPACK) and absorption correction (face-indexed Gaussian integration[17] or numeric analytical methods[18]) were performed in CrysAlisPro.[19] Structures were solved by direct methods in ShelXT[20] or by charge flipping in SuperFlip.[21] Subsequent refinement was performed by full-matrix least-squares on F^2 in ShelXL. Olex2[22] was used for viewing and to prepare CIF files. PLATON[23] was used extensively for SQUEEZE,[24] ADDSYM[25] and TwinRotMat. Many disordered solvent molecules were modeled as rigid fragments from the Idealized Molecular Geometry Library.[26] ORTEP graphics were prepared in CrystalMaker.[27] Thermal ellipsoids are rendered at the 50% probability level.

Any non-routine refinement details are provided. Unless noted, hydrogen atoms were placed in calculated positions and refined with riding isotropic ADPs and coordinates. Non-H atoms were refined anisotropically with any necessary restraints as noted. Thermal ellipsoid plots for each structure are provided at the end of this section, and crystal data for all compounds are given in Table 2.3.

***trans*-$Co_6Se_8(CO)_2(PEt_3)_4$ (1).** The refinement was routine, but the strong 011 reflection was truncated by the beamstop and was excluded from the final refinement.

***cis*-$Co_6Se_8(CO)_2(PEt_3)_4$ (2).** X-ray quality crystals of cis-$Co_6Se_8(PEt_3)_4(CO)_2$ were grown from a solution of EtOAc/n-hexane. The structure crystallized with no solvent. One of the ethyl groups was disordered, and was modeled over two positions.

***mer*-$Co_6Se_8(CO)_3(PEt_3)_3$ (3).** The lattice initially appeared to be orthorhombic C, but weak superstructure reflections were observed at half-integer *h* and *k* values with an unusual pattern of systematic absences. The lattice was transformed to monoclinic P and the *a* axis was doubled, which allowed half of the superstructure reflections to be indexed. When a twofold axis of the orthorhombic metric was included as a twin law, the other half of the superstructure reflections were indexed. A view of the reciprocal lattice is included with superstructure reflections of the monoclinic cell indicated in blue (first twin component) and green (second component).

The data set was integrated as a two-component non-merohedral twin and the structure was solved in ShelXT using the isolated/detwinned reflections of one component. Solutions in $P2_1/n$, Pn and $P2_1$ were examined and the $P2_1/n$ solution was acceptable. Refinement proceeded with the full HKLF 5 data set because the overlapping data were much stronger than the isolated reflections.

The refinement was difficult because of the very near pseudotranslation *a*/2 + *c*/2. In addition, the quality of the crystal was poor, with anisotropically broadened reflections causing unexpected overlap in the data set. Numerous weak high-angle reflections were contaminated by unaccounted overlap from strong adjacent reflections. All C and O ADPs were restrained with RIGU and SIMU, and the three carbonyl and three phosphine ligands were respectively made equivalent with SAME. Platon Squeeze was used to identify a void of 180 $Å^3$ which was estimated to contain solvent equivalent to 35 electrons. This disordered solvent (very roughly the

size and electron count of a toluene molecule) was modeled as a diffuse contribution to the overall scattering.

***fac*-$Co_6Se_8(CO)_3(PEt_3)_3$ (5).** The triclinic crystal was clearly a non-merohedral twin, and CrysAlis identified (001) as a twin axis. When the data reduction was performed with default parameters, the resulting refinement showed strong electron density peaks corresponding to a twofold rotation around *c**, i.e. the originally identified twin law. Numerous other warning signs of twinning were present, including high K for weak reflections and many $F_o>>F_c$ outliers. Inspection of the diffraction frames showed that many reflections were broadened and there was a high degree of unaccounted overlap in the integration. The integration was repeated with masks 1.5x the default size to ensure all overlap was detected. This gave worse R(int) and R(sigma) because of higher background, but the refinement appeared free of systematic errors. are rendered as thermal ellipsoids at the 50% level. C and O are rendered as spheres. A non-crystallographic translation of 0.5 0.5 0.174 is apparent.

Anistropic refinement of light atoms was still not possible. Co, Se, and P atoms were refined with anisotropic ADPs restrained by RIGU. C and O atoms were refined with unrestrained isotropic ADPs.

$Co_6Se_8(CO)(PEt_3)_5$ (6). One of the phosphine ligands was disordered in a 1:1 ratio by a small rotation around the Co-P bond. This was refined with SAME and RIGU restraints on both components of the disorder. All other non-H atoms were refined anisotropically with no restraints.

trans-$Co_6Se_8(^iPrNC)_2(PEt_3)_4$ (7). The structure solved readily in C2/m with one-fourth cluster in the asymmetric unit. The isonitrile ligand was disordered over two independent positions, each lying roughly in the mirror plane and angled toward the 001 and 00-1 directions. Inspection of the structure showed that each independent position of the ligand would overlap with its own adjacent symmetry-equivalent atoms, related by a twofold rotation plus the translation (101). Removing the twofold axis to give a model in polar Cm with one-half cluster in the asymmetric unit corrects this problem.

The model in Cm gave a difficult refinement as expected for a severely pseudocentrosymmetric structure. The Flack parameter was refined to 0.497(16). The atomic positions in the isonitrile ligand were unstable because the twofold twin law exchanges the two independent positions of the ligand. Therefore, it was necessary to apply DFIX restraints to all 1,2 and 1,3 distances in the ligand. The distances in the (iPrN) fragment are predictable and they were restrained to the distances obtained for the well-behaved disordered model in C2/m. The Co-C-N angle was restrained to be nearly linear by creating strict "floating" DFIX restraints with d(Co-N) equal to d(Co-C) + d(C-N). The ADPs in the isonitrile ligands, which are still disordered over the mirror plane, were restrained with RIGU and SIMU. The ADPs of the phosphine C atoms were restrained with RIGU.

***trans-* $Co_6Se_8(PEt_2C_6H_4SMe)_2(PEt_3)_4$ (8).** A toluene molecule of solvation was located on an inversion center and refined as a rigid fragment from the IMGL with ADPs restrained by SIMU and RIGU. All other non-H atoms were refined anisotropically with no restraints.

***trans*-$Co_6Se_8(CNC_6H_4NC)_2(PEt_3)_4$ (9).** The refinement was routine.

***cis*-$Co_6Se_8(CNC_6H_4NC)_2(PEt_3)_4$ (10).** A disordered molecule of hexane was located on a general position and refined in 2 independent positions with 1,2 and 1,3 distances restrained using DFIX. All other non-H atoms were refined anisotropically with no restraints.

***trans*-$Co_6Se_8(CNC_6H_3Me_2)_2(PEt_3)_4$ (12).** The crystal was slightly cracked, which caused many split reflections that could be treated as a non-merohedral twin by a 3° rotation around the arbitrary reciprocal vector (-.06 -1 .18). The two components of the "twin" were present in a roughly 80/20 ratio, and the isolated reflections of the weaker second component were omitted from the data set. The model and twin scale factor were refined against a merged HKLF 5 file.

Several phosphine alkyl groups were disordered over two positions, which were modeled with restrained geometry using SAME, RIGU and SIMU restraints.

$[Co_{12}Se_{16}(PEt_3)_{10}(CNC_6H_4NC)][PF_6]_2$ (14). The diffraction was extremely weak, with I/σ less than 1 for all data shells outside 1.4 Å resolution. However, structure solution proceeded normally in ShelXT with the cluster dimer found on an inversion center. Most non-H atoms were located quickly in successive Fourier maps.

The bridging diisonitrile ligand did not appear readily in difference maps, but it was located successfully by placing its atoms approximately and applying DFIX restraints for all 1,2 and 1,3 distances and a FLAT restraint for all atoms.

All 5 independent phosphine ligands were made equivalent with a SAME instruction.

There were 2 independent PF_6^- anions in the asymmetric unit. One anion was fully ordered on an inversion center. The other anion appeared in difference maps on a general position, but the difference peak was not large enough for a fully occupied PF_6^- molecule. The central P atom was

placed and its U_{iso} was constrained at the U_{equiv} of the P atom in the ordered anion. This atom's occupancy was varied by hand until the difference map around the atom was flat; this condition was met at 50% occupancy. When the 6 F atoms were placed, it was clear the anion was disordered over two independent positions in a 4:1 ratio and a total occupancy of 0.5. The major position of the anion was refined with approximate octahedral symmetry imposed by SADI instructions; the minor position was refined as a rigid fragment. The other 50% of the site occupancy is presumably disordered solvent which failed to appear in difference maps when the PF_6^- anions had been located.

Finally, a toluene molecule was located on a general position and refined as a rigid fragment. The data set was truncated at 1.4 Å resolution for the final refinement. Co, Se, and P atoms were refined anisotropically with no restraints. Other non-H atoms were refined isotropically. The isotropic ADPs of the diisonitrile ligand, the PF_6^- fluorine atoms, and the toluene molecule were stabilized with SIMU. Hydrogen atoms were refined with riding isotropic ADPs and coordinates.

$Co_6Se_8(CO)_5(PPh_3)$. X-ray quality crystals of $Co_6Se_8(CO)_5(PPh_3)$ were grown from a solution of EtOAc/*n*-hexane. The structure crystallized with no solvent, and there were no disorders.

***cis*-$Co_6Se_8(CO)_4(PPh_3)_2$.** X-ray quality crystals of cis-$Co_6Se_8(CO)_4(PPh_3)_2$ were grown by vapor diffusion from a saturated solution of toluene/*n*-hexane at room temperature. The structure crystallized with one disordered molecule of hexane, which was modeled over two positions.

***trans*-$Co_6Se_8(CO)_4(PPh_3)_2$.** X-ray quality crystals of trans-$Co_6Se_8(CO)_4(PPh_3)_2$were grown from a solution of toluene/*n*-hexane. The structure crystallized with one disordered molecule of

toluene, which was modeled over two positions.

***fac*-$Co_6Se_8(CO)_3(PPh_3)_3$.** X-ray quality crystals of fac-$Co_6Se_8(CO)_3(PPh_3)_3$ were grown from a solution of EtOAc/*n*-hexane. The structure crystallized with no solvent, and there were no disorders.

***trans*-$Co_6Te_8(CO)_2(PEt_3)_4$.** The refinement was routine except for an unusual Fourier difference feature near Co1, the atom bonded to the carbonyl ligand. The atom was surrounded by an hourglass-shaped region of negative density, and there was a significant difference peak (2.81 e^- $Å^{-3}$) at a distance of 1 Å toward the inside of the cluster. Several possible corrections for systematic error were tested, including extinction correction, different absorption routines, modified scattering factors, and f' and f'' refinement, but these did not improve the Fourier map. The crystal may be a solid solution with an unknown decomposition product; the occupancy of Co1 is 0.95 when freely refined. However, no satisfactory disordered model could be identified. In view of the model's excellent R-factor, reasonable ADPs, and unremarkable molecular geometry, the molecular connectivity and stereochemistry are established conclusively.

***cis*-$Co_6Te_8(CO)_2(PEt_3)_4$.** Complete data were collected to 0.815 Å using Cu Kα radiation, but the data were ultimately truncated to 1 Å, outside of which I/σ was less than 1 and R(int) was greater than 0.5. The crystal was slightly cracked and was treated as a non-merohedral twin with a small rotation between the domains as described above for **AC-1-189**. The isolated reflections of the weaker second domain were excluded from the data set. An HKLF 5 file was generated from 27028 reflections within the resolution limit (7794 unique, 2949 observed) with R(int)

14.7% and R(sigma) 16.1% after analytical absorption correction. The data were extremely weak but still solved readily using the isolated reflections of a single twin component. The weak data required the use of extensive restraints to stabilize the refinement. All four independent PEt_3 ligands and the two independent Co-C-O moieties were each made equivalent using SAME instructions. The ADPs of all C and O atoms were restrained using SIMU and RIGU. Finally, a molecule of hexane was located on an inversion center and refined with isotropic ADPs and atomic positions stabilized by absolute (DFIX) restraints on 1,2 and 1,3 distances.

Figure 2.35. Molecular structure of **1.**

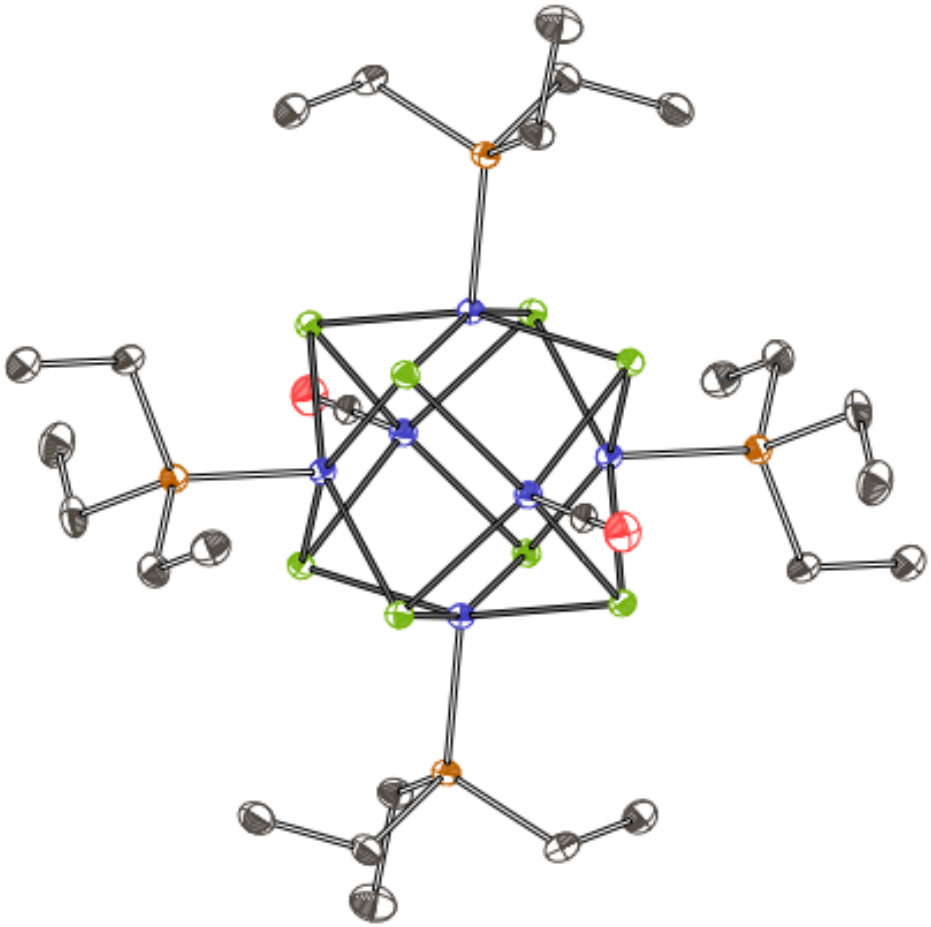

Figure 2.36. Molecular structure of **2.**

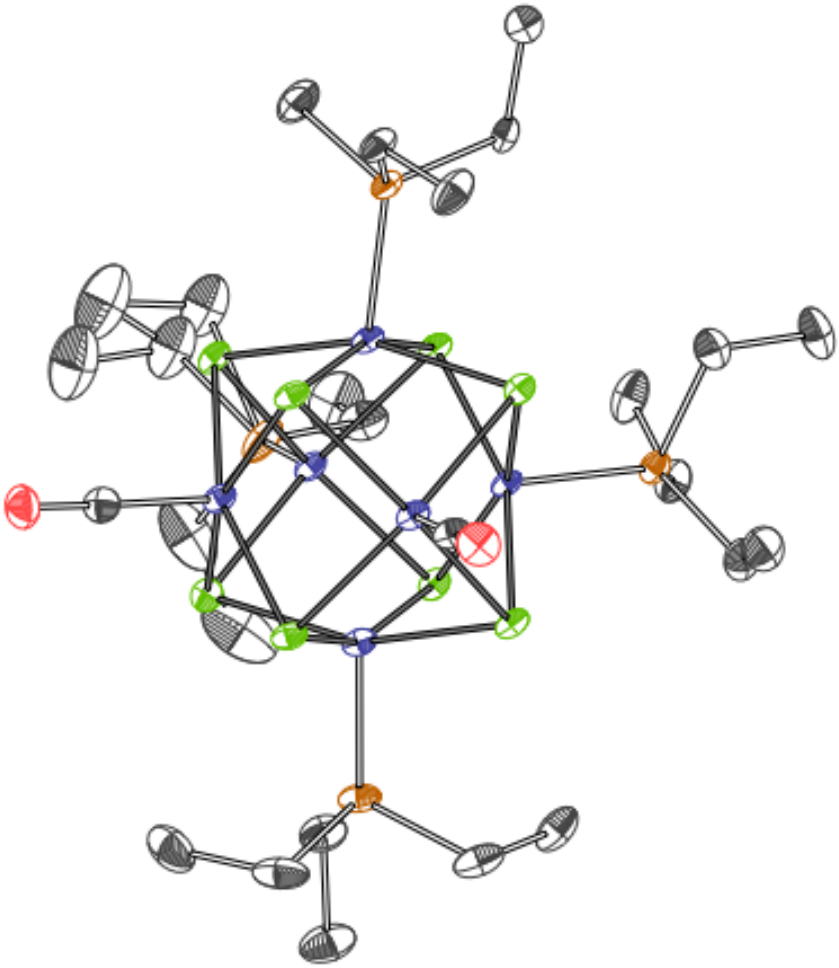

Figure 2.37. Molecular structure of **3.**

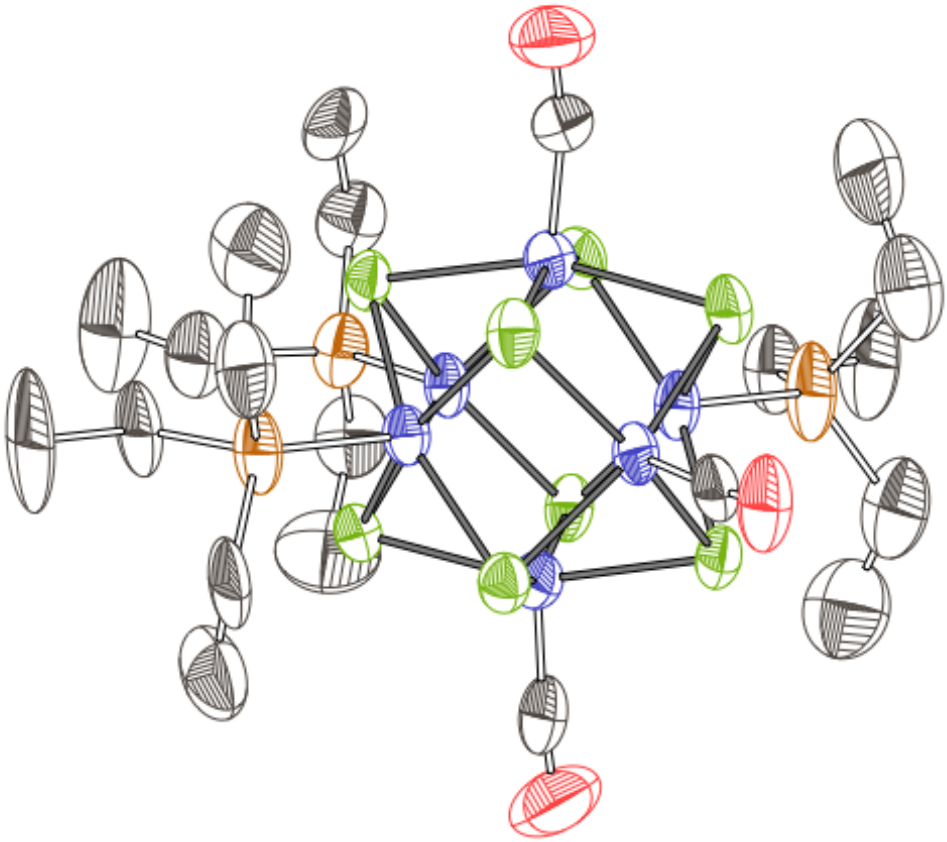

Figure 2.38. Molecular structure of **5** with two molecules in the asymmetric unit.

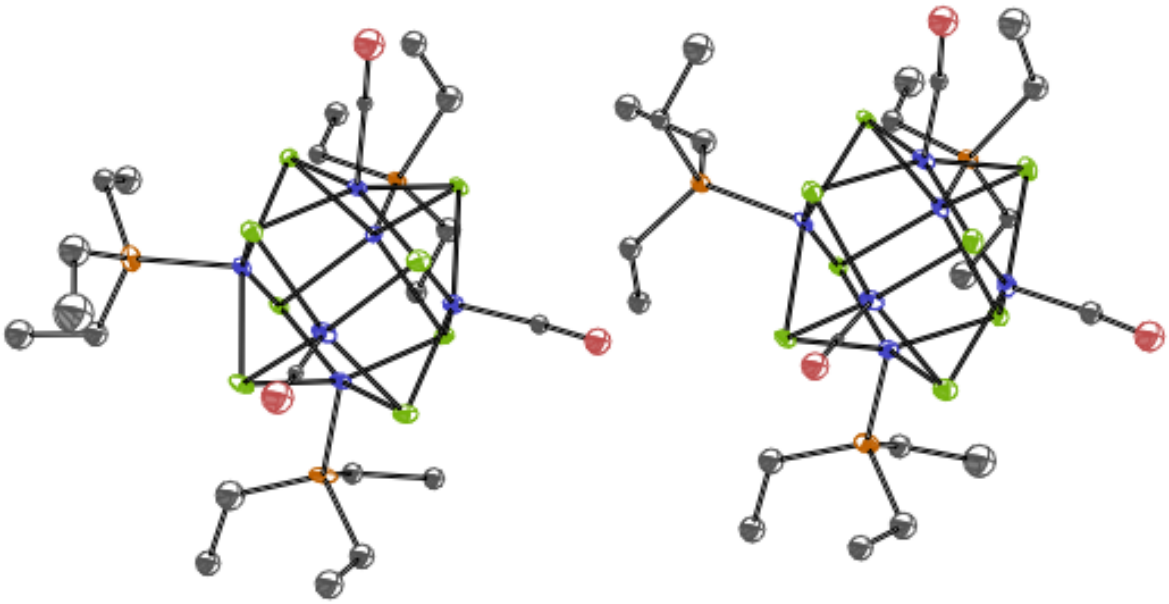

Figure 2.39. Molecular structure of **6.**

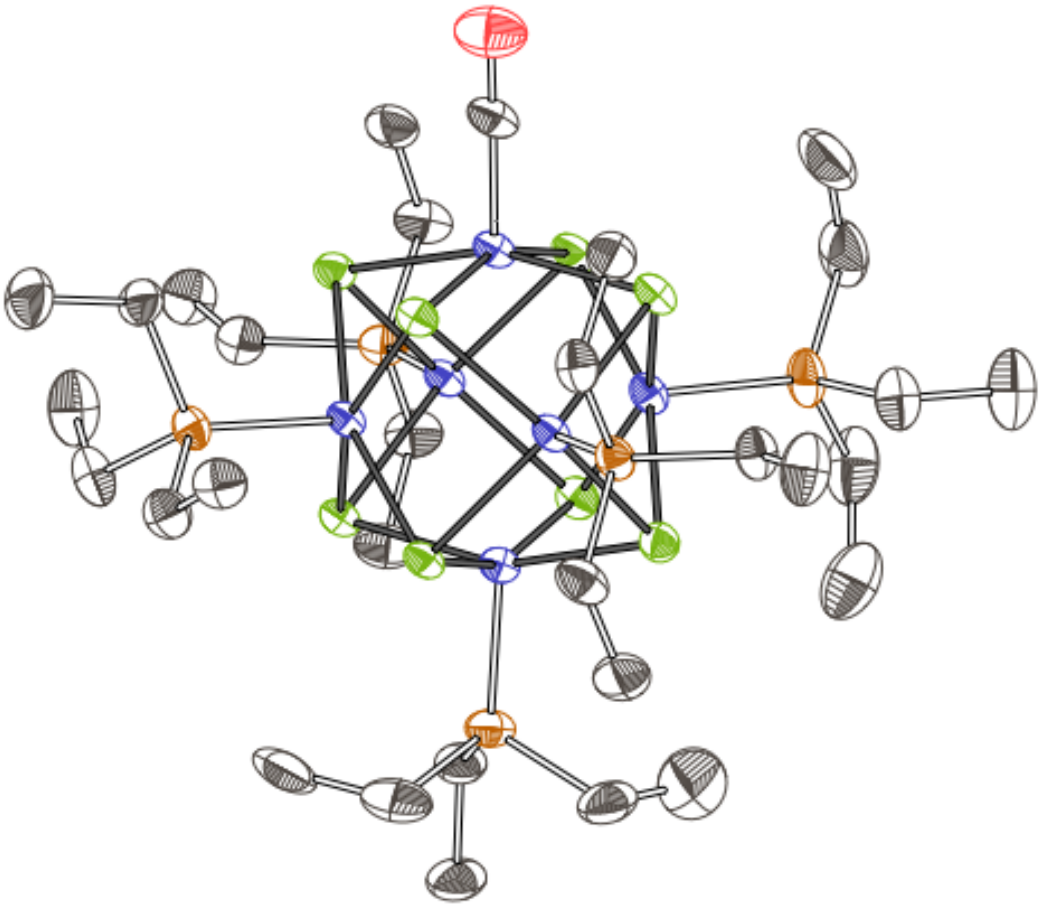

Figure 2.40. Molecular structure of **7**.

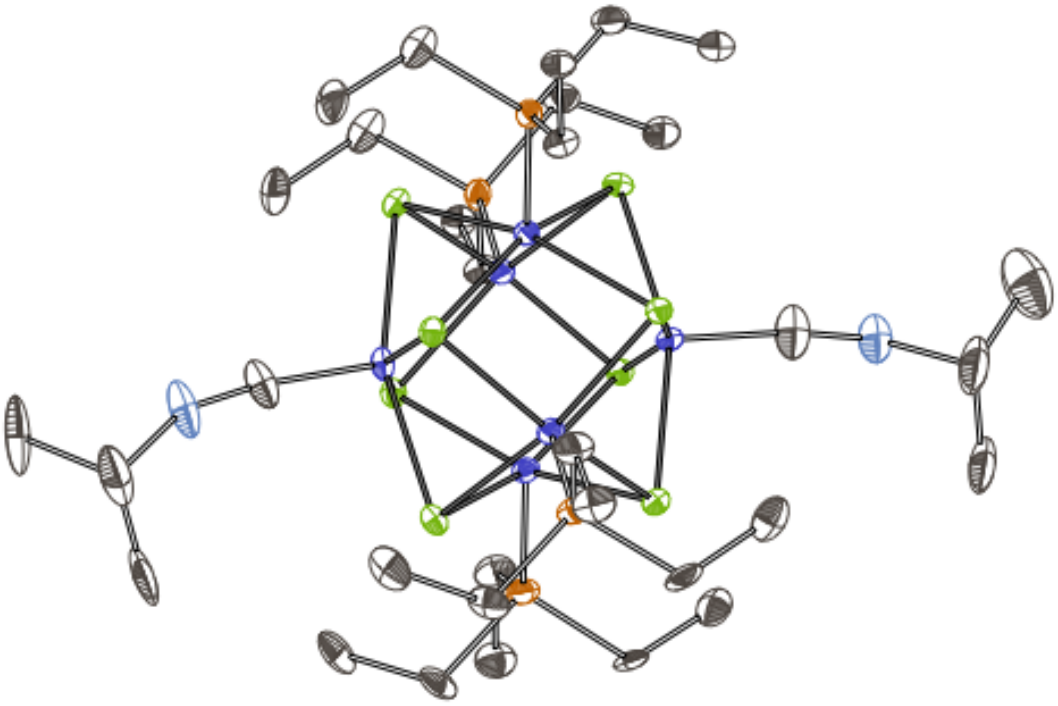

Figure 2.41. Molecular structure of **8**.

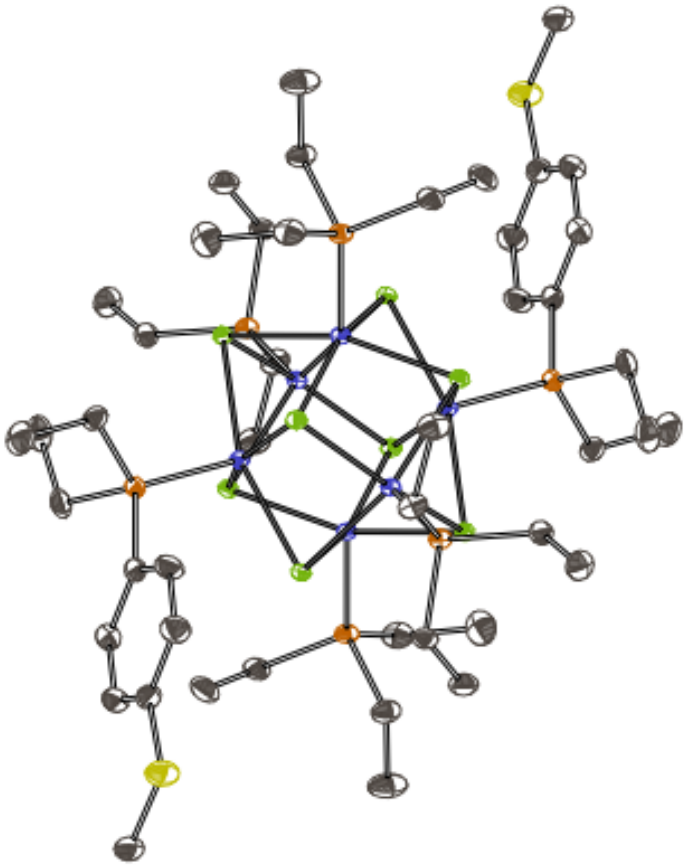

Figure 2.42. Molecular structure of **9.**

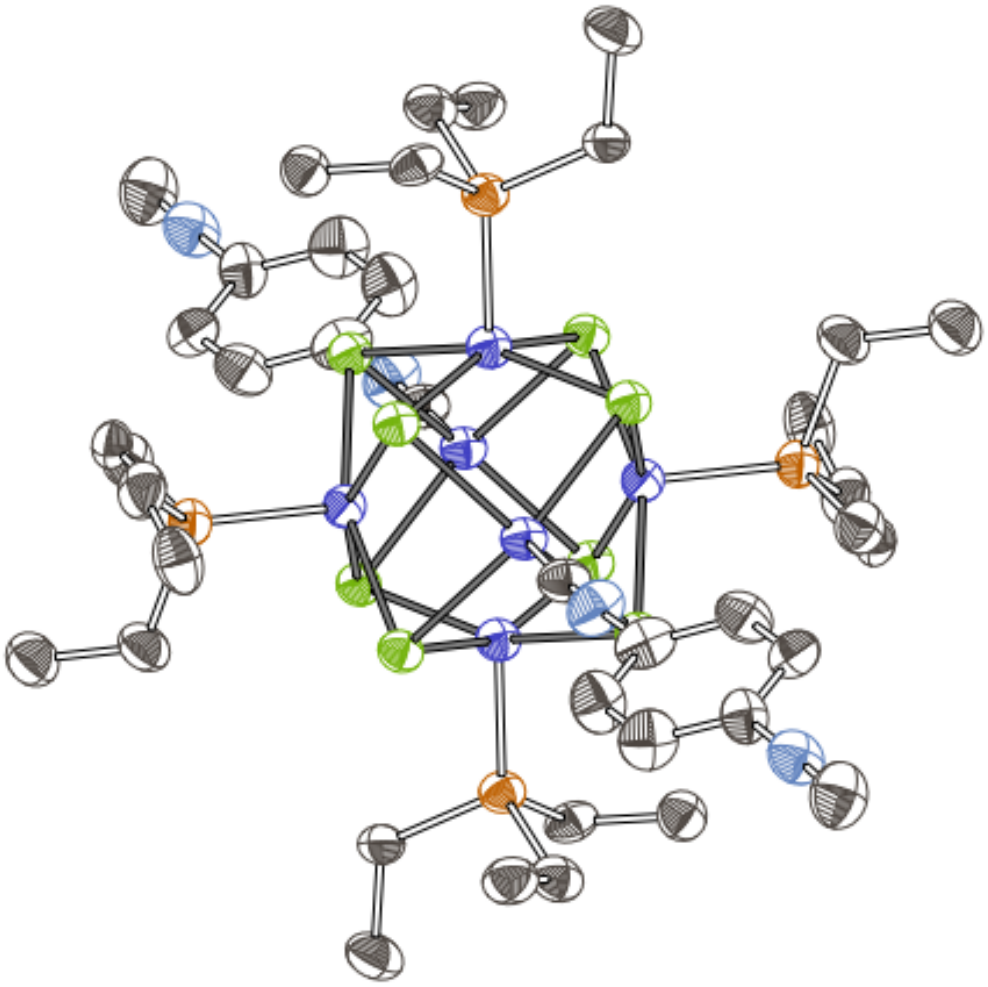

Figure 2.43. Molecular structure of **10**.

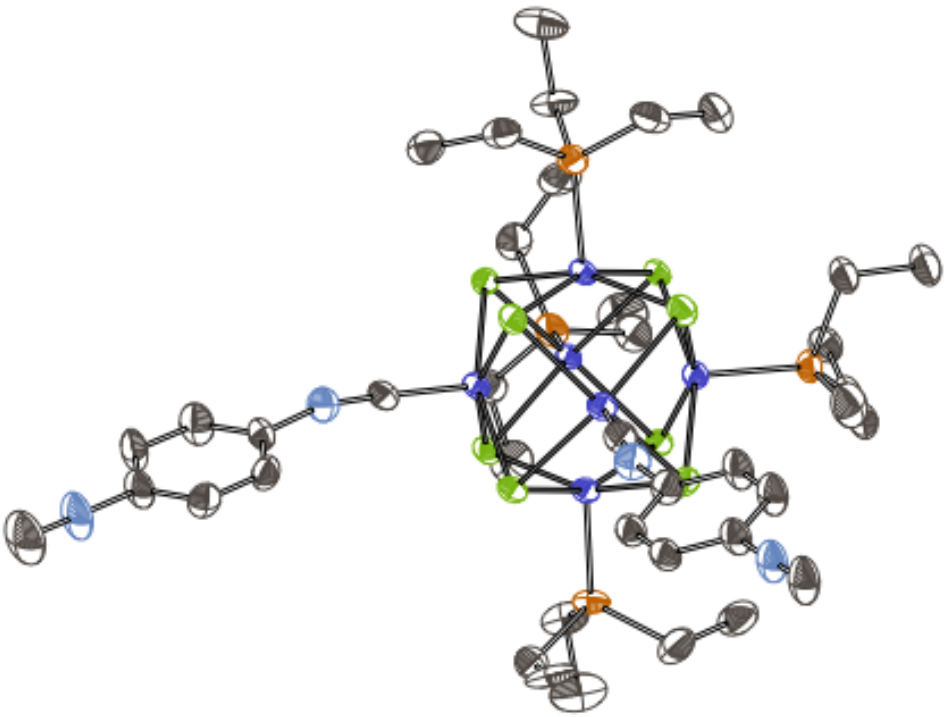

Figure 2.44. Molecular structure of **12**. The minor positions of disordered atoms are omitted for clarity.

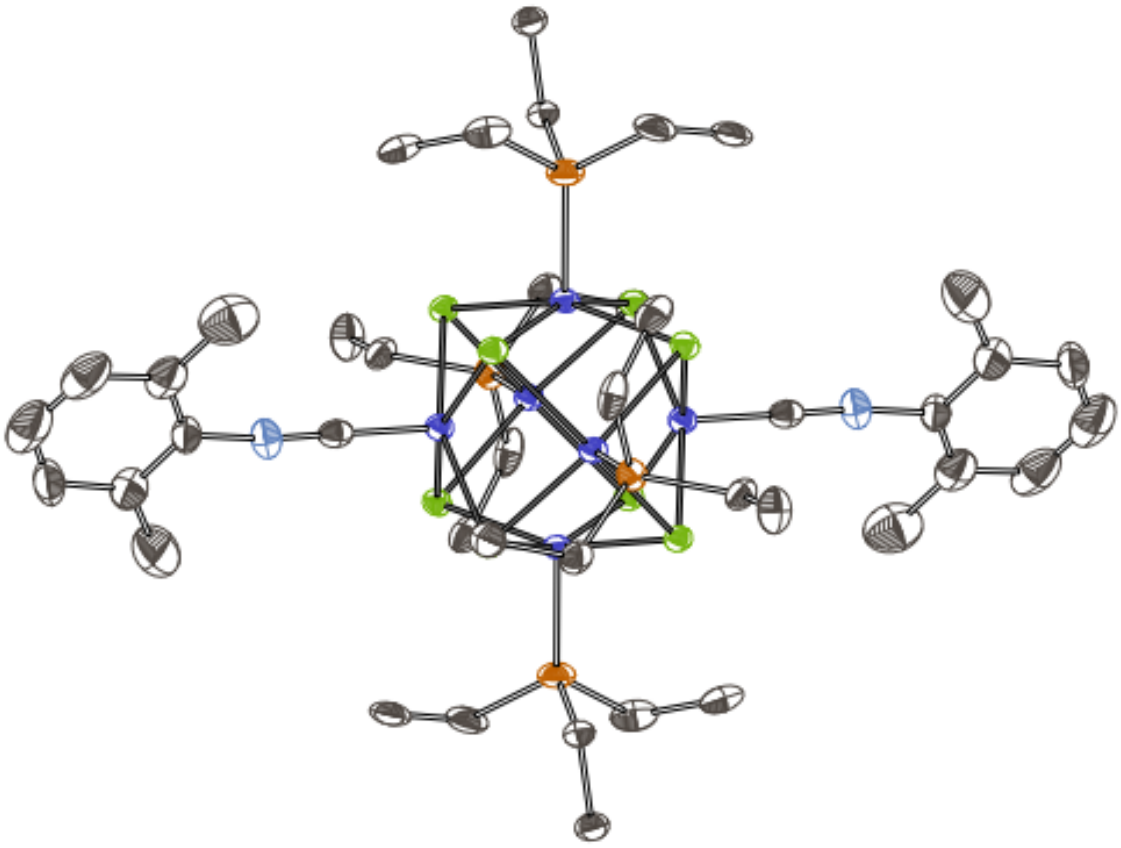

Figure 2.45. Molecular structure of **14** with both independent PF_6^- anions. The minor position of the disordered PF_6^- are omitted for clarity. Co, Se, and P atoms are rendered as thermal ellipsoids at the 25% level. C, N, and F are rendered as spheres.

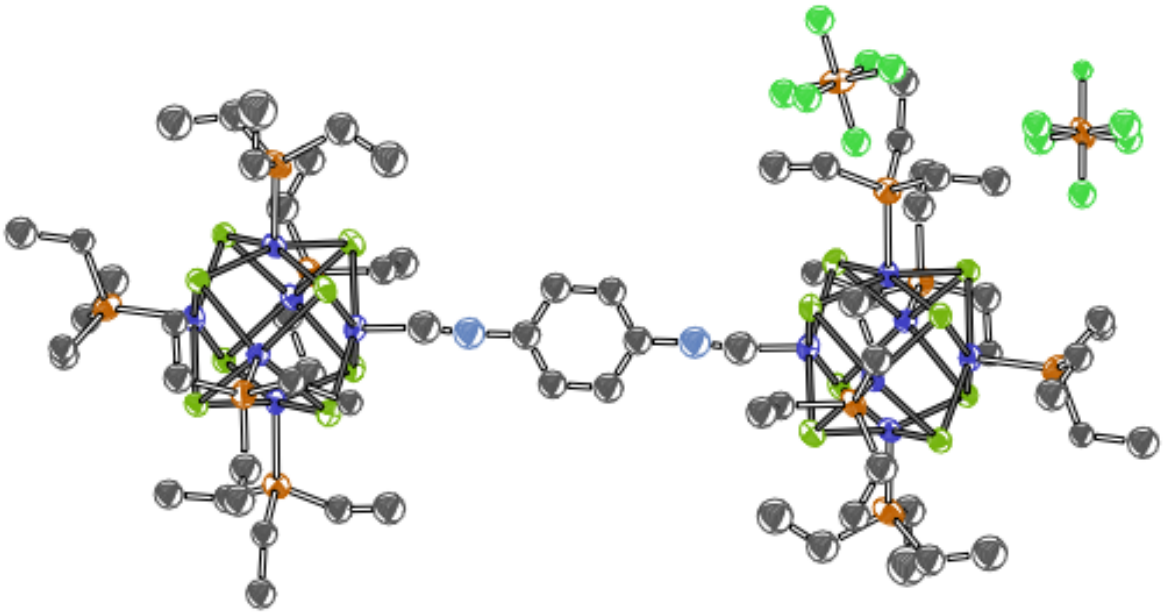

Figure 2.46. Molecular structure of $\mathbf{Co_6Se_8(CO)_5(PPh_3)}$.

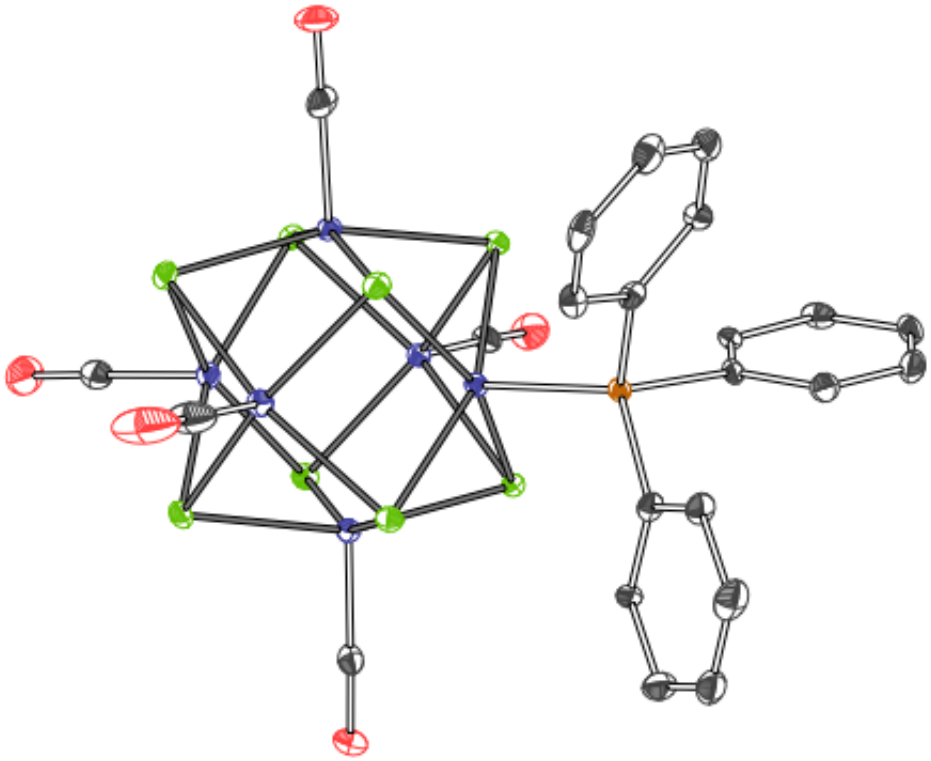

Figure 2.47. Molecular structure of ***cis*-$Co_6Se_8(CO)_4(PPh_3)_2$**

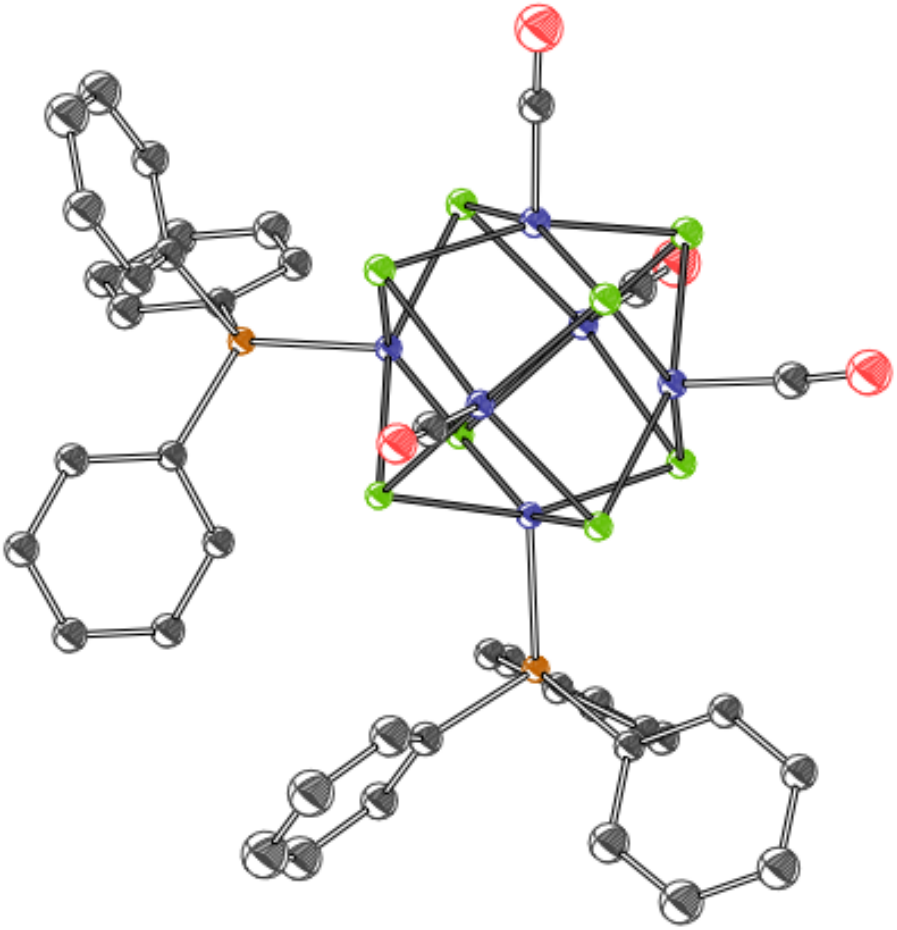

Figure 2.48. Molecular structure of ***trans*-$Co_6Se_8(CO)_4(PPh_3)_2$.**

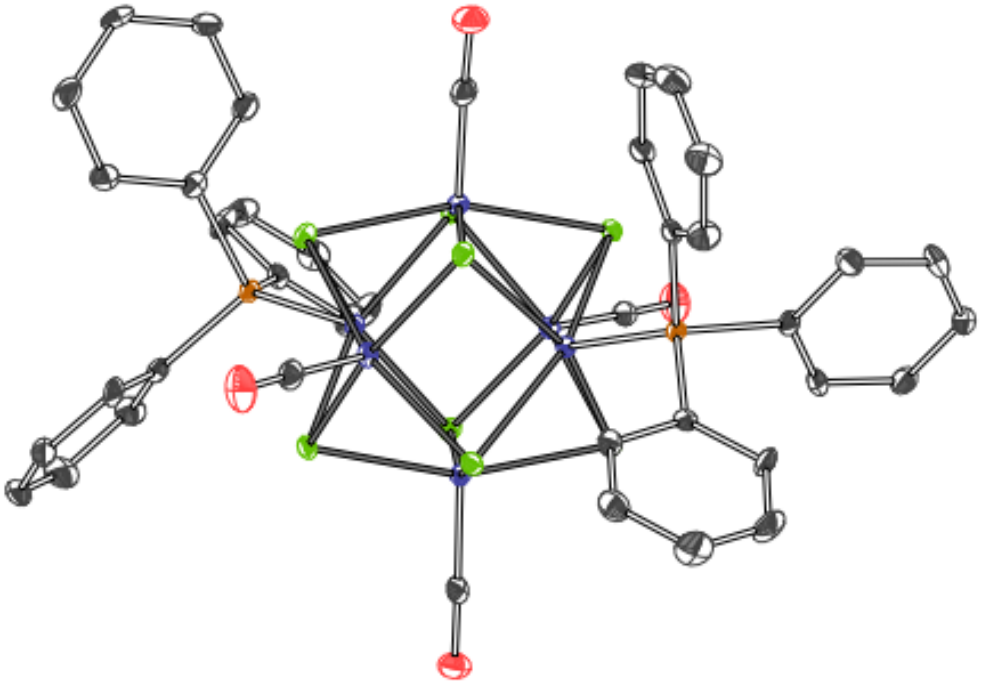

Figure 2.49. Molecular structure of ***fac*-$Co_6Se_8(CO)_3(PPh_3)_3$.**

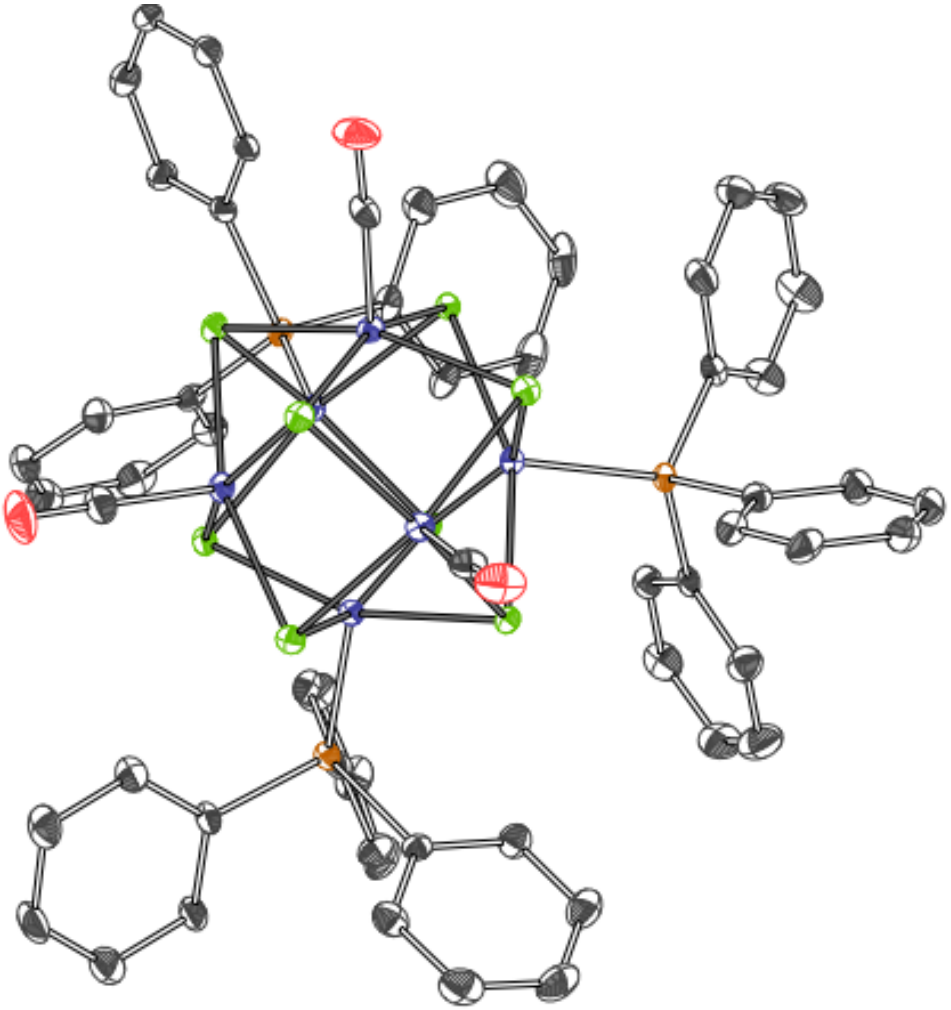

Figure 2.50. Molecular structure of *trans*-$Co_6Te_8(CO)_2(PEt_3)_4$.

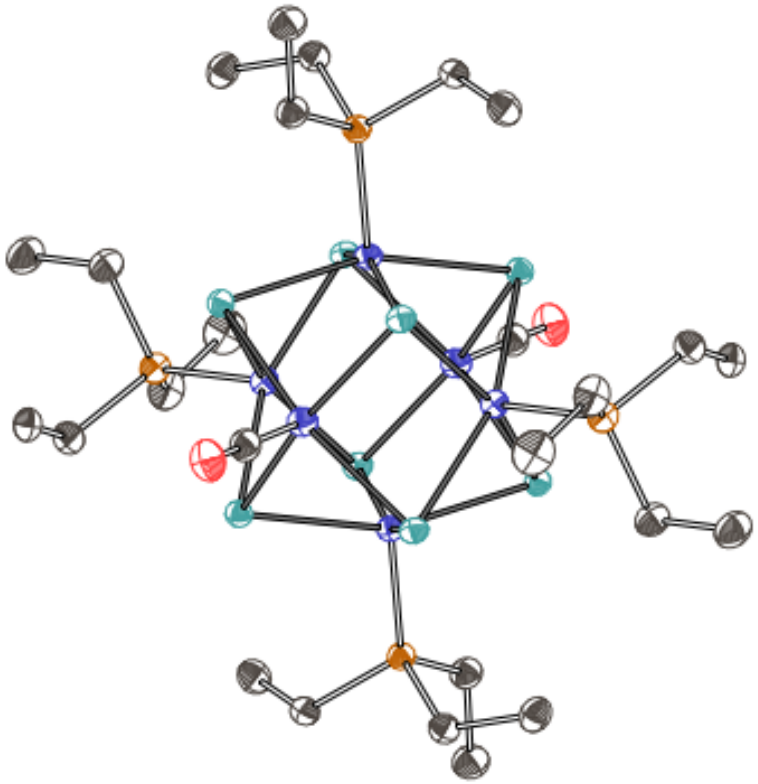

Figure 2.51. Molecular structure of *cis*-$Co_6Te_8(CO)_2(PEt_3)_4$. Thermal ellipsoids are rendered at the 25% level.

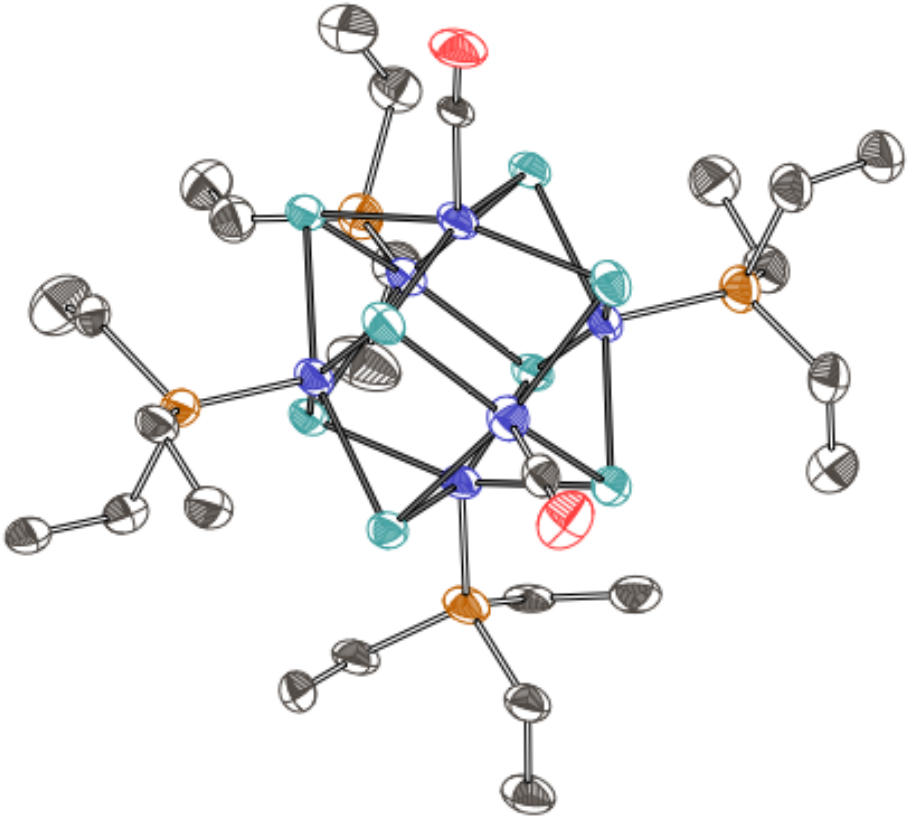

Table 2.3. Selected crystallographic data.

Compound	**1**	**2**	**3**
Formula	$C_{32}H_{74}O_2P_4Co_6Se_8$	$C_{26}H_{60}Co_6O_2P_4Se_8$	$C_{21}H_{45}O_3P_3Co_6Se_8$
MW	1600.05	1513.88	1423.74
Space group	$P2_1/c$	I2/a	$P2_1/n$
***a* (Å)**	13.3752(2)	22.0520(3)	11.4207(5)
***b* (Å)**	14.95799(19)	19.1535(3)	17.7298(5)
***c* (Å)**	13.2922(2)	22.7013(4)	21.5253(12)
***α* (°)**	90	90	90
***β* (°)**	109.3482(19)	109.3914(17)	98.657(4)
***γ* (°)**	90	90	90
V (Å^3)	2509.12(7)	9044.5(2)	4308.9(3)
Z	2	8	4
ϱ_{calc} (g cm^{-3})	2.118	2.224	2.195
T (K)	100	293	100
λ (Å)	1.54184	1.54184	1.54184
$2\theta_{min}$, $2\theta_{max}$	9.2, 143	9.182, 143.188	9.3, 143
Nref	13656	26859	148364
R(int), R(σ)	.032, .035	0.0400, 0.0415	.220, .096
μ(mm^{-1})	23.231	25.731	26.630
Size (mm)	.08 x .05 x .02	0.1 × 0.1 × 0.05	.10 x .05 x .03
T_{max}, T_{min}	.690, .379	1.00, 382	.489, .177

Data	4769	8622	13261
Restraints	0	837	315
Parameters	242	441	371
R_1(obs)	0.0252	0.0313	0.1195
wR_2(all)	0.0608	0.0711	0.3865
S	1.057	1.009	0.994
Peak, hole (e^- Å^{-3})	0.60, -0.59	1.05/-0.49	2.10, -1.17
Flack			

Compound	**5**	**6**	**7**
Formula	$C_{21}H_{45}Co_6O_3P_3Se_8$	$C_{31}H_{75}P_5Co_6Se_8O$	$C_{32}H_{74}N_2P_4Co_6Se_8$
MW	1423.74	1604.02	1596.07
Space group	P-1	$P2_1/n$	Cm
***a* (Å)**	9.1823(7)	14.1096(2)	12.6479(3)
***b* (Å)**	19.193(2)	18.8504(3)	19.4425(4)
***c* (Å)**	21.587(2)	19.3083(3)	11.7698(3)
***α* (°)**	87.269(9)	90	90
***β* (°)**	88.529(7)	96.4299(15)	115.481(3)
***γ* (°)**	83.427(8)	90	90
V (Å^3)	3774.4(7)	5103.15(14)	2612.74(12)
Z	4	4	2
ϱ_{calc} (g cm^{-3})	2.505	2.088	2.029

T (K)	100	100	100
λ (Å)	1.54184	1.54184	1.54184
$2\theta_{min}$, $2\theta_{max}$	10.0, 143	9.2, 143	9.7, 143
Nref	21131	98405	17241
R(int), R(σ)	.157, .137	.079, .037	.038, .037
μ(mm^{-1})	30.401	23.118	22.290
Size (mm)	.06 x .03 x .02	.09 x .04 x .02	.06 x .03 x .02
T_{max}, T_{min}	.659, .366	.671, .323	.755, .449
Data	14523	9920	5070
Restraints	684	126	222
Parameters	500	515	281
R_1(obs)	0.0815	0.0440	0.0251
wR_2(all)	0.2178	0.1225	0.0611
S	0.968	1.019	1.052
Peak, hole (e^- $Å^{-3}$)	2.45, -2.89	1.10, -0.94	0.51, -0.38
Flack			0.497(16)

Compound	**8**	**9**	**10**
Formula	$C_{53}H_{102}Co_6P_6S_2Se_8$	$C_{40}H_{68}N_4P_4Co_6Se_8$	$C_{46}H_{82}N_4P_4Co_6Se_8$
MW	1974.54	1714.12	1800.29
Space group	$P2_1/n$	$P2_1/n$	P-1

***a* (Å)**	15.5071(2)	10.2202(4)	11.6182(3)
***b* (Å)**	15.01109(17)	24.3296(11)	16.8320(6)
***c* (Å)**	15.9180(2)	11.1716(4)	17.2555(4)
***α* (°)**	90	90	79.670(3)
***β* (°)**	108.0086(14)	96.550(3)	88.604(2)
***γ* (°)**	90	90	72.703(3)
V (Å^3)	3523.84(8)	2762.16(19)	3168.12(18)
Z	2	2	2
ϱ_{calc} (g cm^{-3})	1.861	2.061	1.887
T (K)	100	100	100
λ (Å)	.71073	1.54184	1.54184
$2\theta_{min}$, $2\theta_{max}$	7.0, 59.4	9.4, 143	9.4, 143
Nref	95592	27021	61950
R(int), R(σ)	.037, .023	.113, .082	.076, .052
μ(mm^{-1})	5.740	21.161	18.484
Size (mm)	.12 x .09 x .05	.15 x .07 x .02	.13 x .10 x .02
T_{max}, T_{min}	.815, .682	.778, .275	.779, .293
Data	9314	5374	12306
Restraints	87	0	38
Parameters	365	286	620
R_1(obs)	0.0216	0.0741	0.0565
wR_2(all)	0.0436	0.1998	0.1603

S	1.029	1.030	1.030
Peak, hole (e^- Å^{-3})	0.50, -0.52	1.72, -1.26	1.35, -0.99
Flack			

Compound	**12**	**14**	$Co_6Se_8(CO)_5(PPh_3)$
Formula	$C_{42}H_{78}N_2P_4Co_6Se_8$	$C_{82}H_{170}N_2F_{12}P_{12}Co_{12}Se_{16}$	$C_{23}H_{15}Co_6O_5PSe_8$
MW	1720.20	3754.35	1387.58
Space group	$P2_1/c$	$P2_1/n$	$P2_1/c$
***a* (Å)**	11.3964(2)	13.480(2)	9.25595(11)
***b* (Å)**	19.0296(3)	21.743(3)	19.9372(3)
***c* (Å)**	13.9524(3)	22.651(5)	18.0683(3)
***α* (°)**	90	90	90
***β* (°)**	107.494(2)	105.73(2)	102.1241(15)
***γ* (°)**	90	90	90
V (Å^3)	2885.89(11)	6390(2)	3259.91(8)
Z	2	2	4
ϱ_{calc} (g cm^{-3})	1.980	1.951	2.827
T (K)	100	100	293
λ (Å)	1.54184	1.54184	1.54184
$2\theta_{min}$, $2\theta_{max}$	9.3, 143	9.1, 66.8	8.9, 143
Nref	33481	13741	11554

R(int), R(σ)	.057, .0703	.148, .174	.0241, .0319
μ(mm^{-1})	20.243	18.941	34.342
Size (mm)	.03 x .03 x .01	.03 x .02 x .02	0.1 × 0.1 × 0.05
T_{max}, T_{min}	.860, .660	.802, .689	1.000, 0.357
Data	7866	2442	5375
Restraints	254	456	0
Parameters	357	396	388
R_1(obs)	0.0293	0.0525	0.0335
wR_2(all)	0.0375	0.1441	0.0845
S	0.991	0.851	1.056
Peak, hole (e^- Å^{-3})	0.55, -0.52	.40, -.35	1.03, -0.86
Flack			

Compound	*trans*-$Co_6Se_8(CO)_4(PPh_3)_2$	*cis*-$Co_6Se_8(CO)_4(PPh_3)_2$	*fac*-$Co_6Se_8(CO)_3(PPh_3)_3$
Formula	$C_{47}H_{38}Co_6O_4P_2Se_8$	$C_{43}H_{37}Co_6O_4P_2Se_8$	$C_{57}H_{45}Co_6O_3P_3Se_8$
MW	1713.97	1664.92	1856.1
Space group	P-1	C2/c	$P2_1/c$
***a* (Å)**	13.4288(3)	27.8318(3)	21.11266(13)
***b* (Å)**	13.6490(4)	10.33627(8)	11.33907(8)
***c* (Å)**	14.4787(4)	35.4535(3)	24.67553(16)

α (°)	108.491(2)	90	90
β (°)	95.463(2)	109.5328(10)	94.3661(6)
γ (°)	92.156(2)	90	90
V (Å^3)	2498.89(11)	9612.19(16)	5890.13(7)
Z	2	8	4
ϱ_{calc} (g cm^{-3})	2.278	2.301	2.093
T (K)	293	293	293
λ (Å)	0.71073	1.54184	1.54184
$2\theta_{min}$, $2\theta_{max}$	6.674, 59.156	9.196, 142.988	8.586, 143.07
Nref	66160	97797	94599
R(int), R(σ)	.0555, .0521	.0686, .0319	.0532, .0263
μ(mm^{-1})	7.88	23.742	19.701
Size (mm)	0.1 × 0.1 × 0.05	0.2 × 0.1 × 0.1	0.1 × 0.1 × 0.05
T_{max}, T_{min}	1, 0.76698	1, 0.49567	1, 0.345
Data	12648	9362	11451
Restraints	1371	1276	0
Parameters	670	654	694
R_1(obs)	0.0380	0.0329	0.0275
wR_2(all)	0.058	0.07	0.0658
S	1.032	1.082	1.035
Peak, hole (e$^-$ Å^{-3})	0.63, -0.58	0.85, -0.50	0.84, -0.62
Flack			

Compound	*trans*-$Co_6Te_8(CO)_2(PEt_3)_4$	*cis*-$Co_6Te_8(CO)_2(PEt_3)_4$
Formula	$C_{32}H_{74}O_2P_4Te_8Co_6$	$C_{29}H_{67}Co_6O_2P_4Te_8$
MW	1989.17	1946.08
Space group	$P2_1/c$	P-1
***a* (Å)**	13.4771(3)	12.7011(16)
***b* (Å)**	15.4641(3)	12.8199(12)
***c* (Å)**	13.5727(3)	15.9382(12)
***α* (°)**	90	80.252(7)
***β* (°)**	108.615(2)	89.797(8)
***γ* (°)**	90	87.786(9)
V (Å^3)	2680.70	2555.8(4)
Z	2	2
ϱ_{calc} (g cm^{-3})	2.464	2.529
T (K)	100	100
λ (Å)	1.54184	1.54184
$2\theta_{min}$, $2\theta_{max}$	8.9, 143	9.0, 101
Nref	42897	27028
R(int), R(σ)	.066, .032	.147, .161
μ(mm^{-1})	49.200	51.583
Size (mm)	.05 x .03 x .02	.06 x .05 x .03
T_{max}, T_{min}	.443, .187	.429, .233

Data	5223	7794
Restraints	0	410
Parameters	242	428
R_1(obs)	0.0264	0.1207
wR_2(all)	0.0648	0.3407
S	1.023	1.034
Peak, hole (e^- Å^{-3})	2.81, -1.03	2.72, -2.56
Flack		

2.11. References

1. (a) Khanna, S. N.; Jena, P. *Phys. Rev. B.* **1995**, *51*, 13705. (b) Claridge, S. A.; Castleman, A. W.; Khanna, S. N.; Murray, C. B.; Sen, A.; Weiss, P. S. *ACS Nano* **2009**, *3*, 244. (c) Qian, M. C.; Reber, A. C.; Ugrinov, A.; Chaki, N. K.; Mandal, S.; Saavedra, H. M.; Khanna, S. N.; Sen, A.; Weiss, P. S. *ACS Nano* **2010**, *4*, 235. (d) Luo, Z. X.; Castleman, A. W. *Acc. Chem. Res.* **2014**, *47*, 2931.

2. (a) Alivisatos, A. P.; Johnsson, K. P.; Peng, X. G.; Wilson, T. E.; Loweth, C. J.; Bruchez, M. P.; Schultz, P. G. *Nature* **1996**, *382*, 609. (b) Mirkin, C. A.; Letsinger, R. L.; Mucic, R. C.; Storhoff, J. J. *Nature* **1996**, *382*, 607. (c) Li, Y. L.; Liu, Z. Y.; Yu, G. M.; Jiang, W.; Mao, C. D. *J. Am. Chem. Soc.* **2015**, *137*, 4320.

3. (a) Wang, Y. F.; Wang, Y.; Breed, D. R.; Manoharan, V. N.; Feng, L.; Hollingsworth, A. D.; Weck, M.; Pine, D. J. *Nature* **2012**, *491*, 51. (b) Jones, M. R.; Mirkin, C. A. *Nature* **2012**, *491*, 42. (c) Glotzer, S. C.; Solomon, M. J. *Nat. Mater.* **2007**, *6*, 557.

4. Yin, S. N.; Yang, S. Y.; Wang, C. F.; Chen, S. *J. Am. Chem. Soc.* **2016**, *138*, 566.

5. (a) Roy, X.; Lee, C. H.; Crowther, A. C.; Schenck, C. L.; Besara, T.; Lalancette, R. A.; Siegrist, T.; Stephens, P. W.; Brus, L. E.; Kim, P.; Steigerwald, M. L.; Nuckolls, C. *Science* **2013**, *341*, 157. (b) Lee, C. H.; Liu, L.; Bejger, C.; Turkiewicz, A.; Goko, T.; Arguello, C. J.; Frandsen, B. A.; Cheung, S. C.; Medina, T.; Munsie, T. J. S.; D'Ortenzio, R.; Luke, G. M.; Besara, T.; Lalancette, R. A.; Siegrist, T.; Stephens, P. W.; Crowther, A. C.; Brus, L. E.; Matsuo, Y.; Nakamura, E.; Uemura, Y. J.; Kim, P.; Nuckolls, C.; Steigerwald, M. L.; Roy, X. *J. Am.*

Chem. Soc. **2014**, *136*, 16926. (c) Turkiewicz, A.; Paley, D. W.; Besara, T.; Elbaz, G.; Pinkard, A.; Siegrist, T.; Roy, X. *J. Am. Chem. Soc.* **2014**, *136*, 15873.

6. Choi, B.; Yu, J.; Paley, D. W.; Trinh, M. T.; Paley, M. V.; Karch, J. M.; Crowther, A. C.; Lee, C. H.; Lalancette, R. A.; Zhu, X. Y.; Kim, P.; Steigerwald, M. L.; Nuckolls, C.; Roy, X. *Nano Lett.* **2016**, *16*, 1445.

7. (a) Fenske, D.; Ohmer, J.; Hachgenei, J. *Angew. Chem. Int. Ed.* **1985**, *24*, 993. (b) Saito, T.; Yamamoto, N.; Yamagata, T.; Imoto, H. *J. Am. Chem. Soc.* **1988**, *110*, 1646. (c) Steigerwald, M. L.; Siegrist, T.; Stuczynski, S. M. *Inorg. Chem.* **1991**, *30*, 2256. (d) Hessen, B.; Siegrist, T.; Palstra, T.; Tanzler, S. M.; Steigerwald, M. L. *Inorg. Chem.* **1993**, *32*, 5165. (e) Thiele, G.; You, Z. L.; Dehnen, S. *Inorg. Chem.* **2015**, *54*, 2491.

8. (a) Stuczynski, S. M.; Kwon, Y. U.; Steigerwald, M. L. *J. Organomet. Chem.* **1993**, *449*, 167. (b) Kamiguchi, S.; Imoto, H.; Saito, T. *Chem. Lett.* **1996**, 555.

9. (a) Zheng, Z. P.; Holm, R. H. *Inorg. Chem.* **1997**, *36*, 5173. (b) Zheng, Z. P.; Long, J. R.; Holm, R. H. *J. Am. Chem. Soc.* **1997**, *119*, 2163. (c) Orto, P. J.; Nichol, G. S.; Wang, R. Y.; Zheng, Z. P. *Inorg. Chem.* **2007**, *46*, 8436.

10. Long, J. R.; Williamson, A. S.; Holm, R. H. *Angew. Chem. Int. Ed.* **1995**, *34*, 226.

11. (a) Leduc, L.; Padiou, J.; Perrin, A.; Sergent, M. *J. Less-Common Met.* **1983**, *95*, 73. (b) Leduc, L.; Perrin, A.; Sergent, M. *Acta. Crystallogr. C.* **1983**, *39*, 1503.

12. (a) Steigerwald, M. L.; Siegrist, T.; Stuczynski, S. M. *Inorg. Chem.* **1991**, *30*, 4940. (b) Diana, E.; Gervasio, G.; Rossetti, R.; Valdemarin, F.; Bor, G.; Stanghellini, P. L. *Inorg. Chem.* **1991**, *30*, 294. (c) Gervasio, G.; Kettle, S. F. A.; Musso, F.; Rossetti, R.; Stanghellini, P. L. *Inorg. Chem.* **1995**, *34*, 298.

13. Strohmeier, W. *Angew. Chem. Int. Ed.* **1964**, *3*, 730.

14. We treat the starting material with an excess of the linker (5 equivalents) to prevent undesired oligomerization, and subsequently remove the leftover linker by trituration.

15. Creutz, C. *Prog. Inorg. Chem.* **1983**, *30*, 1.

16. Barriere, F.; Camire, N.; Geiger, W. E.; Mueller-Westerhoff, U. T.; Sanders, R. *J. Am. Chem. Soc.* **2002**, *124*, 7262.

17. Blanc, E.; Schwarzenbach, D.; Flack, H. D. *J. Appl. Cryst.* **24** (1991), 1035-1041.

18. Clark. R. C.; Reid, J. S. *Acta Cryst.* **A51** (1995), 887-897.
19. Version 1.171.37.35 (2014). Oxford Diffraction /Agilent Technologies UK Ltd, Yarnton, England.

20. Sheldrick, G. M. *Acta Cryst*. **A71** (2015), 3-8.

21. Palatinus, L.; Chapuis, G. *J. Appl. Cryst*. **40** (2007), 786-790.

22. Dolomanov, O. V.; Bourhis, L. J.; Gildea, R. J.; Howard, J. A. K.; Puschmann, H. *J. Appl. Cryst*. **42** (2009), 339-341.

23. Spek, A. *Acta Cryst*. **D65** (2009), 148-155.

24. Van der Sluis, P.; Spek, A. L. *Acta Cryst*. **A46** (1990), 194-201.

25. Le Page, Y. *J. Appl. Cryst*. **21** (1988), 983.

26. Guzei, I. A. *J. Appl. Cryst*. **47** (2014), 806-809.

27. CrystalMaker Software Ltd, Oxford, England *(www.crystalmaker.com)*.

Chapter 3. Electrocrystallization of [Co_6Se_8] Superatoms into Woven 2D Material

3.1. Preface

This chapter is based on a published manuscript titled "Weaving Nanoscale Cloth through Electrostatic Templating" by Anouck M. Champsaur, Cécile Mézière, Magali Allain, Daniel W. Paley, Michael L. Steigerwald, Colin Nuckolls, and Patrick Batail (*Journal of the American Chemical Society,* **2017**, *139* , 11718). I synthesized all [Co_6Se_8] molecules and set up electrocrystallization experiments. Cécile Mézière synthesized polyoxometalate clusters ($Mo_6O_{19}^{2-}$ and $W_6Cl_{14}^{2-}$) and also set up electrocrystallization experiments. Magali Allain performed single crystal refinement, with additional help from Daniel Paley.

3.2. Background

Electrocrystallization is a synthetic tool that assembles solid state materials from molecular components in solution. In the experimental setup, a weak current slowly oxidizes (or reduces) an electroactive material in the presence of an electrolyte. Figure 3.1 displays a typical electrocrystallization cell. Over time, crystalline materials composed of the ionic components from the solution are assembled at the electrode. This technique thus assembles molecular ions from solution into crystalline solids of high purity; we wished to extend this technique to *superatomic* ions.

Beyond creating co-crystals of superatomic components, we wished to access materials of unprecedented complexity. Could we use electrocrystallization to create *covalently linked* superatomic assemblies?

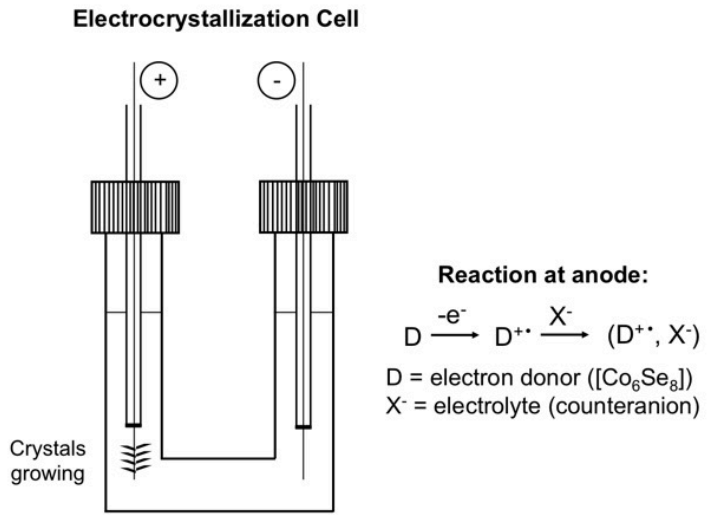

Figure 3.1. Cartoon of an electrocrystallization cell.

To answer this question, we needed appropriate superatomic building blocks that would satisfy the important condition of being reactive upon oxidation. Specifically, we required superatoms with labile ligands. We tackled this challenge using the carbonylated $[Co_6Se_8]$ superatoms I introduced in Chapter 2. I was given the opportunity to travel to France and learn electrocrystallization firsthand in Professor Batail's laboratory at Université d'Angers from Cécile Mézière.

Once the appropriate electroactive building block is identified, a variety of parameters can be tuned in the experimental setup: solvent, current magnitude, temperature, and electrolyte. For electrolytes, we started with the tetrabutylammonium (TBA) salts of well-known polyoxometalate ions like $Mo_6O_{19}^{2-}$ and $W_6Cl_{14}^{2-}$ because they are size complementary to $[Co_6Se_8]$ and readily crystallize.

The CO-isomers of $[Co_6Se_8]$ superatoms were ultimately not ideal candidates for electrocrystallization themselves due to the sturdiness of the CO ligand upon oxidation of the superatom to 1+ and even 2+ states. To illustrate this, I combined $Co_6Se_8(PEt_3)_5(CO)$ in an electrocrystallization cell with $(TBA)_2(Mo_6O_{19})$, with tetrahydrofuran as the solvent and an

applied current of 0.5 μA. Figure 3.2 displays the crystal structure of $[Co_6Se_8(PEt_3)_5(CO)][Mo_6O_{19}^{2-}]$, the ionic solid obtained on the anodic electrode after two days. $Co_6Se_8(PEt_3)_5(CO)$ is present in the crystal as a 2+ ion.

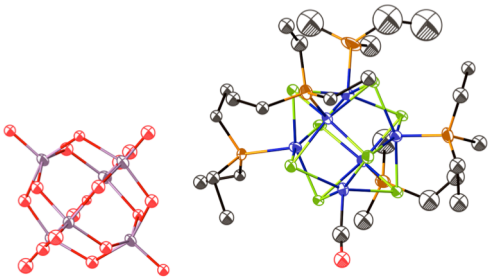

Figure 3.2. Molecular structure of $[Co_6Se_8(PEt_3)_5(CO)][Mo_6O_{19}^{2-}]$, obtained from the electrocrystallization of the *mono*-CO $[Co_6Se_8]$ superatom.

Fortunately, CO-isomers provide a means to access $[Co_6Se_8]$ clusters with labile ligands. I discovered that the bis-isonitrile superatom introduced in Chapter 2, *trans*-$Co_6Se_8(CNC_6H_4NC)_2(PEt_3)_4$, was unstable electrochemically and had labile isonitriles ligands in oxidized states. The remainder of this chapter outlines these findings.

3.3. Introduction

In this study we describe a method to weave a two-dimensional cloth from polymeric strands of electroactive superatoms. Weaving nanoscale building blocks promises to endow a nanomaterial with the strength and toughness typically associated with everyday textiles but also to incorporate the emergent and tunable properties of the nanoscale subunits. It is easy to imagine that two-dimensional nanoscale cloth would provide a new generation of smart, multifunctional materials, coatings, and surfaces[1,2]; yet despite this promising vision, while a variety of interwoven coordination polymers exist, [3-11] there are only limited and highly specific methods available to covalently form two-dimensional, woven nanomaterials.[12] Here we disclose a simple route to nanoscopic 2D woven structures reminiscent of the weaving that produces macroscopic textiles in that an electrostatic template directs the directionality of the weaving.

The simplest weave is a box weave, in which the strands outline a square (Figure 3.3a). This square acts as a template that directs the strands to create four points where the strands cross over and under each other. We show here that the same principle can be applied on the nanoscale to create two-dimensional molecular cloth with polymeric strands (molecular thread).

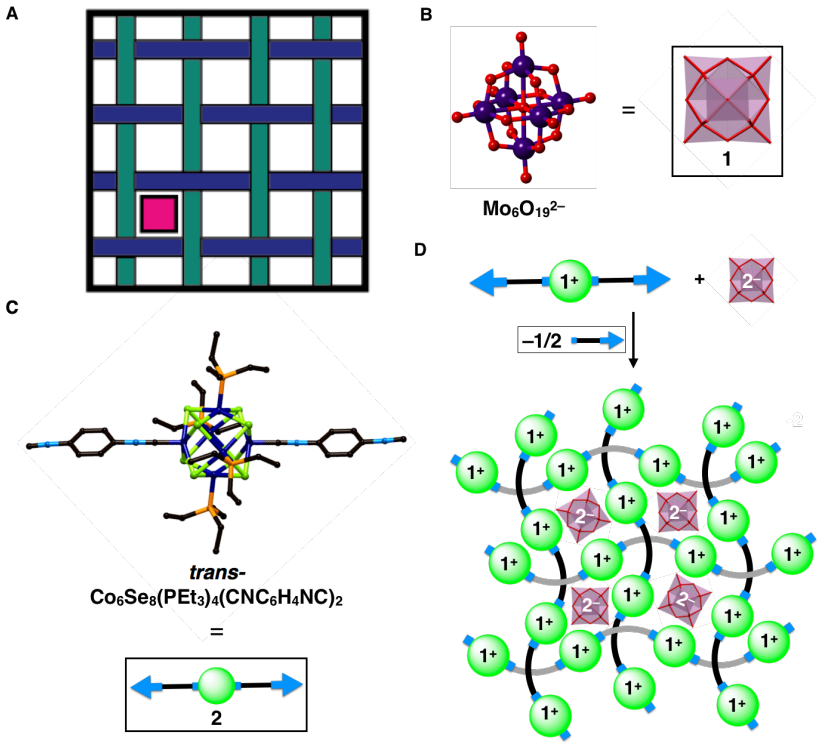

Figure 3.3. (a) A two-dimensional box weave. The magenta square represents a template for the box weave. (b) Lindqvist dianion $Mo_6O_{19}^{2-}$ **1** and its polyhedral representation. (c) *Trans*-$Co_6Se_8(PEt_3)_4(CNC_6H_4NC)_2$ (**2**) and cartoon. (d) Two-step assembly between $Mo_6O_{19}^{2-}$ template and $[Co_6Se_8(PEt_3)_4(CNC_6H_4NC)_2]^{1+}$ to form a box weave.

For the nanoscale weaving we utilize an anionic template to direct and organize the position and concurrent polymerization of a superatom monomer. The counterion plays an important role in tuning and stabilizing the assembly and properties of certain cluster-based materials.[13,14] Here, the anionic template and the growing strands are attracted to each other through ionic charge complementarity, and the directionality of the weave is determined by the symmetry of the template. For our initial target of the box weave, we used the Lindqvist dianion $Mo_6O_{19}^{2-}$ (**1**, Figure 3.3b) because of its tetragonal symmetry.[15-19] Furthermore, the shared oxygen

atoms on the surface of **1** are the most basic and are known to act as hydrogen bond acceptors.[15] The nanoscale threads within the weave are formed from the linking of synthetically programmed, trans-substituted $Co_6Se_8(PEt_3)_4(CNC_6H_4NC)_2$ clusters (**2**), which we call superatoms,[20-23] into one dimensional polymers through isonitrile-cobalt bonds (Figure 3.3c).[24] In general, the superatoms are electroactive, and each can give up to three electrons. Recent studies have shown that these and similar metal chalcogenide clusters have low ionization potentials and can form charge-transfer complexes with electron-deficient moieties.[20,25,26] When the superatom is substituted with bis-isonitriles to form **2**, only the first of these oxidations is reversible. Figure 3.4 displays the cyclic voltammogram of **2**.

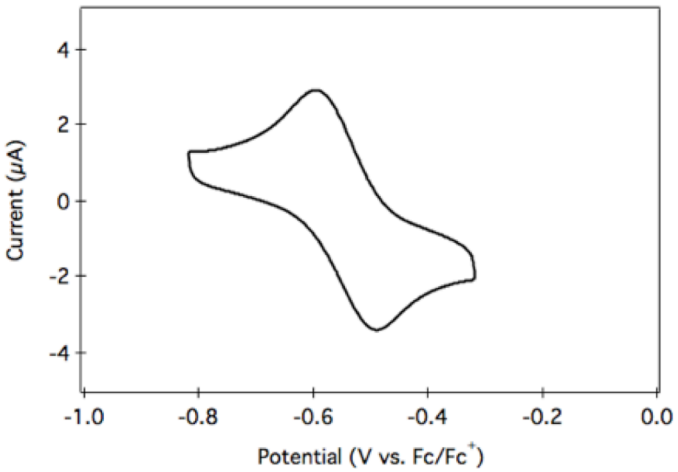

Figure 3.4. Cyclic voltammogram of *trans*-$Co_6Se_8(PEt_3)_4(CNC_6H_4NC)_2$ (**2**) in THF at 150 mV/s scan rate in 0.1 M tetrabutylammonium hexafluorophosphate. First reversible oxidation is shown, with $E_{1/2}$ = -0.542 V.

We have also observed that the isonitriles on the oxidized clusters became more labile and would thus encourage the substitution reaction to form the macromolecular strands. We anticipated that the cationic superatoms would associate with the anionic template and as the polymer chains grew they would express the 4-fold symmetry of the template (Figure 3.3d). The charge complementarity between the components creates a long-range ordered electrostatic "loom". This loom is further reinforced by the phenyl-to-phenyl distance in **2**, which corresponds to the edge length of the anionic template and encourages pi-pi stacking in the crossing points of the woven material.

3.4. Experimental Procedures

In order to accomplish this chemical weaving, we combined **1** and **2** in an electrocrystallization cell. The synthesis of compound **2** is described in Chapter 2. **1** was prepared as previously reported. The chemical weaving is accomplished in two steps. The crystals were first grown using electrocrystallization (1), and subsequently annealed at 150 °C to remove any remaining, unbound isonitriles (2). The annealing is a crystal-to-crystal transformation that preserves the tetragonal space group, *P4/ncc* and long-range order of the lattice that was established by the initial electrocrystallization.

(1) Electrocrystallization. A solution of $(Mo_6O_{19})(n\text{-}Bu_4N)_2$ [1] (**1**) (40 mg, 29 μmol) in tetrahydrofuran (12 mL, HPLC-grade, filtered over basic alumina) was prepared and sonicated. *Trans*-$Co_6Se_8(PEt_3)_4(CNC_6H_4NC)_2$ (**2**) (3 mg, 1.7 μmol) was then oxidized in the presence of **1.** The electrocrystallization experiment[3] was carried out in a two-compartment cell with platinum wires (l = 2 cm, Ø = 1 mm) at constant current (0.5 μA) at 20°C (in a temperature-controlled thermostat) for 13 days, yielding black needles on the anode.

(2) Crystal-to-crystal transformation. The presence of unbound isonitriles and partially polymerized strands in the protocloth lattice prompted us to perform a single crystal-to-single crystal annealing experiment. On the diffractometer, a single crystal of the protocloth was heated by temperature increments every 20 minutes up to 423 K; the unit-cell volume increases smoothly to: 21.83 Å, 22.78 Å, 28.51 Å, 89.81°, 89.90°, 89.52°, V = 14 175 Å^3. After the crystal was kept at this temperature for one hour, the unit-cell experiences significant shrinking to 21.66 Å, 21.75 Å, 28.89 Å, 89.88°, 89.99°, 90.05°, V = 13 613 Å^3 and remains stable in time. After 3h, held at this temperature, the measured unit cell is 21.64 Å, 21.61 Å, 28.95 Å, 89.62°, 89.90°, 90.60°, V = 13 533 Å^3. Remarkably, sharp Bragg peaks persist through the crystal transformation

indicating that long-range order is preserved in the lattice. The transformed crystal was then slowly cooled back down to 100 K for a full data collection.

3.5. Results and Discussion

Electrocrystallization is an invaluable tool for growing high quality electronic and magnetic materials in which a constant electrical current adjusts the state of oxidation of the growing components and assembles them in the solid state.[27] Figure 3.5 displays the structure from single crystal X-ray diffraction (SCXRD) of the assembled box weave fabric resulting from the electrocrystallization of these two components.

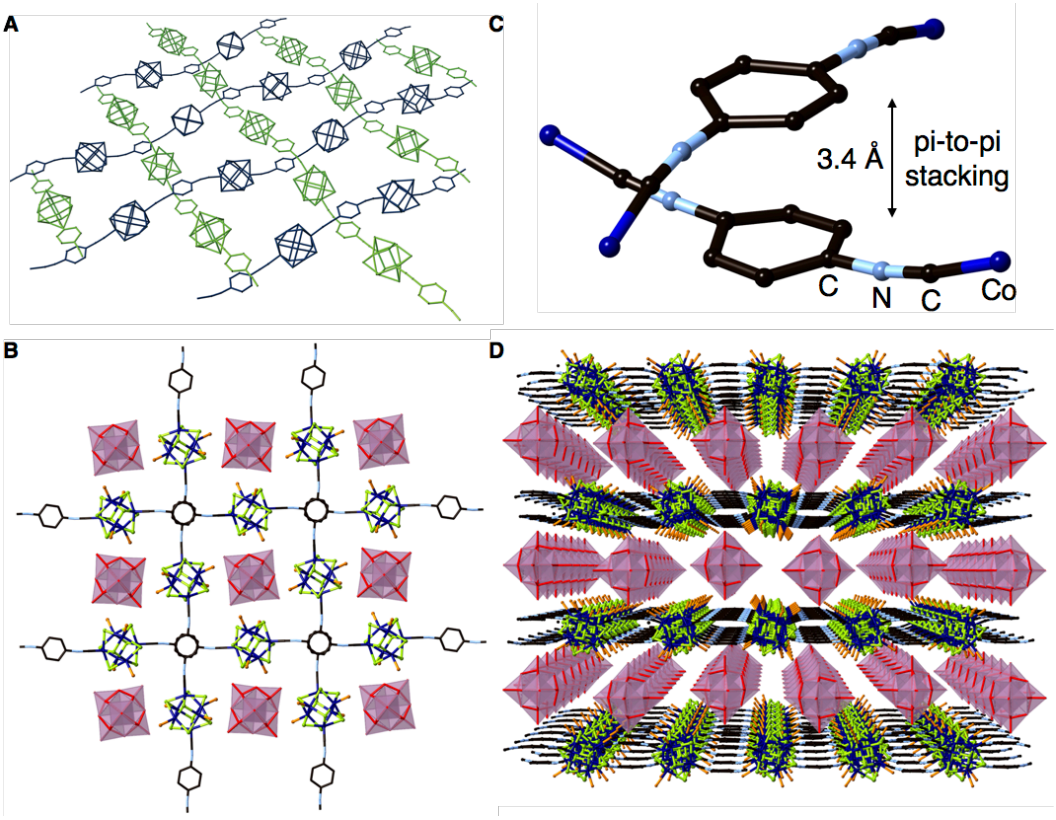

Figure 3.5. (a) SCXRD of the woven structure formed from building blocks **1** and **2**. The triethyl phosphine groups and hydrogen atoms have been removed to clarify the view. (b) The templation utilizes the 4-fold axis of $Mo_6O_{19}^{2-}$. (c) Pi-to-pi interactions holding the strands in registry. (d) Side view of the crystal packing showing the cationic and anionic layers (*a*-axis). Note that the ethyl groups from the phosphine subunits, which envelop the surface of the

templating Lindqvist nanooxides with directional C–H•••O hydrogen bonds, have been omitted in b and d to clarify the view.

SCXRD reveals that in the annealed crystal, monodisperse polymer strands of **2** are woven into a two-dimensional material, or molecular "cloth" (Figure 3.5a). Each of the $[Co_6Se_8]$ clusters has a single positive charge, and the Mo_6O_{19} is dianionic, thus the chemical formula for the nanoscale cloth is $\{[Co_6Se_8(PEt_3)_4^+](CNC_6H_4NC)\}_2[Mo_6O_{19}^{2-}]$. Each Co-C-N angle is bent from linear by about 10° to allow each strand to undulate as necessary to form the box weave. Figure 3.5b shows how the $Mo_6O_{19}^{2-}$directs the perpendicular arrangement of strands. In addition to the electrostatic templating, the $Mo_6O_{19}^{2-}$ further expresses its tetragonal symmetry through directional hydrogen bonds with the oligomeric strands. Neighboring strands cross at the aromatic rings of their linkers. The neighboring isonitriles are rotated 90 ° with respect to each other, and they are stacked, cofacially, within their van der Waals radii of ~3.4 Å (Figure 3.5c). If we substitute in the electrocrystallization experiment the Lindqvist dianion with a dianion that lacks tetragonal symmetry $[(W_6Cl_{14})(TBA)_2]$, we do not observe the crystalline woven structure.

It is even more remarkable that the layers of the cloth pack as alternating charged layers into a stack of nanoscale fabric. The layer-by-layer packing has the anionic layer of $Mo_6O_{19}^{2-}$ anions compensated by the cationic layer of nanoscale cloth (Figure 3.5d). Moreover, the different cationic layers are stacked in registry, thus the Lindqvist dianion not only directs the formation of two-dimensional cloth, but also of the three-dimensional fabric.

The molecules-to-fabric transformation occurs in two general stages: the formation of the ionic "loom", and the subsequent interweaving of the polymeric "thread." We know this because when we omit the post-electrocrystallization annealing step, we arrest the weaving process at a partially polymerized stage and isolate the intermediate that we call the "protocloth". Figure 3.6 displays the SCXRD structure of the partially polymerized strands within the protocloth. The

protocloth is a solid solution that has long-range order containing both woven (bridging isonitriles) and unwoven (terminal isonitriles) oligomeric fragments.

We find that nanoscale weaving has a further analogy to macroscopic weaving. When weaving, a "warp" strand is the stationary strand held in place by a loom through which the "weft" strand weaves. In the protocloth, there are covalently bound polydisperse, oligomeric strands, the "warp" strands, and there are segments in the crystals where the bridging reaction has not yet occurred and an extra equivalent of the bis-isonitrile linker remains, the "weft" strands (Figures 3.6a). The crystallographic occupancies in the crystal for the "warp" (woven) and "weft" (unwoven) strands in the protocloth is 0.64 to 0.36, respectively. Thus the overall formula is $\{[Co_6Se_8(PEt_3)_4^+][(CNC_6H_4NC)_{0.36}(CNC_6H_4NC)_{1.28}]\}_2[Mo_6O_{19}^{2-}]\bullet THF$.

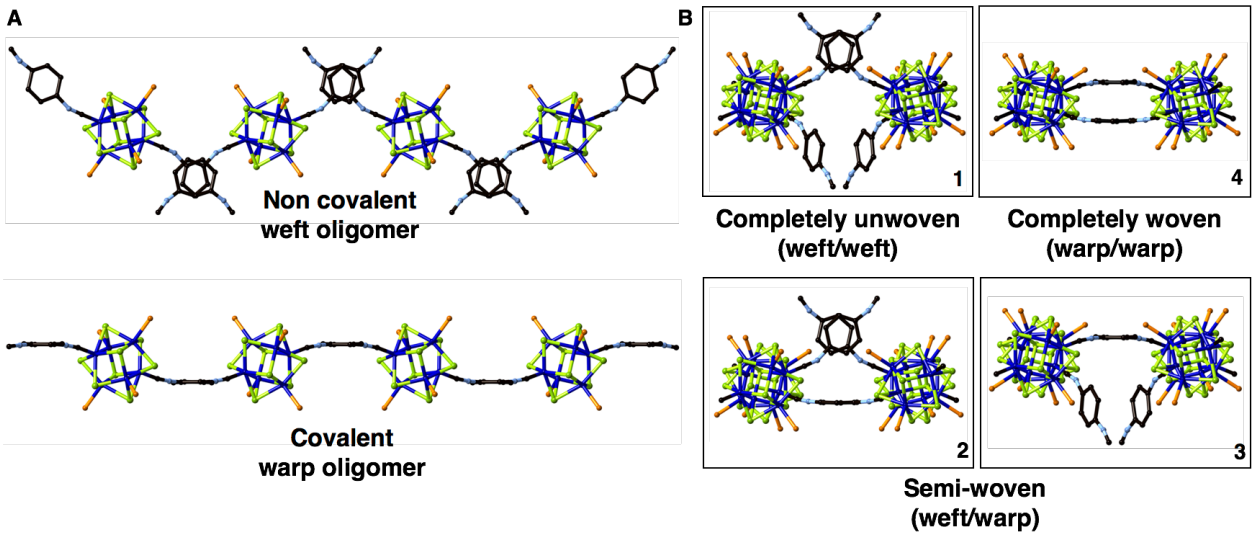

Figure 3.6. (a) The protocloth consists of unwoven, oligomeric weft segments and woven oligomeric warp segments. (b) Different possible configurations of crossing points in the warp (woven) and weft (unwoven) strands. The warp and weft strands that make up the protocloth are polydisperse in length. The warp/warp combination does not occur in the crystal.

The bis-isonitrile ligands are distributed with unbalanced occupancies over the four crossing points in the unit cell with distinct spatial configurations. We define the three possible crossing points as "weft-weft", "weft-warp", and "warp-warp" crossings (Figure 3.6b). From the

crystal structure refinement it is clear that "warp-warp" crossings cannot exist in the protocloth because this would impose an energetically unfavorable 2.7 Å pi-to-pi distance between aryl rings. However, a mixture of "warp-weft", "weft-weft", and "weft-warp" crossing points are present. The "weft" strands are held in place by the electrostatic templating of the superatoms with the anions and by a loose pi-stacking (~3.5 Å) between the dangling aryl-isonitriles. As such, these free isonitriles, which are in excess in the lattice, are held in a perfectly predisposed position to bridge upon heating to release the bis-isonitrile. This last transformation forms the woven cloth.[29]

3.6. Conclusions

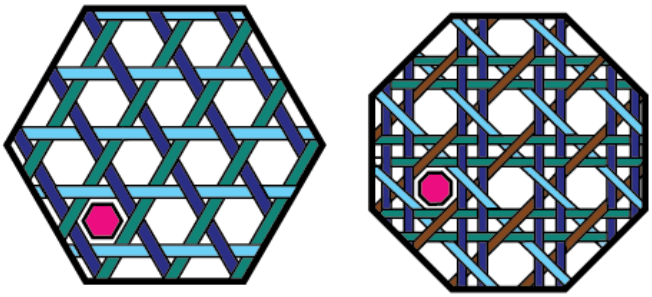

Figure 3.7. Higher order weaving. Hexagonal or octagonal weaving utilizes either a hexagonal or octagonal template shown in magenta.

Beyond the box weave there are other basic textile weaves such as the hexagonal weave and the octagonal weave that should now be possible (Figure 3.7). The higher order weaves differ by how the strands of thread are oriented with respect to each other. For a box weave, two strands cross each other, for a hexagonal weave three strands cross over each other, and so on for the octagonal weave. These types of weaves on the nanoscale will adjust their durability and their topology. To create these higher order nanoscale weaves it will be necessary to utilize electrostatic templates with hexagonal symmetry and octagonal symmetry (Figure 3.7).[30] This study reveals a method to make a new type of two-dimensional nanomaterial, a woven cloth.

These materials are interesting because they could be exfoliated electrochemically to release the free standing, two-dimensional sheet. The electronic and magnetic properties of this new two-dimensional cloth will be coupled with its presumed strength and toughness that is imparted by the weave.

3.7. References

1. Weng, W.; Chen, P. N.; He, S. S.; Sun, X. M.; Peng, H. S. *Angew. Chem. Int. Ed.* **2016**, *55*, 6140.

2. Wagner, S.; Bauer, S. *MRS Bull.* **2012**, *37*, 207.

3.Luan, X. J.; Wang, Y. Y.; Li, D. S.; Liu, P.; Hu, H. M.; Shi, Q. Z.; Peng, S. M. *Angew. Chem. Int. Ed.* **2005**, *44*, 3864.

4. Han, L.; Zhou, Y. *Inorg. Chem. Comm.* **2008**, *11*, 385.

5. Baburin, I. A.; Blatov, V. A.; Carlucci, L.; Ciani, G.; Proserpio, D. M. *J. Solid State Chem.* **2005**, *178*, 2452.

6. Blatov, V. A.; Carlucci, L.; Ciani, G.; Proserpio, D. M. *CrystEngComm.* **2004**, *6*, 377.

7. Carlucci, L.; Ciani, G.; Proserpio, D. M. *Coord. Chem. Rev.* **2003**, *246*, 247.

8. Hyde, S. T.; Chen, B. L.; O'Keeffe, M. *CrystEngComm.* **2016**, *18*, 7607.

9. Alexandrov, E. V.; Blatov, V. A.; Proserpio, D. M. *Acta Cryst. A* **2012**, *68*, 484.

10. Wadhwa, N. R.; Hughes, N. C.; Hachem, J. A.; Mezei, G. *RRS Adv.* **2016**, *6*, 11430.

11. Liu, Y. Z.; Ma, Y. H.; Zhao, Y. B.; Sun, X. X.; Gandara, F.; Furukawa, H.; Liu, Z.; Zhu, H. Y.; Zhu, C. H.; Suenaga, K.; Oleynikov, P.; Alshammari, A. S.; Zhang, X.; Terasaki, O.; Yaghi, O. M. *Science* **2016**, *351*, 365.

12. Wang, Z. B.; Blaszczyk, A.; Fuhr, O.; Heissler, S.; Woll, C.; Mayor, M. *Nat. Comm.* **2017**, *8*.

13. Qian, M. C.; Reber, A. C.; Ugrinov, A.; Chaki, N. K.; Mandal, S.; Saavedra, H. M.; Khanna, S. N.; Sen, A.; Weiss, P. S. *ACS Nano* **2010**, *4*, 235.

14. Mandal, S.; Reber, A. C.; Qian, M. C.; Weiss, P. S.; Khanna, S. N.; Sen, A. *Acc. Chem. Res.* **2013**, *46*, 2385.

15. Dolbecq, A.; Guirauden, A.; Fourmigue, M.; Boubekeur, K.; Batail, P.; Rohmer, M. M.; Benard, W.; Coulon, C.; Salle, M.; Blanchard, P. *J. Chem. Soc. Dalton Trans.* **1999**, 1241.

16. Coronado, E.; Gomez-Garcia, C. J. *Chem. Rev.* **1998**, *98*, 273.

17. Che, M.; Fournier, M.; Launay, J. P. *J. Chem. Phys.* **1979**, *71*, 1954.

18. Davidson, A.; Boubekeur, K.; Penicaud, A.; Auban, P.; Lenoir, C.; Batail, P.; Herve, G. *J. Chem. Soc. Chem. Comm.* **1989**, 1373.

19. Fourmigue, M.; Batail, P. *Chem. Rev.* **2004**, *104*, 5379.

20. Roy, X.; Lee, C. H.; Crowther, A. C.; Schenck, C. L.; Besara, T.; Lalancette, R. A.; Siegrist, T.; Stephens, P. W.; Brus, L. E.; Kim, P.; Steigerwald, M. L.; Nuckolls, C. *Science* **2013**, *341*, 157.

21. Khanna, S. N.; Jena, P. *Phys. Rev. B* **1995**, *51*, 13705.

22. Luo, Z. X.; Castleman, A. W. *Acc. Chem. Res.* **2014**, *47*, 2931.

23.Walter, M.; Akola, J.; Lopez-Acevedo, O.; Jadzinsky, P. D.; Calero, G.; Ackerson, C. J.; Whetten, R. L.; Gronbeck, H.; Hakkinen, H. *Proc. Natl. Acad. Sci.* **2008**, *105*, 9157.

24. Champsaur, A. M.; Velian, A.; Paley, D. W.; Choi, B.; Roy, X.; Steigerwald, M. L.; Nuckolls, C. *Nano Lett.* **2016**, *16*, 5273.

25. Chauhan, V.; Reber, A. C.; Khanna, S. N. *J. Am. Chem. Soc.* **2017**, *139*, 1871.

26. Turkiewicz, A.; Paley, D. W.; Besara, T.; Elbaz, G.; Pinkard, A.; Siegrist, T.; Roy, X. *J. Am. Chem. Soc.* **2014**, *136*, 15873.

27. Batail, P.; Boubekeur, K.; Fourmigue, M.; Gabriel, J. C. P. *Chem. Mater.* **1998**, *10*, 3005.

28. Details for the electrochemistry and SCXRD can be found in the Supporting Information.

29. We also note that there is a tetrahydrofuran (THF) located in the equatorial plane of Lindqvist anions in the crystal which, when heated, is expelled along with unbound bis-isonitriles to complete the weave.

30. Boubekeur, K.; Riccardi, R.; Batail, P.; Canadell, E. *C. R. Acad. Sci., Ser. IIc: Chim.* **1998**, *1*, 627.

Chapter 4. 2D and 3D Coordination Frameworks from COOH-Functionalized [Co_6Se_8] Superatoms

4.1. Preface

This chapter is based on a published manuscript titled "Two-Dimensional Nanosheets from Redox-Active Superatoms" by Anouck M. Champsaur, Jaeeun Yu, Xavier Roy, Daniel W. Paley, Michael L. Steigerwald, Colin Nuckolls, and Christopher M. Bejger (*ACS Cent. Sci.*, **2017**, *3*, 1050). I synthesized all [Co_6Se_8] molecules and frameworks, exfoliated the materials, and performed electrochemical studies. Jaeeun Yu performed all imaging (optical, SEM, AFM). Dan Paley performed single crystal refinement. Christopher Bejger conceptualized this project, realized the first synthesis of the cluster using a different route, and developed some of the framework-forming conditions.

4.2. Introduction

In this chapter we connect transition metal chalcogenide molecular clusters into 3D and 2D solids, as well as free-floating nanosheets. Monolayer 2D materials such as graphene and transition metal dichalcogenides show promise for next-generation electronics, yet are plagued by the occurrence of defects, and it is not easy to modify them synthetically.[1,2] The type of nanosheet we disclose here, due to the redox activity and multinuclearity of its superatom components, provides a new level of complexity and synthetic sophistication to 2D materials. Our building blocks are atomically defined entities whose isolated electronic and redox properties can be incorporated into extended structures in which the structural element is preserved. Recent theoretical calculations have established that polynuclear $Co_6Se_8L_6$ clusters behave as "superatoms".[3-8] We have previously used such superatoms to form solids from two

different yet electronically complementary building blocks; directed-layer fullerene assemblies from phenanthrene-decorated clusters; and covalent assemblies through directed ligand exchange.[9-12] Redox-active $[M_6Se_8]$ clusters (M = Re, W; E = S, Se) have previously been functionalized with reactive ligands to generate frameworks of these preformed entities through cyanide and bipyridine coordination with transition metal ions.[13-18] Others have employed a variety of techniques to direct clusters and nanocrystals into extended lattices. [19-22]

The key to unlocking both the structural utility and the functional solid-state infrastructure of the superatoms is the ability to manipulate their surface properties at will. In this study, we demonstrate a method to do so by converting the $Co_6Se_8[PEt_2(4\text{-}C_6H_4Br)]_6$ superatom (Figure 4.1) into one that presents six carboxylic acids (Figure 4.2). We then introduce zinc carboxylate bonds via a solvothermal reaction to produce two types of crystalline solids, a trigonal 3D dimensional solid (**Trig$_{3D}$**) and a tetragonal 2D solid (**Tet$_{2D}$**) (Figure 4.1). Single crystal X-ray diffraction (SCXRD) reveals that **Trig$_{3D}$** is a three-dimensional network of superatoms held together with zinc carboxylate bonds, but **Tet$_{2D}$** forms two-dimensional sheets that then stack through non-covalent forces into a three-dimensional solid. We find it remarkable that the two-dimensionality of **Tet$_{2D}$** is robust: individual 2D sheets can be exfoliated intact from the solid, and these exfoliated sheets can be subsequently redeposited on

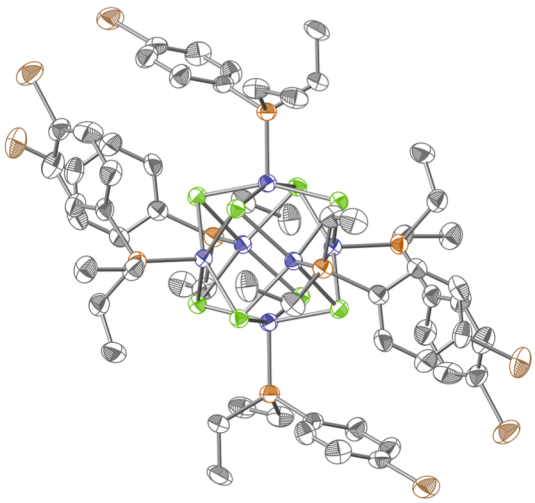

Figure 4.1: Solid state molecular crystal structure of $Co_6Se_8[PEt_2(4\text{-}C_6H_4Br)]_6$. Carbon, black; bromine, brown; cobalt, blue; selenium, green; phosphorus, orange. Thermal ellipsoids are set at 50% and hydrogen atoms are omitted to clarify the view.

arbitrary substrates. When we cast them on electrode surfaces they retain the redox activity of the superatom building blocks.

4.3. Synthesis of Reactive [Co_6Se_8] Monomer Functionalized with COOH groups

We previously organized these superatoms into extended van der Waals solids; our new objective was to connect the superatoms to make extended solids through bonds. Our simple, phosphine-terminated superatoms, however, are inert in the sense that the phosphines (by design) chemically passivate the cluster surfaces and do not participate in the reaction chemistry. Thus our first challenge was to create appropriately reactive superatom building blocks.

To do so we first treated $Co_2(CO)_8$ and Se with $Et_2P(4\text{-}C_6H_4Br)$ to give $Co_6Se_8[PEt_2(4\text{-}C_6H_4Br)]_6$ (Figure 4.1) in high yield. Other than the obvious differences in the size, shape, and arrangement of the organic components, the inorganic core of $Co_6Se_8[PEt_2(4\text{-}C_6H_4Br)]_6$ is identical to the parent cluster, $Co_6Se_8(PEt_3)_6$.[5] Through a six-fold lithium/halogen exchange followed by the addition of CO_2 gas and subsequent acidification, we converted each Br in this compound to the corresponding carboxylic acid to yield the nanosized octahedral, superatom building block $Co_6Se_8[PEt_2(4\text{-}C_6H_4COOH)]_6$ (**1**) (Figure 4.2). This sequence is facile and high yielding. The lithium/halogen exchange is a harsh process, and the fact that the Co_6Se_8 core is unchanged reveals a new method to easily activate and functionalize superatoms.

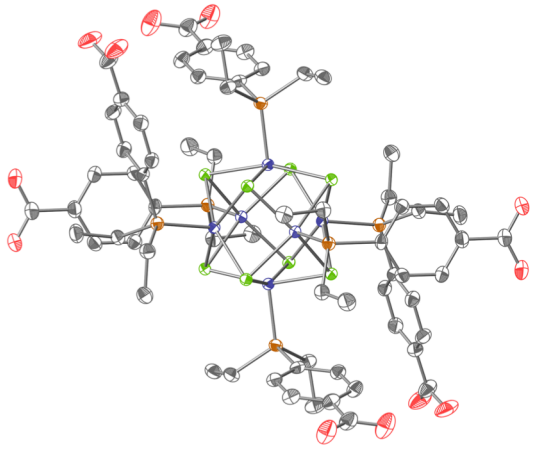

Figure 4.2. Solid state molecular crystal structure of $Co_6Se_8[PEt_2(4\text{-}C_6H_4COOH)]_6$ (**1**). Carbon, black; oxygen, red; cobalt, blue; selenium, green; phosphorus, orange. Thermal ellipsoids are set at 50% and hydrogen atoms are omitted to clarify the view.

We determined the molecular structure of **1** using SCRXD (Figure 4.3a). **1** assembles into an organized, extended, three-dimensional solid via extensive and ordered hydrogen bonding between carboxylic acids on neighboring clusters (Figure 4.3b). We refer to the latter solid as **1-H**. If we represent each cluster as a sphere, we see that this solid forms such that there is hydrogen-bonding between nearest neighbors (Figure 4.3c). The formation of this solid-state compound is reversible: **1-H** dissolves in tetrahydrofuran to regenerate **1**.

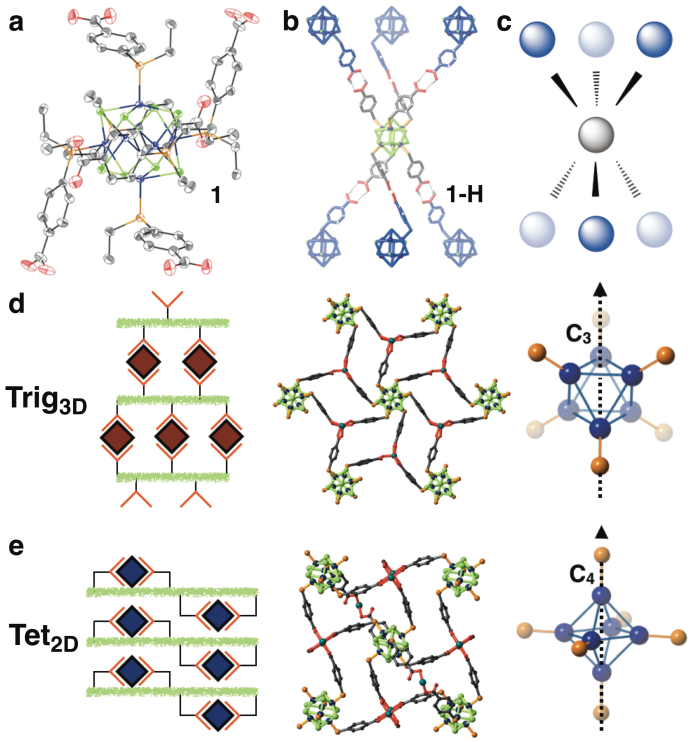

Figure 4.3. (a) Structure of **1** from SCXRD, Co_6Se_8 cluster capped with 4-(diethylphosphine)benzoic acid, $Co_6Se_8[PEt_2(4\text{-}C_6H_4COOH)]_6$. Carbon, black; oxygen, red; cobalt, blue; selenium, green; phosphorus, orange. Thermal ellipsoids are set at 50% probability. Hydrogen atoms are omitted to clarify the view. (b) **1** forms a three-dimensional hydrogen-bond network, named **1-H**. View of **1-H** down the *a*-axis, showing a single superatom and its six hydrogen-bonds to neighboring superatoms (in blue). (c) Representation of the view in (b) with each superatom as a sphere to emphasize the structure of the extended solid. (d) and (e) The solvothermal reaction of $Co_6Se_8[PEt_2(4\text{-}C_6H_4COOH)]_6$ with $Zn(NO_3)_2$ forms two different types of extended solid, $\mathbf{Trig_{3D}}$ and $\mathbf{Tet_{2D}}$, depending upon solvent conditions. (d) In $\mathbf{Trig_{3D}}$ the superatoms are held together within a two-dimensional plane to create a trigonal arrangement of superatoms, and the planes extend in three dimensions via further zinc carboxylate bonds. The axis of symmetry defining a superatom within a $\mathbf{Trig_{3D}}$ sheet is a C_3-axis through the center of two planes defined by Co_3 atoms. (e) In $\mathbf{Tet_{2D}}$ the superatoms are held together within a two-dimensional plane to create a distorted square arrangement. The two-dimensional layers are non-

covalently stacked in the third dimension. The axis of symmetry defining the **Tet$_{2D}$** plane is a C_4-axis through axial atoms of a Co_6 octahedron.

We then sought to create solids from building block **1** through metal-carboxylate bonds**.** For example, would the simple replacement of the two protons with a divalent metal ion result in a structurally diverse family of new solids?[23-40] Thus, we treated our hexatopic superatom with $Zn(NO_3)_2$ to determine the extent to which the carboxylate-carboxylate bonds, which constitute the adhesive that stabilizes this solid, can be modified and improved. Co_6Se_8 superatoms are useful building blocks in this regard because they have tunable ligands, multiply accessible redox states, significant magnetic moments, and charge transport capabilities.[21,41-43] Our building block **1** is preformed and atomically defined, and thus programmable.

4.4. Frameworks from $Co_6Se_8[PEt_2(PhCOOH)]_6$ and $Zn(NO_3)_2$: Synthesis and SCXRD

Using the same building blocks, **1** and Zn^{2+}, we can selectively synthesize two different solids, **Trig$_{3D}$** and **Tet$_{2D}$**, by varying the growth conditions. The synthetic details are found in Section 4.6. It is remarkable that the only significant difference between the two reactions is the use of methanol versus ethanol as solvents. We obtained structures for both solids using SCXRD (details of the refinement can be found in the Supporting Information).

In both solids, all the carboxylic acid hydrogen bonds of **1-H** are replaced by carboxylate-zinc-carboxylate nodes. SCXRD of both solids reveals that while they have the same Zn:[Co_6Se_8] stoichiometric ratio of 3:1, both the dimensionality of their extended structure and orientation of the cluster within the solids differ significantly. **Trig$_{3D}$** is a three-dimensional network (Figure 4.3d) while **Tet$_{2D}$** is a two-dimensional structure with strong in-plane bonding and comparatively weak non-covalent inter-layer interactions (Figure 4.3e).

We combined **1** and $Zn(NO_3)_2$ in a DMF/MeOH solvent mixture under solvothermal conditions at 65 °C, and obtained black hexagonal crystals after 24 h. Figure 4.4 displays the crystal structure of **Trig$_{3D}$**. The structure is a network in which **1** is coordinated to unusual trinuclear zinc nodes in three dimensions (Figure 4.4a). Looking down the *b*-axis we clearly see the distinct pseudotrigonal layers of the solid (Figure 4.4b). Within each layer, the superatoms are bound to six zinc-nodes (Figure 4.4c). These layers are then crosslinked by a single Zn-O bond. The approximate 3-fold symmetry of the pseudotrigonal lattice of **Trig$_{3D}$** arises because the Co_6 octahedron is tilted on its face in the layer, which orients the phosphines such that three point up and three point down (Figure 4.4d). This symmetry mirrors that of **1-H**, replacing hydrogen bonds with an organized trinuclear metal node (labeled Zn_1, Zn_2, and Zn_3 in 4.4e). Unusual trinuclear zinc nodes have been reported previously.[44,45]

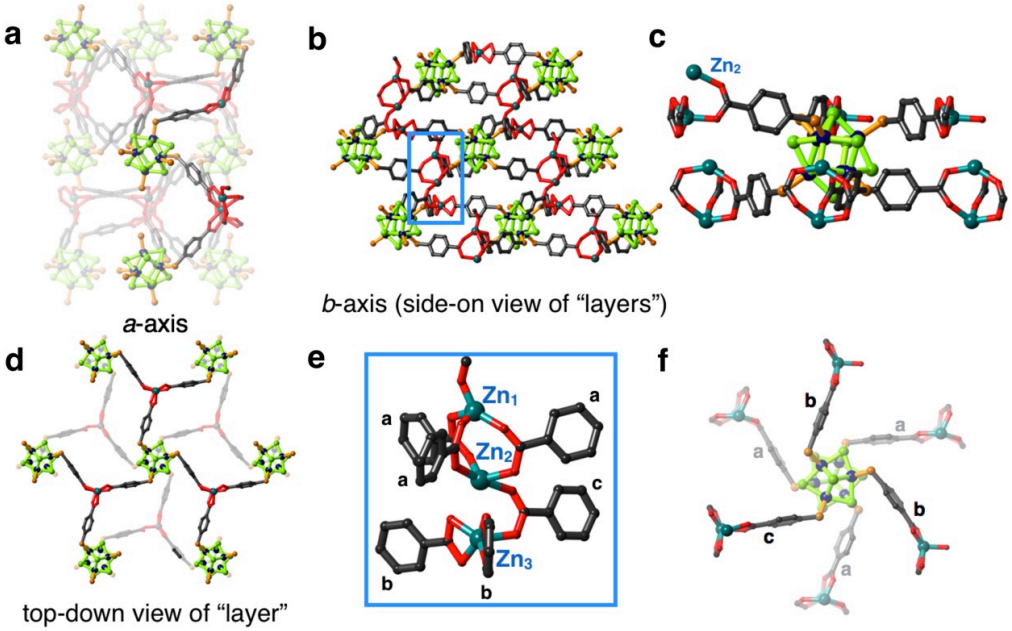

Figure 4.4. Structure of **Trig$_{3D}$** from SCXRD: a three-dimensional network synthesized from the solvothermal reaction of **1** and $Zn(NO_3)_2$ in a MeOH/DMF solvent mixture. Ethyl groups are omitted for clarity. (a) View of the network along the *a*-axis. (b) View along the *b*-axis of the crosslinked pseudotrigonal arrays of superatoms. The blue box highlights the trinuclear zinc node, which is magnified in (e). (c) Side-on view of **1** within a pseudotrigonal layer and (d) top-down view of a single "layer" within **Trig$_{3D}$**. (e) View of the metal node geometry and different

coordination environments around Zn_1, Zn_2 and Zn_3. The blue box around this trinuclear zinc node is the same as in the inset in (b). (f) Top-down view of a single cluster within a **Trig$_{3D}$** layer surrounded by three different Zn-carboxylate binding modes. Three types of carboxylates are shown: a, b, and c.

Each zinc atom in **Trig$_{3D}$** exhibits a different coordination environment. Zn_1 and Zn_2 display distorted tetrahedral geometry and together form a three-bladed trigonal paddlewheel with three bridging μ_2-carboxylates. A solvent molecule (likely MeOH) coordinates Zn_1 axially, and Zn_2 is axially coordinated by a μ_2-carboxylate, whose second oxygen coordinates Zn_3. Zn_3 exhibits a distorted square pyramidal geometry. Each superatom **1** within the solid contains three types of carboxylates, labeled **a**, **b**, and **c** in Figures 4.4e and 4.4f. For **a**, three μ_2-carboxylates form the Zn_1-Zn_2 paddlewheel; for **b**, two carboxylates coordinate Zn_3 in an η_2 fashion; for **c,** a μ_2-carboxylate coordinates both Zn_3 and Zn_2. The latter ligand **c** also serves to crosslink the layers through its carboxylate-Zn_2 bond. This bond has a length of 2.22 Å, which is a long Zn-O contact[46] and suggests the inter-layer carboxylate-Zn_2 bond is a weaker, dative bond compared to intra-layer carboxylate-Zn bonds.

The presence of weak inter-layer zinc bonds in **Trig$_{3D}$** prompted us to modify reaction conditions to eliminate inter-layer bonding and synthesize 2D layers. Thus, we reacted **1** and $Zn(NO_3)_2$ at 65 °C in a DMF/EtOH solvent mixture and obtained black cubic crystals after 24 h. We note that a small fraction of **Trig$_{3D}$** forms under these conditions but can eliminated with the addition of "extra" protons in the form of HCl in the reaction. Under these conditions, we form exclusively the new solid-state compound, **Tet$_{2D}$** (Figure 4.5). **Tet$_{2D}$** also contains complete replacement of proton-nodes with metal nodes, although the types of metal nodes and dimensionality differs from **Trig$_{3D}$**. Distinct layers of superatoms are held together only by non-covalent forces.

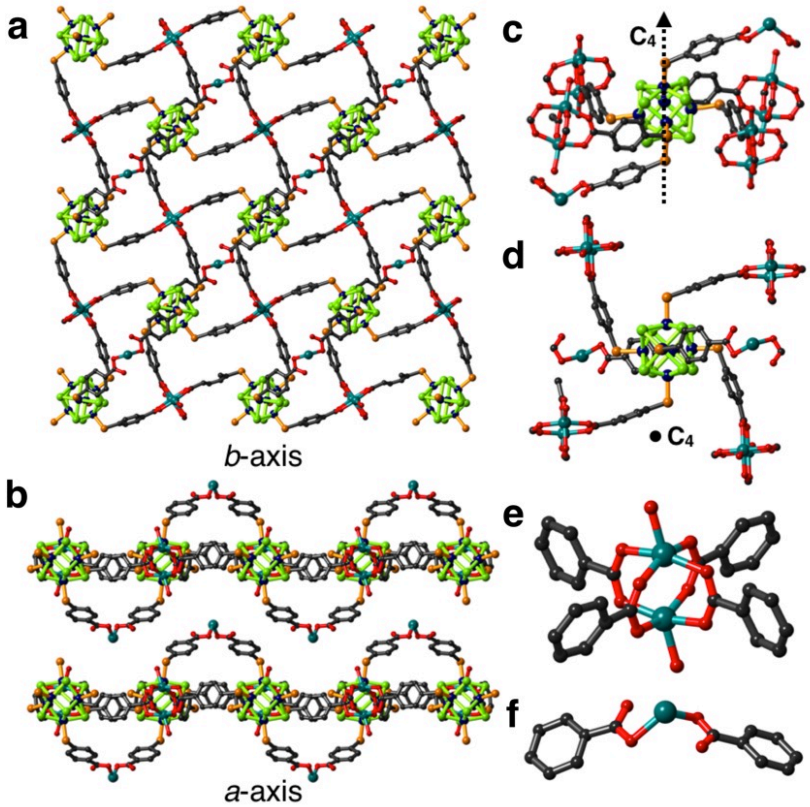

Figure 4.5. Structure of $\mathbf{Tet_{2D}}$ from SCXRD: square sheets in the crystalline state. $\mathbf{Tet_{2D}}$ is two-dimensional network synthesized from the solvothermal reaction of **1** and $Zn(NO_3)_2$ in a EtOH/DMF solvent mixture. Ethyl groups are omitted for clarity. (a) Top-down view of a single layer within $\mathbf{Tet_{2D}}$ along the *b*-axis. (b) Side-on view of $\mathbf{Tet_{2D}}$ layers along the *c*-axis. Non-covalent forces hold the layers together in the third dimension. (c) Single superatom in a $\mathbf{Tet_{2D}}$ layer and the binding interaction of each carboxylate of **1**. Within the two-dimensional plane, each of the four equatorial carboxylate ligands coordinates two Zn^{2+} ions, forming the four-bladed paddlewheel upon coordination of equatorial carboxylate ligands of three adjacent superatoms. The axial carboxylate ligands coordinate an additional Zn^{2+} ion that lies just above or below the square sheet. (d) Top-down view of **1** within the 2D plane. (e) Four-bladed Zn^{2+} paddlewheel. Zn-Zn = 2.867(7) Å. (e) Mononuclear zinc complex with Zn-O distances = 2.20(3) and 2.36(3) Å and a carboxylate-Zn-carboxylate angle of 118.6(12)°.

$\mathbf{Tet_{2D}}$ is a layered two-dimensional material in which each layer is a square arrangement of Co_6Se_8 superatoms with four phosphine ligands residing in the 2D plane and bonding to four-bladed Zn-carboxylate paddlewheels (Figure 4.5a). In the direction normal to the sheet, the axial carboxylate ligands coordinate an additional Zn^{2+} ion that is positioned above or below the square sheet (Figure 4.5b). Figures 4.5c and 4.5d display the binding interaction of each ligand of **1** within the solid. The zinc subunit within the square plane of this solid is a dinuclear four-

bladed Zn-carboxylate paddlewheel (Figure 4.5e). The combination of two Zn^{2+} ions and four bridging μ_2-carboxylate groups yields this Zn_2 cluster with a Zn-Zn distance of 2.867(7) Å that is consistent with other such "four-bladed" paddlewheels in zinc-based metal-organic frameworks.[47] Pairs of apical phosphines on adjacent clusters that are not involved in dinuclear Zn paddlewheels within a single layer are linked via a single Zn atom (in addition to their bonding via the intra-layer Zn_2 node) to form a mononuclear zinc complex. This complex features Zn-O distances of 2.20 (3) and 2.36(3) Å and a carboxylate-Zn-carboxylate angle of approximately 119°. This geometry is typical of pseudotetrahedral $Zn(O_2R)_2L_2$ complexes[48] but in this case we note that the two L-type ligands (presumably ethanol or water) are disordered and could not be located. The layers are self-contained and stack through non-covalent inter-layer interactions in an eclipsed arrangement.

4.5. Scanning Electron Microscopy (SEM) of $\mathbf{Trig_{3D}}$ and $\mathbf{Tet_{2D}}$ Crystals

The crystal packing arrangements of $\mathbf{Trig_{3D}}$ and $\mathbf{Tet_{2D}}$ are propagated in their macroscopic crystal morphologies. Figure 4.6 shows SEM micrographs of the crystals that form after 24 h growth. The black cubes ($\mathbf{Tet_{2D}}$; Figure 4.6a) and hexagonal plates ($\mathbf{Trig_{3D}}$; Figure 4.6b) reflect the tetragonal and trigonal lattices of their crystalline arrangements. In $\mathbf{Trig_{3D}}$, the cluster is tilted on its side such that the symmetry is defined by a C_3-axis through the offset

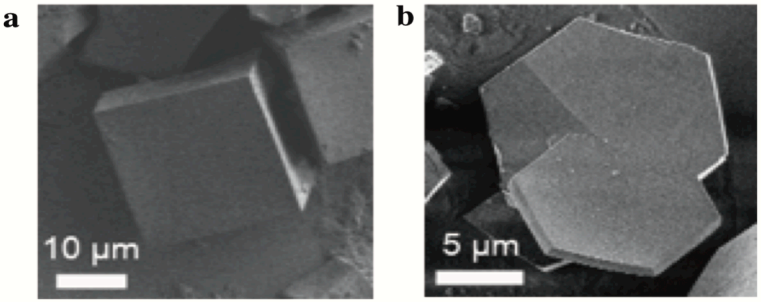

Figure 4.6. SEM images of (a) $\mathbf{Tet_{2D}}$ cubic crystals and (b) $\mathbf{Trig_{3D}}$ hexagonal crystals as synthesized.

triangular stacks of Co_3, whereas in **Tet$_{2D}$** a C_4-axis through the axial cobalt atoms of the Co_6 octahedron generates a square lattice. Powder XRD of each sample shows homogeneous crystalline phases (see Section 4.7 for details).

4.6. Chemical Exfoliation of Tet$_{2D}$ into Redox-Active Nanosheets

The two-dimensional **Tet$_{2D}$** crystals behave like traditional "atomic" layered compounds such as transition metal dichalcogenides in that we can exfoliate these materials without having the layers disintegrate. We reasoned that since the multi-coordinate Zn^{2+} ions in some fashion hold the layers together, a solution of a weak acid would chemically dissociate the layers of **Tet$_{2D}$** and that they would be stable to these conditions (having been originally formed in acidic conditions).

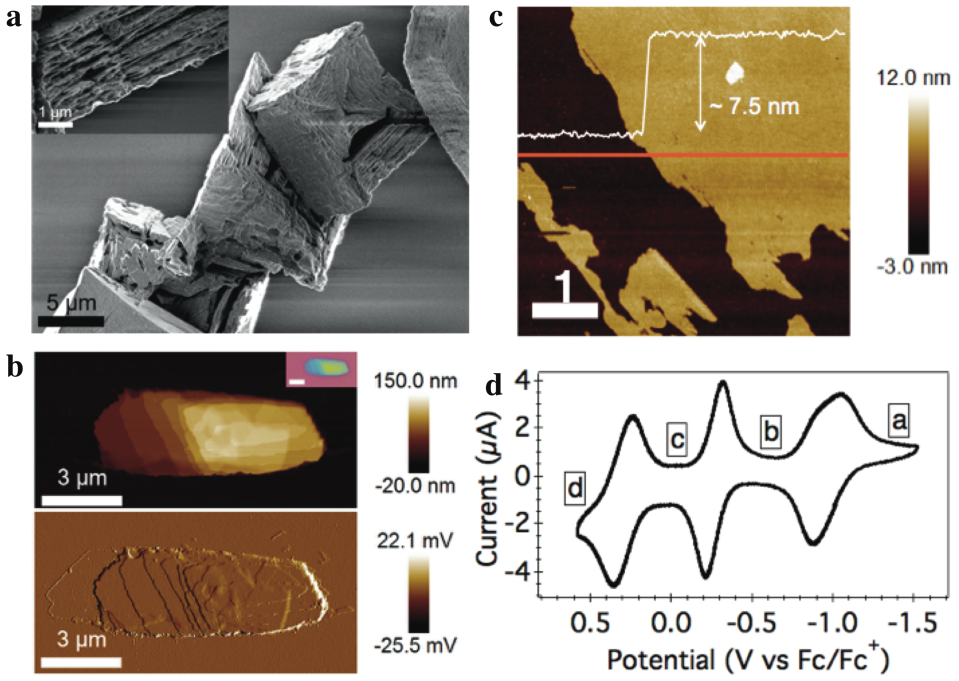

Figure 4.7. (a) SEM images of cubic crystals of **Tet$_{2D}$** immersed in a benzoic acid solution in DMF. Striations in the crystals are apparent. (b) AFM height sensor and peak force error images of multilayered **Tet$_{2D}$** films after immersion in benzoic acid solution in DMF. The scale bar in an inset is 3 μm. (c) AFM topographic image of exfoliated sheets. Sheets remain that are about 7.5

nm in thickness, with distinct step sizes apparent. (d) Solid-state cyclic voltammogram of exfoliated **Tet_{2D}** sheets in 0.1 M $TBAPF_6$ in tetrahydrofuran with a 50 mV/s scan rate. The solution of exfoliated sheets was dropcast onto a glassy carbon electrode.

We first immersed the cubic crystals of **Tet_{2D}** in a 1 mM solution of benzoic acid in DMF.

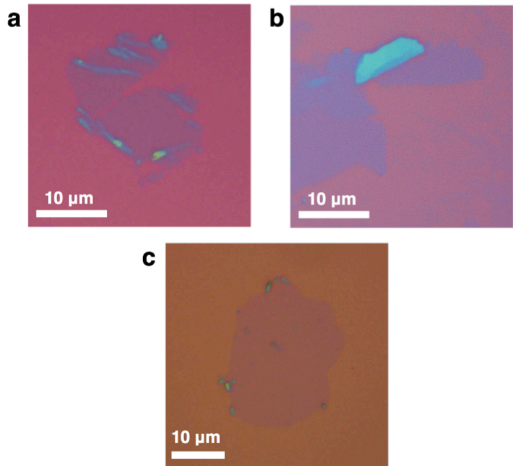

Figure 4.8. (a) to (c) Optical images of chemically exfoliated **Tet_{2D}** sheets on Si/SiO_2 substrates.

SEM micrographs of immersed cubes show visible layered striations within the crystals (Figure 4.7a). Next, we immersed the **Tet_{2D}** crystals in 40 mM benzoic acid overnight and followed the transformation with powder X-ray diffraction (see Section 4.7). The reflections that are due to **Tet_{2D}** disappear, with only low intensity peaks corresponding to trace impurities of **$Trig_{3D}$** still visible. During this process, we observe a color change in the solution from clear to light brown upon suspension in the benzoic acid solution.

We drop-casted this solution on a silicon substrate (SiO_2 on Si) and characterized the films with optical microscopy and atomic force microscopy (AFM). Optical images of chemically exfoliated sheets

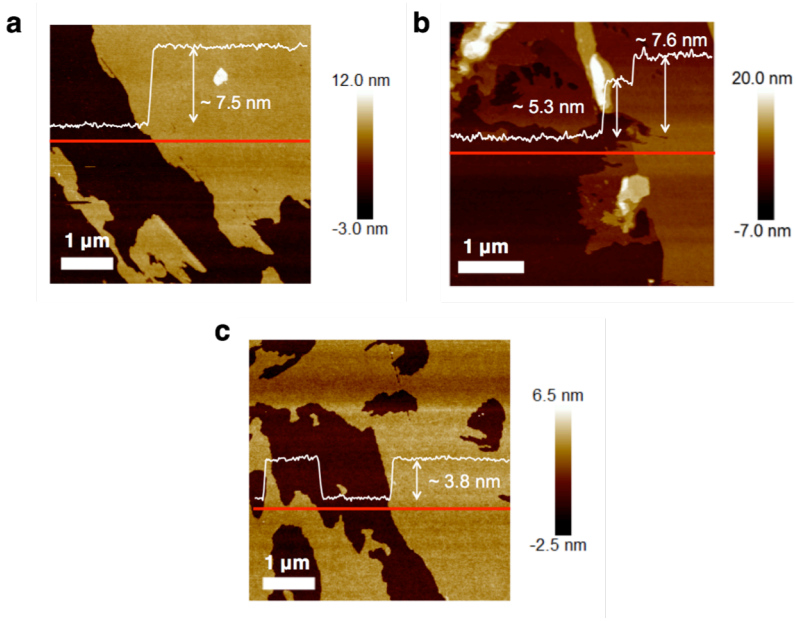

Figure 4.9. (a) to (c) AFM topographic images and height profiles of chemically exfoliated **Tet_{2D}** sheets. Exfoliated sheets are typically around 7.5 nm in thickness ((a) and (b)), with certain thinner areas (3.8 nm).

suggest thin layers (Figure 4.8). Figures 4.7b shows layered two-dimensional sheets by AFM. Thin sheets with a thickness of 7.5 nm are present throughout the samples (Figure 4.7c), with step sizes between the layers corresponding to this thickness. From the SCXRD structure of **Tet$_{2D}$**, the expected thickness of a single sheet is 1.5 nm, corresponding to the Zn-Zn distance between stacked mononuclear Zn atoms in adjacent layers. Thus, 7.5 nm corresponds to five distinct superatom layers. In other images we also observe smaller step sizes of 3.8 nm and 5.3 nm (Figure 4.9), corresponding by SCXRD to three layers and four layers, respectively. These chemically exfoliated sheets of **Tet$_{2D}$** once deposited onto a substrate are clean and flat (Figure 4.10).

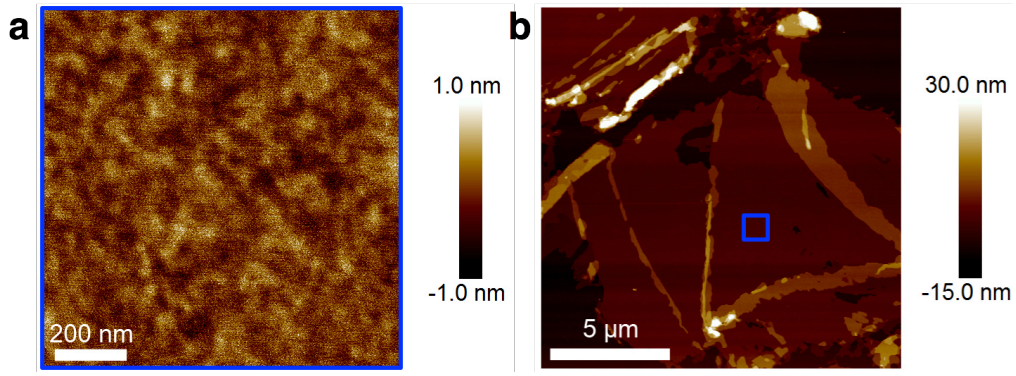

Figure 4.10. (a) AFM image of the surface of exfoliated **Tet$_{2D}$**. The surface is clean and flat, with a roughness of 0.3 nm. The area imaged by AFM is indicated by the blue square in (b).

We can use these thin layers of **Tet$_{2D}$** from solution to coat the surface of electrodes and probe their redox-activity. For comparison, **1** ($Co_6Se_8[PEt_2(4\text{-}C_6H_4COOH)]_6$) displays three reversible oxidations relative to Fc/Fc^+ (Figure 4.11a) and the bulk crystals deposited on the electrode show two broad, quasi-reversible oxidations (Figure 4.11b).

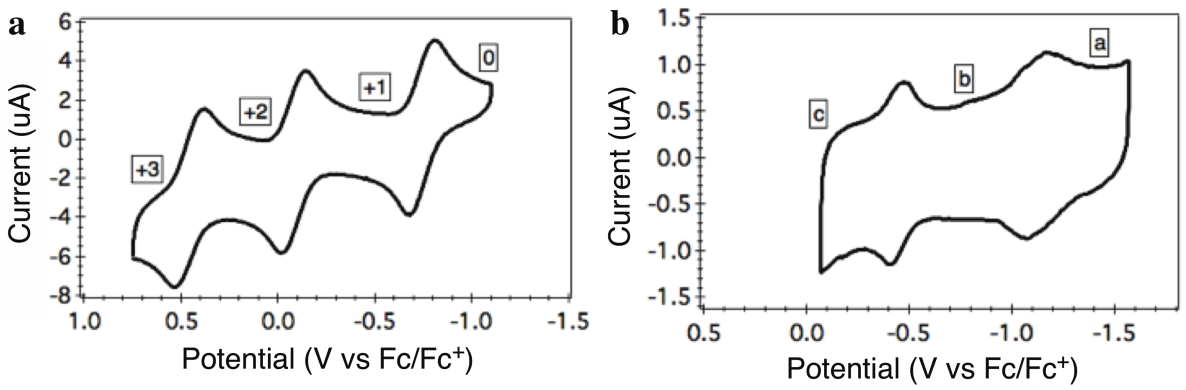

Figure 4.11. (a) Cyclic voltammogram of **1** in 0.1 M $TBAPF_6$ in tetrahydrofuran with a 150 mV/s scan rate. The superatom is neutral as synthesized and displays three reversible oxidations. (b) Solid-state cyclic voltammogram of $\mathbf{Tet_{2D}}$ crystals. A suspension of $\mathbf{Tet_{2D}}$ crystals in ether was dropcast onto the glassy carbon electrode and allowed to dry. The crystals stuck to the electrode surface. The electrode was immersed in a 0.1 M $TBAPF_6$ solution in tetrahydrofuran and the cyclic voltammogram was acquired as usual, with a 50 mV/s scan rate. The voltammogram is labeled a, b, and c and these events roughly align with states 0, +1, and +2 of **1** although they are slightly offset. The peaks are broad relative to those in a.

When we dropcast the exfoliated sheets onto a glassy carbon electrode, the cyclic voltammogram of the exfoliated $\mathbf{Tet_{2D}}$ sheets (Figure 4.7d) reveals that the redox properties of the superatom building block **1** persists within the sheets as they display three reversible oxidations. No material is released into the electrolyte solution during the cyclic voltammetry. The redox potentials of these exfoliated materials in solution are shifted towards slightly more negative values (- 0.2 V difference) relative to those of **1** in solution. We thus assign the oxidation states of the cluster within the sheets (labeled a through d in Figure 4.7d) as $\{Co_6Se_8\}^0$ through $\{Co_6Se_8\}^{3+}$, using the CV of **1** as a reference point. Another interesting feature of the CV of the electrodes that are covered with the 2D layers of $\mathbf{Tet_{2D}}$ is that these are permeable to the electrolyte. Analysis of bulk $\mathbf{Tet_{2d}}$ crystals revealed that the structure contains 43% solvent-accessible void space, predominantly in open channels oriented along [101].[49,50] The porosity of the bulk crystal is thus preserved upon exfoliation. The important finding is that $\mathbf{Tet_{2D}}$ sheets are solution processable, porous, and redox-active.

4.7. Conclusions

In summary, we have developed the reaction chemistry to create the hexatopic $Co_6Se_8[PEt_2(4\text{-}C_6H_4COOH)]_6$ superatom **1**. This superatom assembles into a three-dimensional solid that is held together by a hydrogen bond adhesive. We can change this adhesive from $2H^+$ to Zn^{2+} and create extended crystalline solids $\mathbf{Trig_{3D}}$ and $\mathbf{Tet_{2D}}$. A seemingly small change in the solvent system from DMF/methanol to DMF/ethanol yields remarkable changes in crystal morphology and structure, from a three-dimensional to a two-dimensional extended solid. Both solids are held together via zinc-carboxylate bonds. Two-dimensional $\mathbf{Tet_{2D}}$ can be chemically exfoliated to yield ultrathin yet soluble layers. These layers can be deposited from solution onto substrates. The sheets are redox-active, preserving the redox activity of their component superatoms. These types of porous, ultrathin, and redox-active sheets will find utility in a number of other applications such as modified electrodes for catalysis, batteries, and nanoscale electronic sieves.

4.8. General Synthesis Information

All reactions were performed in a nitrogen atmosphere using standard Schlenk techniques. Selenium powder and dicobalt octacarbonyl (stabilized with 1-5% hexane) were obtained from STREM Chemicals. All other reagents were purchased from Sigma-Aldrich. Chemicals were used without further purification. Anhydrous and anaerobic solvents were obtained from a Glass Contour solvent system consisting of a Schlenk manifold with purification columns packed with activated alumina and supported copper catalyst. DMF, ethanol, and methanol (used for framework synthesis) were purchased as anhydrous bottles, degassed, and stored over 4 Å molecular sieves in the glovebox. ^{1}H NMR spectra were recorded on a Bruker

DRX400 (400 MHz) or a Bruker DMX500 (500 MHz) spectrometer. ^{31}P NMR spectra were recorded on a Bruker DMX500 (500 MHz) spectrometer and referenced to phosphoric acid (H_3PO_4). ^{1}H NMR chemical shifts were referenced to residual protons in the NMR solvent.

Scanning electron microscopy (SEM) images were taken by a Zeiss SIGMA VP at 0.8 kV. The elemental analysis of framework materials was performed on a HITACHI S-4700 SEM equipped with energy dispersive X-ray spectrometer (EDX) analyses at 25 kV. Powder x-ray diffraction data was collected using a PANalytical X'Pert3 Powder diffractometer. Atomic force microscopy (AFM) images were acquired in ScanAsyst mode by a Bruker Dimension Icon system under ambient conditions. Cyclic voltammetry (CV) was performed on a CHI600C potentiostat using a 3 mm diameter glassy carbon working electrode, platinum counter electrode, and platinum pseudo-reference electrode. Measurements were calibrated using the ferrocene/ferrocenium redox couple. A 0.1 M solution of tetrabutylammonium hexafluorophosphate in either DCM or THF was used as the supporting electrolyte. All measurements were done under a dinitrogen atmosphere and at room temperature. Crystallographic data for all compounds was collected on an Agilent SuperNova diffractometer using mirror-monochromated Cu Kα radiation.

4.9. Synthetic Procedures and Characterization of Compounds

(a) (4-Bromophenyl)diethylphosphineselenide. n-BuLi (1.6 M in n-hexane, 20.0 mL, 32.05 mmol, 1.0 eq.) was added dropwise at -78ºC under N_2 to a stirred solution of 1,4-dibromobenzene (7.56 g, 32.05 mmol, 1.0 eq.) in anhydrous THF (90 mL). The mixture was stirred at -78ºC for 1 h and then chlorodiethylphosphine (4.00 g, 32.12 mmol, 1.0 eq.) was added dropwise. The resulting mixture was gradually warmed to room temperature overnight. The

solvent was removed in vacuo and anhydrous toluene was added to the reaction flask. The mixture was stirred for 1 h and Schlenk filtered via cannula transfer into a flask charged with selenium powder (3.00 g, 37.99 mmol, 1.2 eq.). This solution was stirred under N_2 at 60ºC for 1 h and filtered hot in air. The solution was dried *in vacuo* and the resulting yellow oil was subject to silica gel column chromatography (hexanes/dichloromethane 3:2) to yield (4-bromophenyl)diethylphosphineselenide as a clear off-white oil (8.347g, 80%). ^{1}H NMR (300 MHz, chloroform-*d*) δ 7.75 (dd, J = 11.7, 8.4 Hz, 2H), 7.62(dd, J = 8.5, 2.2 Hz, 2H), 2.21 (m, 4H), 1.11 (dt, J = 20.2, 7.5 Hz, 6H). ^{31}P NMR (202 MHz, chloroform-*d*) δ 43.53. FTIR (cm^{-1}): 2970, 2933, 1692, 1572, 1392, 1068, 1007, 815, 776.8. HRMS (FAB+): calculated for $C_{10}H_{15}BrPSe$ 322.9259, observed 322.9269.

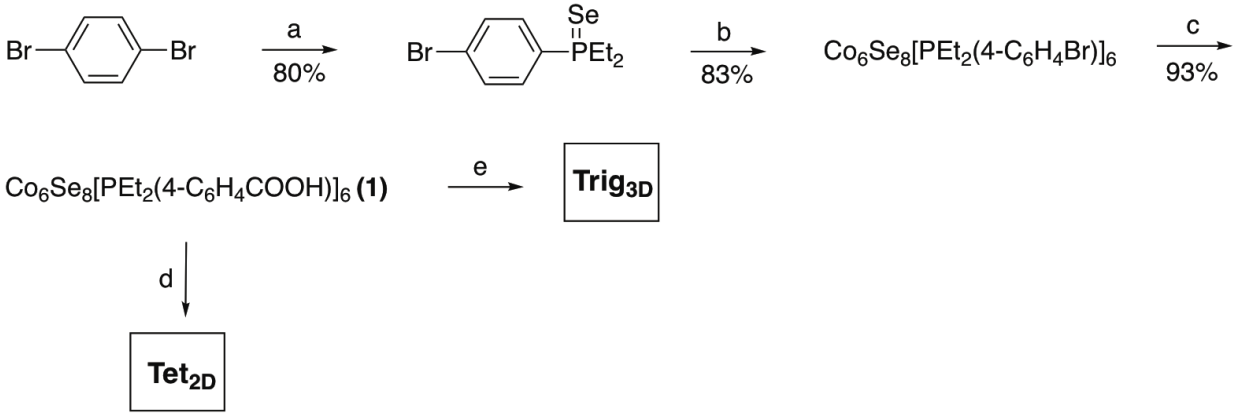

Scheme 4.1. Synthesis of $Trig_{3D}$ and Tet_{2D} frameworks from 1,4-dibromobenzene.

(b) $Co_6Se_8[PEt_2(4\text{-}C_6H_4Br)]_6$. (4-Bromophenyl)diethylphosphineselenide (2.039 g, 6.29 mmol, 4.2 eq.) was placed in a Schlenk flask under N_2 and dissolved in anhydrous toluene (20 mL). Dicobalt octacarbonyl (0.512 g, 1.50 mmol, 1 eq.), dissolved in 10 mL toluene, was added to the solution and the reaction was heated to 120°C for 24 hrs with a reflux condenser. The solvent was removed in vacuo and the solids were brought inside the glovebox. The oily product was dissolved in 15 mL toluene and filtered. The remaining dark brown solid was washed with

pentane and dried, yielding $Co_6Se_8[PEt_2(4\text{-}C_6H_4Br)]_6$ (1.014 g, 83 % based on $Co_2(CO)_8$). This cluster is red when dissolved. When the reaction is not complete, another species is present, $Co_4Se_2(CO)_6(PEt_2PhBr)_4$ (determined crystallographically) which is dark green in solution. ^{1}H NMR (500 MHz, benzene-d_6) δ 7.75 (d, 2H), 7.62(t, 2H), 2.01 (m, 4H), 0.91 (dt, 6H) ppm. ^{31}P NMR (161.9 MHz MHz, benzene-d_6) δ 57.95 (broad) ppm. Molecular structure displayed in Figure S1.

(c) $Co_6Se_8[PEt_2(4\text{-}C_6H_4COOH)]_6$ (1) $Co_6Se_8[PEt_2(4\text{-}C_6H_4Br)]_6$ (0.412 g, 0.17 mmol, 1 eq.) was placed in a Schlenk flask under N_2 and dissolved in anhydrous THF (40 mL). The solution was cooled to -78ºC and n-BuLi (2.5 M in n-hexane, 0.40 mL, 1.0 mmol, 6 eq.) was added dropwise over 5 minutes. The reaction was stirred for 15 minutes. Carbon dioxide was bubbled through the solution for 5 minutes. The reaction was kept at -78ºC for 30 minutes. The cold bath was removed and the reaction was warmed to room temperature over 1-2 h. The solvent was removed in vacuo. In the glovebox, the remaining reddish brown solids were triturated with diethyl ether, then THF. The solids were then suspended in 15 mL THF and acidified with 2M HCl in diethyl ether (2 mL). The deep red solution was filtered and the solvent was removed in vacuo. The remaining solid was triturated with diethyl ether and acetonitrile, then dried to yield **1** as a reddish brown solid (0.351 mg, 93%). ^{1}H NMR (500 MHz, THF-*d8*) δ 10.71 (s, 1H), 8.38-8.08 (m, 2H), 8.00 (dd, 2H), 2.26 (m, 4H), 1.11 (dt, 6H). ^{31}P NMR (202 MHz, d_8-THF) δ 43.99. FTIR (cm^{-1}): 3000-2700 (br-OH), 2974, 1692, 1423, 1294,1095, 1013, 922, 858. Molecular structure displayed in Figure S2.

(e) $Trig_{3D}$. Compound **1** (20 mg, 8.90 mmol, 1 eq.) was dissolved in 5 mL DMF. Zinc nitrate

hexahydrate (13 mg, 43.70 mmol, 4.9 eq.) was dissolved in 5 mL MeOH. The two solutions were mixed, filtered and placed in a 20 mL scintillation vial. The vial was sonicated for 5 minutes, placed in an oven, and heated to 65 ºC for 24 hours. After cooling to room temperature the supernatant was removed and the hexagonal crystals were washed with fresh DMF. Ethyl ether was added to the vial, and the vial was sonicated briefly to remove crystals from the vial walls. The ether was discarded and the crystals were dried under vacuum and then collected. Yield: 13 mg.

(d) $\mathbf{Tet_{2D}}$. Compound **1** (20 mg, 8.90 mmol, 1 eq.) was dissolved in 5 mL DMF. Zinc nitrate hexahydrate (13 mg, 43.70 mmol, 4.9 eq.) was dissolved in 5 mL EtOH. A 5 mM stock solution of HCl in EtOH was prepared from a 2M HCl solution in diethyl ether. 0.4 mL of the 5 mM HCl solution was added to the zinc solution. (We note that a small fraction of $\mathbf{Trig_{3D}}$ forms under these conditions without HCl, but can eliminated with the addition of "extra" protons in the form of HCl in the reaction). The two solutions were mixed, filtered and placed in a 20 mL scintillation vial. The vial was sonicated for 5 minutes, placed in an oven, and heated to 65 ºC for 24 hours. After cooling to room temperature the supernatant was removed and the cubic crystals were washed with fresh DMF. Ethyl ether was added to the vial, and the vial was sonicated briefly to remove crystals from the vial walls. The ether was discarded and crystals were dried under vacuum then collected. Yield: 8 mg.

4.10. Powder X-ray Diffraction of Frameworks

Powder XRD of each sample **Trig$_{3D}$** and **Tet$_{2D}$** shows homogeneous crystalline phases (Figures 4.11 and 4.12 below).

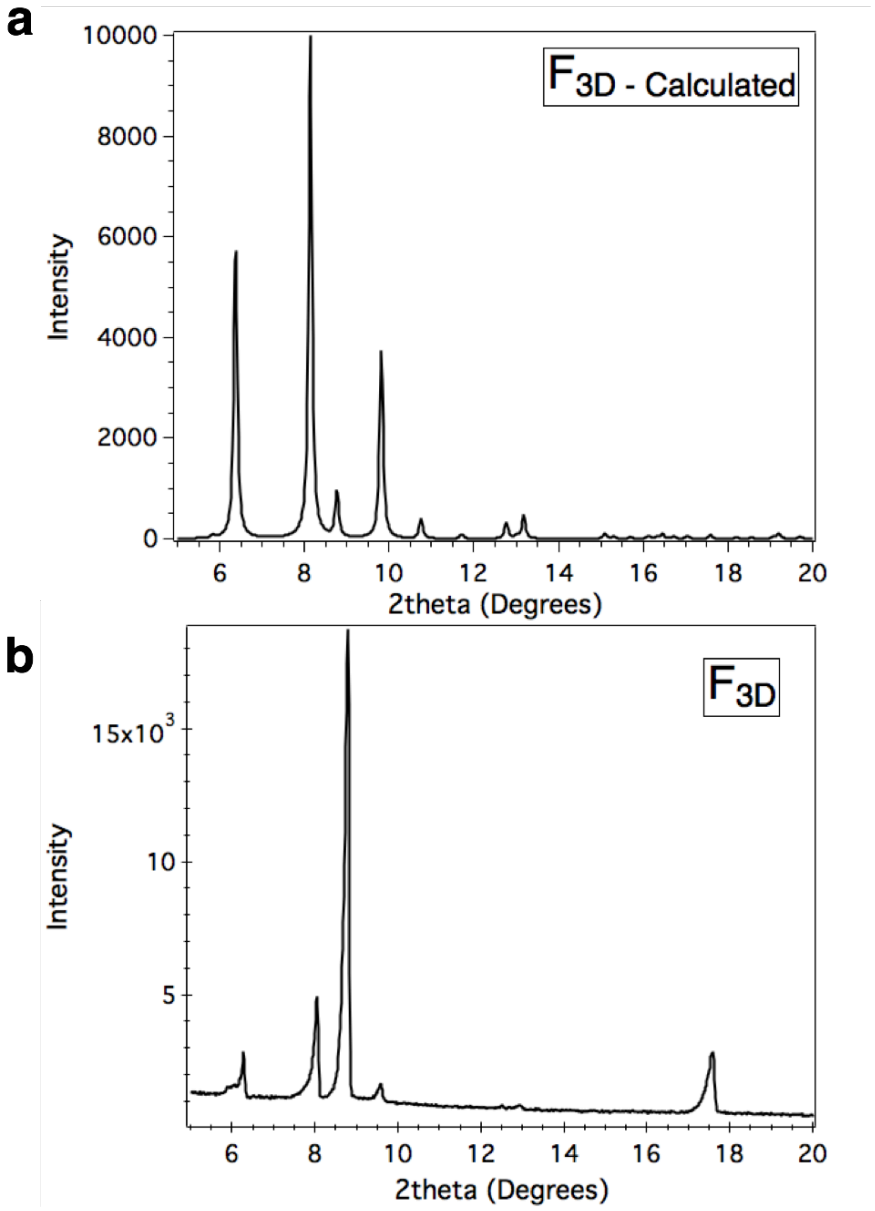

Figure 4.12. (a) Calculated powder XRD pattern of **Trig$_{3D}$** hexagonal plates from single crystal data. (b) Powder XRD of **Trig$_{3D}$** hexagonal plates. The samples were dispersed on a sample holder without grinding and therefore the intensities are strongly affected by preferred orientation. The peak positions are in good agreement with the simulated powder patterns generated from the SCXRD data and confirm the identity and phase purity of the samples. We

note that the simulated patterns were generated from SCXRD run at 100 K, while the PXRD patterns were collected at room temperature, and that some of the solvates are removed from the crystal lattice under ambient conditions.

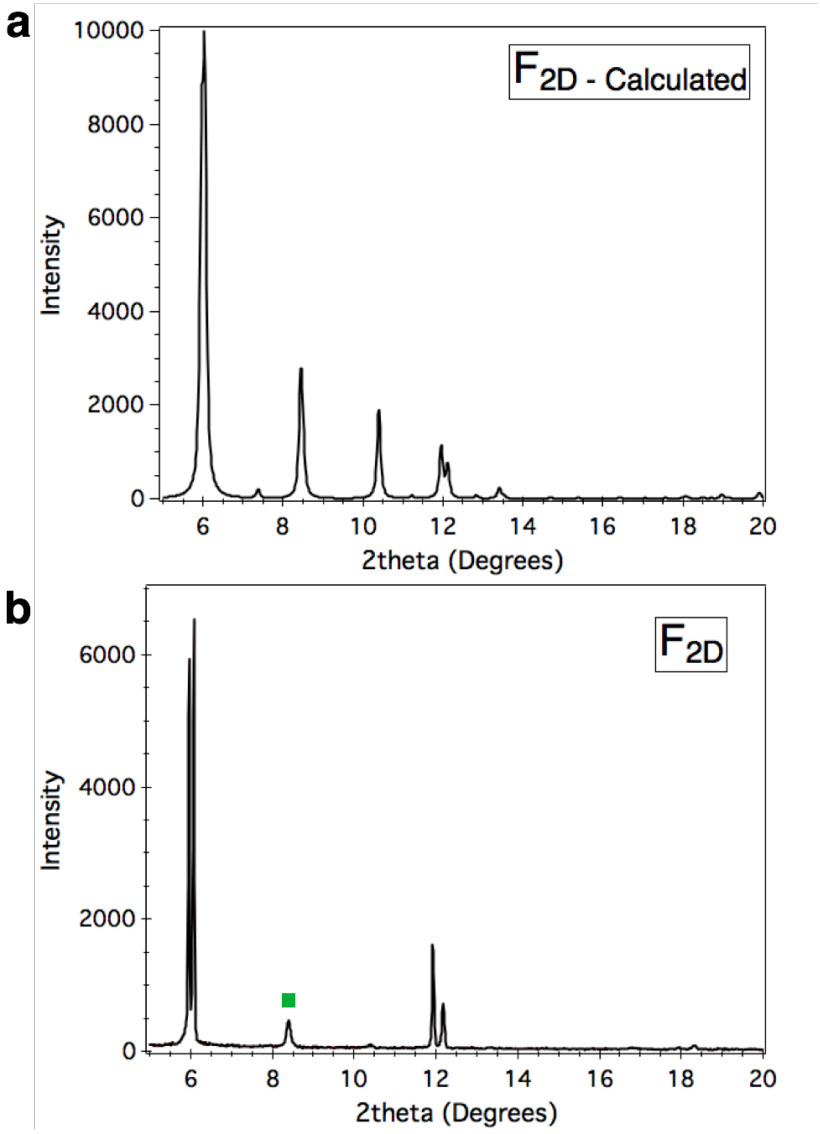

Figure 4.13. (a) Calculated powder XRD pattern of **Tet$_{2D}$** cubes from single crystal data. (b) Powder XRD spectrum of **Tet$_{2D}$** cubes. The samples were dispersed on a sample holder without grinding and therefore the intensities are strongly affected by preferred orientation. Peak positions are in good agreement with the simulated powder patterns generated from the SCXRD data and confirm the identity and phase purity of the samples (the green dot is from **Trig$_{3D}$** impurity present in sample). We note that the simulated patterns were generated from SCXRD run at 100 K, while the PXRD patterns were collected at room temperature, and that some of the solvates are removed from the crystal lattice under ambient conditions.

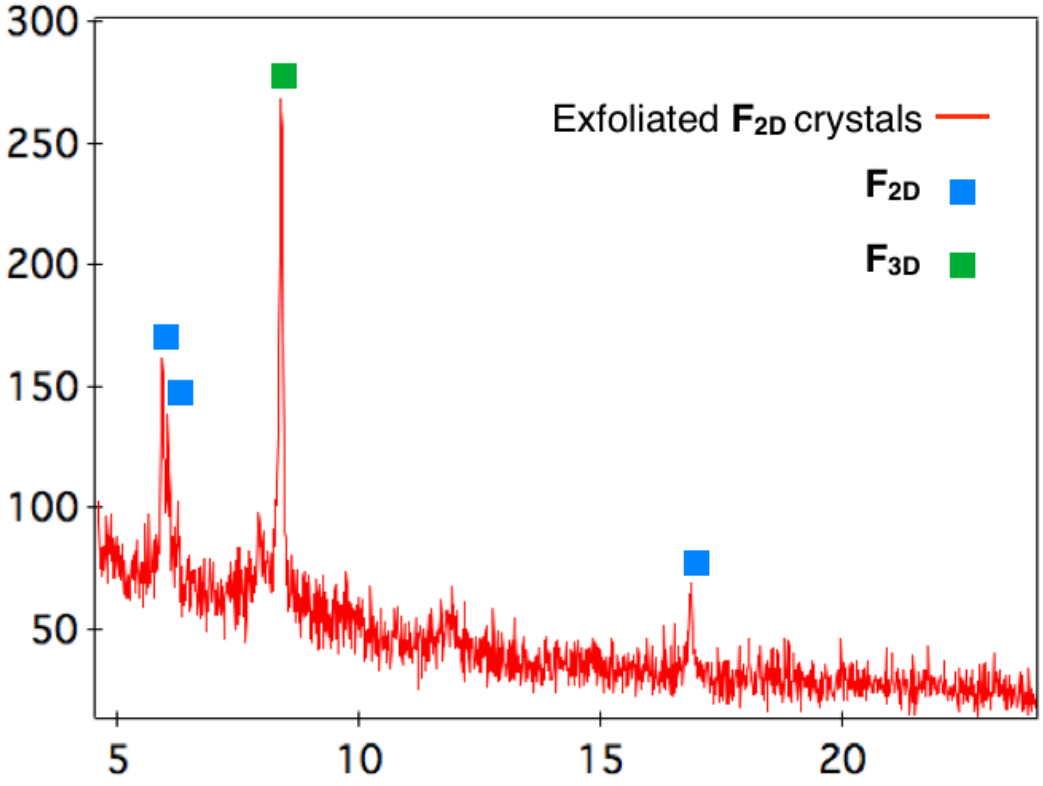

Figure 4.14. Powder XRD spectrum showing the exfoliation of $\mathbf{Tet_{2D}}$ cubes upon immersion in 40 mM benzoic solution in DMF. The initial spectrum of intact $\mathbf{Tet_{2D}}$ crystals is shown in Figure 4.12b. The blue squares highlight the peaks corresponding to $\mathbf{Tet_{2D}}$, whereas the green square highlights traces of $\mathbf{Trig_{3D}}$ present in the as synthesized sample (PXRD spectrum of $\mathbf{Trig_{3D}}$ is shown in Figure 4.11b). A few drops of 40 mM benzoic solution in DMF were added to the crystals directly onto the powder plate. The colorless solution turned a light brown-red color and the cubes become less visible by eye. After 10 minutes, the liquid was removed by syringe and the resulting diffraction was obtained (red trace). Peaks corresponding to $\mathbf{Tet_{2D}}$ have become less intense relative to $\mathbf{Trig_{3D}}$ peaks. Since $\mathbf{Trig_{3D}}$ is a 3D network, we do not expect to be able to exfoliate this material and the crystals should not fall apart under these conditions, as is observed.

4.11. Single Crystal X-ray Diffraction

Data for all compounds was collected on an Agilent SuperNova diffractometer using mirror-monochromated Cu Kα radiation. Crystals were mounted on Mitegen polymer loops with the aid of Paratone oil and cooled on the diffractometer using a Cryostream 700 cooler. Data collection, integration, scaling (ABSPACK) and absorption correction (face-indexed Gaussian integration[13] or numeric analytical methods[14]) were performed in CrysAlisPro.[15] Structure solution was performed using ShelXT[16] or SuperFlip.[17] Subsequent refinement was performed by full-matrix least-squares on F^2 in ShelXL. Olex2[18] was used for viewing and to prepare CIF files. PLATON[19] was used extensively for SQUEEZE,[20] ADDSYM[21] and TwinRotMat. ORTEP graphics were prepared in CrystalMaker.[22] Thermal ellipsoids are rendered at the 50% probability level.

Crystal data for all compounds is provided in Table 4.1 below. The refinements of **1** and $\mathbf{Co_6Se_8[PEt_2(4\text{-}C_6H_4Br)]_6}$ were routine. The structure determinations of $\mathbf{Tet_{2D}}$ and $\mathbf{Trig_{3D}}$ were quite challenging due to twinning, pseudosymmetry and disorder; the refinements are described in detail below.

Crystal structure of $\mathbf{Tet_{2D}}$. Crystals of $\mathbf{Tet_{2D}}$ lost their solvent easily when standing in Paratone, so the crystal was continuously cooled by dry ice on the microscope slide and by a Thermos of liquid nitrogen when transferring to the cold stream. The diffraction also appeared to deteriorate at 100 K, and the best data set was collected at 230 K. A full sphere of data were collected to 0.87 Å resolution, although the data set was ultimately truncated at 1.0 Å.

The diffraction pattern clearly showed a threefold non-merohedral twin. The pattern was indexed on a tetragonal unit cell with a=20.9 Å; c=14.6 Å. With this indexing, the threefold twin axis was *hkl*=201 or *uvw*=101. The degree of overlap was modest and therefore merging statistics and systematic absences were easily assessed. This initially suggested a structure in P4/nmm or twinned P4/n.

Structure solution was attempted on the isolated reflections of one component. Solutions were attempted using Superflip and ShelXT. ShelXT failed to provide a usable solution when assuming any of 4/mmm, 4/m, mmm, 2/m, 2/m11, and 112/m symmetry. Superflip occasionally (1-2 attempts out of 10) provided solutions in either P4/n or P11n that showed some recognizable features, essentially a layered structure with a Co6Se8-sized jumble and a pair of atoms at a typical Zn-Zn 4-bladed paddlewheel distance with the paddlewheel axis aligned with the crystallographic fourfold axis.

We proceeded with the solution in P4/n, placing a rigid $Co_6Se_8P_6$ fragment on a -4 site as suggested by the Superflip solution. In this model, the cluster is disordered over four symmetry-related positions and therefore was placed in PART -1.

At this point, we recalled that the merging statistics had indicated 4/mmm was the point group. A model in P4/n therefore should be a perfect merohedral twin. We introduced a twofold rotation around 110 as a twin law. An obstacle here was the fact that ShelXL handles non-merohedral (HKLF 5) or merohedral (TWIN) twinning but not both simultaneously. We prepared a Python script (see below) that takes an input HKLF 4 or 5 file, transforms each reflection by one or more twin laws, and returns an HKLF 5 file that may implement either several independent merohedral twin operators or simultaneous merohedral and non-merohedral twinning.

For a model in P4/n containing a $Co_6Se_8P_6$ cluster on a -4 site and two Zn atoms on a fourfold axis, different twinning models had the following effect: "detwinned" HKLF 4 from CrysAlisPro: R1=50%. HKLF 4 with twofold merohedral twinning: R1=39%. HKLF 5: R1=35%. HKLF 5 plus twofold merohedral twinning: R1=29%.

We looked for a fully ordered model by removing the fourfold axis around which the cluster is disordered in P4/n. This gives a model in polar P11n, interestingly the space group that Superflip suggested in some attempted solutions. The fourfold axis remains as a twin law, but only has to be applied once because refining 2[001] as a twin law in point group ..m is equivalent to refining the Flack parameter. The model in polar P11n, with 11 independent twin volume fractions, refines to R1=16%.

Finally we noted that Co_6Se_8 clusters typically crystallize on inversion centers and that a four-bladed Zn_2 paddlewheel can also fit on an inversion center. Therefore we transformed the model into P2/n by moving the origin to place the cluster and Zn_2 dimer on inversion centers and deleting inversion-related atoms. The centrosymmetric model also refined to R1=16% and therefore is preferred.

Inspection of difference maps did not give any indication of light atom positions, but it was possible to deduce the positions of 2 out of the 3 independent phosphine $C_6H_4CO_2$ fragments by orienting them toward adjacent Zn_2 nodes. This improved the refinement stability enough to remove the rigid-body constraint on the heavy-atom cluster core and anisotropically refine Co, Se, and P atoms. At this point, a final heavy atom was located between the cluster layers and tentatively identified as Zn. Fourier maps clearly showed the final $C_6H_4CO_2$ group pointing toward this atom.

We proceeded to locate all phosphine C_2H_5 groups by a combination of difference maps and trial and error. Anisotropic ADPs for the heavy atoms and individual isotropic ADPs for C and O were reasonably well behaved. Hydrogen atoms were placed in calculated positions and refined with riding coordinates and ADPs. Disordered solvent was modeled as a diffuse contribution to the overall scattering by the use of SQUEEZE. 5 iterations of the SQUEEZE procedure were required before the final electron count converged.

In the final refinement, all 12 twin orientations were occupied with volume fractions between 5.92(9) % and 13.39(10) %. We note that the determination of a 12-fold twinned structure is extremely unusual. We found only one previous example[23] of a successfully determined structure from a 12-fold twin.

Crystal structure of $Trig_{3D}$. *Note about the deposited cif files for* ***$Trig_{3D}$***: F3d.cif is the model from the refinement, in which the entire structure is disordered by symmetry over an inversion center in I2/a. This is difficult to view, so we prepared the file F3d-ordered.cif in which the structure is ordered in Ia and therefore can be grown normally. This is optimal for viewing but it is important to note that the true structure is disordered.

The data (cell metric and merging statistics) were consistent with a rhombohedral structure, and the structure was initially solved in R-3c. In R-3c, two Zn atoms lie on a threefold axis and are coordinated symmetrically by three μ^2-carboxylates in a three-bladed paddlewheel arrangement. This moiety collides with its own symmetry equivalent and has a significant positive Fourier feature between the two Zn atoms. This suggested a model in which a trinuclear Zn_3 moiety is disordered by symmetry over a twofold axis in R-3c. However, on closer inspection, the third Zn atom was located a small distance from the threefold axis. This requires

that a model in R-3c must be additionally disordered by symmetry around the threefold axis. Therefore, the symmetry was lowered to monoclinic I2/a, a subgroup of R-3c.

In I2/a, the trinuclear Zn_3 moiety is still disordered by symmetry around a twofold axis perpendicular to the Zn-Zn-Zn axis. In addition, in view of the good merging statistics for trigonal symmetry, the threefold axis of the rhombohedral lattice was preserved as a threefold pseudomerohedral twin law.

The geometry of the $Co_6Se_8P_6$ core of the cluster required some restraints to behave in the refinement. All chemically equivalent 1,2- and 1,3- distances were made equivalent with "floating" DFIX restraints. Anisotropic ADPs were refined but required RIGU and SIMU restraints.

The three μ^2-carboxylates of the three-bladed paddlewheel were retained in the monoclinic model; their positions were now independent and were restrained with DFIX or SADI instructions for intramolecular geometry and with soft DFIX restraints for all Zn-O distances. The three carboxylates associated with the third Zn atom were located with difficulty. The displacement of atom Zn3 away from the pseudo-threefold axis creates two shorter P…Zn distances of about 8.2 Å and one longer P…Zn distance of about 8.8 Å. By trial and error we found that $C_6H_4CO_2$ fragments bound η^2 (chelating) to Zn3 fit the shorter P…Zn distances and another $C_6H_4CO_2$ bound μ^2 (bridging) to Zn2 and Zn3 fit the longer P…Zn distance. At this stage, all six carboxylates bound to the Zn_3 node had been located, but restraints on all Zn-O distances were required and several anti-bumping restraints were employed to prevent unrealistically small O-Zn-O angles. Additionally, the light-atom skeletons of the $C_6H_4CO_2$ ligands were stabilized with rigid-body constraints for the phenyl rings and FLAT and DFIX/SADI restraints.

Phosphine ethyl groups were located in difference maps and subsequently refined with all 1,2- and 1,3- distances restrained. Several terminal methyl positions were unstable and ultimately required a combination of anti-bumping restraints and a weak DAMP instruction for the least-squares refinement.

All C and O atoms were refined with a single group isotropic ADP in view of the weak data, twinning and pseudosymmetry. Hydrogen atoms were placed in calculated positions and refined with riding coordinates and ADPs.

Zn3 displays a large and unusually shaped displacement ellipsoid that is likely a sign of unresolved disorder. We were not able to construct an explicit disorder model and therefore have left the unusual ellipsoid as is.

Several voids in the structure were filled with diffuse electron density that could not be modeled explicitly. This was treated by SQUEEZE to model the disordered solvent as a diffuse contribution to the overall scattering without specific atomic positions.

Table 4.1. Crystallographic data for all compounds.

Compound	**Tet_{2D}**	**$Trig_{3D}$**	**1-H**	**$Co_6Se_8(PEt_2C_6H_4Br)_6$**
Formula	$C_{66}H_{84}Co_6O_{14}P_6Se_8Zn_3$	$C_{67}H_{87}Co_6O_{13}P_6Se_8Zn_3$	$C_{66}H_{90}Co_6O_{12}P_6Se_8$	$C_{60}H_{84}Br_6Co_6P_6Se_8$
MW	2468.52	2467.55	2246.45	2455.81
Space group	P2/n	I2/a	P-3	Pbca
***a* (Å)**	20.9263(19)	22.6974(10)	11.9463(2)	19.8484(8)
***b* (Å)**	14.5590(16)	17.9931(7)	11.9463(2)	19.5785(9)
***c* (Å)**	20.9375(19)	28.9694(14)	16.8522(3)	20.0741(8)
***α* (°)**	90	90	90	90
***β* (°)**	89.983(7)	106.838(5)	90	90
***γ* (°)**	90	90	120	90
V (Å^3)	6378.9(11)	11323.8(9)	2082.83(8)	7800.8(6)
Z	2	4	1	4

ϱ_{calc} (g cm^{-3})	1.285	1.447	1.791	2.091
T (K)	230	140	100	140
λ (Å)	1.54184	1.54184	1.54184	1.54184
$2\theta_{min}$, $2\theta_{max}$	8, 101	8, 91	8, 143	8, 147
Nref	83846	21826	8833	44828
R(int), R(σ)	.105, .1353	.0935, .0736	.0325, .0333	.1221, .0809
μ(mm^{-1})	10.183	11.466	14.659	19.071
Size (mm)	.07 x .05 x .05	.06 x .05 x .02	.06 x .05 x .03	.06 x .05 x .03
T_{max}, T_{min}	.685, .587	.825, .609	.739, .539	.705, .462
Data	17119	4899	2703	7767
Restraints	382	1449	1	0
Parameters	277	387	154	394
R_1(obs)	0.0578	0.0859	0.0264	0.0759
wR_2(all)	0.1252	0.2682	0.0637	0.2117
S	0.932	1.047	1.063	1.069
Peak, hole (e$^-$ Å^{-3})	0.74, -0.62	0.63, -0.47	0.44, -0.42	2.44, -2.13

4.12. References

1. (a) Novoselov, K. S.; Jiang, D.; Schedin, F.; Booth, T. J.; Khotkevich, V. V.; Morozov, S. V.; Geim, A. K., *Proc. Natl. Acad. Sci. USA* 2005, *102* (30), 10451-10453; (b) Novoselov, K. S.; Geim, A. K.; Morozov, S. V.; Jiang, D.; Zhang, Y.; Dubonos, S. V.; Grigorieva, I. V.; Firsov, A. A., *Science* 2004, *306* (5696), 666-669.

2. (a) Walter, M.; Akola, J.; Lopez-Acevedo, O.; Jadzinsky, P. D.; Calero, G.; Ackerson, C. J.; Whetten, R. L.; Gronbeck, H.; Hakkinen, H., *Proc. Natl. Acad. Sci. USA* 2008, *105* (27), 9157-9162; (b) Khanna, S. N.; Jena, P., *Phys. Rev. B* 1995, *51* (19), 13705-13716; (c) Luo, Z. X.; Castleman, A. W., *Acc. Chem. Res.* 2014, *47* (10), 2931-2940; (d) Chauhan, V.; Reber, A. C.; Khanna, S. N., *J. Phys. Chem. A* 2016, *120* (33), 6644-6649; (e) Chauhan, V.; Reber, A. C.; Khanna, S. N., *J. Am. Chem. Soc.* 2017, *139* (5), 1871-1877; (f) Chauhan, V.; Sahoo, S.; Khanna, S. N., *J. Am. Chem. Soc.* 2016, *138* (6), 1916-1921.

3. (a) Champsaur, A. M.; Velian, A.; Paley, D. W.; Choi, B.; Roy, X.; Steigerwald, M. L.; Nuckolls, C., *Nano Lett.* 2016, *16* (8), 5273-5277; (b) Choi, B.; Yu, J.; Paley, D. W.; Trinh, M. T.; Paley, M. V.; Karch, J. M.; Crowther, A. C.; Lee, C. H.; Lalancette, R. A.; Zhu, X. Y.; Kim, P.; Steigerwald, M. L.; Nuckolls, C.; Roy, X., *Nano Lett.* 2016, *16* (2), 1445-1449; (c) Tulsky, E. G.; Crawford, N. R. M.; Baudron, S. A.; Batail, P.; Long, J. R., *J. Am. Chem. Soc.* 2003, *125*

(50), 15543-15553; (d) Turkiewicz, A.; Paley, D. W.; Besara, T.; Elbaz, G.; Pinkard, A.; Siegrist, T.; Roy, X., *J. Am. Chem. Soc.* 2014, *136* (45), 15873-15876.

4. (a) Jin, S.; DiSalvo, F. J., *Chem. Mater.* 2002, *14* (8), 3448-3457; (b) Selby, H. D.; Roland, B. K.; Zheng, Z. P., *Acc. Chem. Res.* 2003, *36* (12), 933-944; (c) Welch, E. J.; Long, J. R., *Prog. Inorg. Chem.* 2005, *54*, 1-45; (d) Naumov, N. G.; Virovets, A. V.; Sokolov, M. N.; Artemkina, S. B.; Fedorov, V. E., *Angew. Chem. Int. Ed.* 1998, *37* (13-14), 1943-1945; (e) Beauvais, L. G.; Shores, M. P.; Long, J. R., *Chem. Mater.* 1998, *10* (12), 3783-+; (f) Shores, M. P.; Beauvais, L. G.; Long, J. R., *J. Am. Chem. Soc.* 1999, *121* (4), 775-779.
5. (a) Yoon, B.; Luedtke, W. D.; Barnett, R. N.; Gao, J. P.; Desireddy, A.; Conn, B. E.; Bigioni, T.; Landman, U., *Nat. Mater.* 2014, *13* (8), 807-811; (b) Dong, A. G.; Chen, J.; Vora, P. M.; Kikkawa, J. M.; Murray, C. B., *Nature* 2010, *466* (7305), 474-477; (c) Roy, X.; Lee, C. H.; Crowther, A. C.; Schenck, C. L.; Besara, T.; Lalancette, R. A.; Siegrist, T.; Stephens, P. W.; Brus, L. E.; Kim, P.; Steigerwald, M. L.; Nuckolls, C., *Science* 2013, *341* (6142), 157-160; (d) Auyeung, E.; Cutler, J. I.; Macfarlane, R. J.; Jones, M. R.; Wu, J. S.; Liu, G.; Zhang, K.; Osberg, K. D.; Mirkin, C. A., *Nat. Nano.* 2012, *7* (1), 24-28.

6. (a) Li, H.; Eddaoudi, M.; O'Keeffe, M.; Yaghi, O. M., *Nature* 1999, *402* (6759), 276-279; (b) Jia, J. T.; Sun, F. X.; Fang, Q. R.; Liang, X. Q.; Cai, K.; Bian, Z.; Zhao, H. J.; Gao, L. X.; Zhu, G. S., *Chem. Comm.* 2011, *47* (32), 9167-9169; (c) Long, J. R.; Yaghi, O. M., *Chem. Soc. Rev.* 2009, *38* (5), 1213-1214; (d) Furukawa, H.; Cordova, K. E.; O'Keeffe, M.; Yaghi, O. M., *Science* 2013, *341* (6149), 974; (e) Darago, L. E.; Aubrey, M. L.; Yu, C. J.; Gonzalez, M. I.; Long, J. R., *J. Am. Chem. Soc.* 2015, *137* (50), 15703-15711; (f) Das, M. C.; Xiang, S. C.; Zhang, Z. J.; Chen, B. L., *Angew. Chem. Int. Ed.* 2011, *50* (45), 10510-10520; (g) Humphrey, S. M.; Allan, P. K.; Oungoulian, S. E.; Ironside, M. S.; Wise, E. R., *Dalton Trans.* 2009, (13), 2298-2305; (h) Ding, N.; Armatas, G. S.; Kanatzidis, M. G., *J. Am. Chem. Soc.* 2010, *132* (19), 6728-6734; (i) Li, S. S.; Chen, Y. S.; Mulfort, K. L., *CrystEngComm.* 2015, *17* (5), 1005-1009; (j) Zheng, S. T.; Zhao, X.; Lau, S.; Fuhr, A.; Feng, P. Y.; Bu, X. H., *J. Am. Chem. Soc.* 2013, *135* (28), 10270-10273; (k) D'alessandro, D. M., *Chem. Comm.* 2016, *52* (58), 8957-8971; (l) Zhuang, G. L.; Chen, W. X.; Zhao, H. X.; Kong, X. J.; Long, L. S.; Huang, R. B.; Zheng, L. S., *Inorg. Chem.* 2011, *50* (9), 3843-5; (m) Nguyen, H. L.; Gandara, F.; Furukawa, H.; Doan, T. L. H.; Cordova, K. E.; Yaghi, O. M., *J. Am. Chem. Soc.* 2016, *138* (13), 4330-4333; (n) Qin, J. S.; Du, D. Y.; Guan, W.; Bo, X. J.; Li, Y. F.; Guo, L. P.; Su, Z. M.; Wang, Y. Y.; Lan, Y. Q.; Zhou, H. C., *J. Am. Chem. Soc.* 2015, *137* (22), 7169-7177; (o) Sheberla, D.; Sun, L.; Blood-Forsythe, M. A.; Er, S.; Wade, C. R.; Brozek, C. K.; Aspuru-Guzik, A.; Dinca, M., *J. Am. Chem. Soc.* 2014, *136* (25), 8859-8862; (p) Sun, L.; Campbell, M. G.; Dinca, M., *Angew. Chem. Int. Ed.* 2016, *55* (11), 3566-3579; (q) Sun, L.; Hendon, C. H.; Minier, M. A.; Walsh, A.; Dinca, M., *J. Am. Chem. Soc.* 2015, *137* (19), 6164-6167; (r) Jeon, I. R.; Harris, T. D., *Chem. Comm.* 2016, *52* (5), 1006-1008.

7. (a) Roy, X.; Schenck, C. L.; Ahn, S.; Lalancette, R. A.; Venkataraman, L.; Nuckolls, C.; Steigerwald, M. L., *Angew. Chem. Int. Ed.* 2012, *51* (50), 12473-12476; (b) Stuczynski, S. M.; Kwon, Y. U.; Steigerwald, M. L., *J. Organomet. Chem.* 1993, *449* (1-2), 167-172; (c) Choi, B.; Capozzi, B.; Ahn, S.; Turkiewicz, A.; Lovat, G.; Nuckolls, C.; Steigerwald, M. L.; Venkataraman, L.; Roy, X., *Chem. Sci.* 2016, *7* (4), 2701-2705.

8. (a) Hou, L.; Zhang, J. P.; Chen, X. M., *Cryst. Growth Des.* 2009, *9* (5), 2415-2419; (b) Adam D. Martin, T. L. E., Stephen P. Argent, William Lewis, Alexander J. Blake, Martin Schröder, *CrystEngComm*. 2017, *19*, 603-607.

9. The Cambridge Structural Database was searched using Conquest (I. J. Bruno, J. C. Cole, P. R. Edington, M. Kessler, C. F. Macrae, P. McCabe, J. Pearson, R. Taylor. Acta Cryst. B58, 2002, 389-397) to identify 3855 examples of Zn2 units bridged by carboxylates. The average Zn-O distance is 2.02 ± .09 Å.
10. Vagin, S.; Ott, A.; Weiss, H. C.; Karbach, A.; Volkmer, D.; Rieger, B., *Eur. J. Inorg. Chem.* 2008, (16), 2601-2609.

11. The Cambridge Structural Database was searched using Conquest [ref: I. J. Bruno, J. C. Cole, P. R. Edington, M. Kessler, C. F. Macrae, P. McCabe, J. Pearson, R. Taylor. Acta Cryst. B58, 2002, 389-397.] to identify 140 examples of Zn(O2CR)2(L)2 complexes where the carboxylates are eta2 and the L ligands bind through O or N. Among these examples, the average angle between the two O2CR ligands (measured C-Zn-C) is 115 ± 12 °. The average Zn-O distance (each bond measured individually) is 2.21 ± 0.18 Å and the average after taking the mean of all four bonds in a single molecule is 2.21 ± .05 Å. Therefore, the RCO2-Zn-O2CR angle of 119° and Zn-O distances of 2.14 and 2.37 Å are consistent with previously reported structures.

12. (a) Vandersluis, P.; Spek, A. L., *Acta Crystallogr. A* 1990, *46*, 194-201; (b) Spek, A. L., *Acta Crystallogr. D* 2009, *65*, 148-155.

13. Blanc, E.; Schwarzenbach, D.; Flack, H. D. *J. Appl. Cryst.* **24** (1991), 1035-1041.

14. Clark. R. C.; Reid, J. S. *Acta Cryst.* **A51** (1995), 887-897.

15. Version 1.171.37.35 (2014). Oxford Diffraction /Agilent Technologies UK Ltd, Yarnton, England.

16. Sheldrick, G. M. *Acta Cryst.* **A71** (2015), 3-8.

17. Palatinus, L.; Chapuis, G. SUPERFLIP. *J. Appl. Cryst.* **40** (2007), 786-790.

18. Dolomanov, O. V.; Bourhis, L. J.; Gildea, R. J.; Howard, J. A. K.; Puschmann, H. *J. Appl. Cryst.* **42** (2009), 339-341.

19. Spek, A. *Acta Cryst.* **D65** (2009), 148-155.

20. Van der Sluis, P.; Spek, A. L. *Acta Cryst.* **A46** (1990), 194-201.

21. Le Page, Y. *J. Appl. Cryst.* **21** (1988), 983.

22. CrystalMaker Software Ltd, Oxford, England *(www.crystalmaker.com)*.

23. Onoda, M.; Chen, X.-A.; Kato, K.; Sato, A.; Wada, H. *Acta Cryst.* **B55** (1999), 721-725.

Chapter 5. Superatom Fusion and the Nature of Quantum Confinement

5.1. Preface

This chapter is based on a published manuscript entitled "Superatom Fusion and the Nature of Quantum Confinement" by Anouck M. Champsaur, Taylor J. Hochuli, Daniel W. Paley, Colin Nuckolls, and Michael L. Steigerwald (*Nano Letters*, Article ASAP, June 2018). I synthesized and characterized all compounds. Taylor Hochuli helped synthesize compounds. Daniel Paley finalized all crystallographic refinements. Michael Steigerwald performed all theoretical calculations.

5.2. Abstract

Quantum confinement endows colloidal semiconducting nanoparticles with many fascinating and useful properties, yet a critical limitation has been the lack of atomic precision in their size and shape. We demonstrate the emergence of quantum confined behavior for the first time in atomically defined $Co_6Se_8(PEt_3)_6$ superatoms by dimerizing $[Co_6Se_8]$ units through direct fusion. To accomplish this dimerization, we install a reactive carbene on the $[Co_6Se_8]$ core to create a latent fusion site. Then we transform the reactive carbene intermediate into a material with an expanded core, $[Co_{12}Se_{16}]$, that exhibits electronic and optical properties distinct from the parent monomer. The chemical transformation presented herein allows for precise synthetic control over the ligands and size of these clusters. We show by cyclic voltammetry, infrared spectroscopy, single crystal X-ray diffraction, and density functional theory calculations that the resulting fused $[Co_{12}Se_{16}]$ material exhibits strong electronic coupling and electron delocalization. We observe a bandgap reduction upon expanding the cluster core, suggesting that we have isolated a new intermediate in route to extended solids. These results are further corroborated with electronic structure calculations of a monomer, fused dimer, trimer and

tetramer species. These reactions will allow for the synthesis of extended highly delocalized wires, sheets, and cages.

5.3. Introduction

We describe an unprecedented reaction sequence that fuses metal chalcogenide clusters to yield electronically strongly coupled dimers. This fusion is an early step in the formation of an extended CoSe solid. A combination of electronic structure data and calculations indicates that the strong coupling between the dimer lobes can be interpreted as the onset of band-like behavior. Furthermore, the electronic and optical properties of the fused dimer are drastically different from the parent monomer, whereas a similarly sized bridged dimer material exhibits the same (additive) electronic and optical properties as the monomer. We thus observe the manifestation of quantum size effects in that the bandgap decreases as the size of the nanostructures increases upon fusion.

The metal-chalcogenide clusters fundamental to this study are members of a larger class of clusters with the $[M_6E_8]$ stoichiometry (M = metal, E = chalcogen) that are building blocks for extended materials.[1] Some such clusters are constituent fragments of traditional, inorganic materials with unusual properties such as superconductivity and ferromagnetism (e.g., Chevrel and Zintl phases);[2] while in other cases, clusters with this core stoichiometry have been converted into extended solids in which the $[M_6E_8]$ building block is significantly distorted.[3] The Co_6Se_8 clusters belong to the latter family, and we recently found that we could modify the ligand environment around this core to include designed, stoichiometrically and stereochemically precise combinations of phosphine and CO groups (Figure 5.1a).[4] We have shown that the CO ligand is preferentially labile in these clusters, and it can be replaced photochemically with two-

electron donors such as isonitriles and phosphines to yield, for example, the diisonitrile-bridged dimer shown in Figure 5.1b (**BD**).

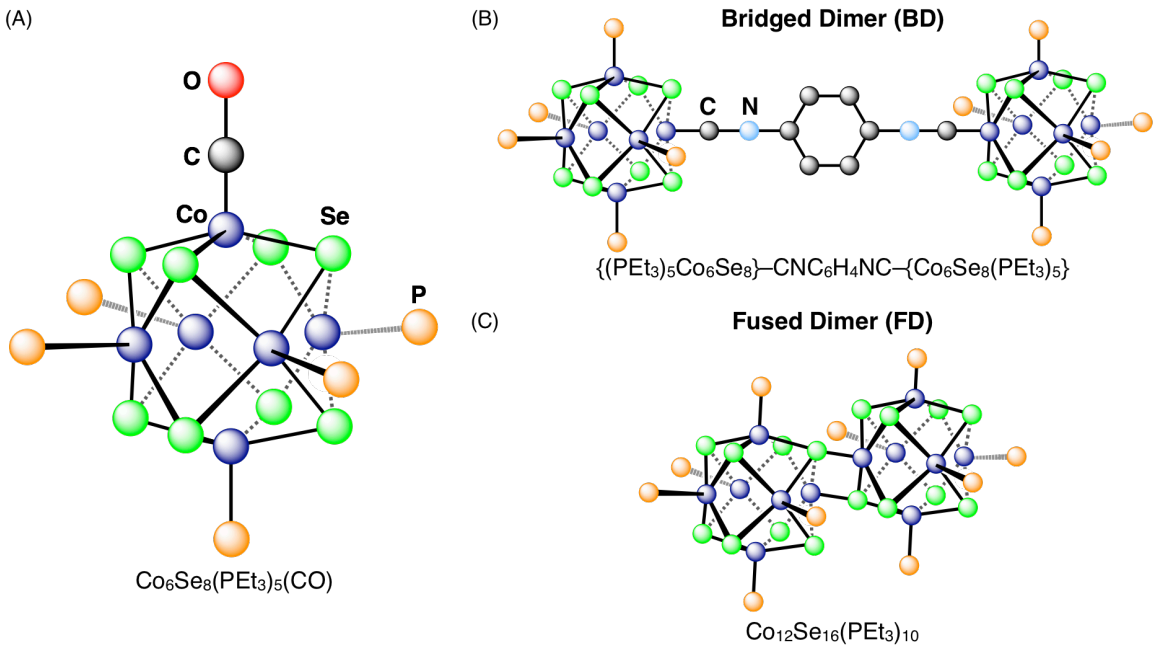

Figure 5.1. (a) CO and phosphine substituted Co_6Se_8 clusters. (b) Bridged superatom dimer (**BD**) with a diisonitrile linker $\{(PEt_3)_5Co_6Se_8\}$–L–$\{Co_6Se_8(PEt_3)_5\}$ (L = CNC_6H_4NC). (c) Fused superatom dimer, $[Co_{12}Se_{16}(PEt_3)_{10}]$ (**FD**).

Structurally, we view these functionalized clusters as superatoms[5] because we have been able to combine them to form dimers, trimers, and polymers through simple substitution reactions of the CO groups in which the $[M_6E_8]$ unit remains intact.[4, 6] Here we show that a CO group can be replaced with a carbene, forming a reactive intermediate species that allows us to crack open the Co_6Se_8 core, and this crack leads to the fusion of two superatoms, yielding the fused dimer, $Co_{12}Se_{16}(PEt_3)_{10}$ (**FD**, Figure 5.1c). We conclude from electrochemistry, optical spectroscopy, density functional theory calculations, and X-ray crystallography that the lobes in these dumb-bell shaped dimers are strongly coupled to each other, so much so that the bonding

between the two is best viewed as covalent. This expansion of the cluster is a step in the growth of the solid and exhibits the essentials of quantum confinement in its electronic structure.

5.4. Synthesis of Reactive Carbene-Terminated $[Co_6Se_8]$ Superatom

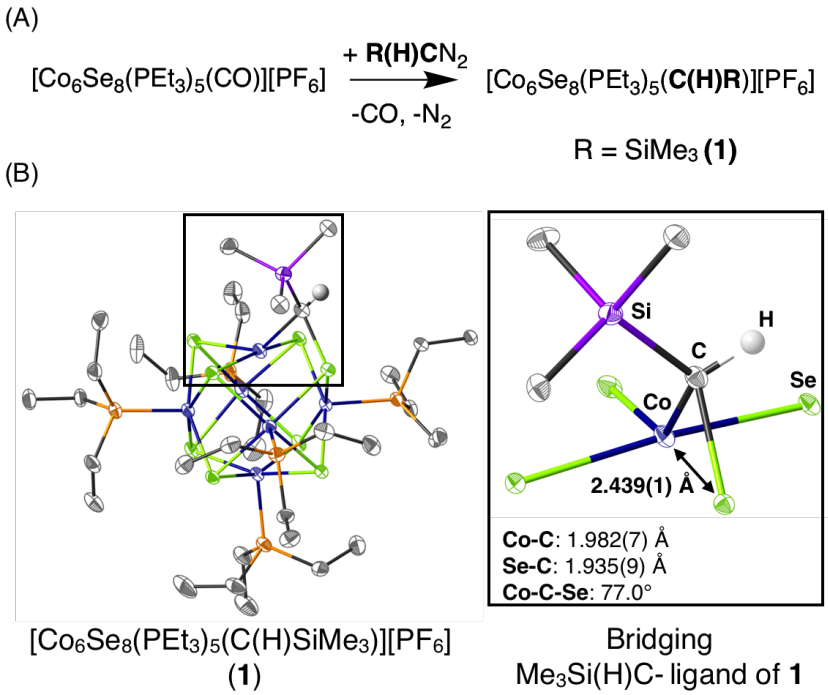

Figure 5.2. (a) Reaction scheme to form the carbene-cluster adduct $[Co_6Se_8(C(H)SiMe_3)(PEt_3)_5][PF_6]$ (**1**) from the reaction of a mono-carbonyl precursor with (trimethylsilyl)diazomethane. (b) Molecular structure from SCXRD of carbene-terminated intermediate $[Co_6Se_8(C(H)SiMe_3)(PEt_3)_5][PF_6]$ (**1**).

Our strategy to fuse superatom cores was to synthesize an intermediate with a labile ligand. To this end, we investigated whether a reactive species could be generated in situ that would displace the CO ligand under the proper conditions and leave the superatom activated for further transformations (Figure 5.2a). The mono-carbonyl precursor $[Co_6Se_8(PEt_3)_5(CO)]^n[PF_6]_n$ (n = 0 or 1)[4] and (trimethylsilyl)diazomethane (TMSD) react when irradiated with visible light to give a carbene-terminated cluster, $[Co_6Se_8(C(H)SiMe_3)(PEt_3)_5]^n[PF_6]_n$ (Figure 5.2a). Irradiation serves the dual purpose of ejecting the carbonyl from the cluster and generating the reactive carbene, :C(H)(TMS). The carbene-cluster adduct is stable and isolable, but the carbene remains

reactive. Details for the ^{1}H- and ^{31}P-NMR used to monitor the reaction and characterize the materials are contained in the Supporting Information. Figure 5.2b displays the structure from single crystal X-ray diffraction (SCXRD) of $[Co_6Se_8(C(H)SiMe_3)(PEt_3)_5][PF_6]$ (**1**).

The carbene terminated cluster (**1**) shows a surprising and unprecedented Se-C-Co binding motif (inset in Figure 5.2b): the carbenoid carbon has inserted into one of the Co-Se bonds in the superatom, and thus has cracked the $[Co_6Se_8]$ shell. The inorganic core of **1** is significantly distorted relative to that of the parent, all phosphine cluster $[Co_6Se_8(PEt_3)_6]^+$ (monomer, **M**).[7] The "cracked" Co-Se distance is significantly longer than the vicinal Co-Se distances in **1** (2.439(5) Å vs. 2.32-2.42 Å, inset in Figure 5.2b), and it is longer than Co-Se bonds in the all-phosphine core (2. 439(5) Å vs. 2.32-2.36 Å).[7] As a result of this distortion, the carbon-bound cobalt atom is pushed into the plane of its four adjacent selenium atoms. This leads to a compression of the corresponding antipodal Co-Co distance to 3.7 Å (compared to the other two antipodal Co-Co distances of 4.1 Å) and thus significant shortening of cis Co-Co distances to 2.670(2), 2.689(2), 2.754(1), and 2.772(2) Å. In **M**, the cis Co-Co distances are 2.90-2.95 Å. The insertion of the carbene into one of the Co-Se bonds not only breaks that particular bond but it also affects the entire $[Co_6Se_8]$ core, as demonstrated by this modulation of the Co-Co distances.

5.5. Formation of Fused Dimer $[Co_{12}Se_{16}]$ (FD)

These Co-C and Se-C bonds in **1** are still quite reactive: the dication of **FD** $[Co_{12}Se_{16}(PEt_3)_{10}][PF_6]_2$ forms in 66% isolated yield when **1** is heated gently (5 h, 70 °C) (Figures 5.2c and 5.2d). We can also prepare the neutral dimer, $Co_{12}Se_{16}(PEt_3)_{10}$, and the 1+ dimer, $[Co_{12}Se_{16}(PEt_3)_{10}][PF_6]$. Details of the syntheses of these species as well as their structures from

SCXRD are in Sections 5.x and 5.x. Table 5.1 contains the important structural metrics for these dimers in different oxidation states.

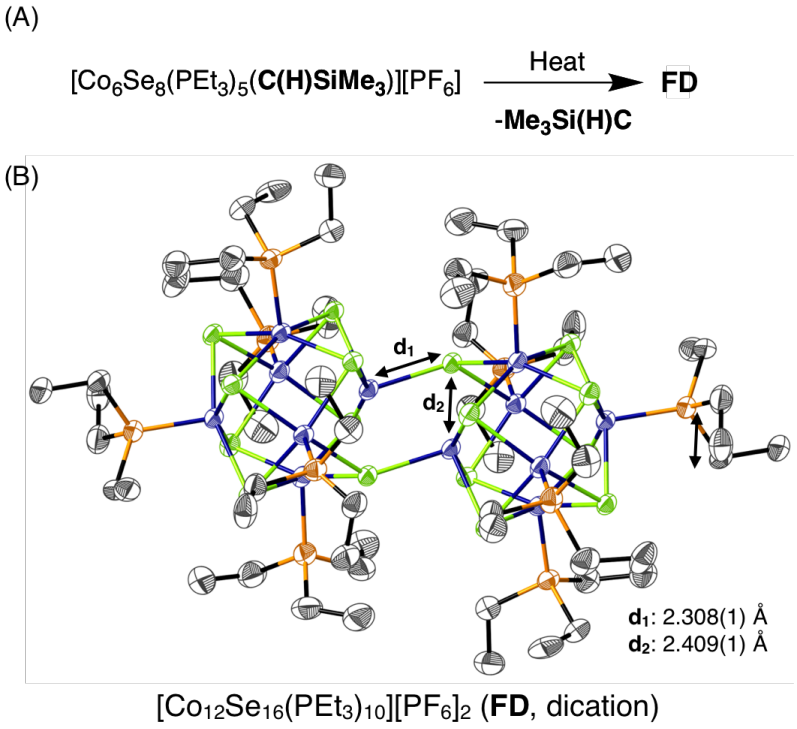

Figure 5.3. (a) Reaction scheme to form the fused dimer (**FD**) dication, $[Co_{12}Se_{16}(PEt_3)_{10}][PF_6]_2$ from the heating of **1**. (b) Molecular structure from SCXRD of the dication of **FD**, $[Co_{12}Se_{16}(PEt_3)_{10}][PF_6]_2$. PF_6^- counterions and hydrogen atoms in (b, d) (except C(*H*)$SiMe_3$) have been omitted to clarify the view. Thermal ellipsoids are set at 20% probability level in (b) and 50% probability level in (d).

	Co-Se*$_{inter}$	**Co-Se*$_{intra}$**	**All Co-Se**	**Co-Co$_{inter}$**	**Co-Co$_{intra}$**	**Co-P**
Neutral (n=0)	2.313(2) Å	2.417(1) Å	2.31-2.39 Å	2.753(1) Å	2.88-3.05 Å	2.13-2.15 Å
+1 (n=1)	2.311(2) Å	2.409(2) Å	2.31-2.37 Å	2.793(2) Å	2.88-3.07 Å	2.13-2.16 Å
+2 (n=2)	2.3087(4) Å	2.409(3) Å	2.32-2.37 Å	2.731(1) Å	2.92-3.03 Å	2.14-2.18 Å

Table 5.1. Bond distances in the series $[Co_{12}Se_{16}(PEt_3)_{10}]^n[PF_6]_n$ (n = 0, 1, 2).

5.6. Results and Discussion

By comparing the electrochemical behaviors of three Co_6Se_8-based systems, a $[Co_6Se_8(PEt_3)_6]$ monomer (**M**), the aryl-diisonitrile bridged dimer $\{(PEt_3)_5Co_6Se_8\}$–L–$\{Co_6Se_8(PEt_3)_5\}]$ (**BD**, Figure 1B),[4] and the fused dimer $[Co_{12}Se_{16}(PEt_3)_{10}]$ (**FD**, Figure 1C), we conclude that there is strong electronic communication between the two superatom lobes in **FD**.

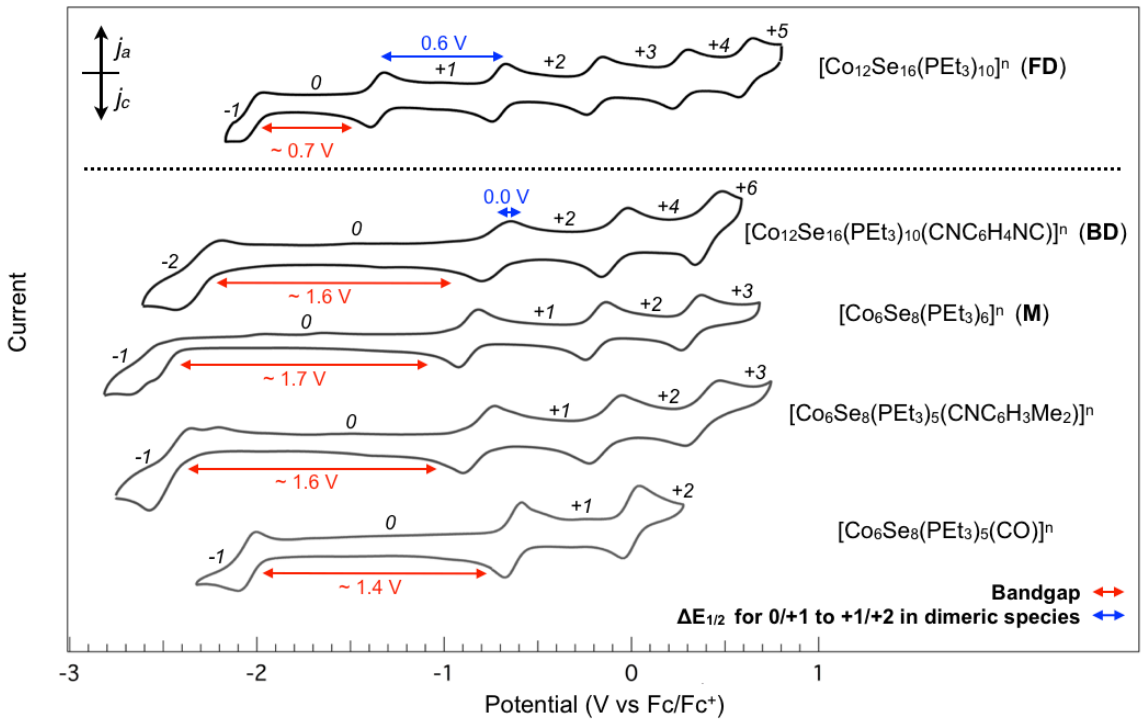

Figure 5.4. CV of fused dimer $[Co_{12}Se_{16}(PEt_3)_{10}]^n$ (**FD**), aryl-diisonitrile bridged dimer $[Co_{12}Se_{16}(PEt_3)_{10}(CNC_6H_4NC)]^n$ (**BD**), parent monomer $[Co_6Se_8(PEt_3)_6]^n$ (**M**), $[Co_6Se_8(PEt_3)_5(CNC_6H_3Me_2)]^n$ and $[Co_6Se_8(PEt_3)_5(CO)]^n$. The red arrow shows the effective bandgap as estimated from CV and the blue arrow shows the $\Delta E_{1/2}$ for the dimeric species.

Figure 3A displays the cyclic voltammograms (CVs) of the three materials. The CV of **M** has three reversible one-electron oxidations from n = 0 to +3, and two reductions to n = –1 and –2, although these latter reductions occur consecutively with a small voltage separation between them. The CV of **BD** also displays three reversible oxidation events at similar potentials in addition to a reduction event, but in contradistinction to the behavior of **M** each transition is a

two-electron event, as we have previously shown.[4] Therefore, again as we have previously shown, the redox behavior of **BD** is essentially that of its monomeric components (except each event is doubled), and **BD** behaves electronically as a sum of its component parts, with little to no electronic coupling between the two lobes.[4] As has been reported, one quantitative measure of the extent of intercluster coupling in dimeric species is the peak separation between the 0/+1 and +1/+2 redox couples ($\Delta E_{1/2}$) as it reflects the stability of the intermediate +1 state.[9] This value is represented by the blue arrow in Figure 3A. In **BD**, $\Delta E_{1/2}$ is essentially zero, since both one-electron oxidations (0/+1 and +1/+2) occur near the same potential, and no such +1 state can be isolated.

In contrast, the electrochemical behavior of **FD** is very different. Its CV has five distinct and reversible one-electron events from n = 0 to +5 and a reversible reduction event from 0 to –1 at –2 V. The significance of the CV of **FD** is that each peak is a one-electron event (determined as with **BD** by measuring the open circuit potential of the neutral, +1 and +2 species), and therefore, the two Co_6Se_8 units are not electrochemically isolated as they are in **BD**. This is significant because although **FD** is structurally composed of two cluster cores, the electronic data shows that the behavior of the material diverges drastically from a simple additive behavior of its component building blocks. Importantly, while we have seen no evidence for the discrete presence of the monocation of **BD**, we have been able to prepare and isolate the monocation of **FD**, $[Co_{12}Se_{16}(PEt_3)_{10}][PF_6]$ (details in the Supporting Information). The stability of this species is correlated to the magnitude of $\Delta E_{1/2}$ between the 0/+1 and +1/+2 redox couples, which is 0.65 V (compared to 0 V in **BD**). Putting this value in the context of other $[M_{12}E_{16}]$ metal chalcogenide fused dimers we find that it is the largest ($[Cr_{12}S_{16}]$: 0.42 V; $[Mo_{12}S_{16}]$: 0.41 V; $[Mo_{12}Se_{16}]$: 0.38 V; $[Re_{12}Se_{16}]$: 0.22 V).[1a, 10] We conclude that intercluster coupling for our cobalt dimer **FD** is

higher than that of previously reported species. Although all of these dimers are structurally similar, important factors detailed below distinguish **FD** from the others.

The separation between the -1/0 and 0/+1 potentials, measured from the peak extrema, has been used to estimate HOMO/LUMO splittings;[11] one striking conclusion from the CV data in Figure 3A is that there is a large reduction of the HOMO/LUMO splitting in **FD** relative to either **M** or **BD** (red arrows in Figure 3A). Markedly, while **BD** is physically as large, if not larger, than **FD**, it has a HOMO/LUMO gap identical to that of **M**. Furthermore, the modulation of this gap is not a result of a change in the ligand environment: Figure 3A displays the CVs of two additional monomeric species, $[Co_6Se_8(PEt_3)_5(CO)]^n$ and $[Co_6Se_8(PEt_3)_5(CNC_6H_3Me_2)]^n$, which have similar HOMO/LUMO splittings as the all-phosphine monomer. The $[Co_6Se_8]$ and $[Co_{12}Se_{16}]$ cluster cores are stoichiometrically similar to the solid state compound Co_3Se_4, which the solid state literature reports is a narrow band gap semiconductor.[12] $[Co_{12}Se_{16}(PEt_3)_{10}]^n$ is both easier to oxidize and easier to reduce than $[Co_6Se_8(PEt_3)_6]^n$, as observed in the decrease in its first oxidation potential and increase in its reduction potential. The direct result of this is the shrinking of the effective bandgap from ~ 1.6 eV in the monomer to ~ 0.7 eV in the fused dimer. In the context of the related solid state compound Co_3Se_4[13] this suggests the onset of the evolution of bulk electronic properties from the molecular regime.

We then compared the optical behaviors of the three Co_6Se_8-based systems and observe drastic differences between the fused species relative to the bridged dimer and monomer. Figure 3B displays the near infrared (IR) of all three species in their different charged states. **M** and **BD** absorptions (all charged states) look quite similar to each other aside from an approximate doubling of extinction coefficient in **BD**. This indicates additive (or non-interacting) monomer units, as was observed with cyclic voltammetry. In contrast, the near IR data of all three fused

dimer species (neutral, +1, +2) show much larger extinction coefficients than those of **M** and **BD**. Furthermore, a small absorption is observed in the neutral and singly charged fused dimer at ~ 1300 nm, and an intense and broad absorption is observed in the +2 species at 1525 nm.

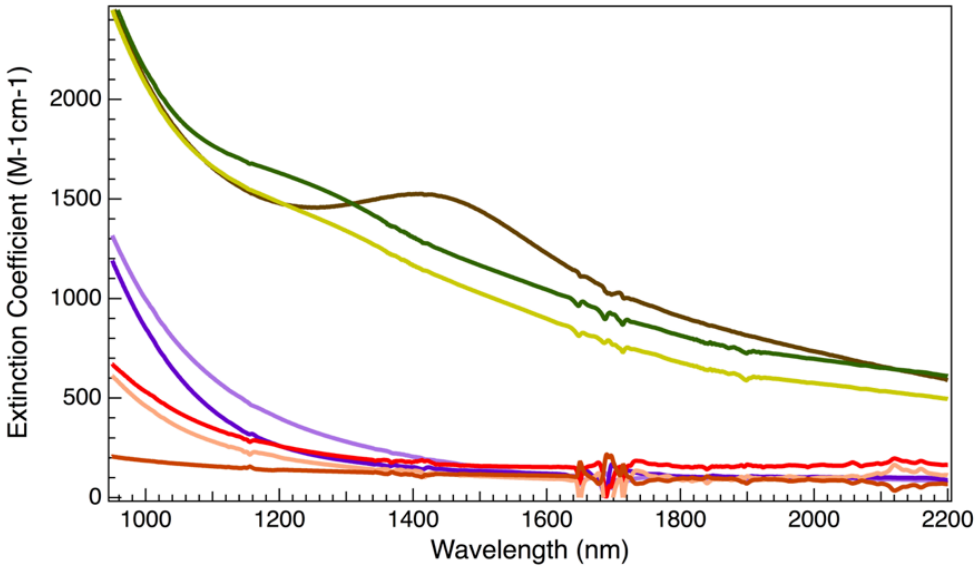

Figure 5.5. Near-infrared spectra of **FD**, **BD**, and **M** in multiple charged states. The data were collected in dichloromethane. Black arrows show the absorption features around 1300 nm and 1500 nm in the spectra of **FD**. The spikes observed at ~ 1700 nm are due to solvent absorption bands. ($Co_6Se_8(PEt_3)_6$ is poorly soluble and therefore its extinction coefficient is lower than expected).

Therefore, both electrochemistry and optical spectroscopy show that while **BD** largely recapitulates the properties of the coordinatively saturated monomer, **FD** is qualitatively different: it is easier to oxidize, easier to reduce, and easier to excite optically. Were the monomer and dimer clusters to be appreciated as small, albeit distorted, fragments of bulk cobalt selenide, and were quantum confinement to occur in this material, one would expect changes such as these.[14]

We sought to explain the dramatic change in properties between the **BD** and **FD**, and why the latter behaves, at least electrochemically and optically, more like the extended solid. We conclude that upon expanding the superatom core from [Co_6Se_8] to [$Co_{12}Se_{16}$] in the dimerization

process, the inter-cluster bonding arrangement implied in Figure 4A dominates. From the crystal structure of **FD** (Figure 2C) we observe that the inter-cluster cobalt-cobalt distance (2.731(1) Å) is significantly shorter than intra-cluster cobalt-cobalt distances (2.92-3.03 Å) but still elongated relative to the Co-Co distance in metallic Co (2.508(8) Å).[15] In addition, the intra-cluster Co-Se bonds at the fusion point (2.409(1) Å) (Se in the fusion point is represented in light pink in Figure 4A) are elongated relative to both the other intra-cluster Co-Se (2.32 – 2.38 Å) and inter-cluster Co-Se bonds (2.3081(9) Å). The length of this elongated intra-cluster Co-Se distance in **FD** is comparable to that of the analogous Co-Se distance in the Co-C-Se motif of carbene **1** (2.439(5) Å). We remove this "bond" in the representation of **FD** in Figure 4A to emphasize the structural reorganization of Co-Se bonds in going from the monomer to the dimer: within each $[Co_6Se_8]$ unit in the fused dimer there is one fewer Co-Se covalent bond, that bond having been "moved" to become an intercluster covalent bond.

	M-M in metal[7]	**E*-M_{intra}**	**E*-M_{inter}**	**E-M_{intra}**	**M-M_{intra}**	**M-M_{inter}**
$[Mo_{12}S_{16}]$	2.941(6) Å	2.486 Å	2.554 Å	2.44-2.45 Å	2.65-2.67 Å	3.419(2) Å
$[Mo_{12}Se_{16}]$	2.941(6) Å	2.596 Å	2.705 Å	2.55-2.57 Å	2.68-2.73 Å	3.551(4) Å
$[Cr_{12}S_{16}]$	2.602(2) Å	2.373 Å	2.307 Å	2.31-2.36 Å	2.58-2.82 Å	2.948(3) Å
$[Re_{12}Se_{16}]$	2.760(8) Å	2.603 Å	2.638 Å	2.51 - 2.52 Å	2.62-2.67 Å	3.417 Å
$[Co_{12}S_{16}]$	2.508(8) Å	N.A.	2.147 Å	2.19-2.26 Å	2.79-2.92 Å	2.635 Å
$[Co_{12}Se_{16}]$	**2.508(8) Å**	**2.409(3) Å**	**2.3087(4) Å**	**2.32-2.37 Å**	**2.92-3.03 Å**	**2.731(1) Å**

Table 5.2. Bond distances for $[Co_{12}Se_{16}]$ (**FD**, in bold) compared previously reported dimers ($[Cr_{12}S_{16}]$, $[Mo_{12}S_{16}]$, $[Mo_{12}Se_{16}]$, $[Re_{12}Se_{16}]$)[10] and M-M bonds in the metal.[15]

While in **FD** we observe the reorganization of Co-Se bonds as shown in Figure 4A, what we find in the apparently analogous cases of $[M_{12}E_{16}]$ (M = Re, Mo, Cr; E = S, Se) is the representation shown in Figure 4B, in which metal-metal bonds and weak inter-cluster

interactions are dominant. Table S2 contains important bond metrics and atomic distances for $[Co_{12}Se_{16}(PEt_3)_{10}]$ compared to these other $[M_{12}E_{16}(PEt_3)_{10}]$ dimers. M-M bonds within each $[M_6]$ unit are comparable to M-M bonds within the metal whereas inter-cluster M-M separations are larger and nonbonding.[15] Furthermore, inter-cluster M-E bonds are significantly longer than the intra-cluster M-E bonds. Thus, as shown in Figure 4B, in the dimerization process there are no bond rearrangements within each core. Instead, the two cluster cores remain the same as in the monomer and thus the overall bonding in the dimer is best represented by two independent metal-bound octahedra connected via weakly interacting M-E bonds across the fusion point.

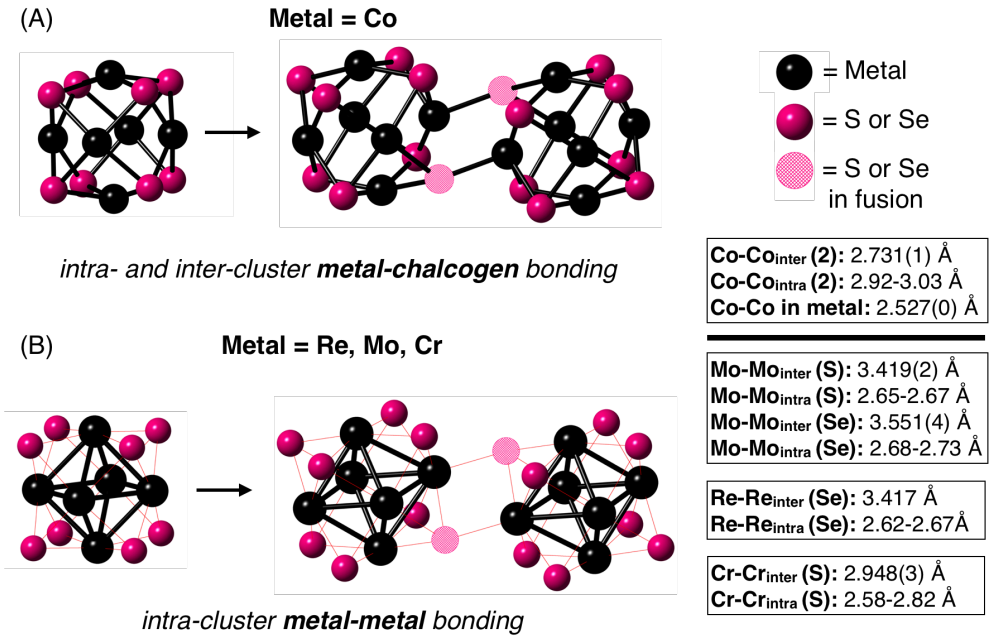

Figure 5.6. (a) The dominant bonds and bond rearrangements in $[Co_{12}Se_{16}]$. The Co-Co distance in elemental cobalt is 2.508(8).[15] (b) The dominant bonds and bond rearrangements in other $[M_{12}E_{16}]$ dimers (M = Re, Mo, Cr; E = S, Se) Black spheres: metal; Pink spheres: chalcogen; Light pink spheres: chalcogen involved in intercluster M-E. Dark black lines represent bonding interactions and dotted red lines represent weaker donor-acceptor interactions.

5.7. Quantum Chemical Calculations

In order to gain more insight into **1**, we studied models of its constituent parts using quantum chemical calculations (see Section 5A.12). One question is the nature of the coordinatively unsaturated superatom, $[(Et_3P)_5Co_6Se_8]^+$, an intermediate that would form were $[(Et_3P)_5Co_6Se_8(CO)]^+$ to lose its CO. We first studied the conceptually simpler electrically neutral system $(Et_3P)_5Co_6Se_8$.[8] We found that while the coordinatively saturated superatom, $(Et_3P)_5Co_6Se_8(CO)$ is a closed shell, singlet species (as is the all-phosphine monomer), the open shell, triplet state of $(Et_3P)_5Co_6Se_8$ is lower in energy than the closed shell singlet. While we had not anticipated this result, on reflection it is not entirely surprising. It is reminiscent of situations in traditional coordination chemistry and organometallic chemistry where strong-field ligands promote low-spin states when they coordinate to previously high-spin subsystems. Apparently, the hypothetical naked superatom, Co_6Se_8, were it to exist, would be a high-spin entity.

We can learn more about the hypothetical intermediate, $(Et_3P)_5Co_6Se_8$, by looking at the two singly-occupied orbitals that characterize the triplet (Figure 5.3.). One of these orbitals is localized on the coordinatively unsaturated Co atom, and the other is distributed among this Co atom and its Se

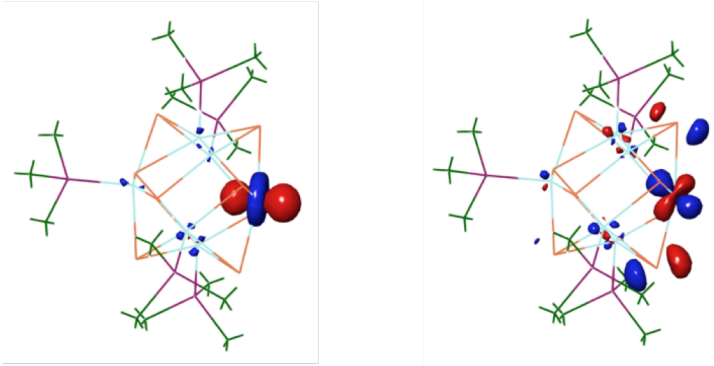

Figure 5.7. Singly-occupied orbitals of the triplet state of $Co_6Se_8(PMe_3)_5$, a coordinatively unsaturated species. One of these orbitals is localized on the coordinatively unsaturated Co atom, and the other is distributed among this Co atom and its Se neighbors. This suggests that a Co-Se bond is cleaved upon removing a carbonyl ligand from the coordinatively saturated parent $Co_6Se_8(CO)(PMe_3)_5$.

neighbors. Although this triplet state is certainly quite complicated, the simplest interpretation is that it shows a broken Co-Se bond. Thus, if and when the CO dissociates from $(Et_3P)_5Co_6Se_8(CO)$ a Co-Se bond cleaves.

Whether or not $(Et_3P)_5Co_6Se_8$ (or its cation) actually occurs during the formation of **1**, the electronic structure of the former hints at the structure of latter: if $(Et_3P)_5Co_6Se_8$ is a triplet, then it is primed to form two covalent bonds to a reaction partner such as a triplet carbene. In simple terms, **1** has a carbene which has inserted into one of the Co-Se bonds of the original cluster. There is one fewer Co-Se bonds in **1** than in **M**, but in compensation there is a new Co-C and a new Se-C covalent bond. We will use this analysis when we discuss below the nature of the fused dimer, **FD**.

We can rationalize this bonding by again considering the $(Et_3P)_5Co_6Se_8$ subunit. Since this unit has a triplet ground state (or at least this state is very low-lying), its two unpaired spins are primed to bond to other triplet-state molecules. Perhaps the simplest candidate for its reaction partner is another copy of itself: two triplet, coordinatively unsaturated monomers combine to form **FD**, this dimer being held together by two Co-Se covalent bonds.

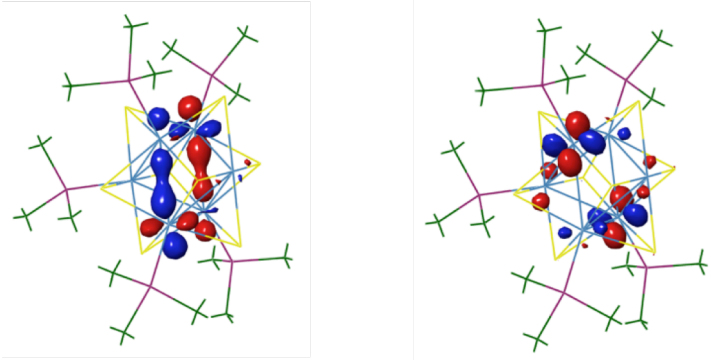

Figure 5.8. Singly-occupied orbitals of the triplet state of the coordinatively unsaturated species, $Mo_6S_8(PMe_3)_5$. The orbitals are localized on the Mo atom centers, with no apparent localization on the chalogen atoms. This suggests that a Mo-Mo bond has been cleaved upon removing a phosphine ligand from the parent $Mo_6S_8(PMe_3)_6$ (rather than a Mo-S bond, as is the case for the cobalt cluster).

We have performed DFT calculations on $(Me_3P)_5Mo_6S_8$ as a prototype coordinatively unsaturated "Chevrel" monomer (see SI for details). In this case the ground state is the simple,

expected singlet, and the lowest-energy triplet is quite high in energy. Furthermore, the two singly-occupied orbitals that describe this triplet state indicate that it is a Mo-Mo bond, not a Mo-S bond, that is cleaved in this triplet (Figure S2). Therefore, even if this triplet were available, inter-cluster Mo-S *covalent* bonding would not be favored. Nevertheless, the Mo, Re, and Cr dimers do form. We conclude that the intercluster Mo-S bonds in the $Mo_{12}S_{16}$ dimer are donor-acceptor (M-L-type) bonds. Conceptually, the intercluster bonding in $Mo_{12}S_{16}(PEt_3)_{10}$ arises from the replacement of Mo-P donor/acceptor bonds with Mo-S donor/acceptor bonds. In contrast, the "intercluster" Co-Se bonds in $Co_{12}Se_{16}(PEt_3)_{10}$ are covalent (M-X-type) bonds. Therefore these particular Co-Se bonds are now part of the backbone of $[Co_{12}Se_{16}(PEt_3)_{10}]$ and covalently connect each cluster core to form a fused entity in which the bonds of the monomer have rearranged to form the dimer with new properties that are more than the sum of two individual $[Co_6Se_8(PEt_3)_6]$ units.

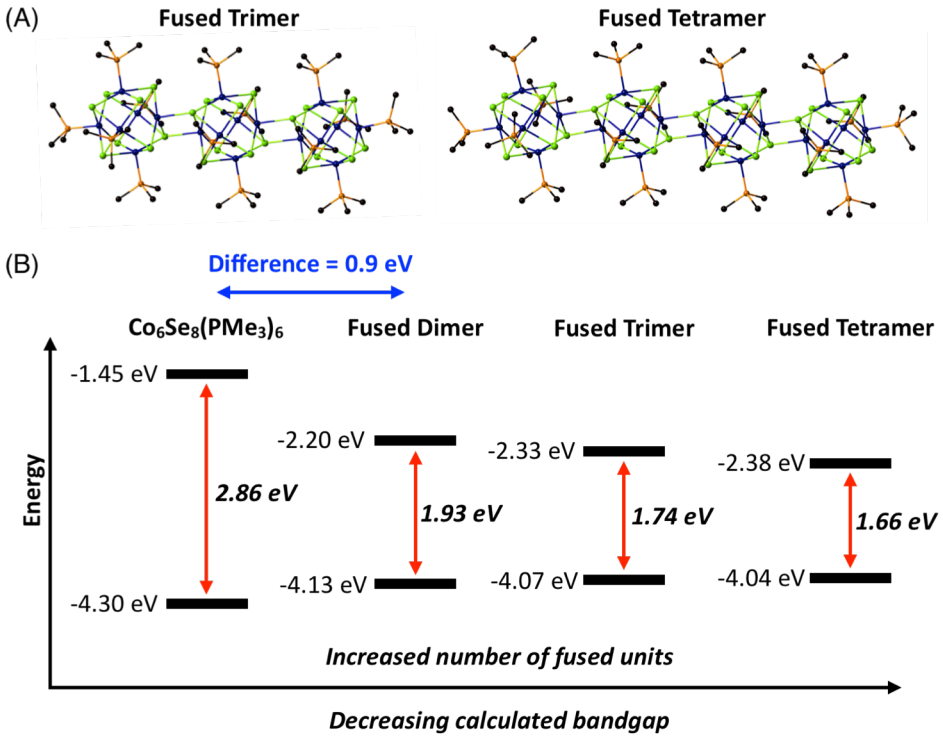

Figure 5.9. (a) Geometry optimized molecular structures a fused trimer, $Co_{18}Se_{24}(PMe_3)_{14}$ and a fused tetramer, $Co_{24}Se_{32}(PMe_3)_{18}$. Hydrogen atoms have been omitted to clarify the view. (b) Calculated HOMO and LUMO energies (PEt_3 ligands replaced with PMe_3) as well as HOMO/LUMO splitting (bandgap), in **M**, **FD**, fused trimer, and fused tetramer.

We thus observe the gradual evolution of bulk electronic properties upon directed expansion of core nuclearity. To corroborate this finding, we calculated the HOMO and LUMO energies of the monomer and fused dimer (with PEt_3 ligands simplified to PMe_3) using density function theory (DFT), in addition to the energies for a fused trimer and fused tetramer ($Co_{18}Se_{24}(PMe_3)_{14}$ and $Co_{24}Se_{32}(PMe_3)_{18}$, respectively). The final calculated geometries for the fused trimer and fused tetramer are displayed in Figure 5.9a. The difference in bandgap between the fused dimer and monomer mirrors our experimental finding (calculated difference: 0.93 eV; actual difference: 1 eV). Our calculations further show that each additional fused $[Co_6Se_8]$ core leads to the nanostructure's bandgap reduction (Figure 5.9b).

5.8. Conclusions

We have expanded on the reaction chemistry of clusters as superatoms. We have shown that coordinatively unsaturated clusters can have diverse electronic states available to them, and these varied states can allow varied reaction pathways. While $L_6Co_6Se_8$ is a ground state singlet, $L_5Co_6Se_8$ is a ground state triplet. We install a reactive carbene on the $[Co_6Se_8]$ core to create a latent fusion site, and we show by cyclic voltammetry and SCXRD that the resulting fused $[Co_{12}Se_{16}]$ material exhibits strong electronic coupling and electron delocalization. Furthermore, the bandgap reduction observed upon expanding the cluster core suggests that we have isolated a more bulk-like intermediate than the $[Co_6Se_8]$ monomer in going from molecules to an extended solid. The isolation of $[Co_{12}Se_{16}(PEt_3)_{10}]^n$ thus represents a significant advancement in observing the manifestation of quantum confinement in an atomically precise nanocluster.

We have now shown that we can dimerize Co_6Se_8 units in two distinct ways: either by direct fusion or by using a ditopic bridging ligand. In the former case the two units are

electronically strongly coupled, in the latter case less so. If we draw a comparison to conjugation in organic molecules and materials, this is reminiscent of conjugated versus non-conjugated dienes, for example 1,3-butadiene (**FD**) and 1,4-pentadiene (**BD**). However, conjugation in these systems involves the overlap of pi orbitals, whereas from a purely chemical bonding standpoint, sigma conjugation dominates the delocalization of our systems. We are currently extending our reaction sequence to prepare higher-order conjugated superatom wires. More broadly, we can extend the design principle used to access a dimer to our building blocks that have multiple CO groups[4] and apply the carbene/fusion sequence to obtain strongly coupled materials with programmed dimensionality. These strongly coupled systems are necessary to discover materials with new and unusual magnetic and electronic properties.

5.9. General Synthesis Information

Unless otherwise noted, all reactions were performed in a nitrogen atmosphere using standard Schlenk techniques or in a nitrogen-filled glovebox. Selenium powder and dicobalt octacarbonyl (stabilized with 1-5% hexane) were obtained from STREM Chemicals. Triethylphosphine (99%) and (trimethylsilyl)diazomethane solution (2.0 M in hexanes) were purchased from Sigma-Aldrich. Chemicals were used without further purification. Anhydrous and anaerobic solvents were obtained from a Glass Contour solvent system consisting of a Schlenk manifold with purification columns packed with activated alumina and supported copper catalyst. ^{1}H NMR spectra were recorded on a Bruker DRX400 (400 MHz) or a Bruker DMX500 (500 MHz) spectrometer. ^{31}P NMR spectra were recorded on a Bruker DMX500 (500 MHz) spectrometer and referenced to phosphoric acid (H_3PO_4). ^{1}H NMR chemical shifts were

referenced to residual protons in the NMR solvent ($CDCl_3$: δ 7.26; C_6D_6: δ 7.16). A Kessil blue LED light (34W maximum, 24 VDC) was used as the light source for the reactions.

Cyclic voltammetry (CV) was performed on a CHI600C potentiostat. A three-electrode setup was used using an $Ag/AgNO_3$ electrode as the reference electrode, a Pt wire counter electrode, and a 3 mm diameter glassy carbon working electrode. All measurements were done under a dinitrogen atmosphere and at room temperature. A 0.1 M solution of tetrabutylammonium hexafluorophosphate in THF or DCM was used as the supporting electrolyte. Measurements were calibrated using the ferrocene/ferrocenium redox couple. Near-infrared absorption was measured using a Nicolet 6700 FTIR spectrometer. The white light source, quartz beamsplitter, and thermoelectrically cooled InGaAs 2.6 μm detector were used to obtain spectra in the range of 13000 – 5000 cm-1 (770 – 2000 nm). Solution samples (dichloromethane solvent) were placed in a 1 mm path-length Suprasil quartz cuvette under a N2 atmosphere with anhydrous dichloromethane as a reference. Crystallographic data for all compounds was collected on an Agilent SuperNova diffractometer using mirror-monochromated Cu Kα radiation.

5.10. Synthetic Procedures and Characterization of Compounds

$[Co_6Se_8(PEt_3)_6]^n[PF_6]_n$ (n = 0, +1, +2), $[Co_6Se_8(PEt_3)_5(CO)]^n[PF_6]_n$ (n = 0, +1), $[Co_{12}Se_{16}(PEt_3)_{10}(CNC_6H_4NC)]^n[PF_6]_n$ (n = 0, +2), and $Co_6Se_8(PEt_3)_5(CNC_6H_3Me_2)$ were prepared as previously reported.[3b, 4]

Synthesis of $[Co_6Se_8(PEt_3)_5(C(H)SiMe_3)][PF_6]$ (1). Inside the glovebox, a J. Young tube was loaded with a solution of $[Co_6Se_8(CO)(PEt_3)_5][PF_6]$ (0.050 g, 0.028 mmol, 1 eq.) in THF (2 mL).

28 μL of a (trimethylsilyl)diazomethane solution (2.0 M in hexanes, 0.056 mmol, 2 eq.) was added. The reaction mixture was irradiated with a blue LED light for 1 hour at room temperature. The ^{31}P NMR spectrum of the crude reaction mixture (Figure S4) shows most of the starting material has been converted to product (^{31}P NMR of starting material $[Co_6Se_8(PEt_3)_5(CO)][PF_6]$ contains the following peaks: –145.0 ($[PF_6]^-$), –441.2 (broad), –492.0 (broad)).[2] The solvent was evaporated *in vacuo*. The solid was triturated with hexanes. Yield: 43 % (0.022 g, 0.012 mmol). X-ray quality crystals were grown from a dichloromethane solution layered with diethyl ether. Figure S5 shows the ^{31}P NMR spectrum of these crystals. ^{31}P NMR (161.9 MHz, THF-d_8) δ = -96 (broad), -131 (broad), -144 ($[PF_6]^-$), -196 (broad), -317 (broad) ppm.

Synthesis of $Co_6Se_8(PEt_3)_5(C(H)SiMe_3)$. Inside the glovebox, a J. Young tube was loaded with a solution of $Co_6Se_8(CO)(PEt_3)_5$ (0.020 g, 0.012 mmol, 1 eq.) in d_6-benzene (1 mL). 12 μL of a (trimethylsilyl)diazomethane solution (2.0 M in hexanes, 0.024 mmol, 2 eq.) was added. The reaction mixture was irradiated with a blue LED light for 3 hours at room temperature. Figure S6 displays the ^{1}H NMR of the crude reaction mixture for this conversion, in which the only visible peaks are attributed to the product, $Co_6Se_8(C(H)SiMe_3)(PEt_3)_5$, and unidentified $SiMe_3$ derivatives from 0.3 ppm to - 0.25 ppm, with complete disappearance of starting material. Figure S7 displays the crude ^{31}P NMR for this conversion. An isolated yield is not reported for this reaction due to the partial conversion to $Co_{12}Se_{16}(PEt_3)_{10}$ observed by ^{1}H NMR upon solvent removal/concentration. The ^{1}H and ^{31}P NMR shifts reported below are from the crude reaction mixture. ^{1}H NMR (300 MHz, benzene-d_6) δ = 6.24 (s, 1H), 1.85-1.95 (m, 24H), 1.68-1.79 (m, 6H), 1.07-1.17 (m, 36H), 0.94-1.02 (m, 9 H), 0.36 (s, 9H) ppm. ^{31}P NMR (161.9 MHz, benzene-d_6) δ = 47 (broad) ppm.

Synthesis of $[Co_{12}Se_{16}(PEt_3)_{10}][PF_6]_2$ (FD, dication). $[Co_6Se_8(C(H)SiMe_3)(PEt_3)_5][PF_6]$ (**1**) was first synthesized as described above and the reaction was then carried forward directly to $[Co_{12}Se_{16}(PEt_3)_{10}][PF_6]_2$ without isolation of **1**. Inside the glovebox, a J. Young NMR tube was loaded with a solution of $[Co_6Se_8(CO)(PEt_3)_5][PF_6]$ (0.025 g, 0.014 mmol, 1 eq.) in THF (2 mL). 14 μL of a (trimethylsilyl)diazomethane solution (2.0 M in hexanes, 0.028 mmol, 2 eq.) was added. The reaction mixture was irradiated with a blue LED light for 1 hour at room temperature to yield **1**. The solvent was evaporated *in vacuo*, the solid was dissolved in acetonitrile (2 mL) and the J. Young tube was heated at 70°C for 5 hours under N_2 (Note: the starting CO-material and **1** are both soluble in THF and acetonitrile. $[Co_{12}Se_{16}(PEt_3)_{10}][PF_6]_2$ is poorly soluble in THF but soluble in acetonitrile, so the transformation **1** to $[Co_{12}Se_{16}(PEt_3)_{10}][PF_6]_2$ is carried out in acetonitrile). The solution was filtered, the solvent was evaporated *in vacuo* and the solid triturated with toluene and dried. Mass of solid: 16 mg (66% yield, 0.0046 mmol). X-ray quality crystals (black needles) were grown from the vapor diffusion of pentane into a chloroform solution of $[Co_{12}Se_{16}(PEt_3)_{10}][PF_6]_2$. ^{31}P NMR (161.9 MHz, chloroform) δ = -53 (broad), -77 (broad), -144 ($[PF_6]^-$), -185 (broad) ppm.

Synthesis of $[Co_{12}Se_{16}(PEt_3)_{10}][PF_6]$ (FD, monocation) <u>From the reduction of **FD** dication:</u> Inside the glovebox, a 20 mL scintillation vial was loaded with a solution of $[Co_{12}Se_{16}(PEt_3)_{10}][PF_6]_2$ (0.008 g, 0.002 mmol, 1 eq.) in dichloromethane (5 mL). A 1 mg/mL stock solution of cobaltocene in dichloromethane was prepared. 0.4 mL of this solution (0.4 mg, 0.002 mmol, 1 eq.) was added and the solution was stirred for 1 hour. The solvent was removed *in vacuo* and the remaining solids were dissolved in toluene. X-ray quality crystals (3 mg, 0.001 mmol, 45 % yield) of $[Co_{12}Se_{16}(PEt_3)_{10}][PF_6]$ were grown from the vapor diffusion of pentane

into this toluene solution. This species is NMR-silent, therefore ^{1}H and ^{31}P NMR spectra are not available.

Synthesis of $Co_{12}Se_{16}(PEt_3)_{10}$ (FD, neutral). Method A: From the reduction of **FD** dication**.** Inside the glove box, a 20 mL scintillation vial was loaded with a suspension of $[Co_{12}Se_{16}(PEt_3)_{10}][PF_6]_2$ (0.029 g, 0.008 mmol, 1 eq.) in toluene (15 mL). A 1 mg/mL stock solution of cobaltocene in toluene was prepared and 3 mL of this solution (3 mg, 0.016 mmol, 2 eq.) was added to the suspended solids. The solution gradually a turned deep brown color aas the solids went into solution and the reaction was stirred for 1 hour. The solvent was removed *in vacuo* and the remaining solids were triturated in acetonitrile then dried, yielding 14 mg of $Co_{12}Se_{16}(PEt_3)_{10}$ (56 % yield, 0.004 mmol). X-ray quality crystals of $Co_{12}Se_{16}(PEt_3)_{10}$ were grown from the vapor diffusion of pentane into a benzene solution. ^{1}H NMR (300 MHz, benzene-d_6) δ = 7.68 (broad), 4.68 (broad), 2.17 (broad), 1.80 (broad), 1.47 (broad), 0.81 (broad) ppm. ^{31}P NMR (161.9 MHz, benzene-d_6) δ = 71 (broad), -29 (broad) ppm.

Synthesis of $Co_{12}Se_{16}(PEt_3)_{10}$ (FD, neutral). Method B: From $Co_6Se_8(PEt_3)_5(C(H)SiMe_3)$ (**1**, neutral) via a pyridine carbene trap. $Co_6Se_8(C(H)SiMe_3)(PEt_3)_5$was first synthesized as described above and the reaction was then directly carried forward to $Co_{12}Se_{16}(PEt_3)_{10}$ without isolation of the carbene-terminated intermediate. Inside the glovebox, a J. Young tube was loaded with a solution of $Co_6Se_8(CO)(PEt_3)_5$ (0.010 g, 0.006 mmol, 1 eq.) in C_6D_6 (0.5 mL). 6 μL of a (trimethylsilyl)diazomethane solution (2.0 M in hexanes, 0.012 mmol, 2 eq.) was added. The reaction mixture was irradiated with a blue LED light for 3 hours at room temperature until full conversion to $Co_6Se_8(C(H)SiMe_3)(PEt_3)_5$ was observed by ^{1}H NMR. An excess of pyridine was then added to the solution (1 μL), and by ^{1}H NMR we observe the disappearance of peaks corresponding to $Co_6Se_8(C(H)SiMe_3)(PEt_3)_5$ and appearance of the same broad peaks observed

from the ^{1}H NMR spectrum of $Co_{12}Se_{16}(PEt_3)_{10}$ obtained via Method A, within one hour. X-ray quality crystals of $Co_{12}Se_{16}(PEt_3)_{10}$ (4 mg, 42 % yield) were grown from the vapor diffusion of pentane into this solution. The unit cell matched the unit cell of the crystals of $Co_{12}Se_{16}(PEt_3)_{10}$ grown from the synthesis via Method A. (The neutral fused dimer can also be prepared by removing benzene *in vacuo* from the solution of $Co_6Se_8(C(H)SiMe_3)(PEt_3)_5$, and then dissolving the remaining solids in neat pyridine. Then, removal of pyridine *in vacuo* followed by the dissolution of the solids in benzene yields the fused dimer).

NMR spectra of selected compounds

Figure 5.10. ^{31}P NMR spectrum of $[Co_6Se_8(PEt_3)_5(C(H)SiMe_3)][PF_6]$ (**1**).

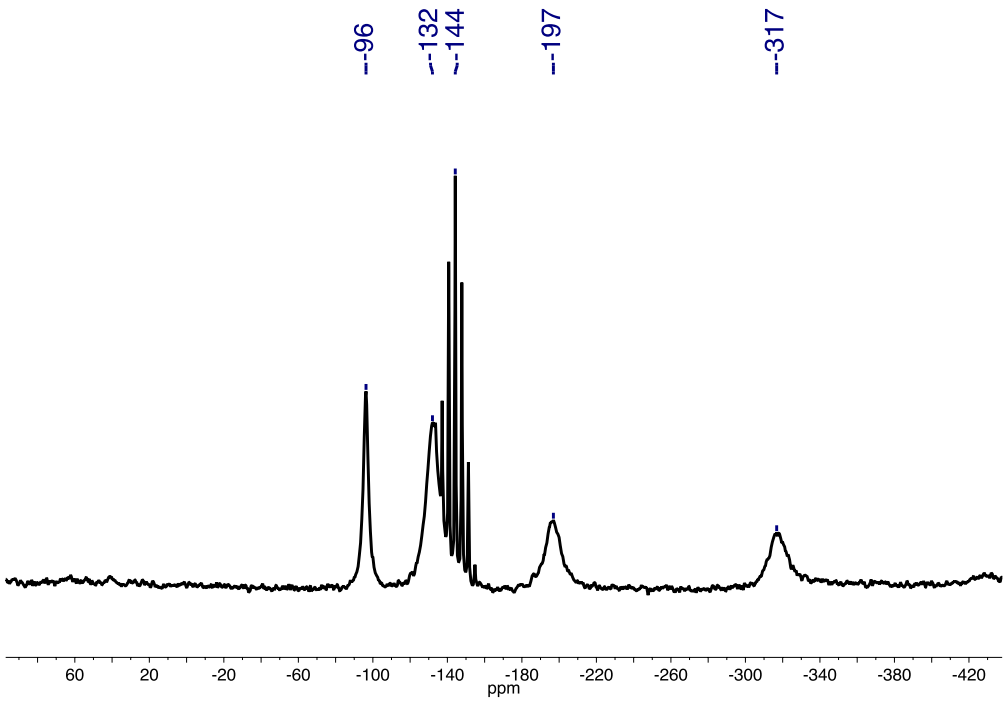

Figure 5.11. ^{1}H NMR spectrum of $Co_6Se_8(PEt_3)_5(C(H)SiMe_3)$ (crude reaction mixture).

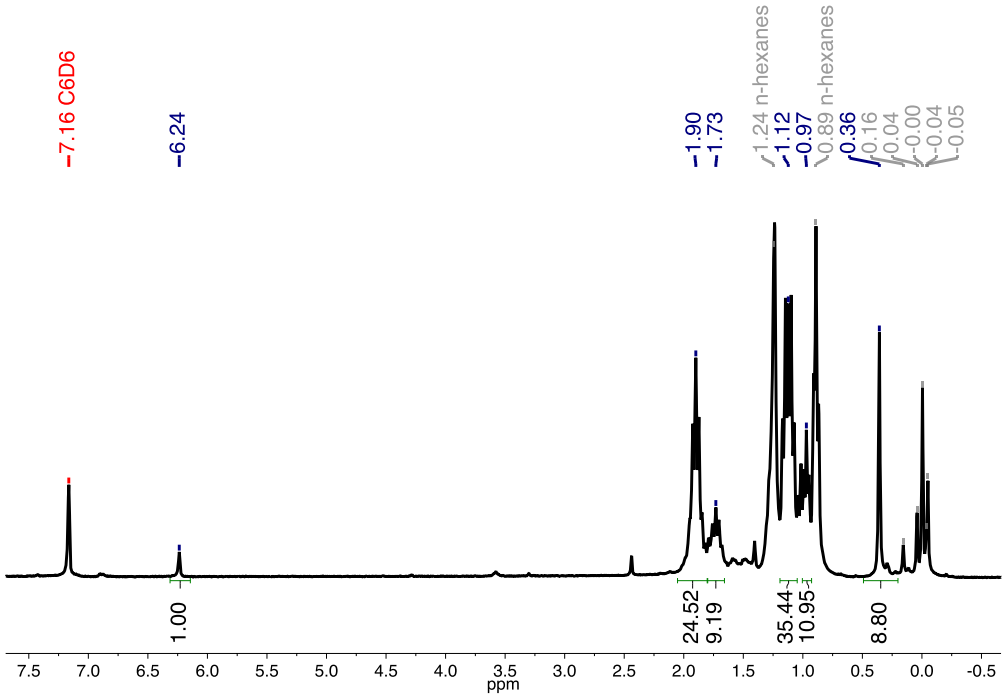

Figure 5.12. ^{31}P NMR spectrum of $Co_6Se_8(C(H)SiMe_3)(PEt_3)_5$ (crude reaction mixture).

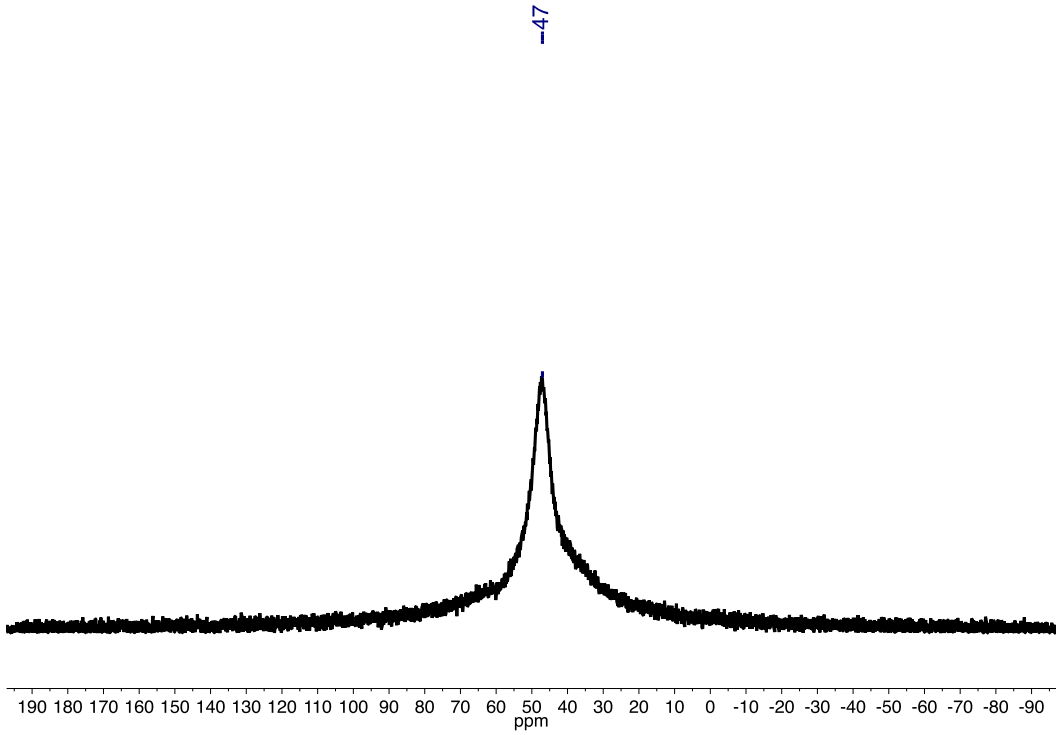

Figure 5.13. ^{31}P NMR spectrum of $[Co_{12}Se_{16}(PEt_3)_{10}][PF_6]_2$ (**FD**, dication).

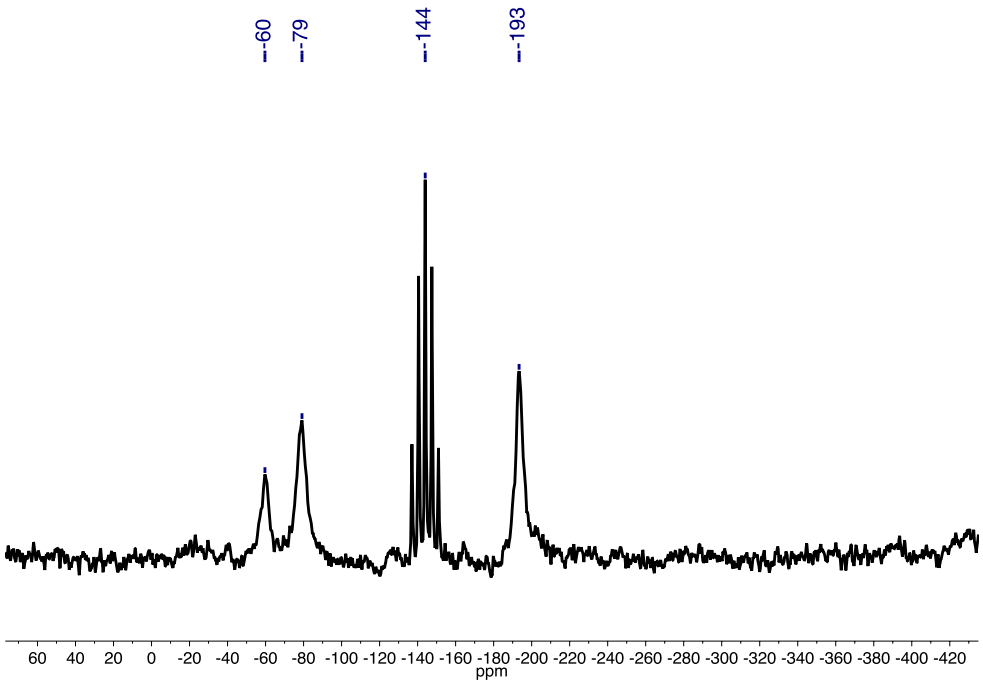

Figure 5.14. ^{1}H NMR spectrum in C_6D_6 of single crystals of $Co_{12}Se_{16}(PEt_3)_{10}$ (**FD**, neutral; dark blue labels) obtained via Method A (reduction of **FD**, dication). Peaks at 1.97 ppm and 1.12 ppm correspond to $Co_6Se_8(PEt_3)_6$ impurity.

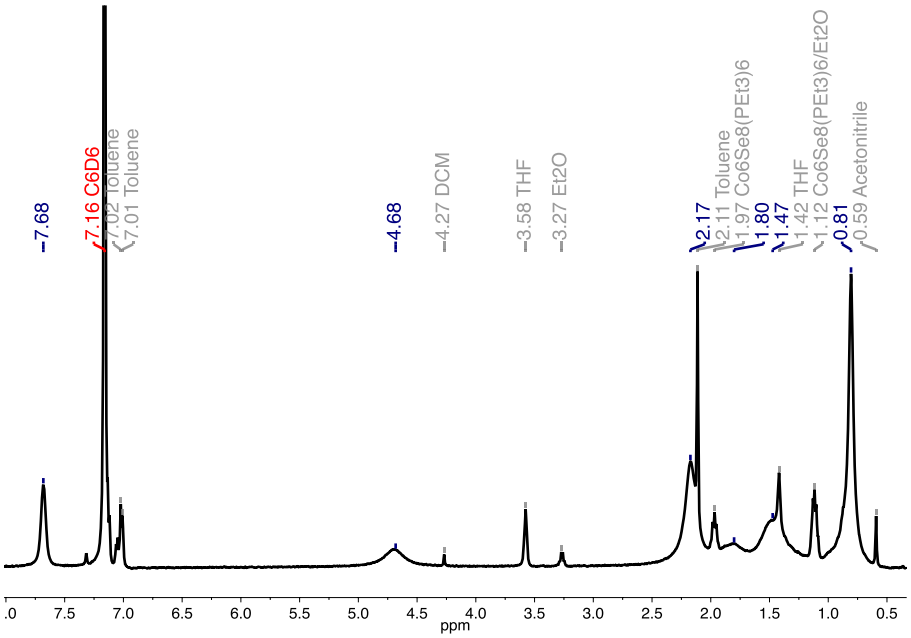

Figure 5.15. ^{1}H NMR spectrum in C_6D_6 of single crystals of $Co_{12}Se_{16}(PEt_3)_{10}$ (**FD**, neutral; dark blue labels) obtained via Method B (pyridine). Peaks at 1.97 and 1.12 ppm correspond to $Co_6Se_8(PEt_3)_6$ impurity. The product peaks are slightly shifted upfield compared to the product peaks obtained via Method B.

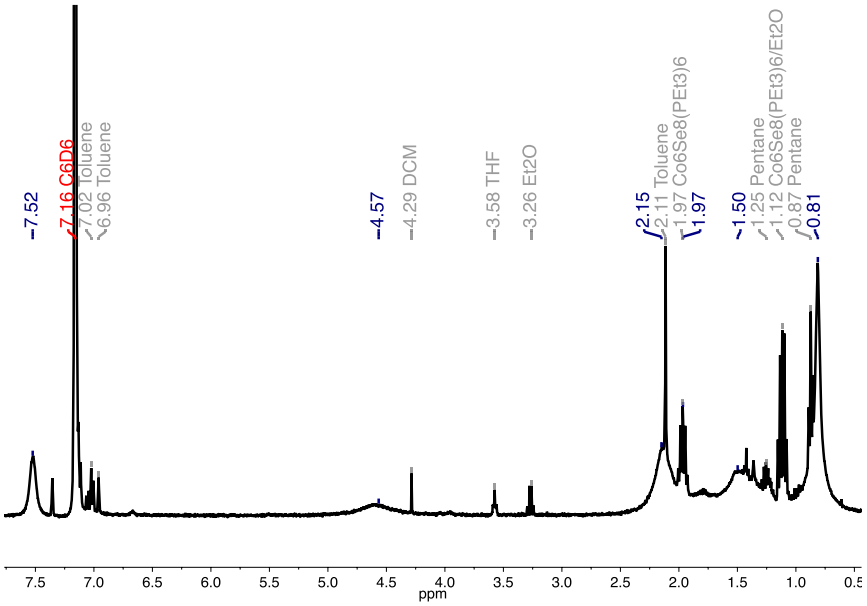

Figure 5.16. ^{31}P NMR spectrum of $Co_{12}Se_{16}(PEt_3)_{10}$ (peak at 60 ppm corresponds to $Co_6Se_8(PEt_3)_6$ impurity, as confirmed by ^{1}H NMR of $Co_{12}Se_{16}(PEt_3)_{10}$).

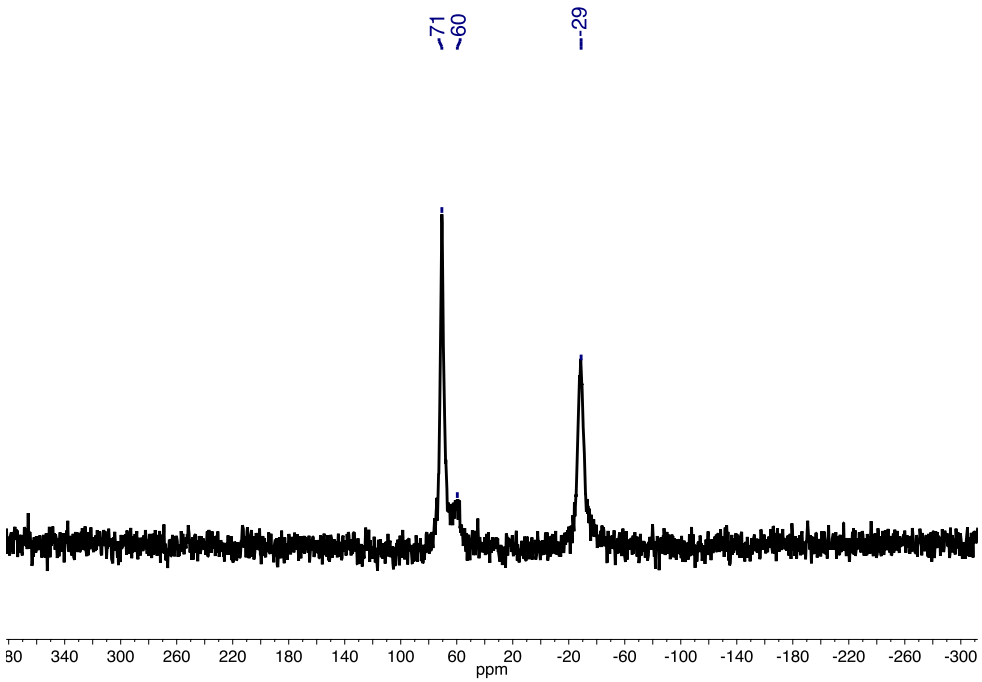

5.11. Electrochemical Data

Table 5.3. Electrochemical data of the series $[Co_{12}Se_{16}(PEt_3)_{10}]^n$ (**FD**), $[Co_6Se_8(PEt_3)_6]^n$ (**M**), $[Co_{12}Se_{16}(PEt_3)_5(CNC_6H_4NC)]^n$ (**BD**), $[Co_6Se_8(PEt_3)_5(CNC_6H_3Me_2)]^n$, and $[Co_6Se_8(PEt_3)_5(CO)]^n$.

Reduction potentials ($E_{1/2}$) vs $Fc^{0/+}$ (V)[a]					
$[Co_{12}Se_{16}(PEt_3)_{10}]^n$ (**FD**)					
$[Co_{12}]^- \rightleftharpoons [Co_{12}]^0 \rightleftharpoons [Co_{12}]^+ \rightleftharpoons [Co_{12}]^{2+} \rightleftharpoons [Co_{12}]^{3+} \rightleftharpoons [Co_{12}]^{4+} \rightleftharpoons [Co_{12}]^{5+}$					
-2.03	- 1.35	- 0.70	- 0.19	0.26	0.61
$[Co_6Se_8(PEt_3)_6]^n$ (**M**)					
$[Co_6]^{2-} \rightleftharpoons [Co_6]^- \rightleftharpoons [Co_6]^0 \rightleftharpoons [Co_6]^+ \rightleftharpoons [Co_6]^{2+} \rightleftharpoons [Co_6]^{3+}$					
~ - 2.53		- 0.87	- 0.18	0.32	
$[Co_{12}Se_{16}(PEt_3)_{10}(CNC_6H_4NC)]^n$ (**BD**)					
$[\{Co_6\}\text{-L-}\{Co_6\}]^{2-} \rightleftharpoons [\{Co_6\}\text{-L-}\{Co_6\}]^0 \rightleftharpoons [\{Co_6\}\text{-L-}\{Co_6\}]^{2+} \rightleftharpoons [\{Co_6\}\text{-L-}\{Co_6\}]^{4+} \rightleftharpoons [\{Co_6\}\text{-L-}\{Co_6\}]^{6+}$					
~ - 2.31		- 0.72	- 0.08	0.41	
$[Co_6Se_8(PEt_3)_5(CNC_6H_3Me_2)]^n$					
$[Co_6]^- \rightleftharpoons [Co_6]^0 \rightleftharpoons [Co_6]^+ \rightleftharpoons [Co_6]^{2+} \rightleftharpoons [Co_6]^{3+}$					
~ - 2.42	- 0.81	- 0.13	0.38		
$[Co_6Se_8(PEt_3)_5(CO)]^n$					
$[Co_6]^- \rightleftharpoons [Co_6]^0 \rightleftharpoons [Co_6]^+ \rightleftharpoons [Co_6]^{2+}$					
- 2.04	- 0.62	0.01			

[a]In cases where the peak extrema are not well defined, or the redox event is irreversible, the $E_{1/2}$ was estimated (e.g. for the 0/-1 couples of $[Co_6Se_8(PEt_3)_6]^n$ and $[Co_6Se_8(PEt_3)_5(CNC_6H_3Me_2)]^n$).

5.12. Details of Density Functional Theory Analysis

All quantum chemical calculations were performed using Jaguar, version 9.5, Schrodinger, Inc., New York, NY, 2017.[16] All calculations were done using density functional theory, using the B3LYP functional and 6-31g**/LACVP** basis sets for the light/heavy atoms, respectively. The geometries of all of the molecules referred to in the text were optimized, and geometrical coordinates will be provided upon request. In each of the molecules studied trimethylphosphine ($P(CH_3)_3$) was used as the two-electron donor ligand rather than triethylphosphine ($P(C_2H_5)_3$). In order to ensure that the calculations resulted in authentic spin-states, spin-restricted methods were used throughout.

$Co_6Se_8(PMe_3)_5$: In order to determine the electronic structure of this molecule we determined that of the parent, $Co_6Se_8(PMe_3)_6$, removed one of the phosphine ligands, and optimized the structure of the coordinatively unsaturated molecule in both its singlet and triplet states. We found no significant differences between the optimized geometries of the two states. We found the total energy of lowest-energy singlet state to be (-3250.4757 h), and that of the lowest-energy triplet state to be (-3250.4821 h). Thus, these calculations indicate that the triplet is lower than the singlet by ~6 mh, or roughly 4 kcal/mol.

$Mo_6S_8(PMe_3)_5$: We followed a similar procedure to determine the electronic structure of this molybdenum sulfide cluster. We found the total energy of the lowest-lying singlet state to be (-5897.0953 h), and that of the lowest-lying triplet state to be (-5897.0773 h). This indicates that the singlet state is lower than the triplet by ~18 mh, or roughly 11 kcal/mol.

The complexities of the electron-correlation problem in these cases make the quantitative accuracy of these splittings problematic, but we believe the trends are qualitatively reliable. The remarkably different characters of the two coordinatively unsaturated clusters is illustrated by

pictures of the two singly-occupied orbitals in the two triplet clusters (see below). In the Co_6Se_8 cluster the two singly-occupied orbitals suggest a broken Co-Se bond; in the Mo_6S_8 cluster they suggest a broken Mo-Mo bond.

Passivated Oligomers of $[Co_6Se_8]$: Using the observed molecular structure of the fused dimer of Co_6Se_8 as a guide, we examined the structures (both geometrical and electronic) of the fused dimer, trimer and tetramer of this cluster. In each case we added a PMe_3 ligand to each exposed Co atom. We considered just a "linear" arrangement of the clusters. We optimized each structure as described above. The energies we quote in the text are from these optimized geometries.

5.13. Single Crystal X-ray Diffraction

Table 5.4. Crystallographic data for **1**, **2**, $[Co_{12}Se_{16}(PEt_3)_{10}][PF_6]$, and $Co_{12}Se_{16}(PEt_3)_{10}$.

	$[Co_6Se_8(PEt_3)_5(C(H)SiMe_3)][PF_6]$ (**1**)	$[Co_{12}Se_{16}(PEt_3)_{10}][PF_6]_2$ (**FD**, dication)
Chemical formula	$C_{34}H_{85}Co_6F_6P_6Se_8Si$	$C_{62}H_{152}Cl_6Co_{12}F_{12}P_{12}Se_{16}$
Formula weight	1807.18	3680.69
Space group	$P2_1/c$	$P\text{-}1$
***a* (Å)**	15.2307(4)	13.1702(3)
***b* (Å)**	17.9156(6)	13.9813(4)
***c* (Å)**	21.9420(4)	15.7568(4)
α (deg)	90	77.901(2)
β (deg)	99.304 (2)	81.519(2)
γ (deg)	90	88.796(2)
***V* (Å^3)**	5154.0 (4)	2805.78(13)
Z	4	1
μ (mm^{-1})	20.631	22.826
T (K)	100	140
***R*1[a] (*wR*2[b])**	0.0510 (0.1372)	0.0554 (0.1572)
Reflections	11777	11195

Table 5.4. *Continued…*

	$[Co_{12}Se_{16}(PEt_3)_{10}][PF_6]$ (**FD**, monocation)	$Co_{12}Se_{16}(PEt_3)_{10}$ (**FD**, neutral)
Chemical formula	$C_{60}H_{150}Co_{12}F_6P_{11}Se_{16}$	$C_{60}H_{150}Co_{12}P_{10}Se_{16}$
Formula weight	3296.98	3152.01
Space group	*P–1*	*P–1*
***a* (Å)**	12.6453(4)	14.6247(3)
***b* (Å)**	13.7404(5)	17.2494(4)
***c* (Å)**	16.3357(6)	43.0975(6)
α (deg)	108.819(3)	79.8075(16)
β (deg)	103.331(3)	81.7011(15)
γ (deg)	98.564(3)	65.298(2)
***V* (Å^3)**	2536.24(16)	9691.2(4)
Z	1	4
μ (mm^{-1})	23.498	24.315
T (K)	100	100
***R*1[a] (*wR*2[b])**	0.0673 (0.1984)	0.0531 (0.1435)
Reflections	7382	38093

Figure 5.17. Molecular structure of $[Co_6Se_8(PEt_3)_5(C(H)SiMe_3)][PF_6]$ (**1**). Hydrogen atoms (except C(*H*)$SiMe_3$) and PF_6^- counterion have been omitted to clarify the view. Thermal ellipsoids are set at 50% probability level.

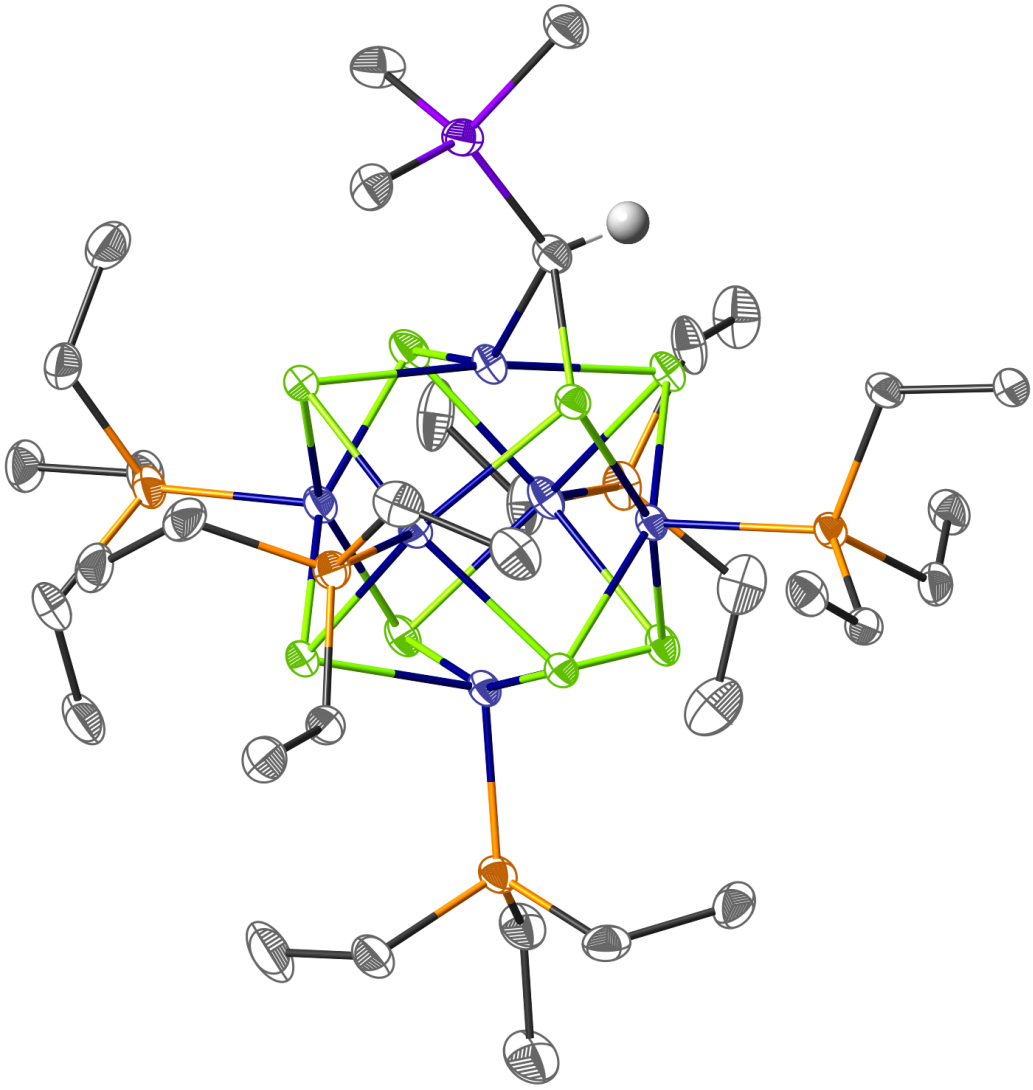

Figure 5.18. Molecular structure of $[Co_{12}Se_{16}(PEt_3)_{10}][PF_6]_2$ (**FD**, dication). Hydrogen atoms have been omitted to clarify the view. Thermal ellipsoids are set at 50% probability level.

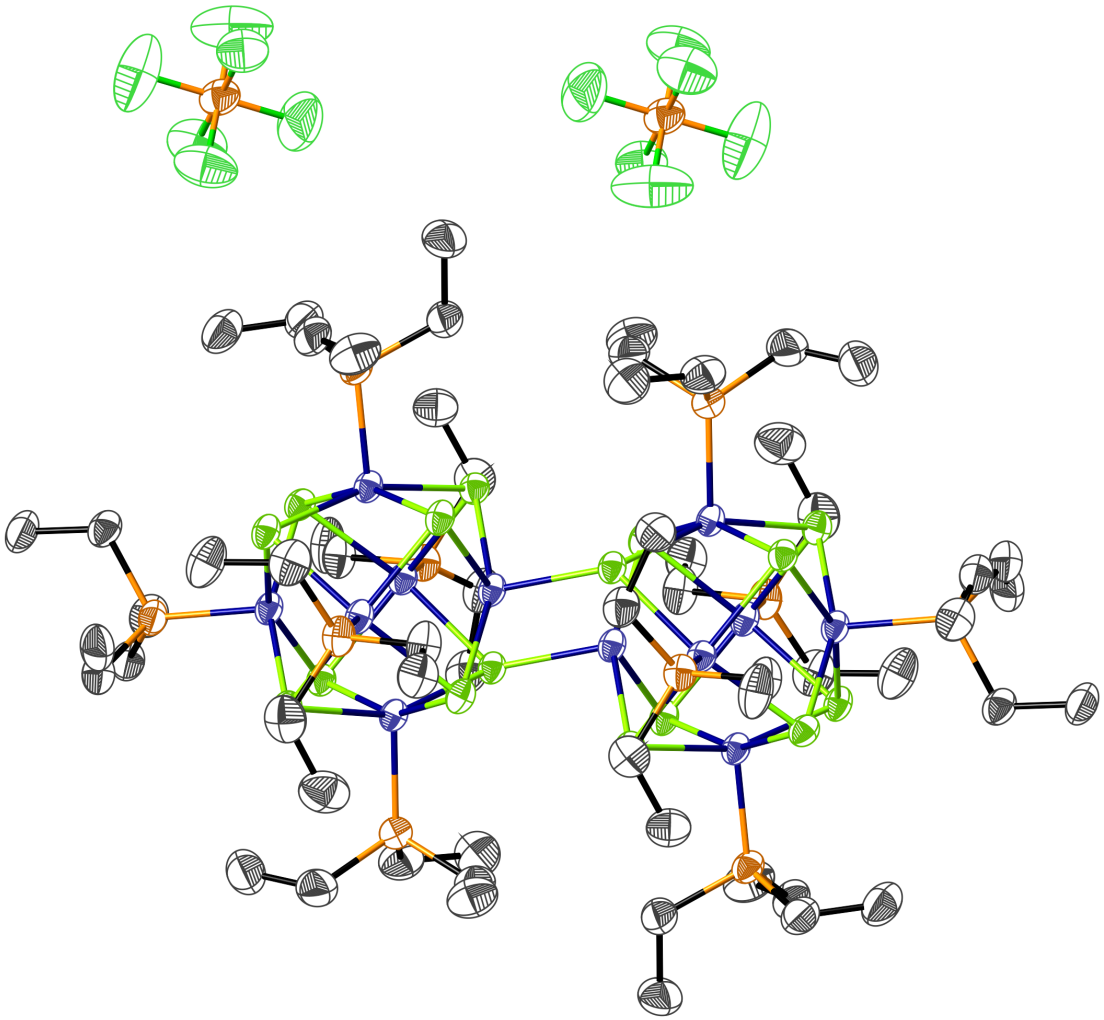

Figure 5.19. Molecular structure of $[Co_{12}Se_{16}(PEt_3)_{10}][PF_6]$ (**FD**, monocation). Hydrogen atoms have been omitted to clarify the view. Thermal ellipsoids are set at 50% probability level.

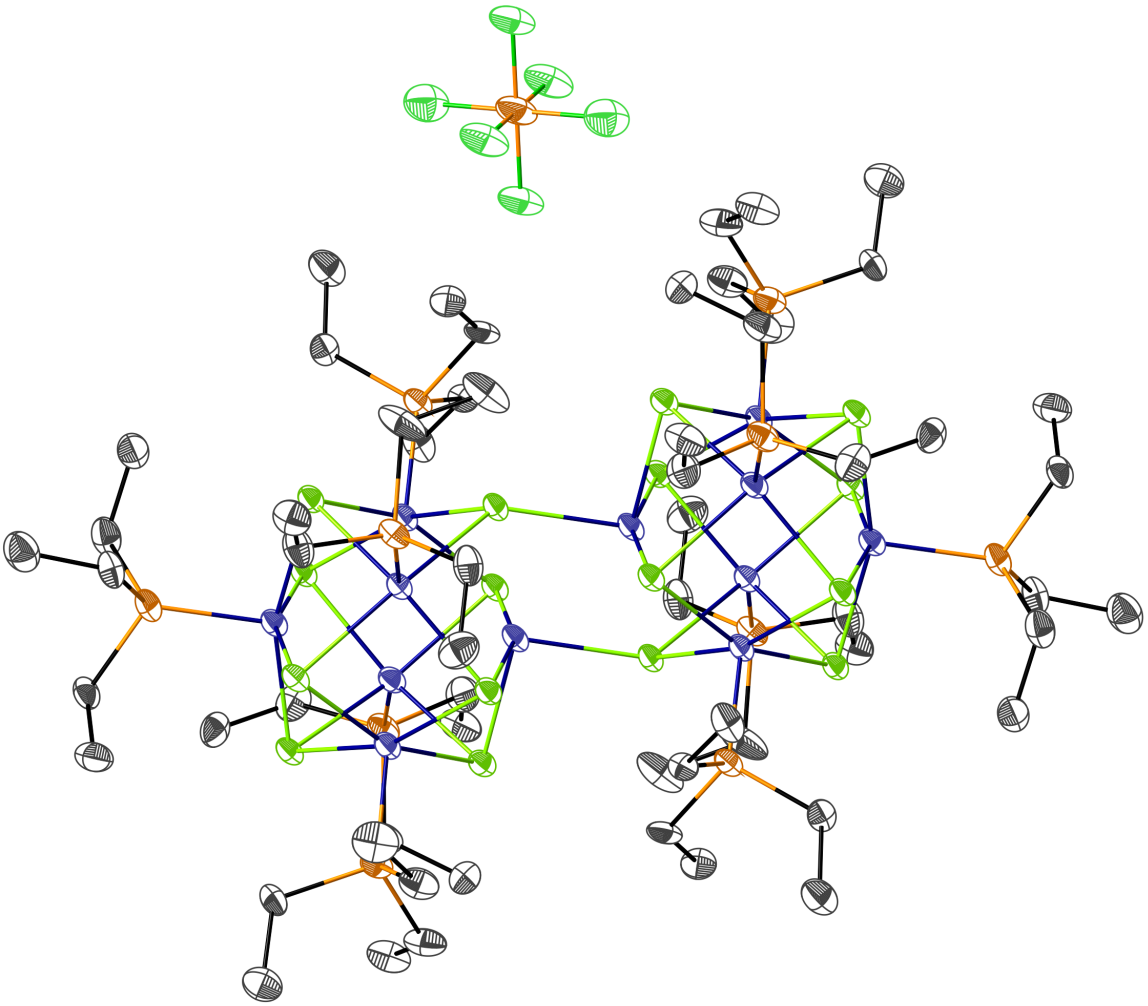

Figure 5.20. Molecular structure of $Co_{12}Se_{16}(PEt_3)_{10}$ (**FD**, neutral). Hydrogen atoms have been omitted to clarify the view. Thermal ellipsoids are set at 50% probability level.

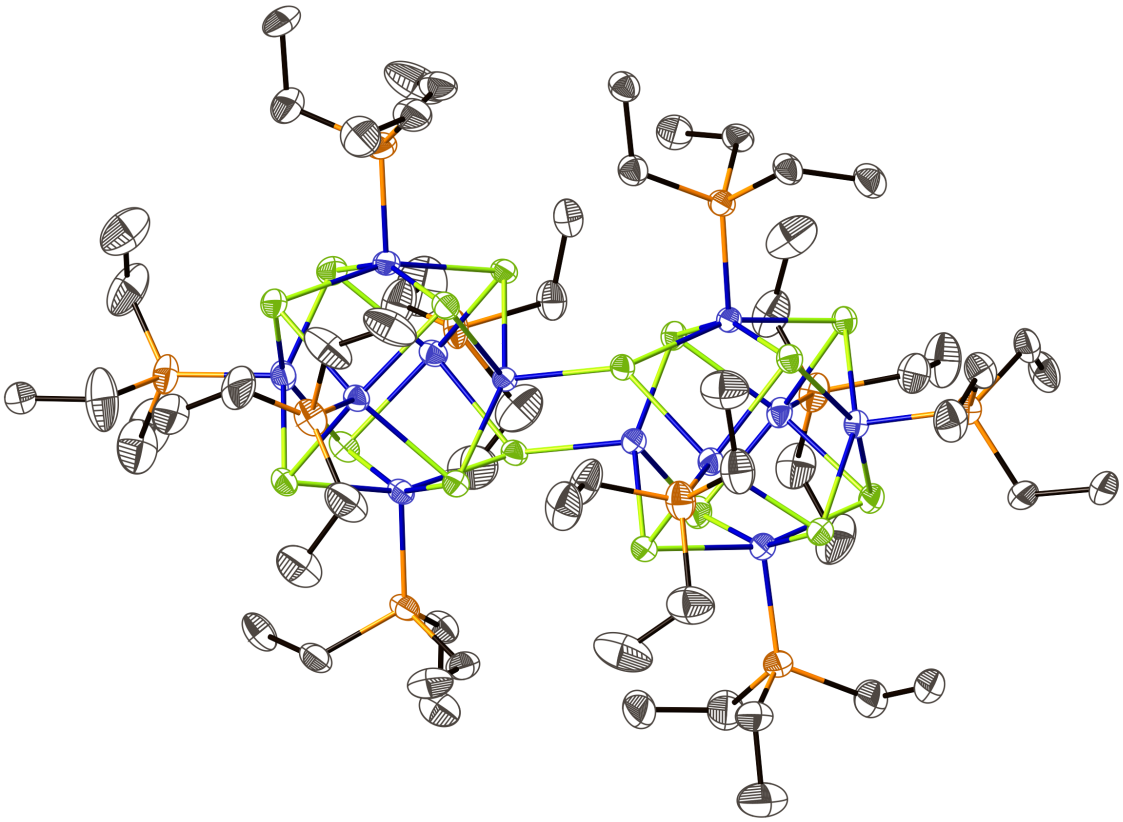

5.14. [Co_6Se_8] Precursor to One-Dimensional Wires

In this chapter I described a new reaction sequence that fuses metal chalcogenide clusters to yield electronically strongly coupled dimers. I briefly share some recent experimental findings that suggest it is possible to extend the design principle used to access a dimer to our building blocks that have multiple CO groups.

For instance, *trans*-$Co_6Se_8(C(H)SiMe_3)_2(PEt_3)_4$ can be readily prepared from its carbonylated precursor, *trans*-$Co_6Se_8(CO)_2(PEt_3)_4$. ^{1}H NMR and single crystal X-ray diffraction confirm this and the synthesis follows.

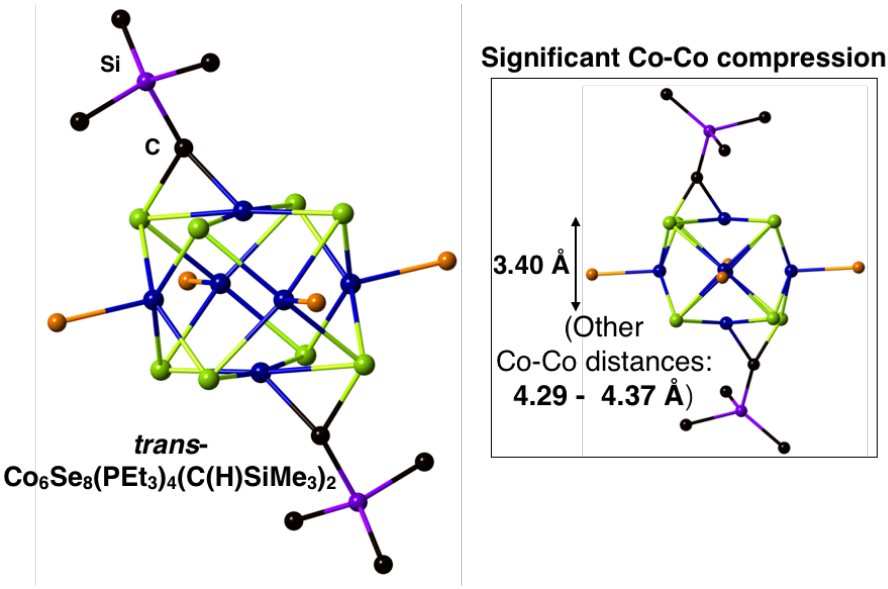

Figure 5.21. Molecular structure of *trans*-$Co_6Se_8(PEt_3)_4(C(H)SiMe_3)_2$.

Synthesis of *trans*-$Co_6Se_8(C(H)SiMe_3)_2(PEt_3)_4$. Inside the glovebox, a J. Young tube was loaded with a solution of *trans*-$Co_6Se_8(PEt_3)_4(CO)_2$ (0.010 g, 0.006 mmol, 1 eq.) in d_6-benzene (1 mL). 13 µL of a (trimethylsilyl)diazomethane solution (2.0 M in hexanes, 0.024 mmol, 4 eq.) was added. The reaction mixture was irradiated using a 450 nm LED light for 2 hours at room temperature. Figure 5.X displays the ^{1}H NMR of the crude reaction mixture for this conversion, in which the only visible peaks are attributed to the product, *trans*-

$Co_6Se_8(PEt_3)_4(C(H)SiMe_3)_2$, and unidentified $SiMe_3$ derivatives from 0.3 ppm to - 0.25 ppm, with complete disappearance of starting material. The d_6-benzene was removed in vacuo, and the solids were triturated with pentane. The solids are partially soluble in pentane and this solution was saved. Figure 5.x displays the ^1H NMR of the washed solids. Single crystals grew from the pentane supernatant.

The crystal data was not of good enough quality and must be re-obtained, but it nevertheless reveals important information about the bis-$C(H)SiMe_3$ species. The molecule is shown in Figure 5.xa. The core is compressed even more dramatically than in the mono-carbene species, with an antipodal Co-Co distance of 3.4 Å (compared to 3.7 Å in $[Co_6Se_8(PEt_3)_5(C(H)SiMe_3)][PF_6]$.

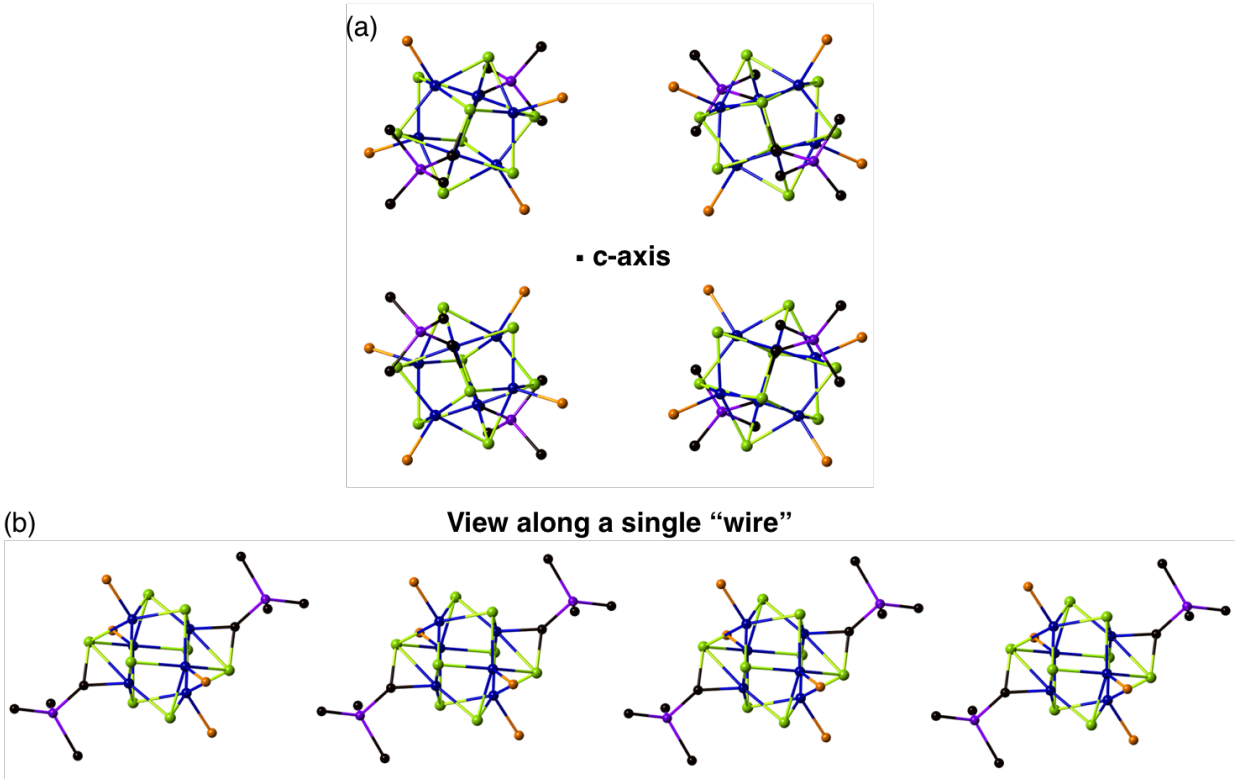

Figure 5.22. (a) Structure of *trans*-$Co_6Se_8(PEt_3)_4(C(H)SiMe_3)_2$ from SCXRD, showing a view of the packing along the c-axis into 1D wires. (b) Single wire along its axis, showing the alignment of $–C(H)SiMe_3$ groups and "fusion sites" predisposed to polymerize.

Perhaps significantly, the molecule packs into wires along the *c*-axis (Figure 5.xa). Figure 5.xb shows one of these "wires". The orientation of the –C(H)$SiMe_3$ groups and "fusion sites" suggest that, under the right conditions, the crystal could undergo a reaction in the solid state to create 1D wires in which the cores fuse and remain intact.

This polymerization is also something that should be pursued in solution. Dissolving [C(H)$SiMe_3$]–containing [Co_6Se_8] clusters into coordinating solvents like pyridine leads to the formation of pyridine-coordinated species. In the case of $Co_6Se_8(PEt_3)_5$(C(H)$SiMe_3$), this seems to form $Co_6Se_8(PEt_3)_5$(pyridine). Upon removal of the pyridine and subsequent dissolution in C_6D_6, the fused dimer forms (observed by ^{1}H NMR). By controlling the amount of non-coordinating solvent added to a pyridine solution (through slow diffusion, for example), it may be possible to access oligomers of fused [Co_6Se_8], by applying this pyridine/benzene sequence to *trans*-Co_6Se_8(C(H)$SiMe_3)_2(PEt_3)_4$.

Figure 5.23. ^{1}H NMR spectrum in C_6D_6 of *trans*-$Co_6Se_8(PEt_3)_4$(C(H)$SiMe_3)_2$ (crude reaction mixture).

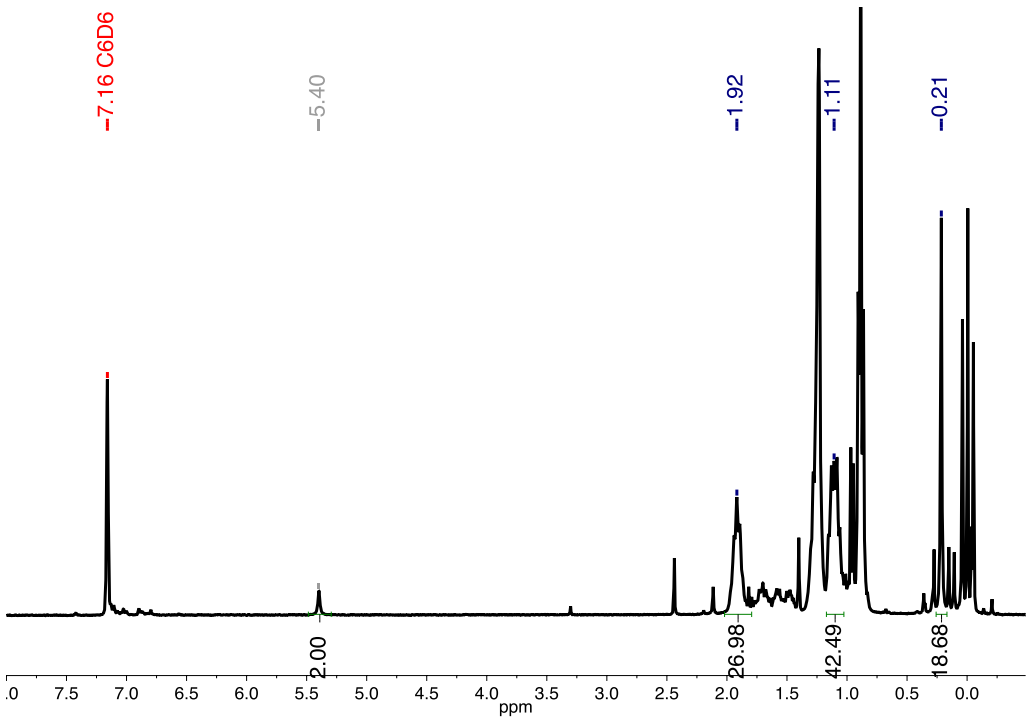

Figure 5.24. ^{1}H NMR spectrum in C_6D_6 of *trans*-$Co_6Se_8(PEt_3)_4(C(H)SiMe_3)_2$ (washed with pentane).

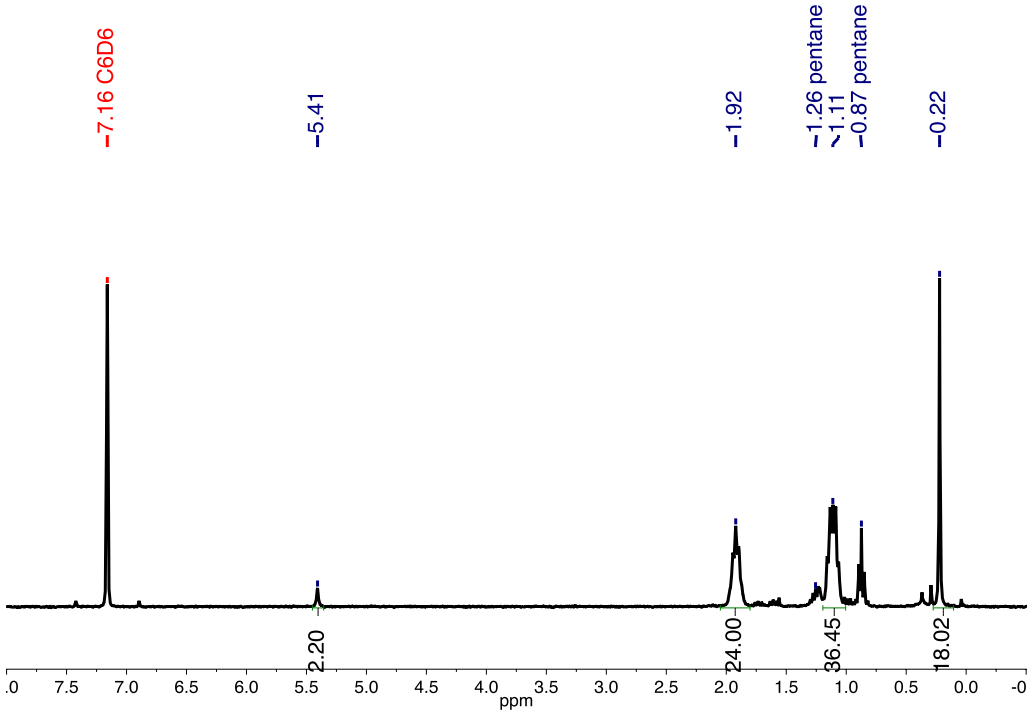

5.15. References

1. (a) Zheng, Z. P.; Long, J. R.; Holm, R. H., *J. Am. Chem. Soc.* **1997,** *119* (9), 2163-2171; (b) Shores, M. P.; Beauvais, L. G.; Long, J. R., *J. Am. Chem. Soc.* **1999,** *121* (4), 775-779; (c) Beauvais, L. G.; Shores, M. P.; Long, J. R., *Chem. Mater.* **1998,** *10* (12), 3783-+; (d) Tulsky, E. G.; Crawford, N. R. M.; Baudron, S. A.; Batail, P.; Long, J. R., *J. Am. Chem. Soc.* **2003,** *125* (50), 15543-15553; (e) Choi, B.; Yu, J.; Paley, D. W.; Trinh, M. T.; Paley, M. V.; Karch, J. M.; Crowther, A. C.; Lee, C. H.; Lalancette, R. A.; Zhu, X. Y.; Kim, P.; Steigerwald, M. L.; Nuckolls, C.; Roy, X., *Nano Lett.* **2016,** *16* (2), 1445-1449; (f) Naumov, N. G.; Virovets, A. V.; Sokolov, M. N.; Artemkina, S. B.; Fedorov, V. E., *Angew. Chem. Int. Ed.* **1998,** *37* (13-14), 1943-1945; (g) Jin, S.; DiSalvo, F. J., *Chem. Mater.* **2002,** *14* (8), 3448-3457; (h) Roy, X.; Lee, C. H.; Crowther, A. C.; Schenck, C. L.; Besara, T.; Lalancette, R. A.; Siegrist, T.; Stephens, P. W.; Brus, L. E.; Kim, P.; Steigerwald, M. L.; Nuckolls, C., *Science* **2013,** *341* (6142), 157-160.

2. (a) Fischer, O., *Appl. Phys.* **1978,** *16* (1), 1-28; (b) Scharfe, S.; Kraus, F.; Stegmaier, S.; Schier, A.; Fassler, T. F., *Angew. Chem. Int. Ed.* **2011,** *50* (16), 3630-3670; (c) Saito, T.; Imoto, H., *Bull. Chem. Soc. Jpn.* **1996,** *69* (9), 2403-2417; (d) Perrin, A.; Perrin, C., *Cr Chim* **2012,** *15* (9), 815-836; (e) Toberer, E. S.; May, A. F.; Snyder, G. J., *Chem. Mater.* **2010,** *22* (3), 624-634; (f) Chevrel, R.; Hirrien, M.; Sergent, M., *Polyhedron* **1986,** *5* (1-2), 87-94; (g) Schafer, H.; Eisenman.B; Muller, W., *Angew. Chem. Int. Ed.* **1973,** *12* (9), 694-712.

3. (a) Steigerwald, M. L., *Polyhedron* **1994,** *13* (8), 1245-1252; (b) Stuczynski, S. M.; Kwon, Y. U.; Steigerwald, M. L., *J Organomet. Chem.* **1993,** *449* (1-2), 167-172; (c) Steigerwald, M. L.; Siegrist, T.; Stuczynski, S. M., *Inorg. Chem.* **1991,** *30* (10), 2256-2257.

4. Champsaur, A. M.; Velian, A.; Paley, D. W.; Choi, B.; Roy, X.; Steigerwald, M. L.; Nuckolls, C., *Nano Lett.* **2016,** *16* (8), 5273-5277.

5. (a) Khanna, S. N.; Jena, P., *Phys. Rev. B* **1995,** *51* (19), 13705-13716; (b) Tomalia, D. A.; Khanna, S. N., *Chem. Rev.* **2016,** *116* (4), 2705-2774; (c) Claridge, S. A.; Castleman, A. W.; Khanna, S. N.; Murray, C. B.; Sen, A.; Weiss, P. S., *ACS Nano* **2009,** *3* (2), 244-255; (d) Castleman, A. W.; Khanna, S. N., *J. Phys. Chem. C* **2009,** *113* (7), 2664-2675; (e) Chauhan, V.; Reber, A. C.; Khanna, S. N., *J. Am. Chem. Soc.* **2017,** *139* (5), 1871-1877.

6. Champsaur, A. M.; Meziere, C.; Allain, M.; Paley, D. W.; Steigerwald, M. L.; Nuckolls, C.; Batail, P., *J. Am. Chem. Soc.* **2017,** *139* (34), 11718-11721.

7. Hong, M. C.; Lei, X. J.; Huang, Z. Y.; Jiang, F. L.; Liu, H. Q., *Chinese Sci. Bull.* **1992,** *37* (21), 1798-1803.

8. We have performed similar analysis for the cationic species and obtained similar results. In $[(Et_3P)_5Co_6Se_8]^+$ the lowest energy state is a quartet, with a doublet lying slightly higher in energy. The neutral case is simpler to describe, so we chose that case as our focus.

9. Ward, M. D., *Chem. Soc. Rev.* **1995,** *24* (2), 121-134.

10. (a) Kamiguchi, S.; Imoto, H.; Saito, T., *Chem. Lett.* **1996,** (7), 555-556; (b) Amari, S.; Imoto, H.; Saito, T., *Chem. Lett.* **1997,** (10), 967-968; (c) Amari, S.; Imoto, H.; Saito, T., *J Chin Chem Soc-Taip* **1998,** *45* (4), 445-450; (d) Zheng, Z. P.; Holm, R. H., *Inorg. Chem.* **1997,** *36* (23), 5173-5178; (e) Cecconi, F.; Ghilardi, C. A.; Midollini, S.; Orlandini, A., *Inorg. Chim. Acta* **1993,** *214* (1-2), 13-15.

11. (a) Kucur, E.; Riegler, J.; Urban, G. A.; Nann, T., *J. Chem. Phys.* **2003,** *119* (4), 2333-2337; (b) Haram, S. K.; Quinn, B. M.; Bard, A. J., *J. Am. Chem. Soc.* **2001,** *123* (36), 8860-8861.

12. Cao, S.; Chen, Y.; Kang, L.; Lin, Z. S.; Fu, W. F., *J. Mater. Chem. A* **2015,** *3* (36), 18711-18717.

13. Garcia-Garcia, F. J.; Larsson, A. K.; Noren, L.; Withers, R. L., *Solid State Sci.* **2004,** *6* (7), 725-733.

14. Brus, L., *J. Phys. Chem.* **1986,** *90* (12), 2555-2560.

15. Wyckoff, R. W. G., *Crystal Structures 1*. Interscience Publishers: 1963.

16. Bochevarov, A. D. *et al*. Jaguar: A high-performance quantum chemistry software program with strengths in life and materials sciences. *Int. J. Quantum. Chem.* **113**, 2110-2142 (2013).